Transport processes at the earth magnetopause

Roch Smets

Résumé

Transport Processes at the earth magnetopause

The thin interface between the solar wind flowing around the Earth and the inner magnetosphere is a key region for mass, momentum and energy transfer. Yet, it is very controversial to identify the procress of such transfer as well as any quantitative measure of their efficiency. This transition region, called the magnetopause, is the loci of importants gradient in the particle density, bulk flow velocity, magnetic field direction and magnitude. We review in this thesis the nonlinear particle dynamics in such thin current sheet and the anomalous transport resulting from the Kelvin-Helmholtz instability (chapter 1), the diffusion process resulting from electromagnetic fluctuations (chapter 2), the collisionless magnetic reconnection process in asymmetric current sheets (chapter 3), and some new perspectives on magnetic reconnection (chapter 4).

Processus de transports à la magnétopause terrestre

La fine interface entre le vent solaire en écoulement autour de la Terre et sa magnétosphère interne est une région clé pour le transfert de masse, d'impulsion et d'énergie. L'identification de processus de transport ainsi qu'une mesure quantitative de leur efficacité est encore un sujet controversé. Cette région de transition que l'on appelle la magnétopause est le lieu d'importants gradients de la densité de particules, de la vitesse du flot moyen, et de la direction et/ou du module du champ magnétique. Dans ce manuscrit, nous revenons sur la dynamique non linéaire des particules dans une telle couche de courant ainsi que sur le transport anormal qui résulte de l'instabilité Kelvin-Helmholtz (chapitre 1), sur les processus de diffusion associés aux fluctuations électromagnétiques (chapitre 2), sur les processus de reconnection magnétique non-collisionnelle dans les couches de courant asymetriques (chapitre 3), ainsi que sur de nouvelles perspectives sur la reconnection magnétique (chapitre 4).

n^{o} d'ordre :

UNIVERSITE PIERRE ET MARIE CURIE
-PARIS 6-

HABILITATION A DIRIGER LES RECHERCHES

Présentée par
Roch SMETS

Spécialité : Physique
Mention : Physique des Plasmas

TRANSPORT PROCESSES AT THE EARTH MAGNETOPAUSE

soutenu le 30 Septembre 2013 devant le jury composé de

Francesco CALIFANO	Rapporteur
Patrick HENNEBELLE	Examinateur
Fabrice MOTTEZ	Rapporteur
Thierry PASSOT	Rapporteur
Benoit SEMELIN	Président

Contents

Introduction

I started my PhD work using test-particle simulations to investigate the structure of particle distribution functions in different regions of the Earth magnetosphere. To do so, we use a prescribed electric and magnetic field and calculate the particle orbits. Using various statistical methods, we build distribution functions, and try to find analytical models to describe the obtained structures, as well as their occurence in satellites data. This implies to understand the appearance of chaos in particle dynamics and their non-integrability : the statistical treatment means that one has to know how a particle orbit is representative of other particles in a close subset of the phase space. A major criticism of the test-particle approach is that in plasma with $\beta \sim 1$ (ratio of kinetic to magnetic pressure) the self-consistency is important. This work is not detailed in this thesis because at the end of my PhD work, I started to work with self-consistent electromagnetic codes.

I started my own research work in trying to revisit the results obtained with test-particle calculations with a self-consistent code. More specifically, I was interested in the physics of the magnetopause, the transition region between the cold dense solar wind flowing around the Earth and its hot tenuous plasmas magnetized by the planetary magnetic field. In such transition region, thin current sheets are associated to gradients of the magnetic field, density, temperatures,... As a result, when the gradient scales are of the order of the Larmor radius, particle dynamics is generally no more adiabatic. I was interested in understanding how such non-adiabatic motion were associated to electromagnetic structures. To do so, I used a hybrid code (ions are treated as macro-particles with a Particle-In-Cell technique, and electrons are treated as a massless fluid) that I wrote during and after my post-doc in GSFC with Thomas Moore and Michael Hesse.

I started to work on the Kelvin-Helmholtz instability that can develop on the flank of the magnetopause, because of the velocity shear between the shocked solar and the stagnant plasma of the inner magnetosphere. In magnetized plasmas, this instability has a threshold in which the magnetic field can play a stabilizing role, depending on its direction. This work is detailed in chapter 1 where we investigate the development of the electromagnetic fluctuations as well as the non-linear particle dynamics in the current sheet. We tried to exhibit the kinetic structures observed in such topologies, as well as the efficiency of the mass exchange process. From these

studies, it appeared that the electromagnetic fluctuations play an important role. More specifically, these fluctuations are the sources of anomalous transport across the magnetic field that is necessary to the mass transfer across the boundary. It took me a while to understand that the problem of anomalous diffusion (i.e. not associated to any collisions) was the most important point to investigate in this context. In chapter 2, we detail how we understand the concept of diffusion, the way to evaluate a diffusion coefficient in self-consistent simulations, as well as the relative importance of electric and magnetic fluctuations (as well as their coupling). The beginning of an analytical work is also proposed. Concomitantly, Nicolas Aunai started a PhD thesis on collisionless magnetic reconnection that Gérard Belmont and I supervised. His work will be presented in chapter 3. Using the same hybrid code, he investigated the nature and structure of the electric field in the reconnection region, and exhibited its relations with the particle dynamics and the associated fluid moments. He also investigated how reconnection develops in asymmetric current sheet to quantify the relative importance of the heating process and the acceleration process. In chapter 4, I present a collaborative work with Gérard Belmont and Nicolas Aunai on a kinetic equilibrium that can be used in hybrid simulations to study asymmetric current sheets. In this chapter, I will also present preliminary numerical results of magnetic reconnection in a topology encountered in laser-induced magnetic reconnection. This work is devoted to the preparation of laboratory experiments using laser in High Energy Density Plasmas.

— 1 —

Kelvin-Helmholtz instability at the Earth magnetopause

The origin of magnetospheric plasma has been extensively studied using both *in situ* observations, theoretical models and numerical simulations. The ionosphere and the solar wind being the two possible sources, their relative importance are still discussed.

Several observations have demonstrated that the ionosphere supplies plasma to the Earth magnetosphere (MSP) (e.g. [**?**], [**?**]). Using 3D multi-fluid simulations for different Interplanetary Magnetic Field (IMF) directions, [**?**] showed that under southward IMF, the convection of ionospheric plasma out of the polar cap region is the major contribution to the plasma sheet population.

Mass entry process from the solar wind can also supply magnetospheric plasma and many observations have been collected at the magnetopause (MP). The occurrence of high-speed plasma flows has been interpreted as a signature of reconnection processes (e.g. [**?**], [**?**]) associated to mass transport.

At the Earth MP, the strong velocity shear between the magnetosheath (MSH) plasma (the shocked solar wind flowing in the anti-solar direction) and the quasi-stagnant plasma of the inner MSP can be the source of a Kelvin-Helmholtz instability. This instability can be associated with magnetic reconnection (see [**?**]), but could also result in mass exchange process through the MP by a diffusive process, without invoking magnetic reconnection. We investigate this question more in details in this chapter. In section 1.1, we give insights on the MP structure and dynamics resulting from the collection of many satellites observations, in section 1.2, we present the results obtained with a test-particle approach, and in section 1.3, we present the results obtained with hybrid self-consistent simumlations.

1.1 Structure and dynamics of the Earth magnetopause

Using ISEE 1 and 2 measurements, [**?**] showed that the average thickness of the low-latitude dayside MP is about 800 km. The average MP speed in the normal direction is a few tens of kilometers per second, and β (the ratio of kinetic pressure over magnetic pressure) is about 1, this value being larger (smaller) in the MSH (MSP) (see e.g. [**?**]).

The magnetic topology of the MP is of primary importance as it controls the mass loading process from the solar wind in the inner MSP. The first model of open magnetosphere proposed by [**?**] invokes, at least locally, a component of the magnetic field normal to the MP. Examining EXPLORER 12 magnetic field measurements, [**?**] showed that in most MP crossings, the magnetic field component normal to the MP is very weak, and the magnetopause is thus essentially a tangential discontinuity (i.e. the magnetic field is always tangential to the MP). Studying the MP polarization, [**?**] also identified it as a tangential discontinuity, and showed a rotation of the magnetic field from its asymptotic values on both sides of the MP.

When the MSP is closed, the magnetic flux pile-up against MP —first predicted by [**?**]— and the resulting plasma depletion layer are observed (e.g. [**?**]). The absence of magnetic flux pile-up is sometimes interpreted as a consequence of the open structure of the MP (see e.g. [**?**]). The characteristics of the Earth MP are reported in appendix I, as well as the dimensionless parameters used in the forthcoming computations.

The Kelvin-Helmholtz instability appears in a fluid flow in the presence of a shear velocity. In the classical hydrodynamical framework, there is no instability threshold for non-viscous fluid and a velocity shear is always unstable (see e.g. [**?**]). In magnetized plasmas, the magnetic tension of the magnetic field lines tends to limit their bending and thus has a stabilizing effect. It yields an instability threshold (minimum value of the velocity shear) which depends on the parameters of the shear flow. It can easily be shown that, in the incompressible case, the wave vector of the instability in the direction normal to the interface is purely imaginary. The resulting perturbation is a surface wave localized at the interface. The incompressible case with an infinitely thin layer can be easily carried out analytically, and is reported in [**?**].

The solutions of these equations have been discussed for different magnetospheric cases by [**?**]. Let's just emphasize two particular cases : (i) when the magnetic field

is normal to the velocity shear, the flow is unstable whatever the value of the shear, (ii) when the magnetic field is parallel to the velocity shear and densities are equal on each side of the interface, the instability criterion is $\Delta v > 2v_A$.

A major question arising from the development of a KH instability is its ability to trigger any kind of exchange : mass, momentum or energy. To investigate this large scale problem, fluid simulations have been extensively used. Using compressible 2D MHD code, [**?**] showed that up to 2 % of the energy flux can cross the magnetic boundary. [**?**] also showed that the anomalous tangential stress associated with the instability ensures a momentum transport across the discontinuity that can reach a few percents. But of course, the question of mass exchange can hardly be investigated with the same formalism : Any Eulerian description of a plasma can put forward the existence of low or high density structures in the system, but cannot unambiguously make any relation between such structures and an associated mass exchange process. To do so, a Lagrangian description is needed to track the plasma (that can be described in a fluid way or in a kinetic one). It can easily be done using test-particle, PIC self-consistent codes, and could also be done using Smooth Particle Hydrodynamics (or more precisely SPMHD) codes, see e.g. [**?**]. We treat this problem using test-particles (section 1.2) in a topology given by a MHD code, as well as hybrid simulations (section 1.3).

1.2 Test-particle calculations of mass-exchange process

In the incompressible case, [**?**] showed that the growth rate of the instability is such as $\gamma \simeq k\Delta v$. The explicit form of the gradient in the normal direction has to be kept to take into account the thickness of the interface. [**?**] studied the growth rate of the unstable mode depending on the wave vector k. He showed that compressibility yields a bell-shaped curve, that is to say, γ increases with k until a maximum value and then decreases to zero. Denoting a the half thickness of the interface, γ is maximum for $2ka \simeq 1$. An enhancement of the plasma compressibility leads to a decrease of both the growth rate γ and the associated wave vector k. Most of the simulations done by Miura have been done with a length L of the simulation box such as the most unstable mode had a wavelength equal L. It has the advantage to save CPU time as the instability destabilizes quickly. For a larger box size, the most unstable mode can also grow, but with several wavelengths in the simulation box. As put forward by [**?**], the time evolution of the KH instability can give rise

to vortex pairing. As a consequence, small scale eddies feed larger scale ones, this being called the inverse cascade, by opposition with the classical turbulent direct cascade, which is most often from large to small scales.

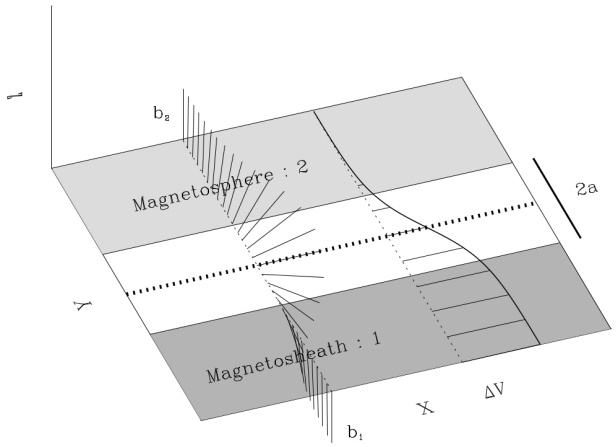

Figure 1.1: Schematic of the initial structure of the MP : rotation of π rad of the magnetic field direction associated to a velocity shear, from [**?**].

In [**?**], hereinafter refered as paper B, we use a $2D^{\frac{1}{2}}$ MHD code (see [**?**]), to compute the magnetic field in the KH instability region. This code solves the classical MHD equations with a polytropic law for the closure equation. Due to numerical resistivity, the magnetic Reynolds number R_M cannot be larger than 8000. The simulations of this study are performed with $R_M = 2000$. The initial geometry of the MP used for MHD simulations is sketched in Fig. 1.1 : the density is uniform, the magnetic field magnitude is constant, its direction rotates through the MP, and there is a velocity shear across the MP. The time evolution of the KH instability can be appreciated in Fig. 2 of paper B, where inverse cascade is clearly depicted.

Single particle dynamics

In [**?**], refered hereinafter as paper A, we put forward the kind of orbits associated to this electric and magnetic topology and in paper B, we explore whatever particles can cross the associated current sheet, and when so, exhibit the associated signatures in the distribution functions. Hence, we use static magnetic maps from MHD results without any electric field to keep a conservative system, and follow the particle

motion in such topology across the MP. The case of particle tracking in a time evolving electromagnetic field is quite tough and is discussed in paper B.

Single particle dynamics in such bended magnetic field is discussed in paper A. Depending on the particle energy value (a dimensionless parameter κ_{RS} is proposed to structure the different dynamical regimes), a particle can experience Speiser, transient or 8-like orbits in the vicinity of the current sheet. Considering an infinitely thin current sheet with $B_X = +1$ for $y > 0$ and $B_X = -1$ for $y < 0$:

- Speiser orbits. The particle experiences a half cyclotron turn in the $y > 0$ half-space around the $B_X > 0$ component following a half cyclotron turn in the $y < 0$ half-space around the $B_X < 0$ component.

- Transient orbits (considering a small B_Z component). A slower gyration around the small B_Z component is associated to the Speiser orbits. Because the fast meandering sequence can only exist if there is a component of the particle velocity in the YZ plane, this sequence cannot last more than half a cyclotron time associated to B_Z.

- 8-like orbits (with a negligible B_Z component). The particle can stay indefinitely trapped in the current sheet. The succession of 2 half cyclotron turns draws a "eight".

Fig. 1.2 illustrates the three kinds of orbits that can be observed (upper panel), as well as the way they can be combined (lower panel). Furthermore, particles can be trapped in the current sheet, certainly as a consequence of the absence of normal component of the magnetic field in the current sheet. In paper B, test-particle calculations are done in dimensionless way, but mainly concern the protons as their Larmor radius are of the order of the MP thickness. We investigate the efficiency of the crossing process, depending on the initial particle energy, pitch angle, as well as the obtained pitch angle distribution (PAD) after scattering. But the first important thing is to evaluate the efficiency of the crossing process.

Efficiency of the crossing process

The number of particles crossing the MP of course depends on the initial number of particles in the simulation as well as the length of the box along the discontinuity. We thus define the crossing rate (CR) as the ratio between the number of crossing

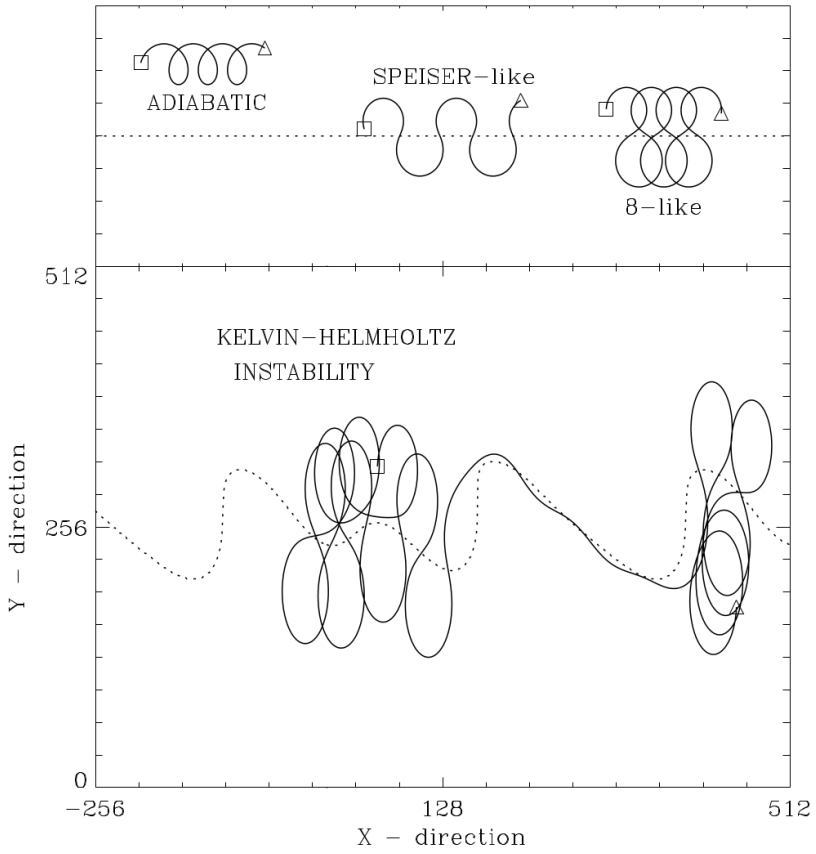

Figure 1.2: Different orbit types in a tangential discontinuity : adiabatic, Speiser-like and 8-like (upper panel). KH instability essentially allows transitions between these different types of motion, from [**?**].

particles to the number of particles located at less than 2 Larmor radius from the MP. As a matter of fact, particles that are initially too far from the MP will never reach it, since the magnetic field is uniform and unbended. In fact, particles can slowly drift toward the discontinuity because of the magnetic fluctuations. This is the problem of particle diffusion in magnetic fluctuations that will be discussed more in details in chapter 2.

Fig. 5 of paper B shows that the CR is not depending on the initial particle energy. This essentially comes from the way the CR is defined (the larger the particle energy, the larger the associated Larmor radii, the wider the strip considered for the

normalization). Fig. 1.3 depicts the CR depending on the initial pitch angle. The CR is larger at small pitch angle, decreases until the initial pitch angle reach $\pi/6$ rad, and then gently increases. This shows that field-aligned particles preferentially cross the MP. If one wants to characterize the PAD after crossing, the value of the particles pitch angle after crossing are important. From Fig. 7 and 8 of paper B, it clearly appears that particles crossing the MP are essentially scattered in the perpendicular direction.

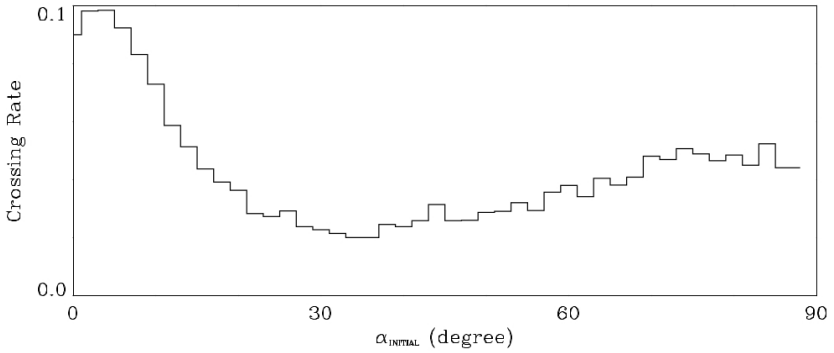

Figure 1.3: Crossing rate of particles depending on their initial pitch-angle, from [**?**].

This suggests that if such particles have to be observed by a satellite, such anisotropy is a key parameter. Nonetheless, a satellite observes at a given point (and at a given time) the whole plasma, composed of crossing and non-crossing particles. Of course, if the non-crossing particles are the dominant population, this peculiar PAD will not be observable. This is an important point for which a clear assertion is difficult ; with test-particle calculations, the particles time-of-flight is not considered. Hence, the characteristic time scale needed to build this PAD is not considered, neither the characteristic time scale associated with its destruction because of kinetic instability.

Entry gates associated to KH instability

Another problem that can be addressed with a test-particle approach is the locus (or loci) of the "entry gates". When the KH instability develops, the interface gets corrugated, and the problem is no more invariant in the direction along the interface. As a consequence, vortices form, collapse, merge, and reform. We cannot investigate

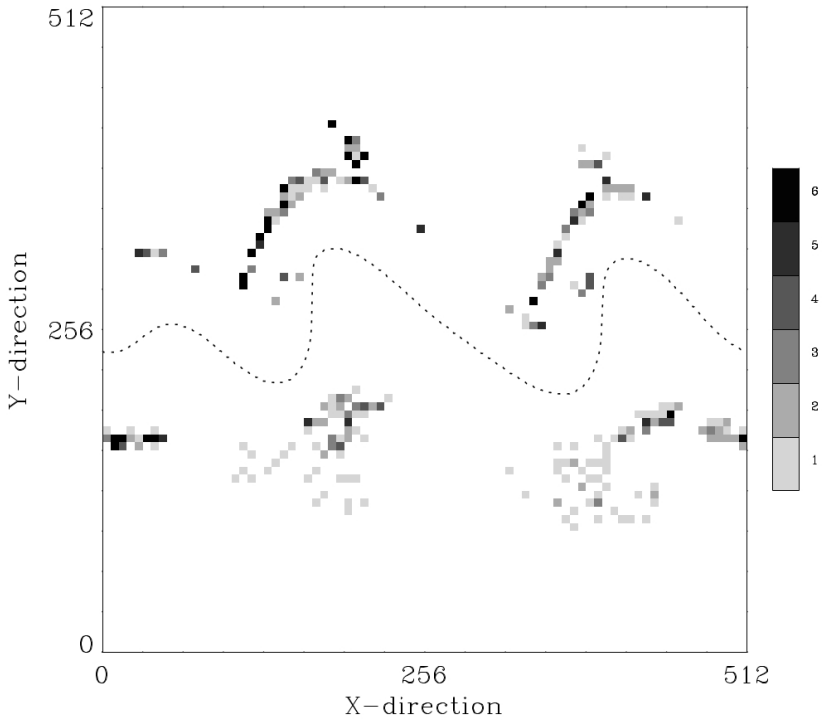

Figure 1.4: Color-coded number of particles crossing the MP. Initial and finel position are depicted in the XY plane, from B.

properly this problem, because it necessitates long simulations and large domains to allow the inverse cascade to occur. Furthermore, as said above, this formalism is not well suited to study the time evolution of the system. Fig. 1.4 depicts the number of crossing particles (in color code) according to the location of the associated entry and exit of the MP. This figure shows that the islands of escaping particles are localized near the edge of each wave front, while they end up narrowly localized near the steep part of the wave profile on the other side of the MP. This point was raised in paper B without any clues for its origin. An explanation can now be suggested.

Fig. 1.5 is a schematic view of the magnetic field lines around the MP. The MP is the locus where the Z component of the magnetic field lines changes sign. In Fig. 1.5, it is the thick dashed line 0. On each side of the MP, the magnetic field lines have also an out-of-plane component, but their projection in the XY plane are depicted by line 1 and line 2. They are less bended than line 0 because the magnetic tension is more effective as the shear velocity (and the source of bent) is smaller.

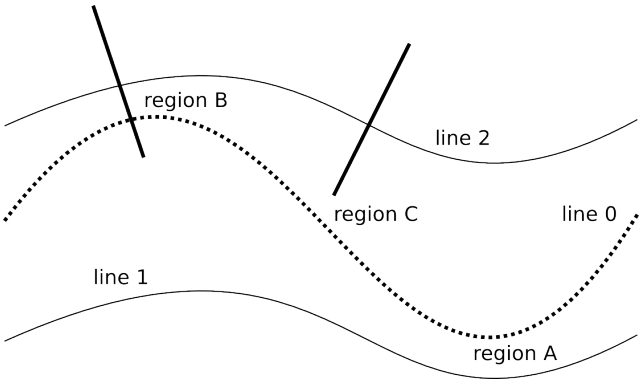

Figure 1.5: Schematic description of the crossing process at the MP, because of FLR effect.

Let's consider a particle on line 2. The projection of its Larmor radius is indicated by a solid thick line, and in region C, it does not encompass line 0. In region A and B, line 1 and 2 tend to be less bent. As a result, the flux tubes of region A and B are pinched. Panel 2 of Fig. 4 of paper B indicates the magnetic pressure. In region C, the magnetic pressure is larger, meaning that the associated Larmor radius is smaller, and hence does not allow to cross the MP. On the other hand, in region B, the magnetic pressure is smaller, hence associated to a larger Larmor radius. The entry gates are hence located where the particles can encompass the MP during their non-adiabatic motion.

This study put forward that protons can cross the MP, because of FLR effects, and stimulated by the development of a KH instability. The larger the particle energy, the larger the number of crossing particles. The efficiency of this process almost not depends on the initial particle pitch angle, but essentially produces perpendicular distributions. Furthermore, the entry gates are essentially located near the edges of the wave front. The same kind of inquiry is now proposed in [**?**] using a self-consistent hybrid code.

1.3 Hybrid simulations of mass-exchange process

The previous study was based on the use of test-particle calculations. This light, flexible and fast technique allows to investigate various problems. But as mentioned, a long standing criticism is that such approach is not self-consistent. In

plasmas where β is not very small, this can be questionable. As a consequence, I started to work on a hybrid code. I got this one during my short post-doc in GSFC in 1999. This is the code originally written by Winske and Quest (see [**?**]). It is based on a predictor-corrector scheme (see [**?**]) to solve the electric and magnetic field. I have totally rewritten this code (in C language) : it is now 3D, parallelized under MPI, and quite versatile regarding the initial and boundary conditions. It is called HECKLE while a companion (fully kinetic PIC) code should also be develloped, named JECKLE[1]. Details on the equations, approximations, numerical scheme, initial and boundary conditions are in appendix K.

Up to now, few studies have been dedicated to the problem of mass exchange through the MP because of KH instability using PIC codes. Using $2D\frac{1}{2}$ hybrid simulations, [**?**] studied the time evolution of a mixing index, providing insights on the total surface close to the instability where particles, initially from both sides of the discontinuity, are mixed. [**?**] also used 2D hybrid simulations to demonstrate the existence of small-scale structures (on the order of the ion Larmor radius) possibly related to such flux transfer events. [**?**] extended this investigation and focused on mass transport, showing that the mixing is quicker and larger than that due to finite Larmor radius overlapping at the interface. [**?**] obtained similar results with 3D hybrid simulations for the same geometry, but showed that a rotation of the magnetic field stabilizes the system, and leads to a less efficient mass transport.

The MP plasma being collisionless, the origin of diffusion cannot be classical viscosity, and many studies (see e.g.[**?**], [**?**]) have been dedicated to diffusion processes in collision-less plasma. On the whole, it is commonly admitted that diffusion is less efficient than magnetic reconnection to ensure mass loading of the inner magnetosphere from the shocked solar wind. Furthermore, diffusion is a quite stationary process while magnetic reconnection is more oftenly an impulsive process. For the mass exchange problem, one can wonder whatever a fast impulsive and localized process (magnetic reconnection) is actually more efficient than a slow, stationary and non-localized process (diffusion). The studies by [**?**] and [**?**] investigated the coupling of the KH instability with smaller scale process, and the resulting turbulence. As a result, in [**?**], hereinafter refered as paper C, we investigate the time evolution of the electric and magnetic field and the associated particle dynamics (in

[1] I'm heckle and jeckle, all rolled into one, people say I'm lots of fun, 'cause I am heckle and jeckle ,buh dum buh duh dum buh duh bah dee dum bah dee dum buh duh dum buh duh bah dee dum...

a self-consistent way) to study the nature and efficiency of the crossing process.

In paper C, the approach is similar as in paper B. We take as initial condition a discontinuity between 2 counter-moving plasmas, and an associated rotation of the magnetic field of π rad on the finite thickness of the discontinuity. This topology is depicted in Fig. 1 of paper C. For the plasma, we have on both sides of the discontinuity a Maxwellian with the same density and the same temperature and a sheared flow velocity. There is no gradient on the magnetic field magnitude and the pressure balance is hence satisfied. This fluid equilibrium is not a kinetic one ; during the first steps of the simulation, small magnetosonic waves (containing the excess of energy) propagate perpendicular to the mean magnetic field. As detailed in paper C (by inspection of the heat flux) an equilibrium is reached before the triggering of the KH instability.

Efficiency of the crossing process

The hybrid formalism is nice for this problem because one can follow each macro-particle. From eq. (K.9) and (K.10), it is clear that the dynamics of macro-particles is the same as the one of particles. In fact, the electric and magnetic field involved in eq. (K.9) and (K.10) are the mean ones. The electric field results from the Ohm's law for the electrons. Hence, this fluid equation cannot take into account any kind of binary collisions (the classical form of the collisional term being an approximation). But in the present case, the plasma is collisionless, meaning that macro-particle dynamics and particle dynamics are exactly the same.

One can unambiguously identify each particle and their initial position. Hence it is an easy task to enumerate how many particles cross the MP[2], and build the associated distribution function.

A first remark is that, as depicted in Fig. 4 of paper C, the number of crossing particles increases through time, in a monotonic way, but at a rate that can gently change through time. In Fig. 1.6, it is clearly demonstrated that the rate of crossing particles (its derivative is represented in solid thick line) increases with the width of the k-spectrum. As discussed in the previous section, the wave front of the KH instability gets steeper while the instability develops, until their sharp structures collapse eventually resulting in vortex-pairing. This is in qualitative agreement with

[2]The MP is defined as in paper B ; this is the loci where the Z component of the magnetic field changes sign

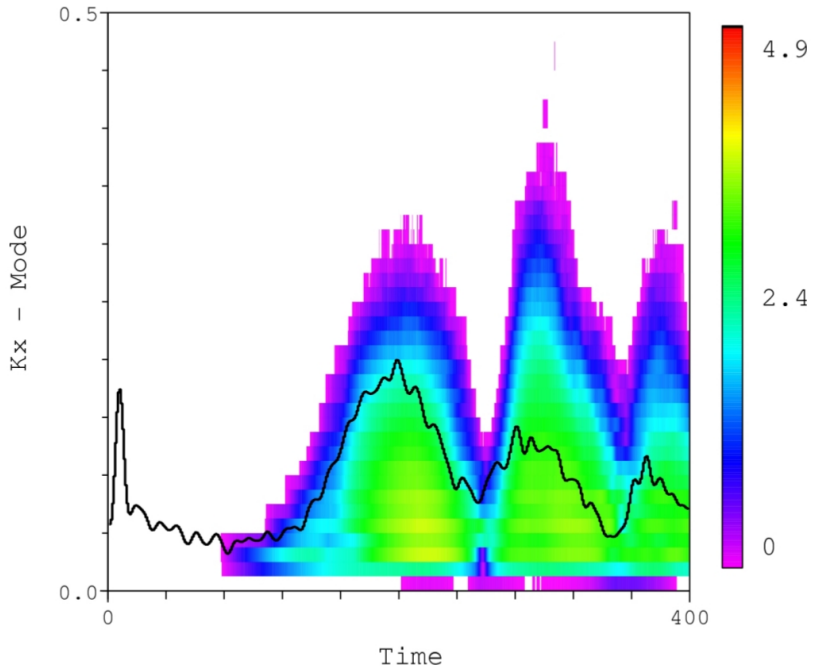

Figure 1.6: Color-coded Y component of the magnetic field depending on the k_X mode (after spatial Fourier transformation) and time. The solid thick line is the time evolution of the derivative of the crossing rate, from [**?**].

the mechanism detailed in Fig. 1.5 ; when the wave front get steeper, the magnetic tension is larger, and amplify the crossing mechanism. Once the vortex crashes, the flux tubes get temporarily more rectilinear and the crossing process gets less efficient. The entry gates are the same as the one described in paper B, showing that test-particle and hybrid formalism can provide the same results.

Distribution functions associated to KH instability

One can also build the distribution function of the crossing particles to see if some peculiar structures appear. Such distributions are depicted in Fig. 1.7. The left panel clearly shows that there is no favored direction in the perpendicular plan, meaning that the distribution is gyrotropic. On the other hand, in the $V_{\parallel} - V_{\perp}$ plan, a very clear "Lima-bean" structure appears. The mean parallel velocity of this distribution can be calculated, and several computation showed that the velocity

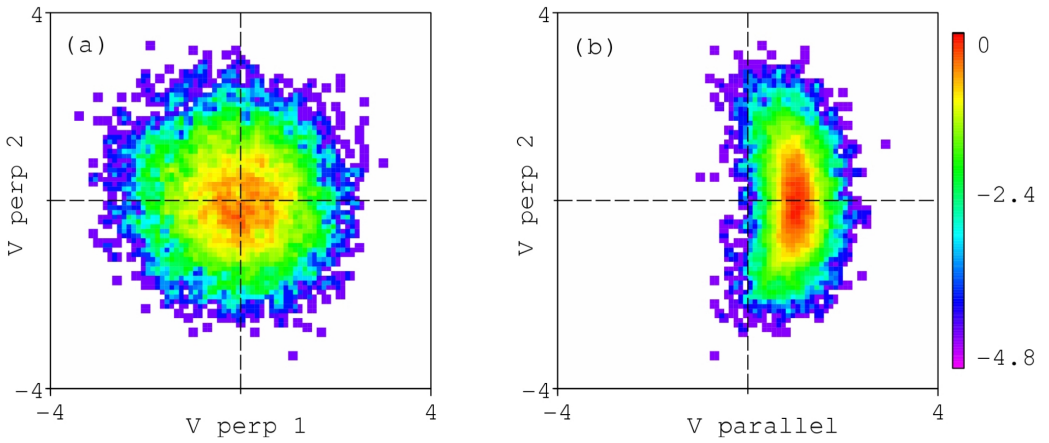

Figure 1.7: Color-coded phase space density of crossing particles : (left) in the perpendicular plane (right) in the parallel-perpendicular plane, from [**?**].

increases with the thickness of the MP, in a very linear way as depicted in Fig. 9 of paper C. To unambiguously demonstrate this, we perform several simulations with varying velocity shear, magnetic field magnitude, density or β value. None of these parameters influence the crossing process.

Simple analytical model

A heuristic interpretation of the penetration process can be obtained with a rough picture of the magnetic field reversal. As a matter of fact, details of the magnetic profile (hyperbolic tangent in the present case) is not necessary and knowledge of the asymptotic value of the magnetic field in each side and at the center of the discontinuity is enough to drive the essential features. The associated process is depicted in Fig. 1.8. One considers side 1 and 2 with a constant magnetic field in the $+Z$ direction and -Z direction respectively, and neglects the drift effect of the electric field : the associated fluid velocity being tangential to the discontinuity, it does not play a significant role in this process. At the interface (the reversal sheet), one also considers a constant magnetic field, in the $+X$ direction.

Let's consider a particle, initially on side 2, with a positive parallel velocity. Starting from an initial position with a positive Z value, this particle, because of its parallel velocity, goes toward the $Z = 0$ plane. Furthermore, because of the magnetic field and its perpendicular velocity, the particle gyrates around a magnetic field line,

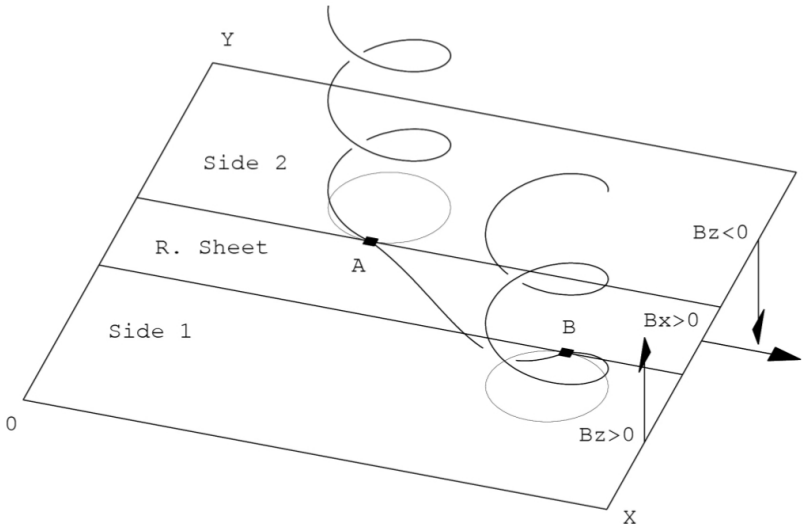

Figure 1.8: Schematic view of the typical orbit followed by a particle crossing the magnetic field reversal, from [**?**].

with a constant Larmor radius. With the appropriate initial position (as chosen in Fig. 1.8), this particle skims the interface between side 2 and the reversal sheet. Because of magnetic fluctuations, this particle can step aside in the reversal sheet. This point is marked A in Fig. 1.8, and for simplicity, chosen to be in the $Z = 0$ plane. To reach side 1 at point marked B, the Larmor radius in the reversal sheet has to be equal to the half thickness of the discontinuity λ. At point A, the perpendicular velocity needed in the calculation of the Larmor radius is in the -Z direction, that is the parallel velocity in side 2. Because there is no electric field, the kinetic energy of the particle is constant, and the parallel velocity in side 1 is equal to the parallel velocity in side 2 (that turns to be a perpendicular velocity in the reversal sheet).

From the mean parallel velocity $V_{\parallel}$ of the "Lima bean", one can compute

$$\zeta = \frac{V_{\parallel}}{\Omega_C} \tag{1.1}$$

where Ω_C is the gyropulsation corresponding to the asymptotic magnetic field magnitude. This is the average distance traveled along the magnetic field by the particles during a cyclotron turn. Hence, the crossing particles are the ones for which the ζ value is equal or larger than λ. This distribution results from a filtering effect on an

initially Maxwellian distribution function for which only particles with $\zeta > \lambda$ cross the interface. This is illustrated in Fig. 13 of paper C.

Paper C hence puts clearly in evidence the way a particle can cross the MP. The results obtained with an hybrid formalism are quite similar to the results obtained with test-particle calculations. Nevertheless, there is a standing problem that drastically influences the efficiency of the mechanism. Far from the discontinuity, the particle motion is the superposition of a gyromotion around the magnetic field lines directed along Z and a drift in the X direction. Both motions cannot influence or modify the distance of a particle (or let say its guiding center) to the discontinuity. Hence, even if a particle satisfy $\zeta > \lambda$, it will not have any chance to cross the MP if it is too far from it. An important problem is hence also to wonder how particles can get close (or far) from the MP.

A first answer is the existence of a fluid drift. As an example, considering the density gradient in the X direction (the far MP is tenuous compared to the dense near one) and the Z direction of the magnetic field, a gradient drift appears in the Y direction, that can bring particles close to the MP. This mechanism certainly exists, but its efficiency is very small if considering the average value of the magnetic field magnitude and the associated density gradient.

Another possibility is the existence of a diffusion process across the mean magnetic field. This can result from the development of small-scales magnetic fluctuations. This is the so-called magnetic turbulent diffusion. As discussed for example by [**?**] and [**?**], KH instability can trigger the appearance of small scales structures in a turbulent way, and this turbulence can be associated to anomalous diffusion. This point will be discussed in chapter 2.

As a conclusion of this chapter, in the absence of magnetic reconnection, particles can cross the MP because of finite Larmor radius effects. When this is the case, a filtering effects results in producing a "Lima bean", initially localized close to the most bended edges of the surface wave. The associated pitch-angle scattering produces a population essentially in the perpendicular direction. But for that issue, a particle needs to get close to the MP. The most efficient mechanism seems to be the magnetic turbulent diffusion. The way to investigate this with self-consistent simulations as well as its efficiency is investigated in chapter 2.

— 2 —

Particle diffusion by electromagnetic fluctuations in magnetized plasmas

It was clear from the previous chapter that particles can cross the magnetopause because of finite Larmor radius (FLR) effects. To do so, the particles have to be close to the magnetopause (MP), i.e. at about a Larmor radius from it. For particles initially far from the MP, we need to identify a possible transport mechanism to drive them close to it. The solar wind plasma being magnetized, this mechanism has to be a transport process across the magnetic field. We investigate in this chapter how magnetic fluctuations can diffuse particles across the magnetic field. We also investigate the influence of the associated electric fluctuations, as well as their possible coupling. In section 2.1, we discuss the different definitions of the diffusion process and introduce the way to calculate it and in section 2.2 we discuss the electric and magnetic contributions to the diffusion coefficient.

2.1 How to calculate the perpendicular diffusion coefficient ?

In a static and uniform magnetized plasma, the motion of a charged particle is completely determined by its gyropulsation ω_C and its Larmor radius ρ_L. When spatial and/or temporal fluctuations exist, the particle dynamics is modified, possibly leading to spatial diffusion. Noting ΔY the displacement in a given direction Y perpendicular to the local mean magnetic field during a time Δt, and $\langle \cdots \rangle$ the average on all the particles, the quantity $\langle \Delta Y^2 \rangle$ allows a quantization of how efficiently a population is spreading in space (in the Y direction). More specifically, if one can define

$$\lim_{\Delta t \to \infty} \frac{\langle \Delta Y^2 \rangle}{2\Delta t} = \kappa_\perp \tag{2.1}$$

$\kappa_\perp$ is called the diffusion coefficient in real space. Similar ratios can be calculated in velocity space to evaluate diffusion in energy or pitch angle.

Particle diffusion in collisionless plasmas is important for cosmic ray modulation in interstellar media (see e.g. [**?**]), particle transport in tokamaks (see e.g. [**?**]), or filling up the magnetosphere with solar wind particles (see e.g. [**?**]). The first major analytical treatment of this problem by [**?**] put forward the two possible contributions : particles can spread by following braided magnetic field lines, or by departing from the magnetic field lines to which they were initially attached. The first mechanism can be studied focusing on the topological properties of the magnetic field lines (see e.g. [**?**]). When this is the only contribution, the particles follow the magnetic field lines like "beads on a string". This has been recently addressed by [**?**] where the braided nature of the magnetic field lines is captured by the calculation of the magnetic field line diffusion coefficient $D_\perp$. The perpendicular diffusion coefficient $\kappa_\perp$ linearly depends on $D_\perp$. This is the so-called Field Line Random Walk (FLRW) model. It should be emphasized that this mechanism cannot be responsible for the filling up of solar wind plasma on magnetospheric field lines without magnetic reconnection. The second mechanism needs a careful investigation of particle dynamics. It has been done up to now using mainly test-particles.

An ansatz for the perpendicular diffusion coefficient was proposed by [**?**] (BAM from the names of its authors). In this model, the stochastic behavior of particles is contained in a single and self-explanatory parameter $\nu_\perp$: the perpendicular decorrelation time (associated with the perpendicular velocity). The two models BAM and FLRW provide lower and upper limits, respectively, for the numerical results of test-particle simulations (see e.g. [**?**]). The Non Linear Guiding Center (NLGC) model of [**?**] could be considered as an achievement of this task as suggested by the nice agreement between analytical model and test-particle simulations. It is worth noticing however that NLGC model needs 3 parameters not determined a priori. Another question raises from these studies ; comparisons have always been done with test-particles simulations in magnetostatic turbulence. This questions the importance of self-consistency and the role of electric fluctuations (and the coupling with magnetic fluctuations).

We hence addressed this problem using the HECKLE code. The first goal is to measure $\langle \Delta Y^2 \rangle$ and see if particle transport across the magnetic field is a diffusive (proportional to t), sub-diffusive (proportional to t^α with $\alpha < 1$) or superdiffusive (proportional to t^α with $\alpha > 1$) process. The second is to evaluate how the diffusion coefficient can depends on the type of fluctuations and its level. We address this problem in [**?**], referenced in appendix as paper D.

Methodology associated to the self-consistent approach

The first way to trigger magnetic and electric fluctuations is naturally the Kelvin-Helmholtz (KH) instability. It was clear in chapter 1 that during the development of the KH instability, magnetic fluctuations can grow, their spectra and level depending on the vortex pairing as illustrated in Fig. 1.6. To make some comparisons, we determined another way to do so. After several tries, we chose an agyrotropic instability as it is the way to generate magnetic fluctuations (and the associated electric fluctuations) in a magnetized plasma in a time scale very small compared to the diffusion time scale, and having stationnary statistical properties. This kind of runs are called 2B because we used two 'beams" in the direction perpendicular to the magnetic field, and details can be found in paper D.

The concept of diffusion comes in when, in a medium, the scales larger than some characteristic scale can be modeled in a closed way, the smaller scales being supposed sufficiently chaotic so that their effect on the large ones can be estimated correctly by their only statistically averaged properties, without any deterministic description of them. The basic notion of "molecular diffusion", invoked in hydrodynamics, can conveniently be taken as a reference, and the other types of diffusion extrapolated from it. In molecular diffusion, the characteristic scale is the collisional mean free path. Taking averages over dimensions large with respect to it, and therefore over a large number of collisions, one can calculate the way the individual particles separate from each other in average because of them and the consequences this separation has on the mean flow, i.e. on the flow integrated over a large number of such particles.

Fluid moments such as density, velocity, and higher moments are defined at a fluid scale l_F, meaning that they result from an average on a volume l_F^3. If some diffusion process takes place because of phenomena at scales larger than l_F, it can be classified as turbulent fluid diffusion and it can be fully described by the fluid equations without introducing any extra term. On the other hand, if some diffusion occurs because of phenomena at scales smaller than l_F, it cannot be described by the ideal fluid theories and some non-ideal terms have to be added, involving in particular the diffusion coefficients. The way to estimate these extra-terms consists in first determining the probability distribution finction (PDF), *i.e.* the distribution function integrated over velocity space and divided by the total number of particles in the system. As outlined by [**?**], this distribution is indeed the organic link between the fluid term associated to dissipation and the value $\langle \Delta Y^2 \rangle$.

Of course, a particle displacement in a given Y direction is a direct consequence of its velocity in this direction. Furthermore, a diffusion process is a departure from a "mean flow", meaning that if v is the particle velocity, and V is the fluid velocity averaged at the particle position on a volume l_F^3, hence, the turbulent displacement is associated to $v - V$. As a consequence, the value of $\langle \Delta Y^2 \rangle$ depends on the scale l_F at which V is defined. A diffusion coefficient is thus defined at a given scale, and it is the way to statistically consider the consequences of the particle motion at smaller scales. In paper D, the scale l_F at which is defined the fluid velocity is the grid size, which is a fraction (generally 0.2) of the proton inertial length (that is close to the proton Larmor radius since $\beta \sim 1$). Hence, the diffusion coefficient $\kappa_\perp$ calculated in this paper is associated to irreversible transport due to the phenomena that are at scales smaller than the proton inertial length.

These remarks are important because they outline the necessity to define for a given value of a particle velocity v the associated value V. As an example, prior the develomnent of the KH instability, there is a mean fluid flow. The associated particle transport is balistic, with $\Delta Y = V \Delta t$. In the absence of any magnetic fluctuation, this would be the only contribution to transport, and one could falsely conclude to a superdiffusive transport with $\langle \Delta Y^2 \rangle = V^2 t^2$. This outlines the clear necessity to define, at a given scale, the associated local mean velocity in order to properly define ΔY^2. For this reason, we disagree with the results obtained in self-consistent simulations by [**?**] and [**?**].

ΔY has to be the difference in the particle position during Δt calculated in the local frame where the fluid is at rest. Of course, the definition of this frame is non-local and non-stationary. Calling $V(t)$ the fluid velocity[1] at position $Y(t)$ at time t, the particle displacement free of large scale fluid motion ΔY during time $\Delta t = t$ is

$$\Delta Y = Y(t) - Y^\star(t) - Y(0) \tag{2.2}$$

where $Y^\star(t)$ is the position of the fluid particle at time t that was located at $Y(0)$ at $t = 0$. It is obtained from the time integration of $d_t Y^\star(t) = V(t)$ with the initial condition $Y^\star(0) = Y(0)$.

Overall features of the diffusion process

As mentioned above, the first step is to calculate the PDF of ΔY. In Fig. 2.1, the PDF of ΔY in KH run is displayed. It very clearly appears that this PDF is

[1] As said above, this velocity results from a local average of particle position in a volume l_F^3.

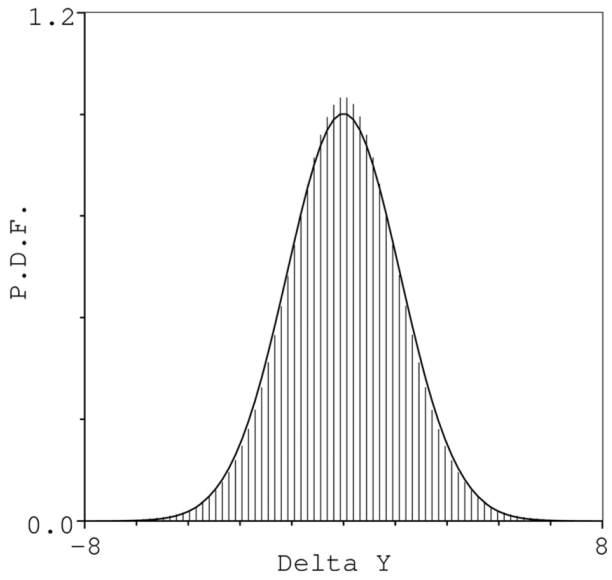

Figure 2.1: Probability density function of ΔY in the KH run. The solid line is a Gaussian fit. From [**?**].

Gaussian, as it is the case for Brownian systems. Furthermore, Fig. 2.2 displays the time evolution of the mean square value $\langle \Delta Y^2 \rangle$ for the same KH run. One observes that $\langle \Delta Y^2 \rangle$ is piecewise linear with small variation of the slopes that are associated to the vortex pairing. A conclusion of these 2 figures is that the associated process is clearly diffusive (or Brownian), the slope of $\langle \Delta Y^2 \rangle$ (divided by 2) being the diffusion coefficient. This is in total contradiction with the super-diffusive process invoked in the study of [**?**], which is obviously a consequence of the importance of considering eq. (2.2) to calculate the perpendicular diffusion coefficient $\kappa_\perp$.

Carrying the same kind of calculations with a 2B runs, we reached the same conclusion about the Brownian nature of the diffusion process. As an example, Fig. 2.3 displays the time evolution of $\langle \Delta Y^2 \rangle$ for a weakly magnetized plasma. By doing so, we magnify the FLR effects resulting in the large oscillations observable at small t that damp at larger t because of phase mixing.

The calculation of $\kappa_\perp$ is a consequence of the development of magnetic fluctuations in both KH and 2B runs. As a consequence, it is interesting to identify the kind of modes that exist in such fluctuating plasmas. For KH runs, the initial velocity shear prevents the development of any "classical" linear modes. Furthermore, in KH

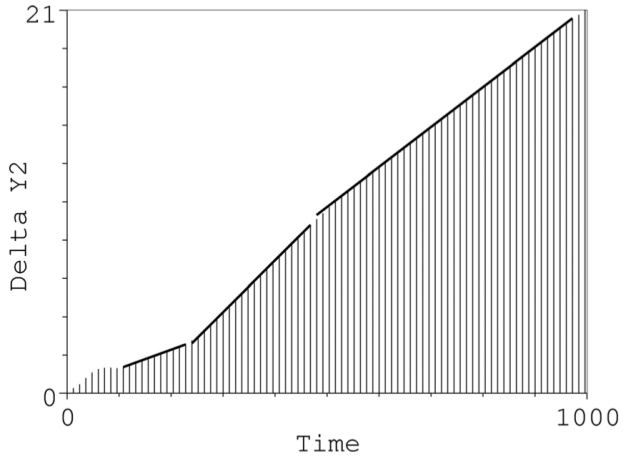

Figure 2.2: Time evolution of $\langle \Delta Y^2 \rangle$ associated to the particle motion in the KH run. Solid thick line is a linear fit. From [**?**].

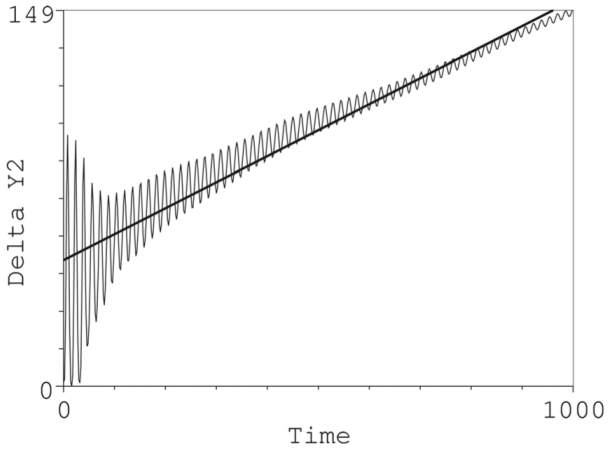

Figure 2.3: Time evolution of $\langle \Delta Y^2 \rangle$ associated to the particle motion in the 2B run. Solid thick line is a linear fit. From [**?**].

runs, the vortex pairing results in a non-stationary situation. We also compute the k-spectrum of the power spectral density of the longitudinal magnetic fluctuations and found a clear power-law spectrum with an increase of the slope at $k\rho_L \sim 2\pi$, eventually associated to dissipation. On the other hand, for the 2B runs, the magnetic fluctuations are stationary, with a flat spectrum (wide band white noise), and

clearly associated to the linear Ion Bernstein Waves as illustrated in Fig. 5 of paper D.

As a conclusion, these runs show that we find a diffusive process associated to particle transport by magnetic fluctuations in very different physical situations. Nonetheless, this do not perclude the fact that in some situations, particle transport could be sub- or super-diffusive. It clearly outlines the importance to properly compute the diffusion coefficient. More specifically, the turbulent particle transport defined at a given scale has to be free of any motion existing at a larger scale. This challenges the results obtained in test-particle calculation. In this kind of calculations, as particles are not considered as a whole, a fluid velocity (or let say a velocity averaged at a given scale) cannot be computed. To make clear this problem, we have in mind (in a close future) to compute test-particle simulations in static magnetic fluctuations. Defining a grid, one can compute in each associated cell the mean velocity through time. For an isotropic case, this velocity value should be null. If not, a correlation between the particle mean displacement ΔY^2 and the existence of such non-null fluid velocity could suggest that super-diffusive behaviour could be also or partly the consequence of the reminiscence of a mean fluid velocity.

2.2 Electric and magnetic contributions to $\kappa_\perp$

The logical continuation of this work is to identify the relative importance of electric and magnetic fluctuations as well as their coupling in particle diffusion. Furthermore, in the existing simple analytical models, the diffusion coefficient depends on the particle velocity either in a linear or in a quadratic way. We also want to investigate the way $\kappa_\perp$ depends on the particle perpendicular velocity $v_\perp$. This work has been published in [**?**], refered hereinafter as paper E.

To investigate the role of the electromagnetic fluctuations and the importance of the term $Y^\star$ from eq. (2.2) in the calculation of the perpendicular diffusion coefficient, we compute $\kappa_\perp$ with eq. (2.1) and ΔY with eq. (2.2) with different components of the electromagnetic fluctuations and different values of $V(t)$. The different situations are detailed in Tab. 2.1. The first row is the type of particles (macro-particles or passive tracers, detailed hereinafter), the second row is the electromagnetic fields used to compute the particle motion, the third row is the value of $V(t)$ used in eq. (2.2) and the fourth row is the tags used in the following figures. All the runs are similar to the 2B runs of [**?**], and the parameters of the agyrotropic

Part. type	E.M. Fields	V	Tag
passive tracers	$\mathbf{B}$, $\mathbf{E}$	0	A
passive tracers	$\mathbf{B}$	0	B
passive tracers	$\mathbf{B}_0$, $\mathbf{E}$	0	C
macro-particles	$\mathbf{B}$, $\mathbf{E}$	0	D
macro-particles	$\mathbf{B}$, $\mathbf{E}$	$\mathbf{E} \times \mathbf{B}$	E
macro-particles	$\mathbf{B}$, $\mathbf{E}$	$\mathbf{V}_p$	F

Table 2.1: The first row is the type of particles, the second row is the electromagnetic fluctuations considered for their motion, the third row is the value of $V(t)$ in eq. (2.2) i.e. the velocity fluctuations and the fourth row is the name of the population.

instability are such as the level of fluctuations is about $\delta B \sim 0.11$. Another set of runs with $\delta B \sim 0.21$ gives qualitatively the same results.

Contributions of the electric and magnetic fields to $\kappa_\perp$

To investigate the respective role of electric and magnetic contributions as well as their coupling, we follow the particle motion in electric fluctuations (their motion is calculated considering only the electric part of the Lorentz force, population C), magnetic fluctuations (their motion is calculated considering only the magnetic part of the Lorentz force, population B) and both electric and magnetic fluctuations (their motion is calculated considering the whole Lorentz force, population A) as reported in Tab. (2.1). The particles to consider can hence not be macro-particles because of the self-consistency of the code. To do so, we use passive tracers ; their motion are calculated in the self-consistent time evolving electromagnetic field, but have no back-action on these electromagnetic fields as the macro-particle do. The obtained results are depicted in Fig. 2.4. The $\kappa_\perp$ value is calculated for a given subset of the perpendicular particle velocity $v_\perp$ to investigate how $\kappa_\perp$ depends on $v_\perp$.

The curve for population B passes through the origin, its derivative at the origin is close to zero, grows with $v_\perp$, and at larger values is close to a linear relation. This emphasizes the point that $\kappa_\perp$ does not explicitly depend on $v_\perp$ with a single power law, even if it might be the case in some ranges of $v_\perp$. One can notice in particular

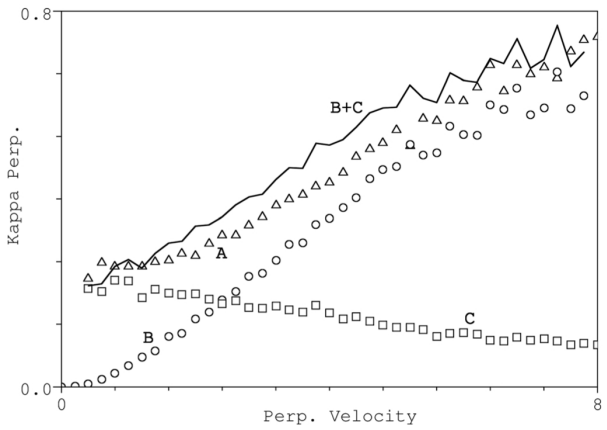

Figure 2.4: Perpendicular diffusion coefficient $\kappa_\perp$ depending on the particle prependicular velocity $v_\perp$. Triangles are associated to population A (magnetic, electric and velocity fluctuation), circles to population B (magnetic and velocity fluctuations) and squares to population C (electric and velocity fluctuations). The solid thick line is obtained by summing B and C. From [**?**].

that a quadratic model is better suited at low energy and a linear model at high energy. The simple analytical models where $\kappa_\perp$ is linear (see [**?**]) or quadratic (see [**?**]) with $v_\perp$ can therefore not adequately describe the diffusion coefficient for a wide range of particle velocities. The linear model invokes a correlation length and the quadratic one a correlation time. As shown in paper D, these arguments cannot be general. It is worth recalling in particular that, in our numerical experiments, the magnetic fluctuation power spectrum is flat : according to the Wiener-Kintchine theorem, it corresponds to a coherence length close to zero (or to the grid size).

The results for population C are totally different. $\kappa_\perp$ reaches its maximum value for $v_\perp$ close to zero, decreases for increasing $v_\perp$ and goes to zero. The fact that the electric part of the Lorentz force does not depend on the particle velocity can qualitatively explain why $\kappa_\perp(0) \neq 0$.

The result for population A is a mix between B and C : $\kappa_\perp$ is non-zero at $v_\perp = 0$ and grows with $v_\perp$. To facilitate the comparison, the sum of curves B and C is depicted in solid line in Fig. 2.4. The increase of curve A seems weaker than for curve B, but, apart from a slight overestimation, the addition of B and C is equal to A : electric and magnetic contributions to the diffusion coefficient are associated to very different mechanisms, but act together in a very linear way. This supports

the point that both contributions can be studied independently.

Nature of the electromagnetic fluctuations

We discuss in paper D the nature of the electromagnetic fluctuations for 2B runs. We put forward that at low level of magnetic fluctuations, the associated modes were the Ion Bernstein Wave (IBW). But it is not so clear that at a higher level of fluctuations, the nature of theses fluctuations is the same : one gets farther from the linear theory where the amplitude of the fluctuations is small compared to the zero order level. Fig. 2.5 depicts the $\omega - k$ spectrum of the Z component of the magnetic field. The obtained pattern is not as clear as the usual IBW, but one can recognize the energy deposited on the 3 first cyclotron harmonics, mostly along the fast mode. It will be the purpose of a future work to investigate the importance of the nature of the modes for particle diffusion.

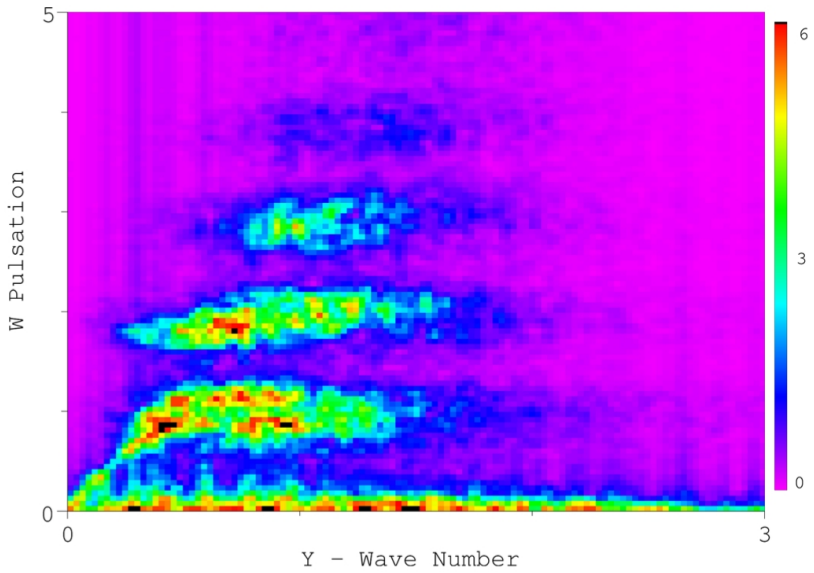

Figure 2.5: Power spectral density in the "pulsation-wave number" plane for the Z component of the magnetic field. Low energies are color coded in purple and high energies are color coded in black/red with a linear scaling. From [**?**].

Contributions of the velocity fluctuations to $\kappa_\perp$

The role of the velocity fluctuations for the diffusion process can be investigated by varying the term $V(t)$ in eq. (2.2). If $V(t)$ is null, there is no correction, and the particle diffusion is also a consequence of the fluctuations of the velocity field defined at the scale of the grid. On the other hand, if $V(t)$ is the fluid velocity defined at the scale of the grid, the associated particle diffusion coefficient is free of these fluctuations. An intermediate situation is to consider only the zero-order fluid veolcity fluctuations, associated to the cross-field drift $\mathbf{E} \times \mathbf{B}/B^2$. In our case, it turns to be the first order drift given by $\delta\mathbf{E} \times \mathbf{B}_0/B_0^2$. For this purpose, Fig. 2.6 depicts $\kappa_\perp$ as a function of $v_\perp$ for population D (circles, with full velocity fluctuations), E (triangles, without the cross field part of the velocity fluctuations) and F (squares, without any velocity fluctuations). All these results involve both magnetic and electric fluctuations. The curve obtained for population D is very similar to the one obtained for population A : the only difference is the nature of the particles, namely passive tracers for population A and macro-particles for population D.

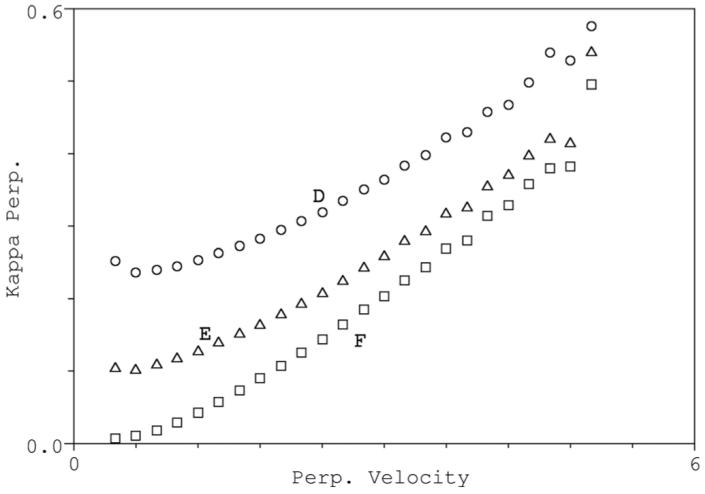

Figure 2.6: Perpendicular diffusion coefficient $\kappa_\perp$ depending on the particle perpendicular velocity. Circles are associated to population D (full velocity fluctuations), triangles to population E (velocity fluctuations without their cross field part) and squares to population F (no velocity fluctuations). From [**?**].

A striking point between Fig. 2.4 and Fig. 2.6 is the apparent similarities between the results obtained for population B and F. It contributes to identify mainly four issues in these results :

- The $\kappa_\perp$ associated to magnetic fluctuations is a growing function of $v_\perp$ with $\kappa_\perp(0) = 0$.
- The $\kappa_\perp$ associated to electric fluctuations is non-null for $v_\perp = 0$.
- The $\kappa_\perp$ associated to both magnetic and electric fluctuations is somewhat the sum of the two previous ones.
- The contribution of the velocity fluctuations to $\kappa_\perp$ seems close to the one of the electric fluctuations.

Qualitative explanations

The main observed features can be understood, at least qualitatively, by inspection of the particle dynamics. The particle motion is essentially a cyclotron motion around a guiding center. The guiding center motion can be estimated analytically as shown in many plasma textbooks. Several contributions can be exhibited like detailed in [**?**]. Noting $\mathbf{b}$ the unit vector along the magnetic field (Z direction in our case), and $\mathbf{u}_E$ the cross field drift velocity ($\mathbf{u}_E = \mathbf{E} \times \mathbf{B}/B^2$), the perpendicular guiding center velocity (considering only zero and first order terms) is

$$\mathbf{v}_{GC\perp} = \mathbf{u}_E + \frac{\mathbf{b}}{\omega_C} \times \left[v_\perp^2 \frac{\boldsymbol{\nabla} B}{B} + v_\parallel \left(\partial_t \mathbf{b} + v_\parallel \partial_Z \mathbf{b} + \mathbf{u}_E . \boldsymbol{\nabla} \mathbf{b} \right) + \left(\partial_t \mathbf{u}_E + v_\parallel \partial_Z \mathbf{u}_E + \mathbf{u}_E . \boldsymbol{\nabla} \mathbf{u}_E \right) \right] \tag{2.3}$$

The four issues listed above can be answered with the help of eq. (2.3) :

• First issue: Why is $\kappa_\perp$ associated to magnetic fluctuations a growing function of $v_\perp$ with $\kappa_\perp(0) = 0$? The second term is the well-known gradient drift velocity and is the only one playing a role for population B (other terms are either null or involve the electric field). Hence, for $v_\perp$ going to zero, the associated perpendicular guiding center drift is also going to zero, as well as the associated $\kappa_\perp$. This is why for population B in Fig. 2.4, $\kappa_\perp(0) \sim 0$. The reason why $\kappa_\perp$ depends on $v_\perp$ is more indirect: it may come from the term $\mathbf{b} \times \boldsymbol{\nabla} B$. This term depends on $v_\perp$ because the mean square deviation of the magnetic fluctuations seen by the particle depends on its Larmor radius.

• Second issue: Why is $\kappa_\perp$ associated to electric fluctuations different from zero for $v_\perp = 0$? None of the terms of eq. (2.3) associated to $\delta\mathbf{E}$ depend on $v_\perp$. Accordingly, curve C in Fig. 2.4 is such as $\kappa_\perp(0) \neq 0$. Nonetheless, second order terms in the expression of v_{GC} (not written in eq. 2.3) would involve both $\mathbf{v}_\perp$ and $\delta\mathbf{E}$. This could explain why $\kappa_\perp$ is not constant but a decreasing function of $v_\perp$.

• Third issue: Why is the diffusion coefficient associated to both magnetic and electric fluctuations somewhat the sum of the one associated to magnetic fluctuation and the one associated to electric fluctuations ? All the terms involving the electric field depend on the term $\mathbf{u}_E$. At small level of fluctuations, $\mathbf{u}_E \sim (\delta\mathbf{E} \times \mathbf{b})/B_0$ (considering only the first order contributions) which does not depend on $\delta\mathbf{B}$. In the same way, terms involving $\delta\mathbf{B}$ are free of $\delta\mathbf{E}$. The linearity originates in the small level of fluctuations and the fact that the largest contributors to the guiding center velocity (and hence to $\kappa_\perp$) are first order terms.

• Fourth issue: Why is the contribution of velocity fluctuations to $\kappa_\perp$ is close to the one of electric fluctuations ? A particle velocity $\mathbf{v}_p$ is the sum of its guiding center velocity $\mathbf{v}_{GC}$ and the gyromotion $\mathbf{v}_\Omega$. If one averages these motions over several gyropulsations, one gets

$$\overline{\mathbf{v}_p} = \overline{\mathbf{v}_{GC}} \tag{2.4}$$

$\kappa_\perp$ depends on the square of this velocity,

$$\overline{v_p^2} = \overline{v_{GC}^2} + \overline{v_\Omega^2} + \overline{\mathbf{v}_{GC}.\mathbf{v}_\Omega} \tag{2.5}$$

During few gyropulsations, $\mathbf{v}_{GC}$ is somewhat constant in both modulus and direction. Accordingly, the last term in eq. (2.5) is null. Hence, the first term in the right hand side of eq. (2.5) contains all the contributions of the electric fluctuations and only one of the magnetic fluctuations (the gradient drift). The second term depends only on the magnetic fluctuations (and on $v_\perp$). Hence, the contributions of the electric fluctuations are the same as the contributions of the fluid fluctuations if neglecting the gradient drift in the first term. This could explain why the role of electric fluctuations and velocity fluctuations are similar. If so, this means that the magnetic fluctuations mainly act through the second term of the right hand side of eq. (2.5). These remarks are in agreement with explanations for the first and second issues. For the first issue, v_Ω depends on both $v_\perp$ and δB. The associated diffusion coefficient for population B is such as $\kappa_\perp(0) \sim 0$ and $\kappa_\perp$ grows with $v_\perp$. For the second issue, v_Ω does not depend on δE, meaning that this term has no contribution to $\kappa_\perp$ for population C.

An important consequence is that in eq. (2.3), a mean first order velocity can be associated to the magnetic field structure. Hence, a mean velocity (of smaller order) can also result from magnetic fluctuations. As a consequence, even in magnetostatic fluctuations, a fluid velocity can appear with consequences on the particle motion. As mentioned above, this can wrongly be interpreted as super diffusion. Hence, it seems also important in magnetostatic fluctuations to evaluate the contribution of a mean fluid velocity in the particle motion to properly calculate the diffusion coefficient. This point has never been considered in test-particle calculations, and is the topic of a future work.

Several conclusions can be drawn from this study. First, the physical meaning of the diffusion process has been clarified, because several authors use this name for different meaning. In our work, the diffusion process is the irrerversible one that quantifies the way individual particle can depart from the motion associated to a mean flow, defined at a given scale. As a consequence, to properly calculate a diffusion coefficient, the particle velocity has to be free from this mean flow motion for the calculation of the diffusion coefficient. Furthermore, electric and magnetic fluctuations do not contribute in the same way to particle diffusion. The particle diffusion coefficient associated to magnetic fluctuations is a growing function of the particle velocity (that is null for a zero particle velocity), while this coefficient is a slightly decreasing function of the particle velocity for electric fluctuations. I started an analytical work to calculate the diffusion coefficient. The first results show that the perpendicular diffusion coefficient depends on the PDF of the magnetic fluctuation, and not on the characteristic quantities of its spectrum (total energy, slope, minimum and maximum wave number...). These results need to be finalized, and compared with numerical simulations.

— 3 —

Fluid vs kinetic approach of collisionless magnetic reconnection

Magnetic reconnection has already been invoked in the previous chapters. It is an important process in space and astrophysical plasmas because several questions in astrophysics are tied in to acceleration/heating processes : production/energization of extra-galactic cosmic rays, acceleration of jets in accretion disks, heating of stellar winds... Because of the very high level of energy involved, one has to search for non-classical processes which cannot be described by the simple theories. In most cases, these processes pertain to one (or more) of the 3 categories : shock, magnetic reconnection and turbulence. A common point between these categories is that they all involve a wide range of scales, from the electron kinetic ones, to the large MHD ones. The choice of a treatment is hence very hard, and necessitates to use some approximations.

We discussed in chapter 2 the particle diffusion by electromagnetic fluctuations, and put forward that the development of electric and magnetic fluctuations are associated to particle transport in a non-classical way, i.e. not necessarily associated to a density gradient. The occurrence of turbulence can be strongly correlated to magnetic reconnection (see e.g. [**?**]) meaning that turbulence can modify magnetic reconnection and that magnetic reconnection can affect the turbulence (cascade/dissipation).

Kinetic signatures of magnetic reconnection have been studied in previous papers (see e.g. [**?**], [**?**], [**?**]), without worrying about how to make it appears. In this chapter, we address the way magnetic reconnection can occur in collisionless plasmas as well as the consequences for the plasma structure and dynamics. The work presented in this chapter has been done with Nicolas Aunai during his PhD thesis between 2007 and 2011, that Gerard Belmont and I supervised. A peculiar effort is devoted to comparisons with the signatures and associated mechanisms presented in [**?**]. An extension of this work is presented in chapter 4.

In section 3.1, we present the framework of magnetic reconnection (collisional

and collisionless) as well as what we know from observations (mostly from satellites data). In section 3.2, we present the way protons are accelerated by the electric field in the vicinity of magnetic reconnection region, and the relation with the electric field magnitude. In section 3.3, we revisit the problem of energy budget in and out of the reconnection region, and more particularly when the initial current sheet is asymmetric as is the case in the Earth MP. In this chapter, we will try to outline the relation between the kinetic description we used (with the hybrid code) and the fluid one.

3.1 The framework of magnetic reconnection

A very classical definition of magnetic reconnection is that magnetic reconnection in magneto-fluids is the process by which magnetic field lines break and rejoin in a lower energy state. The excess energy appears as kinetic energy of the plasma downstream of the reconnection point. The mean features of magnetic reconnection are here, but the formulation is misleading. Magnetic reconnection can be a stationary process in which the magnetic energy and plasma kinetic energy are constant through time.

If one considers a volume around the reconnection region, then most of the incoming energy will be magnetic, and most of the outgoing energy will be kinetic. Still, this is not the definition of magnetic reconnection, but one of its most important consequences. Namely, magnetic reconnection is the process by which two magnetic field lines initially different can connect. This concept can be generalized to flux tubes, and of course have consequences for the plasma embedded inside. It is thus clearly a topological definition that demand to define the concept of magnetic field line and its motion.

The velocity of a magnetic field line is the one of the frame in which the associated electric field is null. This purely Electro-Magnetic definition gives

$$\mathbf{V}_{EM} = \frac{\mathbf{E} \times \mathbf{B}}{B^2} \tag{3.1}$$

One recognizes the cross drift velocity. This definition is a direct consequence of the non-relativistic form of the Lorentz transform of the electric field value. Wherever this motion can be defined, magnetic field lines can move, wiggle, braid... but cannot break down. Reconnection can only exist where this motion cannot be defined.

What does that mean for the plasma ? The momentum equation of particles (whatever protons or electrons), in the absence of any spatial gradient and in stationary case (i.e. for modes at very low wave number and pulsation) reduces to

$$\mathbf{E} + \mathbf{V}_s \times \mathbf{B} = 0 \tag{3.2}$$

where $\mathbf{V}_s$ is the velocity of specie s. As a consequence, the plasma follows the magnetic field lines motion (frozen field hypothesis) in the absence of small spatial and temporal scales. It means that the motion of the magnetic field lines is the same as the motion of the plasma. As a consequence, closed magnetic structures like the Earth magnetosphere (both ends of each magnetic field lines are anchored in the ionosphere for a dipolar magnetic field) are synonymous of "particleproof" boundary : neither magnetic flux, nor particles can penetrate in this magnetically closed structure. This is an important point because, while it is quite hard to infer the magnetic topology of the magnetic field lines from *in situ* observations, it is easier to measure the energized plasma. One hence needs to unambiguously link these energetic plasma to the energetization process associated to magnetic reconnection.

The condition of existence of magnetic reconnection is simple : let's consider two points P_1 and P_2 on a given magnetic field line at a given time. Hence, $\mathbf{P_1P_2}\times\mathbf{B} = 0$. If magnetic reconnection occur, then $d_t(\mathbf{P_1P_2} \times \mathbf{B}) \neq 0$. With the Maxwell-Faraday equation, this equation gives

$$(\boldsymbol{\nabla} \times \mathbf{E}_{\|}) \times \mathbf{b} \neq 0 \tag{3.3}$$

where $\mathbf{b}$ is the unit vector along the magnetic field.

The electric field can be obtained from the momentum equation of both species. Of course, eq. (3.2) cannot be associated to magnetic reconnection. One must go beyond ideal MHD to find the conditions for magnetic reconnection to occur. The electric field can be obtained from the momentum equation of a specie of the plasma. For electrons, this equation writes for a collisional plasma with a conductivity σ

$$\mathbf{E} = -\mathbf{V}_i \times \mathbf{B} + \frac{1}{en}\left(\mathbf{J} \times \mathbf{B} - \boldsymbol{\nabla}.\mathbf{P}_e\right) - \frac{m}{e}\frac{d\mathbf{V}_e}{dt} + \frac{ne}{\sigma}\mathbf{J} \tag{3.4}$$

In eq. (3.4), the two first terms cannot trigger magnetic reconnection (the associated electric field has no component parallel to the magnetic field). For a barotropic electron population, the third term can neither do so, unless the electron pressure

tensor is not diagonal. This means that the associated electron distribution function has to be agyrotrop (the two directions in the plan perpendicular to the magnetic field direction are not equivalent). The fourth term can make magnetic reconnection, but as it is proportional to the electron mass, the associated reconnection electric field might be very small. The Fifth term is also able to make magnetic reconnection, providing a sufficiently large resistivity.

The electric field, wrongly called the "reconnection rate" (it is not a rate) quantifies the time variation of the magnetic flux newly connected. It is generally dimensionless, normalized to the product of the upstream Alfvén speed multiplied by the upstream magnetic field. Fig. 3.1 helps to understand the 2-dimensional topology of magnetic reconnection. The plasma is flowing from the upstream region toward the reconnection region at the cross-field velocity in the Y direction. The magnetic field lines are pinched at the center where they reconnect. These peculiar magnetic field lines (dotted lines in Fig. 3.1) are called the separatrices. The green solid lines represent the plasma flow, that flows out of the reconnection region in the X direction. In white regions, the conditions of ideal MHD are satisfied. In green region, electrons are magnetized while protons are not. In this "proton decoupling region" the plasma is described by Hall MHD. In orange region, both protons and electrons are decoupled from the magnetic field. In this "electron diffusion region", even the electrons can hardly be described by fluid theory.

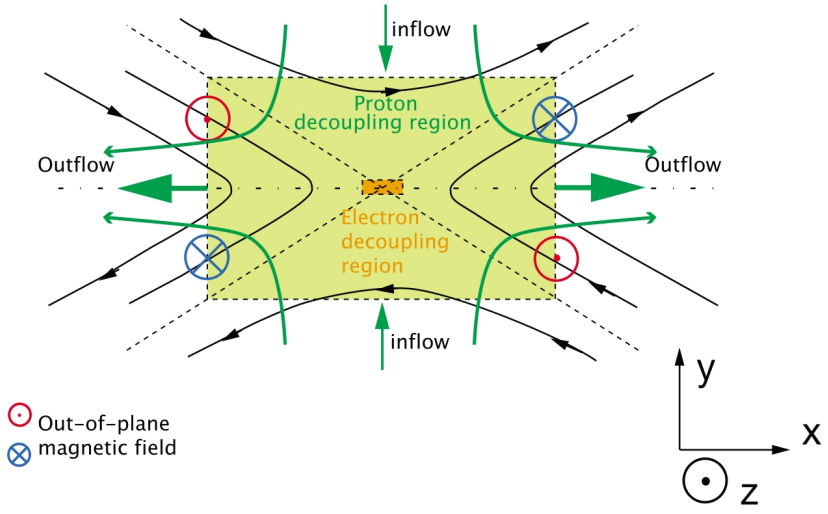

Figure 3.1: Schematic view of the reconnection region, from [?].

The scales of magnetic reconnection

The three regions described above are each associated to still open questions :

- At the electron scale, what is the origin of the reconnection electric field ? When writing a generalized Ohms law, which terms can account for the reconnection electric field ?
- At the proton scale, what is the magnetic field lines structure and dynamics ? What is the associated electric field ? What is the energy budget downstream of the reconnection region ? What are the efficiency of the acceleration or heating processes ?
- At MHD scale, what is the global topology ? Is there a way to control the reconnection rate and the geometry ? What is the importance of the 3D geometry : how to translate the 2D results in 3D ?

Each of these questions are interesting, but cannot be addressed with the same kind of numerical tools. At the electron scales, electrons have to be described kinetically because the way to close the hierarchy of fluid equation is not easy. It can be done using full PIC codes (both electrons and protons are treated as macroparticles) or Vlasov codes (not very popular in the astrophysics community). On the other hand, at MHD scales, 3D fluid codes are necessary to properly describe the large scale dynamics and the associated complicated topology. To investigate the second item, we used the HECKLE code in its $2\frac{1}{2}$ version.

3.2 Particle acceleration by the Hall electric field

The way the plasma is accelerated and/or heated during the reconnection process is yet unclear. The first model by [**?**] and [**?**], the so-called Sweet-Parker model is applicable for collisional system. The finite resistivity of the media is the source of the electric field in the generalized Ohm's law (last term of eq. 3.4). This electric field is in the current direction, and the positive work of this force on the particles is responsible for their energization. In this model, the reconnected electric field, and hence the reconnection rate, depends on the resistivity of the media. In the Earth magnetosphere, the resistivity is almost null (the mean free path of a proton is about 1 A.U.), and the reconnection rate of the Sweet-Parker model is hence almost null.

Later, the Petschek model (see [**?**]) introduced an interesting idea : the loci of the reconnection process is not the same as the loci of the particle energization. In the Sweet-Parker model, the reconnection rate is very small mainly because the electron decoupling region is very small (on the order of the electron skin depth). While protons are accelerated in this zone, this makes a bottleneck that drastically limit the reconnection rate. The idea of Petschek is that the region of acceleration of particles could be larger than the electron decoupling region where magnetic field lines reconnect. In the Petschek's model, the existence of slow-mode shocks along the two separatrices is the cause of the plasma acceleration. Later-on, neither observations nor numerical simulations were able to justify the existence of such structure.

Yet, the idea of Petschek is interesting, and the best scenario is now that magnetic reconnection occurs in the electron decoupling region, and that protons are accelerated in the proton decoupling region. As a result, it is an open question to identify the origin of particles acceleration from a micro-physical point of view. The physical large-scale picture is that the newly reconnected magnetic field lines are highly bent (see the magnetic field lines downstream of the separatrix in Fig. 3.1). As a result, the associated high magnetic tension results in a violent spring force that brings the magnetic field lines in a more rectilinear shape. Once protons are frozen to these magnetic field lines, they are also accelerated. But in the proton decoupling region, protons are not tied to magnetic field lines...

Hall mediated collisionless magnetic reconnection

In the sweet-Parker model, the outflow speed is the Alfvén speed of the input region, because the magnetic perturbations are essentially Alfvénic. Furthermore, the outgoing flux of particles linearly depends on the thickness of the proton decoupling region. As the apex angle of the separatrices is small, this thickness is also small, hence resulting in a limited reconnection rate. A major step was accomplished by [**?**] in understanding collisionless magnetic reconnection. At higher frequency, the compressional Alfvén mode turns to be the whistler mode. It is suggested in this paper that the speed of the plasma jet downstream of the reconnection X point linearly depends on the inverse of the current sheet thickness. As a result, the reconnection rate, proportional to the product of the outflow speed by the current sheet thickness is a constant that explain a fast reconnection rate.

This model has another important consequence : while the Alfvén mode is linearly polarized, the associated magnetic perturbation develops in the plane of polarisation. The whistler mode being circularly polarized, the associated magnetic perturbation gets out of this plane. The important consequence for magnetic reconnection is that in the vicinity of the separatrix in the proton decoupling region, the magnetic field lines get out of the plane, as illustrated in Fig. 3.2 from [**?**].

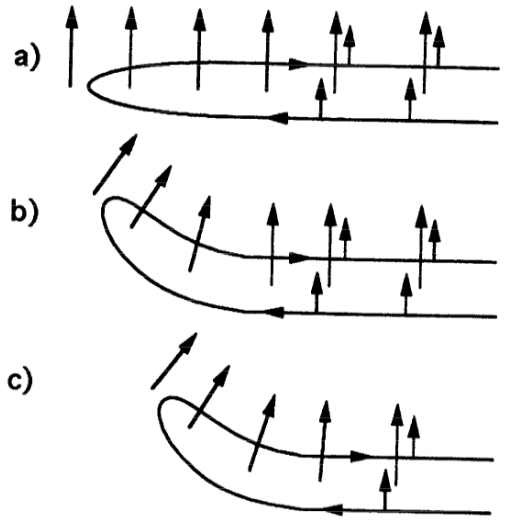

Figure 3.2: Development of the out-of plane magnetic component associated to the Hall effect during reconnection from [**?**]. The arrows represent the electron velocity

In panel (a) of Fig. 3.2, the magnetic field line holds in the polarization plane, and the electron velocity, at the origin of the associated current, is indicated by the perpendicular vertical arrows. The magnetic field being frozen in the electron fluid, the magnetic field line is dragged out of this plane in panel (b). The electron velocity being locally perpendicular to the magnetic field line, a component of the electron velocity develops that convects the magnetic field line away from the reconnection region as indicated in panel (c).

If one represents a second magnetic field line close to the second separatrix, the development of the out-of-plane magnetic component forms a quadrupolar structure (see Fig. 3.3). The quadrupolar structure of the Hall magnetic field is a key parameter of fast reconnection. This point is the main conclusion of the GEM challenge (see [**?**]) : in 2001, a wide bunch of simulators addressed the same problem of magnetic

reconnection (box size, initial and boundary conditions) with various codes, namely resistive MHD, Hall MHD, hybrid and full PIC. The main result of this challenge is that the reconnection rate is almost the same with various codes as long as the Hall effect is included.

This Hall component of the magnetic field is important because it is associated to an electric field. This is illustrated in Fig. 3.3 from the PhD thesis of N. Aunai. It can be seen that the Hall electric field is localized close to the separatrix in the proton decoupling region, mainly in the Y direction toward the mid-plan. Because of the small angle of the separatrices, it also exists a small component of the electric field, in the $+X$ direction for positive X values, and in the $-X$ direction for negative X values. It was suggested by [?] that this electric field could play a role in the energization of protons. Using CLUSTER 2 data, [?] also suggested that this electric field could be responsible for the protons acceleration.

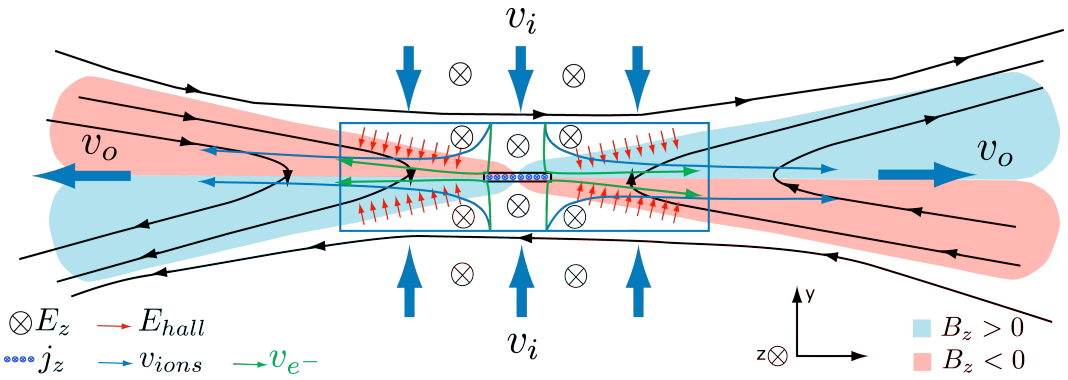

Figure 3.3: Schematic of the reconnection region from the PhD thesis of N. Aunai.

Fluid description of the protons

In [?], hereinfater refered as paper F, we addressed this problem with the HECKLE code. An important and original aspect of this paper is the fluid consequences of the kinetic process for protons. Following a fluid particle initially upstream of the reconnection region, it is accelerated and heated when crossing the separatrix. With the kinetic description of the protons, each term of the proton Ohm's law can be calculated. The results are depicted in Fig. 3.4. Left panel is the projection along the X direction and right panel is a projection in the Y direction of the different terms of the Ohm's law. The abscissa is the curvilinear abscissa along the fluid

path described in Fig. 3 of paper F. From this figure, it is clear that most of the pressure gradient is opposed to the electric field, hence limiting the flow acceleration. As protons are deflected toward the mid-plane, the pressure inside the jet rises, so that the pressure difference with the upstream region is able to dynamically balance the electric field force and maintain the structure open and steady. It has to be noted that in the X direction, the pressure gradient is essentially coming from the off-diagonal term P_{XY} unlike almost fluid models where the pressure is assumed scalar.

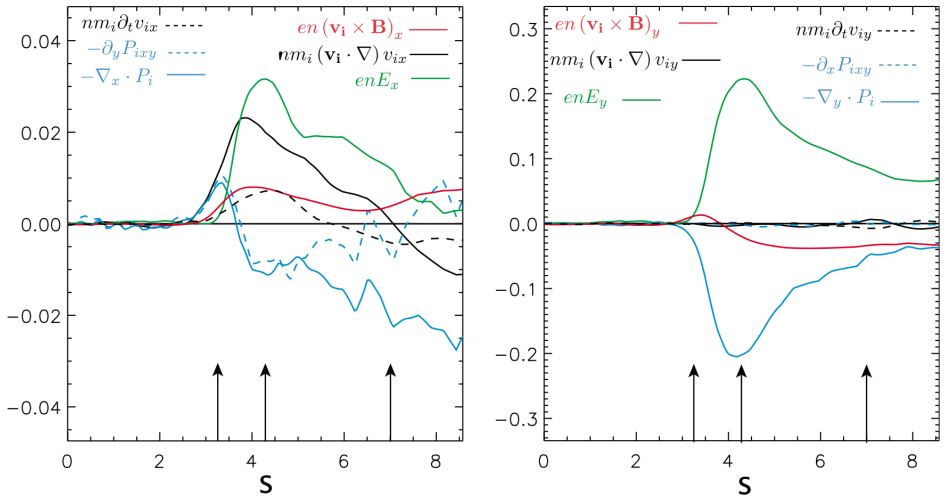

Figure 3.4: Each term of the proton Ohm's law are color coded depending on the curvilinear abscissa in the X (left panel) and Y (right panel) direction, from [**?**].

Kinetic structure of the proton fluid

Of course, the structure of the proton pressure tensor depends on the formalism. Within the fluid framework, it is a consequence of the closure equation. For most of the fluid studies, the pressure tensor is at least diagonal, and even isotropic in many cases. In the hybrid framework, the full proton pressure tensor is a consequence of the particle dynamics, and closely depends on the distribution function. The structure of these proton distribution functions are depicted in Fig. 6 of paper F, for various Y location, namely upstream and downstream of the separatrix. Essentially, these distribution consist of a cold Maxwellian upstream of the separatrix, and 2 cold beams downstream, the relative weight of each beams depending on the Y

location. These distribution functions are depicted in the V_xV_y plan, and can be easily understood by close inspection of particle dynamics.

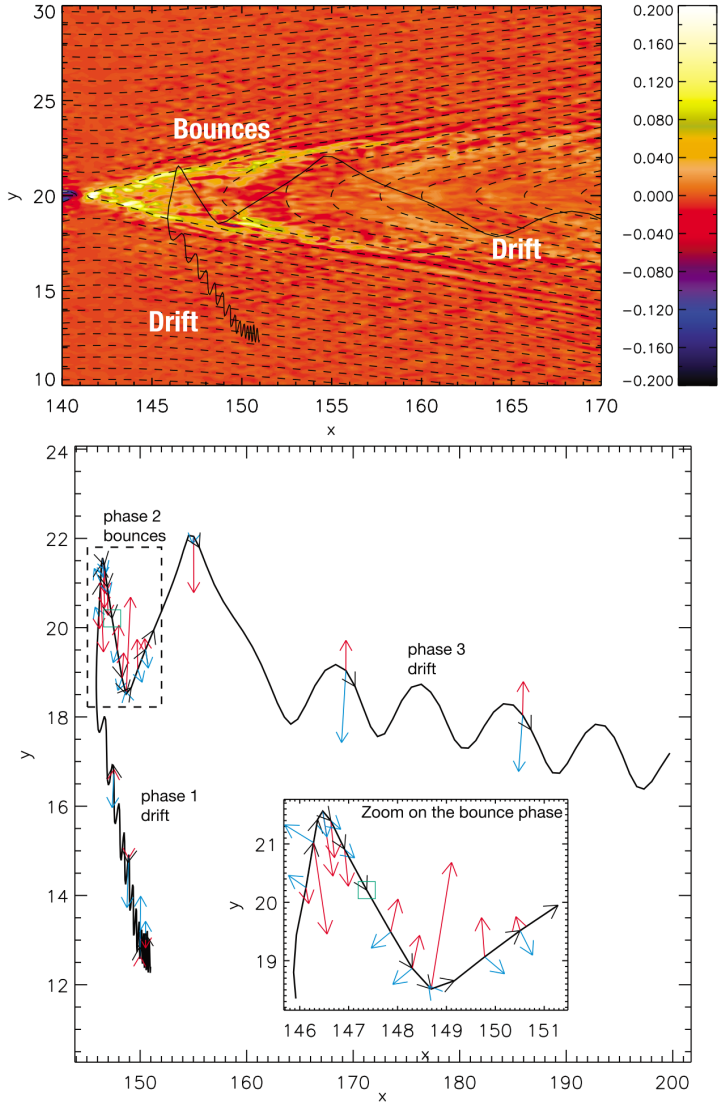

Figure 3.5: From [**?**] : (upper panel) Proton trajectory superposed to the X component of the electric field and (lower panel) zoom of this proton orbits with the electric (red arrows) and magnetic (blue arrows) forces felt by the particle.

In Fig. 3.5, it appears that this particle orbit has 3 sequences : an adiabatic drift from the lobe toward the separatrix, a bounce motion between the 2 separatrices,

and another adiabatic drift motion farther away from the reconnection region. The bounce motion could look very similar to the Speiser orbits. But the close inspection proposed in the lower panel of Fig. 3.5 clearly shows that in the vicinity of the separatrices, the particle motion results from the electric force and not from the magnetic one. This orbit is hence not a Speiser-like one ; the proton is bouncing between the separatrix and is accelerated by the electric field. A Fourier analysis proves that this electric field is essentially electrostatic.

From the upper panel of Fig. 3.5, one can understand the distribution function; at the mid-plane, the distribution function is the superposition of particles accelerated at the upper separatrix ($V_y < 0$) and particles accelerated at the lower separatrix ($V_y > 0$). Both have $V_x > 0$. For symmetry reasons, each beam has the same density. For a lower observation point (closer to the lower separatrix), these two populations are still observable, but the one with $V_y > 0$ is denser, because some of these particles have bounced prior reaching the separatrix.

Concluding remarks

This peculiar structure of the distribution functions is at the origin of the proton pressure tensor. It thus appears that this process is clearly a self-consistent one : particles are accelerated by the electrostatic Hall electric field mainly localized on the separatrix, and the resulting gradient of the proton pressure tensor limits the magnitude of this accelerating electric field.
Several conclusions can be drawn from this study :

- During magnetic reconnection, protons are accelerated essentially by the Hall electrostatic field on the separatrix. As a consequence, the reconnection electric field (in the Y direction) seems to play a secondary role for protons acceleration. The Speiser mechanism is hence void. This is a consequence of the appearance of a Hall electric field never considered in early test-particle calculations.

- These peculiar proton distribution functions limit the magnitude of the electric field, and hence the energetization process. As a result, the reconnection rate is kept at a finite value.

- While there is an angle between the two separatrices, the bouncing motion between the two separatrices accelerates the protons essentially in the Y di-

rection, and part of this velocity turns to be converted in the X direction when protons get farther from the reconnection region. It has important consequences for the competing balance between acceleration and heating that we discuss in the last section of this chapter.

This study puts forward the importance of the self-consistent nature of magnetic reconnection. It also outlines the importance of the closure equation in fluid simulations, since it controls the pressure tensor structure, and hence the limited value of the Hall electric field. As a general feature, the proton outflow in fluid simulations is generally Alfvénic. This can be a consequence of a larger value of the Hall electric field while not limited by the gradient of the off-diagonal terms of the proton pressure tensor. On the other hand, the reconnection rate are somewhat the same in each cases because the outflow channel is wider in PIC simulations.

The quadrupolar structure of the Hall magnetic field as well as the quadrupolar structure of the off-diagonal term of the proton pressure tensor has been studied in [**?**], using CLUSTER 2 data. This study clearly puts forward that if one considers correctly a small guide field in the current direction, these two quadrupolar structures are observed, and can thus be used as a proxy of the Hall-mediated reconnection region.

3.3 Energy budget for asymmetric magnetic reconnection

It was clear from section 3.2 that protons are energized when going through the reconnection region, because the Hall electric field is mainly located on the separatrices. Close to the X line, the small aperture of the separatrices results in an enhancement of the particle velocity essentially in the normal direction (along Y). During the forthcoming bounces, this small aperture results in a progressive enhancement of the particle velocity in the X direction. Far from the reconnection region, the magnetic field lines are essentially in the X direction. Hence, a gain in the X component of the particle velocity will be associated to acceleration while a gain in the Y direction will be associated to heating. The purpose of Ref. [**?**], hereinafter cited as paper G, is to investigate the balance between acceleration and heating of the plasma through the reconnection region. Furthermore, for asymmetric reconnection, this balance can be modified, and can depend on the field asymme-

tries. A recent study addressed this problem ([**?**]) and found that in both cases, the incoming energy of the Poynting flux is equally distributed between bulk flow energy and thermal energy of the protons downstream of the reconnection region. These results were obtained with MHD simulations. We thus want to address this problem with a hybrid code to properly treat the kinetic nature of the proton energization, as described in the previous section.

The three energy equations

This study is based on two runs, named A and B : run A is the classical symmetric case, while run B is the asymmetric case for which a density gradient (densities equal to 1 and 0.25 on side 1 and 2, respectively) is associated to a temperature gradient such as the pressure balance is satisfied with a tangent hyperbolic profile of the magnetic field. The details of the simulations are in paper G. The energy equations for the electromagnetic, bulk and thermal components have to be written, to outline the different terms and their coupling :

$$\frac{\partial M}{\partial t} + \boldsymbol{\nabla}.\boldsymbol{\Pi} = S_m \tag{3.5}$$

$$\frac{\partial K}{\partial t} + \boldsymbol{\nabla}.(K\mathbf{U}) = S_k \tag{3.6}$$

$$\frac{\partial u}{\partial t} + \boldsymbol{\nabla}.(\mathbf{q}+\mathbf{H}) = S_u \tag{3.7}$$

Eq. (3.5) is the conservation equation for the electromagnetic energy, eq. (3.6) is the conservation equation for the bulk flow energy and eq. (3.7) is the conservation equation for thermal energy (the same equation holds for protons and electrons).

In eq. (3.5), M is the magnetic energy (the electric energy is negligible because the speed of light is infinite compared to the Alfvén speed), $\boldsymbol{\Pi}$ is the Poynting flux and $S_m = -\mathbf{J}.\mathbf{E}$. In eq. (3.6) K is the bulk flow energy (negligible for the massless electrons), $\mathbf{U}$ is the mean velocity and $S_k = nq\mathbf{E}.\mathbf{U} - (\boldsymbol{\nabla}.\mathbf{P}).\mathbf{U}$. In (3.7), u is the thermal energy, i.e. the half trace of the full pressure tensor $\mathbf{P}$, $\mathbf{q}$ is the reduced heat flux and $\mathbf{H}$ is the enthalpy (the sum of the thermal energy flux and the work of the pressure force).

For each of these equations, the first term in the left hand side is the explicit derivative with respect to time, the second term in the left hand side is the divergence of the associated flux, and the right hand side is the sum of source and sink terms. Hence, the spatial integration of the right hand side of eq. (3.6) and (3.7)

on a contour containing the proton decoupling region gives the sources of bulk and thermal energies, respectively. For both symmetric (run A) and asymmetric (run B) cases, the time evolution of this value is depicted in the 2 upper panels of Fig. 3.6. The red lines are the bulk energy flux and the black line are the thermal energy flux. It clearly appears that we are far from an equipartition of the magnetic energy : the kinetic particle energy downstream of the reconnection region is dominantly in the thermal part, the bulk flow being smaller. This situations is magnified in the asymmetric case.

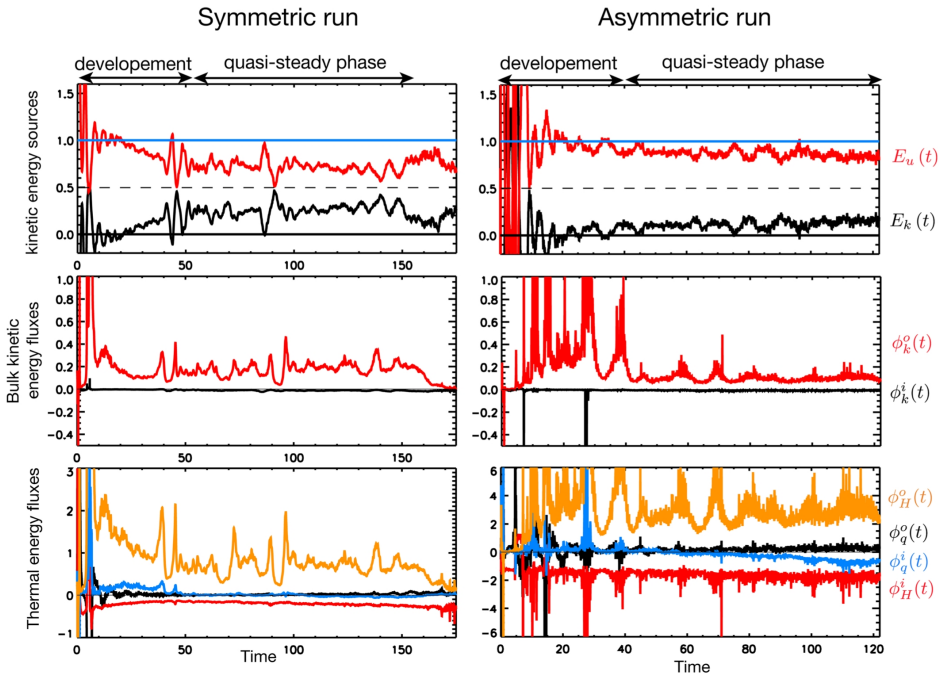

Figure 3.6: From [**?**] : The left panels are for the symmetric case, and the right panels for the asymmetric case. The upper panels depict the time evolution of the bulk energy sources (red line) and thermal energy sources (black line). The middle panels depict the time evolution of the ingoing and outgoing bulk energy fluxes. The lower panels depict the time evolution of the ingoing and outgoing heat flux and enthalpy fluxes.

Computed source terms of the energy equations

From the two upper panels of Fig. 3.6, it is clear that the source of bulk energy is larger than the one of thermal energy, this being more pronounced in the asymmetric case. This is quite different from the MHD results previously published and is a clear consequence of the kinetic nature of the proton energization. The middle panels indicates that the ingoing bulk energy flux is negligible, and that the outgoing one is somewhat equal to the source term of thermal kinetic energy depicted in the upper panels. The lower panels show that the ingoing and outgoing heat fluxes are negligible, and that the outgoing enthalpy flux is larger than the incoming one, in accordance with the enhancement of the thermal energy downstream of the reconnection region.

The conclusion of this study is that the main energy flux in the reconnection region is the Poynting flux. A small part of this Poynting flux gets out of the reconnection region, while the main outgoing flux is the enthalpy flux. Hence, the plasma downstream of the reconnection region is mainly heated, and accelerated in a less efficient way.

Several conclusions rise from this chapter :

- The reconnection electric field partly contributes to the energization process of protons, but the Hall electric field localized on the separatrices is the main source of particle energization. Speiser-like orbits are not observed in the proton decoupling region.
- The protons are accelerated by the Hall electric field, its value being limited by the proton pressure tensor associated to the counter beams distribution function.
- These signatures are observed in-situ by the CLUSTER spacecraft in the close magnetotail of the Earth.
- The energy gained by the protons is more preferentially thermal than in bulk form.

We investigated the fast collisionless magnetic reconnection in both symmetric and asymmetric cases. A natural evolution of this work will be to consider a small guide

field to study how it can affect the proton energization. Former studies like [**?**] already showed that when considering a guide field, the magnetic topology of the reconnection region is not simply the superposition of the Hall magnetic field with the guide field. The normal component of the magnetic field, when subtracting the guide field, is not quadrupolar, and preferentially in the direction of the guide field. As a consequence, one can expect that the Hall electric field is also modified, as well as the bounce motion of protons between the potential wells along the separatrices.

Another promising evolution of this work will be to compare the fast magnetic reconnection mechanism in space plasma (with $\beta \sim 1$) with the case of laboratory plasma. Since less than a decade, magnetic reconnection can also occur in laboratory plasma, at higher β value (about 100 or more). A small collisionality has also to be considered. This will be developed in the next chapter.

— 4 —

New perspectives on magnetic reconnection

To study the onset of magnetic reconnection, one needs the prescription of an initial magnetic field prior magnetic reconnection occurs. For test-particle calculations, one imposes the reconnected magnetic field structure, and the only constraint is to satisfy $\boldsymbol{\nabla}.\mathbf{B} = 0$. For self-consistent fluid simulations, one needs a fluid equilibrium, meaning that the first 3 moments of the distribution function (at least) have to be known, and the associated magnetic field profile has to be such as to satisfy a pressure balance across the current sheet. For self-consistent kinetic simulations, this is the whole distribution function that has to be known, and that has to satisfy the Vlasov equation. We investigate in section 4.1 such class of models more in details as they are of primary importance for magnetic reconnection study. We also present in section 4.2 preliminary results on the onset and dynamics of magnetic reconnection in an original topology.

4.1 Kinetic equilibrium for an asymmetric tangential layer

The study of magnetic reconnection using self-consistent simulations needs the prescription of an initial equilibrium. Hence, the profile of the magnetic field and the associated distribution function has to satisfy the Vlasov equation (even if this equilibrium is unstable, as is the Harris sheet with the tearing mode, see [**?**]). If such an equilibrium is not exact, some energy will be in excess in the system. This energy will hence feed the eigen modes of the system and waves will grow in the simulation. In the case of a current sheet, this has been clearly observed in our simulations of magnetic reconnection in tangential layer discussed in chapter 3. These waves are low frequency (probably fast magnetosonic modes) and generally propagating perpendicularly to the magnetic field.

It exists very few kinetic equilibria because the set of associated integro-differential equations is, on a mathematical point of view, awful. The study of [**?**] is the first one and contains most of the ideas used in the subsequent studies. First of all, a kinetic

equilibrium must satisfy the Vlasov equation ; the distribution function $f(\mathbf{r}, \mathbf{v}, t)$ has to satisfy :

$$\frac{df}{dt} = 0 \tag{4.1}$$

along a particle orbit. As a result, an easy way to satisfy eq. (4.1) is to find a distribution function that only depends on the constants of motion. In his work, [**?**] took a Maxwellian form of the distribution function and found the analytical form of its parameters to satisfy the Maxwell equations. The resulting system being under-determined, hypotheses on the electric field and on the charge carriers yield to the "classical" Harris sheet. An important property of the Harris sheet is to be surrounded by vacuum.

The so-called Harris sheet is well suited for the study of a plasma sheet where the magnetic pressure in the empty lobes counter balance the kinetic pressure of the field reversal sheet. Nonetheless, the existence of a small component of the magnetic field normal to the current sheet plane makes void this configuration to study the stability of the magnetotail, as this small component overthrow the equilibrium and strongly stabilizes the tearing mode as shown by [**?**]. Furthermore, this analytical model is unable to describe an asymmetric current sheet like the magnetopause.

To properly describe a magnetopause, an analytical model should consider the existence of a tearing in the magnetic field direction (see e.g. [**?**]), as well as a gradient in the density profile. This discontinuity is asymmetric because it is the boundary between the dense cold shocked solar wind and the hot tenuous plasma of the magnetosphere. The first analytical model of such an asymmetric sheet was proposed by [**?**]. With two cyclic coordinates (the canonical momenta in the two directions normal to the gradient direction) and without electric field (the Hamiltonian is conserved for such conservative system), there are three constants of motion. With a distribution function separating the Hamiltonian from the two others constants, it is shown that some solutions exist (three are discussed) for which density and magnetic field gradients are co-located and of the same width.

Later on, [**?**] proposed a generalization of the work of [**?**] with a different analytical parametric form of the distribution function. This study yields a wider class of analytical solutions. Nonetheless, these solutions cannot include a drift velocity away from the discontinuity, nor the existence of asymmetries in the density profile. An important point is also that all these models are associated to a null electric field. Later on, [**?**] and [**?**] proposed semi-analytical models lying on the existence of three

populations (one in each side of the discontinuity and one in the middle) modeled as the product of a Maxwellian with an error function. Unfortunately, none of these models are suitable for the initialization of self-consistent kinetic computations.

The model proposed by [**?**] in article H is similar to the former one in the sense that it works with an analytical shape of the distribution function depending on the constants of the motion. This analytical model lies on a different parametrization of the distribution functions, with a wider choice on their free parameters. First, the magnetic field profile is imposed (as well as the associated total current). The magnetic field is the same as the one of the Harris sheet (in the X direction with a gradient in the Y direction), associated to a vector potential $A_z = \ln[\cosh(y/2\lambda)]$. A different choice would allow to use the same method. The three constants of motion are

$$H = \frac{m}{2}(\dot{x}^2 + \dot{y}^2 + \dot{z}^2), \qquad P_x = m\dot{x}, \qquad P_z = m\dot{z} + qA_z \tag{4.2}$$

We will ignore P_x as it does not depend on the Y coordinate ; It will be fixed by the asymptotic value of the distribution function. We note $g(H, P_z)$, the distribution function in the new space which is equal to the distribution function $f(\mathbf{r}, \mathbf{v}, t)$.

It is important to say that $g(H, P_z)$ depends on the Y coordinate through the A_z value. Furthermore, the energy constraint $H > (P_z - qA_z)/2m$, means that all the points of the distribution function are inside the parabola depicted in Fig. 4.1. In other words, f depends on y because g depends on A_z. Else, the function $A_z(y)$ is even, meaning that an asymmetric equilibrium is not possible if g is single-valued. An asymmetric solution therefore essentially relies on the existence of bi-valued functions g.

Overview of the method

One notes s the side of the layer, which can be l (left of the layer) or r (right of the layer). The index of the population p is 1 or 2, side $s = l$ is asymptotically populated by $p = 1$ population, and $s = r$ is asymptotically populated by $p = 2$. Then, on each sides,

$$g_s = g_{1s}e^{-E/k_BT_1} + g_{2s}e^{-E/k_BT_2} \tag{4.3}$$

assuming for g_{ps} the form

$$g_{ps} = g_{ps\infty} + \sum_{i=1}^{N} g_{psi}e^{-k_{si}\delta P_z} \tag{4.4}$$

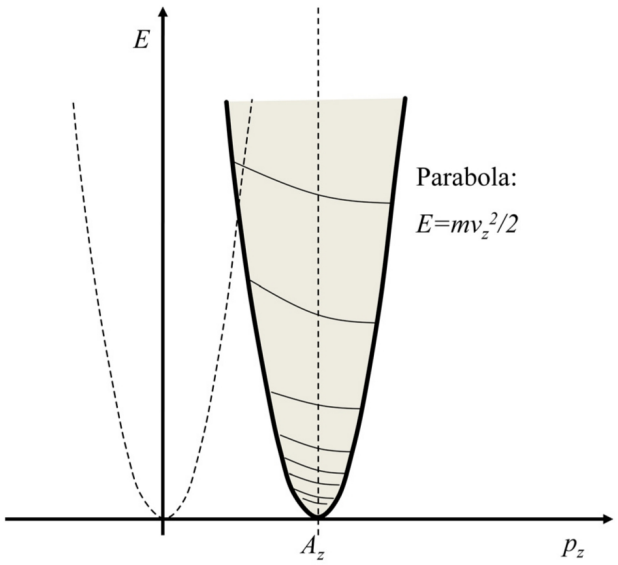

Figure 4.1: For each value of the normal coordinate y, the distribution function $f(\mathbf{v})$ is determined in the entire $\mathbf{v}$ space by the value of the function $g(E, p_z)$ in only the part of the (E, P_z) plane that is inside the drawn parabola. This parabola has its apex in $p_z = A_z(y)$ and, therefore, moves with y. The distribution function can thus vary in y, since the parabola explores different regions of the (E, p_z) plane. From [**?**].

with $\delta P_z = P_z + \sqrt{2mH}$. This arbitrary form results from many tries and errors, and allows to properly converge. The main advantage is that it makes easy the calculation of the moments of the distribution function, and gives for the YY component of the pressure

$$P_{ps} = P_{ps\infty} + \sum_{i=1}^{N} g_{psi} P_{psi} e^{-k_{si} A_z} \tag{4.5}$$

This allows an analytical treatment of the pressure balance condition. The unknowns of the problem are the g_{psi} and k_{si}. Few tries showed a weak dependence of the results on the k_{si} values, and we choose them to vary between 0.5 and 3. Hence, this problem has $4N$ unknowns, and needs $4N$ equations. The constraints on the system are :

- A pressure balance in each side s, resulting on $2N$ constraints

$$g_{1s0}P_{1s0} + g_{2s0}P_{2s0} = B^2/2\mu_0 \quad (4.6)$$
$$g_{1si}P_{1si} + g_{2si}P_{2si} = 0 \quad (4.7)$$

- In the central parabola, the functions g_{1s} and g_{2s} should be equal for $s = l$ and $s = r$ to ensure the continuity of the distribution function. Because of their analytical form, this cannot be exact, and we only impose the equality of their M first derivatives at $\delta P_z = 0$, yielding the $2M + 2$ constraints

$$(g_{pl0} - g_{pr0}) + \sum_{i=2}^{N}(g_{pli} - g_{pri}) = -(g_{pl\infty} - g_{pr\infty}) \quad (4.8)$$
$$k_1^d(g_{pl0} - g_{pr0}) + \sum_{i=2}^{N}(k_{li}^d g_{pli} - k_{ri}^d g_{pri}) = 0 \quad (4.9)$$

for an order of derivation d ranging from 0 to M. The system hence possesses $2N + 2M + 2$ equations and $4N$ unknowns.

To do not over-constrain the problem, N and M should be such as $N \geq M + 1$. The equality $N = M + 1$ leads to a null determinant of the matrix associated to this linear problem. Furthermore, the wider is this inequality, the larger are the degrees of freedom for the distribution profiles.

For paper H, we have $N = 10$ and $M = 4$ which let enough degrees of freedom to impose the shape of the gradient on one side of the layer. We choose to impose the profile of the pressure of population 2, that has to be asymptotically equal to 0 in side 1, and a given P_∞ value in side 2. Details of the P_2 structure are found in paper H.

Fig. 4.2 depicts the analytical P_2 profile (solid thick line) and the associated P_1 profile (dashed thick line), depending on $A^\star$. The pressure profile of Fig. 4.2 is analytically imposed, and is very close to the ones obtained by convergence of the numerical method. On Fig. 4.2 different profiles are depicted, associated to different parametrizations of P_2, and being only constrained by its positiveness. One can note that there is always a local maximum located at $A^\star = 0$, and a local minimum located at $A^\star > 0$ (on the dense side).

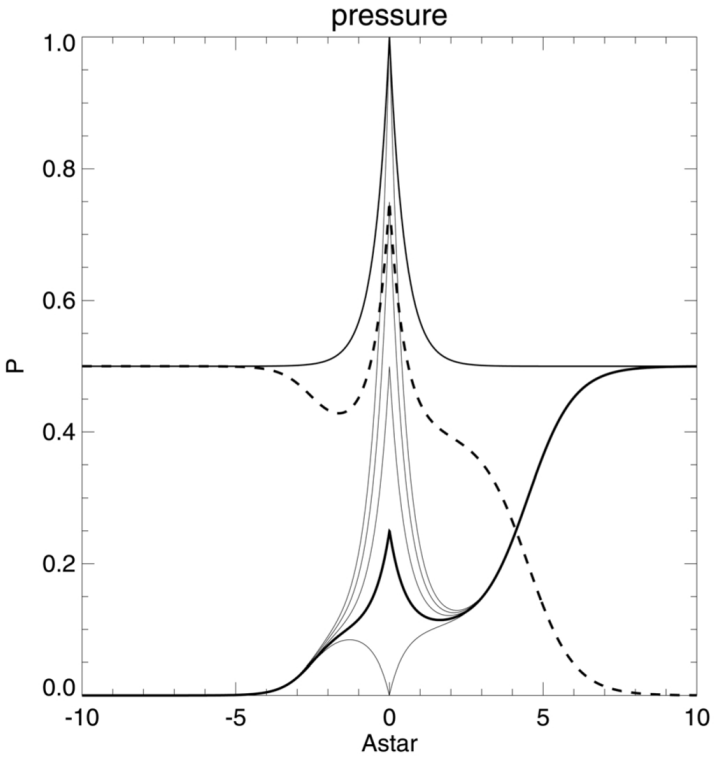

Figure 4.2: Pressure of population 2 as produced by the simple model, in function of the symmetrized vector potential $A^\star = A_z \text{sign} y$), for 6 values of the parameter $\tilde{P}_p$. The particular value marked by a thicker line corresponds to the value of $\tilde{P}_p$ used in the following results. The dashed line corresponds to the pressure of population 1 for the same particular $\tilde{P}_p$. The sum of both gives the total pressure (upper curve) which is imposed in all cases. From [**?**]

Numerical simulation of this kinetic equilibrium

In a yet unpublished study, we investigate with HECKLE whether this profile is a robust kinetic equilibrium. Answering the criticism of a referee of this paper, we included in the model a small electron temperature with $T_e/T_p = 0.1$. As the density is not uniform (depicted hereinafter), the electron temperature can neither be uniform to insure the pressure balance across the discontinuity. This might seem incompatible with the isothermal hypothesis, but the density gradient is in the Y direction while the electron transport is in the X direction (tangential to the layer). For this investigation, we have three runs :

- Run A is initialized with locally Maxwellian distributions for which the moments are hyperbolic tangent functions satisfying the pressure balance condition.
- Run B is initialized with the distribution function given by the above method.
- Run C is initialized with Maxwellian distribution functions for which the moments are those used in run B.

We consider an asymmetric current sheet with a density asymptotically equal to 1 and 4 on both sides. The simulations are approximately 1D with a box length ~ 35 proton inertial length and an adequate time step to satisfy the CFL condition. The total pressure is depicted in Fig. 4.3, depending on the Y position. The four curves are associated to different times, namely $t = 0$, 1, 5 and 10. As mentioned above, some fluctuations associated to eigenmodes appear and grow with time for a system initially not in a kinetic equilibrium. It is clear from Fig. 4.3 that neither case A, nor case C are kinetic equilibrium, while case B is.

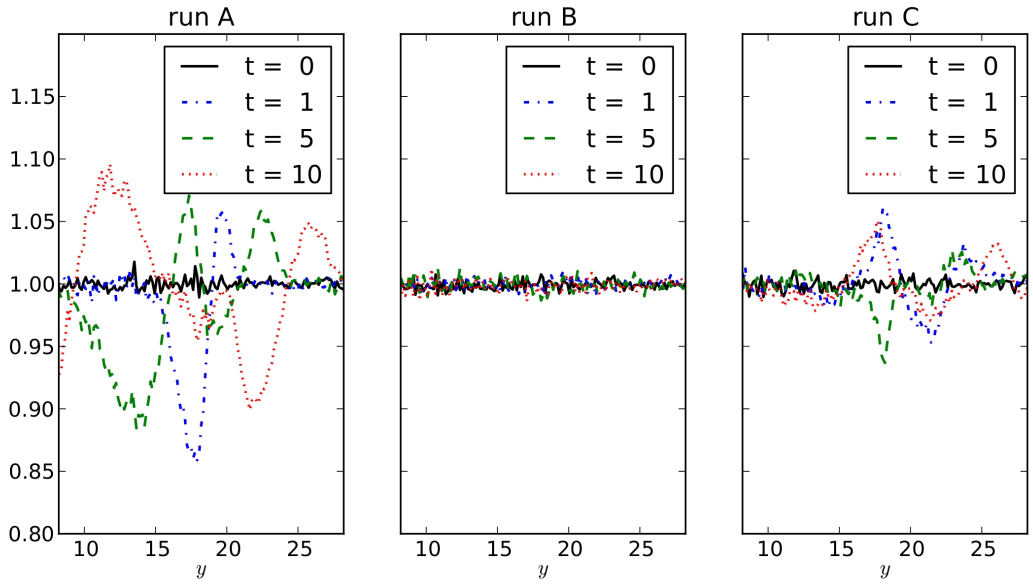

Figure 4.3: Total pressure through the current sheet. The data are averaged in the X direction and plotted as a function of Y for different times and each runs.

An interesting feature of this equilibrium is the density profile. In Fig. 4.4, it is depicted with the dashed line, while the density profile used in run A and C is

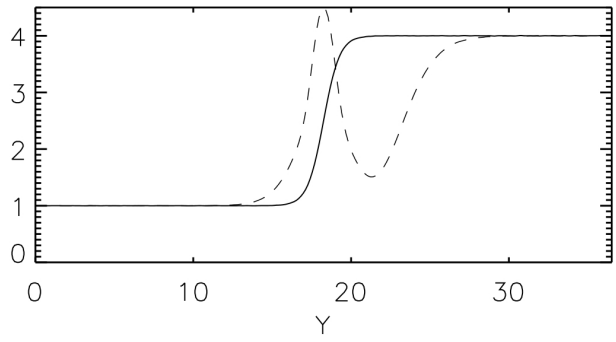

Figure 4.4: Initial density profile for Run A (solid line) and for run B and C (dashed line).

depicted with the solid line. It is noticeable that this profile is not monotonic, which is a common feature of the different equilibria obtainable with this method. More specifically :

- There is always a maximum located at $A^\star = 0$
- This density profile is never monotonic
- There is always a "depletion layer" in the dense side
- The density profile is always thicker than the imposed current profile

This work is quite recent, and yet, this equilibrium has not been used as an initial state to study magnetic reconnection. It will be interesting to note how a nice initial kinetic equilibrium impacts the development of magnetic reconnection.

Another important point is that until now, analytic and numerical models are mostly confronted to in situ spacecraft measurements. Nevertheless, since 15 years, different laboratory experiments have been designed to study the development of magnetic reconnection in laboratory. This point is discussed in the next section.

4.2 Fast reconnection in laser induced HEDP

Up to now, few laboratory studies have been dedicated to magnetic reconnection. Nonetheless, laboratory experiments can be very complementary to data analysis using spacecraft measurements. The interesting point with spacecraft data is that

the electron scales are large enough to be observed in-situ. As a result, a very wide range of scales can be investigated, as illustrated by the inspection of turbulence in the solar wind (see e.g. [**?**]). On the other hand, one can neither choose the position of the spacecraft, nor the conditions of the solar wind. In other words, data collected from spacecraft measurements are not reproducible.

Laboratory experiments have several advantages, as well as drawbacks. Laboratory experiments are generally reproducible, can be instrumented in various way to collect the desired informations, and with initial and boundary conditions imposed by the observer. Furthermore, they are generally far less expensive than spacecraft missions. On the other hand, the scales are quite different, and the resolution of the instruments can be limited to get the needed informations.

For magnetic reconnection, it exists several magnetic devices specifically designed to study the onset and dynamics of magnetic reconnection. These experiments can have a toroidal geometry like the MRX[1] experiments of Princeton (see e.g. [**?**]) or the VTF[2] of the MIT (see e.g. [**?**]). The basic concept is to generate a set of two closed flux tubes by toroidal magnetic coils, and let them reconnect. Other devices like the LAPD[3] experiments of Berkley (see e.g. [**?**]) creates linear flux tubes that can possibly reconnect because of their twisting.

For astrophysical applications, laser experiments can also provide an interesting tool. A review of these experiments using intense laser is proposed in [**?**]. The first experiment on magnetic reconnection using intense laser is the one of [**?**]. The basic idea is very simple : a short intense beam shots a target. A plasma plume is hence created on its surface. Calling Z the axis of the laser, and XY the plane of the target, this plume is associated to a gradient of the electron density that is mainly axial (along Z) and the associated electron temperature gradient that is radial in the XY plane. The resulting electric field is essentially given by the gradient of the electron pressure. Using the Maxwell-Faraday equation, an associated magnetic field is growing in the poloidal direction. This is illustrated in Fig. 4.5. This regime is called “High Energy Density Plasmas”.

It clearly appears in Fig. 4.5 that the magnetic topology is propitious to magnetic reconnection associated to an X point, located where the two magnetic flux tubes meet. The structure and dynamics of the magnetic reconnection process depends

[1]Magnetic Reconnection eXperiment
[2]Versatile Toroidal Facility
[3]Los Angeles Plasma Device

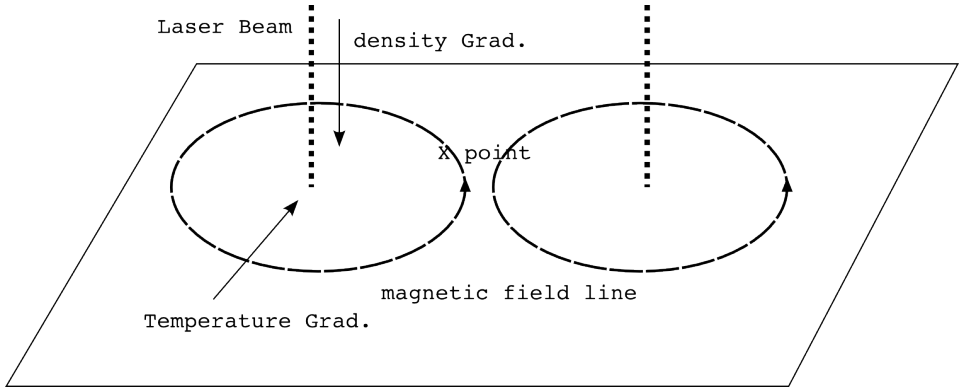

Figure 4.5: Schematic of the laser beam interracting with the target. The density gradient is axial, the temperature gradient is radial, and the associated magnetic field lines are poloidal.

on the characteristic parameters. To ease the comparison with the magnetic reconnection widely studied in the solar wind, a comparison between these parameters in HEDP and solar wind is proposed in appendix J.

The two most importants points are for sure the dimensionless parameters β and Lundqvist number. In HEDP, the plasma is weakly collisional. The Spitzer-Härm resistivity is finite, and associated to a Lundqvist number of the order of few hundreads. This is a big difference with the collisionless magnetic reconnection occuring in the solar wind. Furthermore, it is interesting because numerical simulations cannot run with a null resistivity (generally, the numerical resistivity is associated to a Lundqvist number not larger than few thousands). The other point is that in HEDP, the β plasma parameter can be up to few hundreads. The system is hence dominated by the plasma pressure.

A collaboration is growing between LULI, CEA, LPP and LESIA to investigate magnetic reconnection using laser experiments. Nothing has been published yet, but some numerical simulations have already been done with the HECKLE code. We use initial conditions very similar to the ones of [**?**] and [**?**] ; two closed flux tubes generated by the Biermann-Battery effects described hereabove. With an initial radial velocity, each of these flux tubes expand and get in contact. Then, because of the small resistivity, magnetic reconnection can occur. We present the very first hybrid simulation using $\beta = 1$ and $L = 1000$. We are currently investigating a range of larger β values.

The interesting thing with laser experiments is that one can control the initial magnetic topology through the choice of the targets, their relative position as well as the intensity of the laser shot. As a rough picture, the Z value of the targets can control the kinetic pressure, the intensity of the laser shot can control the magnitude of the magnetic field, and the relative position of the 2 targets can control the magnetic field structure. More clearly, the "classical" configuration is the one with the two targets in the same plane. If not, as depicted in Fig. 4.6, two angles Φ and Ψ can be defined. Φ is the angle around the Y axis cartooned in the left panel, and Ψ is the angle cartooned in the right panel, cartooned in the right panel. For $\Phi \neq 0$, the out-of-plane magnetic field has a quadrupolar structure. For $\Psi \neq 0$, the out-of-plane magnetic field has the structure of a constant guide field.

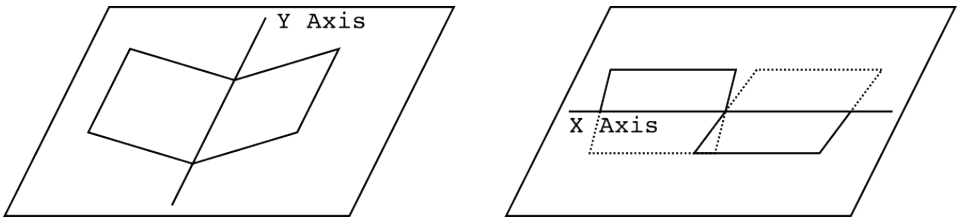

Figure 4.6: Schematic description of the relative positions of the two targets when setting an angle Φ around the Y axis (left panel) or an angle Ψ around the X axis (right panel).

In the case $\Phi \neq 0$, depending on the sign of Φ, the quadrupolar structure of the magnetic field can be in the same direction as the Hall magnetic field, or in the opposite direction. We thus run the HECKLE code with different values of the Φ angle, positive and negative. As initial conditions, we have in the simulation box two magnetic bubbles as illustrated in Fig. 4.7. The main advantage of this configuration is that we can study in the same run two opposite values of the Φ angle in a periodic simulation. We call 0 the lower reconnection site and 1 the upper one.

In Fig. 4.7 the two quadrupolar structures can be observed. The upper one is in the same direction as the Hall one, and the lower one is in the opposite direction. It is important to note that when the Φ angle increases, by geometric effects, the distance between the two outer edges of each flux tubes also increases. Focusing on region 0, Fig. 4.8 displays the Z component of the magnetic field (Hall component) at $t = 0$ (upper panel) and $t = 20$ (lower panel). As will be displayed in Fig. 4.9,

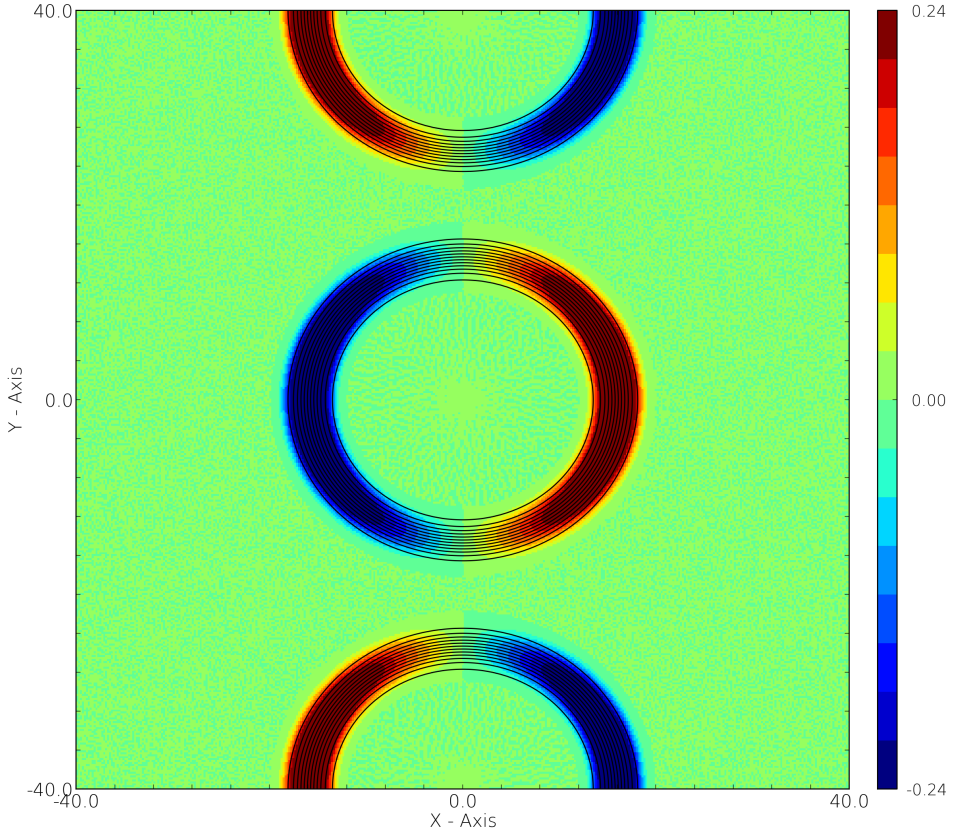

Figure 4.7: Z component of the magnetic field at $t = 0$ for $\Phi = 20^o$ (upper part) and $\Phi = -20^o$ (lower part).

$t = 20$ is just before the reconnection onset. It is very clear on Fig. 4.8 that the initial quadrupolar structure of the magnetic field is destroyed and a new one in the opposit direction (i.e. in the same direction as the Hall component) appears. It is important to note that this Hall component of the magnetic field develops prior the onset of magnetic reconnection.

The time evolution of the reconnected flux for $\Phi = -20^o$ is depicted in Fig. 4.9, in dotted line for region 0 and dashed line for region 1. The two solid lines are the linear interpollations. Their slopes are equal to the electric field at the X line, namely the reconnection rate. One can notice several things. First, the time of the reconnection onset depends on the region. We define the time lag ΔT as the difference between the onsets of reconnection for positive and negative values of

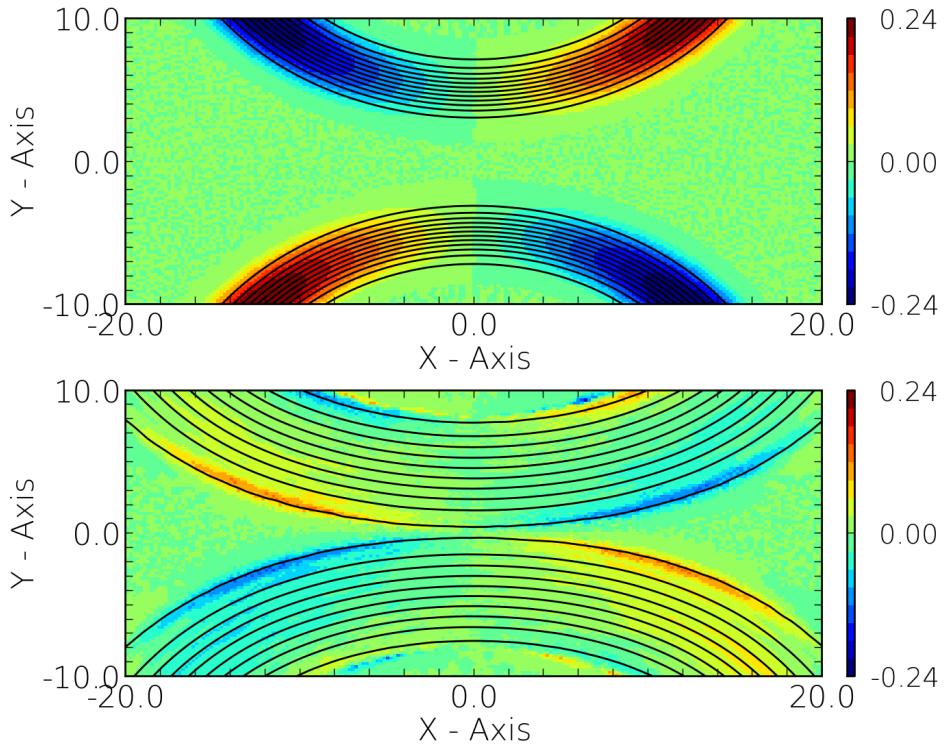

Figure 4.8: Z component of the magnetic field at (upper panel) $t = 0$ and (lower panel) $t = 20$ for $\Phi = -20^o$.

Φ. Interestingly, the onset of reconnection is always later for negative Φ than for positive Φ. The second important remark is that the two reconnection rates (given by the slope of the reconnected flux) are differents, namely 0.13 and 0.10.

In Fig. 4.9, one can observe that the reconnected flux has a slope that slightly varies during time. This slope being the reconnection rate, the time evolution of this values (which is very close to the Z component of the electric field in the reconnection region) is displayed in Fig. 4.10. The 2 shaded rectangles display before and after reconnection, namely when the reconnected flux is constant. This clearly displays a "batman ears" structure that can be observed for whatever values of Φ (positive or negative). This is a new feature that has not been observed in simulations like the ones of the GEM. Furthermore, the begining of the first ear and the end of the second correspond with the onset and extinction of reconnection.

Fig. 4.11 displays for the same run (region 0 and $\Phi = -20^o$) the time evolution of

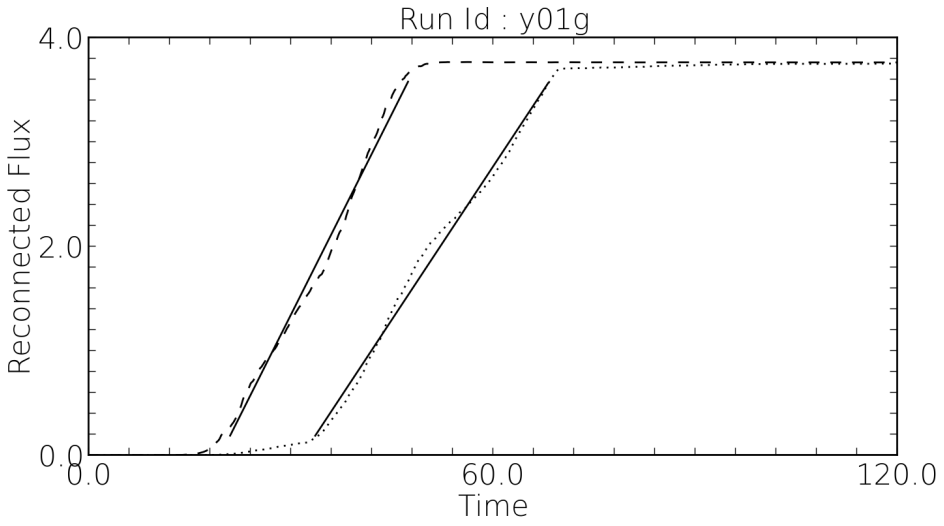

Figure 4.9: Time evolution of the reconnected flux in region 0 (dotted line) and in region 1 (dashed line). The solid lines are the linear interpollation, which slopes are the reconnection rate.

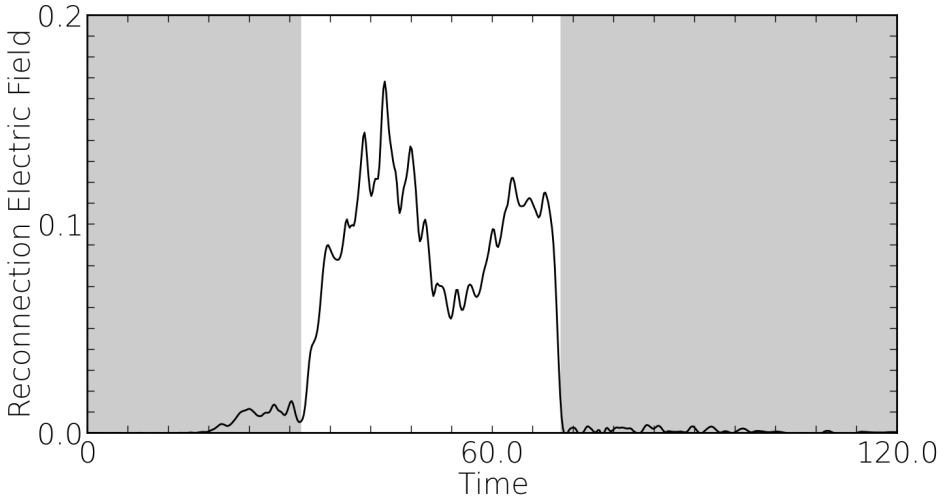

Figure 4.10: Time evolution of the reconnection electric field (Z component) for bubble 0 with $\Phi = 20^o$. The two shaded rectangles indicate befaore and after reconnection.

the maximum value of the Z component of the magnetic field. This value is always

very close to the separatrix as displayed in Fig. 4.8 and is the Hall component as outlined by its quadrupolar structure. The important feature to notice, as already outlined is that when reconnection occur, the Hall component of the magnetic field is already well developped. Up to now, it was believed that the Hall component of the magnetic field was a consequence of the reconnection process : the electrons are drastically accelerated in the Z direction by the reconnection electric field in the electron decoupling region. When the electrons get magnetized in the ion decoupling region, they transport the magnetic field in the Z direction. It was thus believed that Hall magnetic field and reconnection were "simultaneous". The above results would suggest that the Hall component of the magnetic field is a cause and not a consequence of magnetic reconnection.

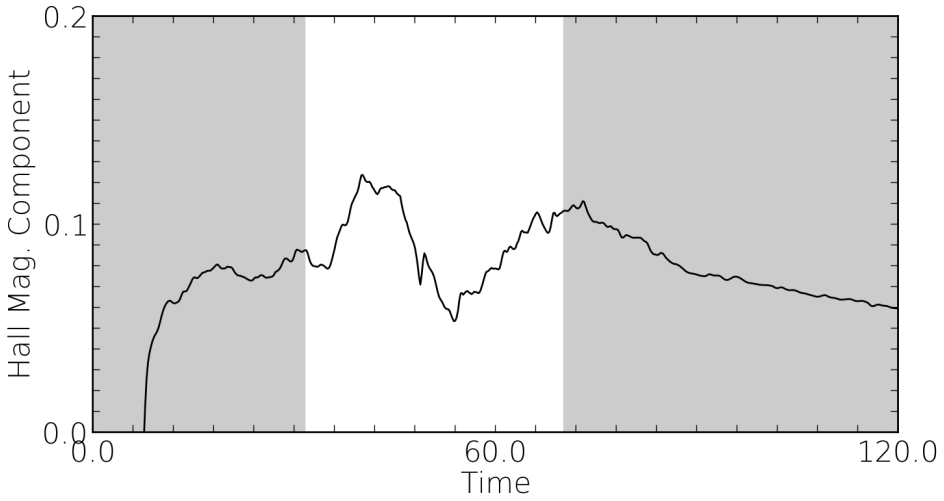

Figure 4.11: Time evolution of the maximum value of the Hall magnetic field among the separatrices for bubble 0 with $\Phi = 20^o$. The two shaded rectangles indicate befaore and after reconnection.

We had 6 different runs with Φ spaning between 0^o and 24^o (with negative and positive values for region 0 and 1, respectively). For each runs, we calculate the mean reconnection electric field and the time lag ΔT. Fig. 4.12 displays the reconnection electric field depending on the Φ angle as a circle, the surface of the circle being proportional to ΔT. It clearly appears that ΔT enhances with Φ, at least for small Φ values. This shows that it takes a longer time to trigger reconnection when the initial Z component of the magnetic field is in the opposite direction as the Hall

component that appears before reconnection.

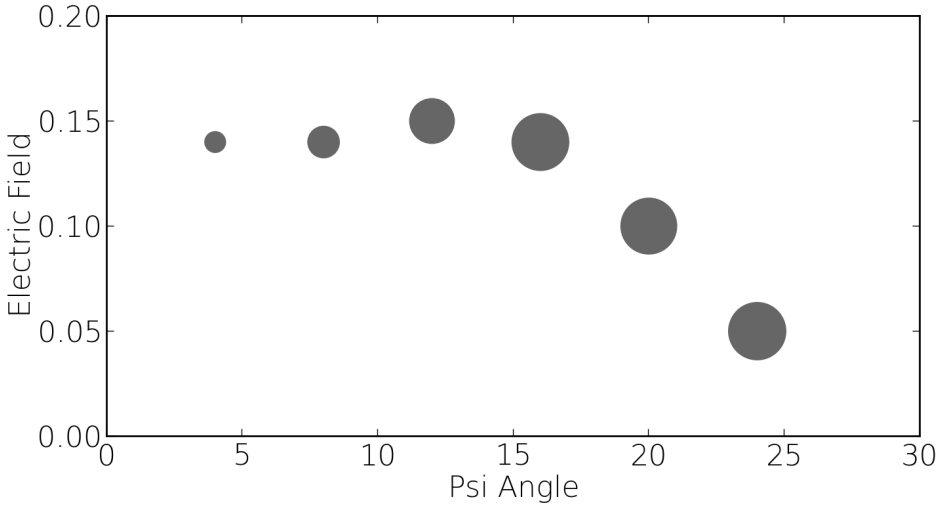

Figure 4.12: Reconnection electric field depending on the Φ angle. The surfaces of the cicrcles are proportional to the ΔT value.

Yet, it is a preliminary work, but there are two observations that leads to the same conclusion :

- The time lag ΔT increases with the Φ value, meaning that it takes a longer time to trigger reconnection in situation where the quadrupolar structure of the Z component of the magnetic field is in the direction opposite to the Hall one.

- The Z component of the magnetic field is already well developped at the onset of reconnection.

Both remarks lead to the same conclusion : the quadrupolar structure of the Hall magnetic field is a cause and not a consequence of collisionless magnetic reconnection. It is yet unclear what is on the origin of this component. Of course, as already discussed, it is associated to a Z component of the electron current, electrons being the main magnetic field carriers in this region where ions are demagnetized. But as can be seen on Fig. 4.10 and Fig. 4.11, B_z is already well developped prior reconnection onset, and the reconnection electric field is very weak. Hence, the electron current in the Z direction cannot result from the reconnection electric field.

Furthermore, in Fig. 4.12, we have not discussed (and not understand) why the reconnection rate decreases at large Φ angle values.

In April 2014, we will have a one week experiment on the PHELLIX laser in GSI to investigate these features. Comparisons with observations are not so easy in laser experiments as we can only measure integrated quantities. As an example, to measure the Hall magnetic field, we use proton radiography. Hence, we can only measure the value of the magnetic field integrated along the path of the proton beam. Even in optimizing the position of the proton source, we need some decorrelation tools to see if the measured signatures are in agreement with the numerical predictions.

We pointed out in this chapter a new method for the kinetic initialization of a thin asymmetric current sheet. This method will be used in forthcoming studies to investigate magnetic reconnection in such topologies and it will be interesting to study how the dynamics of magnetic reconnection is affected by the initial equilibrium.

We also start to address the problem of magnetic reconnection onset in an original topology. This numerical work is important to prepare laboratory measurements of the reconnection process between two laser induced magnetic flux tubes. The interesting difference with the topology generally used (see the GEM challenge, [**?**]) is that the reconnection is not triggered artificially at $t = 0$, but triggers later on. This should help to understand what are the causes, and what are the consequences in this self-consistent process.

Conclusions

The two major topics of my research works are particle diffusion and magnetic reconnection. Yet, we are far from understanding these processes, as well as their coupling. Several studies are already on their way among which :

- Invsetigate anomalous diffusion using particle-test. The goal is to revisit the problem treated in published studies, and see if any structured mean flow can exist that can falsly looks like super-diffuion, because of the associated ballistic effects.
- Go farther in the beginning of the analytical model presented in chapter 2. This include to investigate higher level of magnetic fluctuations to see if the lineraity of the electric and magnetic effects still holds.
- Invsetigate the nature of the electromagnetic fluctuations, depending on the way the system is forced. The PDF of the magnetic fluctuations does not contain the same informations as the associated spectrum. It could question the validity of the random phase oftenly used.
- Invsetigate the dynamics of reconnection in non-coplanar situations. It means to play with the two possible angles between the flux tubes as described in chapter 4. For that issue, we expect to get significant informations from Laboratory experiments. The first one on PHELLIX at GSI (Darmstadt) is scheduled in April 2014.

I also started to study other topics, as a result of new collaborations. At LPP, with Jean-Luc Raimbault, we started to investigate magnetic thruster for spatial propulsion. With Andrea Ciardi, I started to investigate the structure of shocks in Z pich experiments (in collaboration with Imperial college). With Stefano Gabicci and Andrea Ciardi, we start a collaboration on the streaming instability in the interstellar media associated to the flow of low energy cosmic rays (below 10 GeV).

Bibliography

— A —

Charged particle dynamics in a tangential discontinuity

R. Smets,

Laboratory for Extraterrestrial Physics (NASA/GSFC),

Journal of Geophysical Research

Vol. 105, No A11, pages 25009 - 25020, 2000

JOURNAL OF GEOPHYSICAL RESEARCH, VOL. 105, NO. A11, PAGES 25,009–25,020, NOVEMBER 1, 2000

Charged particle dynamics in a tangential discontinuity

Roch Smets[1]
NASA Goddard Space Flight Center, Greenbelt, Maryland

Abstract. We investigate the regularity of particle motion in a magnetopause-like magnetic field topology for a southward interplanetary magnetic field case. For that issue, a rotation of 180° of the magnetic field direction through the magnetopause is considered, while its total magnitude remains constant. Our main interest is to emphasize the different dynamical regimes for charged particles when their Larmor radii are of the order of the thickness of the magnetic field reversal layer. When the interface is a tangential discontinuity, it is shown that particle dynamics is regular, whereas the introduction of a small component of the magnetic field, normal to the interface, results in weakly stochastic dynamics. A new parameter κ_{RL} is introduced to organize the charged particle dynamics. When κ_{RL} is greater than 1, particle motion is adiabatic, and when κ_{RL} is smaller than 1, particle motion is nonadiabatic, its magnetic moment being possibly either damped or unchanged when interacting with the discontinuity. Implications for the pitch angle distribution of a population interacting with such a tangential discontinuity will be discussed.

1. Introduction

A large number of studies have previously been dedicated to nonadiabatic motion of charged particles in the magnetotail. The thin current sheet observed in the nightside of the magnetosphere is on the origin of a tightly curved magnetic field. For the thermal ion population of the plasma sheet (1 keV) the curvature radius R_C of the magnetic field lines at the equator is of the order of the Larmor radius ρ_L in the near tail (at ~ 8 R_E) and is several times smaller in the far tail (after 50 R_E). Considering a magnetic field along the Sun-Earth direction reversing on a small scale length compared to the Larmor radius, the so-called Harris sheet (HS) [see *Harris*, 1962], *Speiser* [1965] showed that charged particles remain infinitely trapped in the neutral sheet, exhibiting a fast oscillation in the direction perpendicular to the HS. The addition of a small component of the magnetic field in the south-north direction (normal to the HS that we will call the modified HS) lead to untrap these particles. In such motion the magnetic moment is not conserved, but the action integral $I_z = (2\pi)^{-1} \oint \dot{z} dz$ (where z is the direction of oscillation) is an adiabatic invariant [see *Speiser*, 1970] and *Sonnerup* [1971] gave its analytic form in a pure HS. This motion is called quasi-adiabatic or super-adiabatic motion.

Performing Poincaré surfaces of section (SOS) displaying the particles' position in the phase space when crossing the plane of minimum magnetic field, *Chen and Palmadesso* [1986] found different behaviors depending on the particles' Hamiltonian. When $R_C \sim \rho_L$, the Poincaré SOS are uniformly filled, which is characteristic of a chaotic dynamics. However, when $R_C < \rho_L$, there are some uniformally filled regions and some regions where the crossing points draw closed curves. These closed curves (also called Kolmogorov Arnold Moser (KAM) surfaces) prove the existence of islands of stability, related to the existence of an adiabatic invariant. *Karimabadi et al.* [1990] displayed Poincaré SOS associated to different magnetotail configurations. *Burkhart et al.* [1995] investigated the influence of the z component of the magnetic field in the Poincaré SOS using a modified HS and *Büchner and Zelenyi* [1991] and *Holland et al.* [1996] studied the influence of a small y component of the magnetic field in the same topology.

Aiming to classify the possible orbits as to their integrability, *Büchner and Zelenyi* [1989] proposed the curvature parameter κ (that we will call later κ_{BZ}), defined as

$$\kappa_{BZ} = \left[\frac{R_{Cmin}}{\rho_{Lmax}}\right]^{1/2}, \qquad (1)$$

where R_{Cmin} is the minium curvature radius of the magnetic field lines and ρ_{Lmax} is the maximum Larmor radius. For $\kappa_{BZ} > 3$ the motion is essentially adiabatic, for $\kappa_{BZ} \sim 1$ the motion is chaotic, and for $\kappa_{BZ} \ll 1$ the motion is either chaotic or super-adiabatic. Chaotic system has to be understood in the sense of high sensitivity to initial conditions. Strictly speaking, this system is a chaotic scattering system [see, e.g., *Eckhardt*,

[1]Permanently at Centre d'étude des Environnements Terrestre et Planétaires, Centre National de la Recherche Scientifique, Vélizy, France.

Paper number 1999JA000173.
0148-0227/00/1999JA000173$09.00

1988]. The magnetic field being constant, particles are not constraint to stay in the stochastic region (in the discontinuity) and escape in the asymptotic region (out of the discontinuity) where the magnetic field is uniform and the particle motion adiabatic. *Chen* [1992] put forward the divergence of two initially nearby orbits in a modified HS computing the average exponent divergence rate (AEDR), which is a modification of the Lyapunov procedure.

Berchem and Russell [1982a] showed on the basis of ISEE 1 and 2 observations that the magnetopause thickness is $\sim$ 800 km, which is of the order of the 1 keV H^+ Larmor radius (see also *Le and Russell* [1994]). We thus expect finite Larmor radius effects at the magnetopause. Examining Explorer 12 magnetic field measurments, *Sonnerup and Cahill* [1967] showed that in most of the magnetopause crossing, the magnetic field component, normal to the magnetopause, is very weak, and the magnetopause is thus essentially a tangential discontinuity (TD), the magnetic field being always tangential to the magnetopause. Studying the magnetopause polarization, *Berchem and Russell* [1982b] also identified it as a TD and showed a rotation of the magnetic field from its asymptotic values in both sides of the magnetopause. *Papamastorakis et al.* [1984] obtained the same result for large field angle rotation and concluded that even for strong southward interplanetary magnetic field (IMF), when reconnection is suspected, the discontinuity is tangential and not rotational.

Several studies have been dedicated to particle dynamics in magnetopause-like magnetic field geometry. Some of the magnetic topology used in testparticle calculations where similar to the one used in the tail during reconnection events with gradient and possible annihilation of the magnetic field [see, e.g., *Speiser et al.*, 1981; *Curran et al.*, 1987; *Curran and Goertz*, 1989]. *Swift and Lee* [1983] studied numerically the magnetopause polarization as its stability for different initial conditions of rotational discontinuity. However very little attention has been devoted to tangential discontinuities and to the associated charged particle dynamics that seems the most relevant magnetic topology for the quiet magnetopause. Using the Hamiltonian mechanics, the stochasticy of charged particles in a slab geometry with a laminar magnetic field, such as the one observed at the magnetopause, is investigated.

The equations of motion in the frame of Hamiltonian mechanics will be introduced in section 2, and the implications for charged particle dynamics will be discussed. Both TD and modified TD (TD with a small component of the magnetic field normal to the interface) will be investigated. The new parameter κ_{RL} will be introduced in section 3 to classify the different behaviors, and phase space structure will be discussed using computed Poincaré SOS. Section 4 will be a focus on the origin of stochasticity of charged particle motions in a modified TD. Section 5 will present a comparison between dynamics in a modified HS and in a modified TD. Section 6 will summarize the obtained results and the implications for the pitch angle distributions at the traversal of the discontinuity will be introduced. This study is focused on the high magnetic shear case with a field rotation angle of 180°. Other cases in which the magnetic shear is smaller than 180° will be also discussed in section 6.

2. Particle Dynamics

The simplest model to describe the magnetic field at the magnetopause (assuming a rotation of 180° from a southward magnetic field in the magnetosheath to a northward magnetic field in the magnetosphere) when there is no gradient of the magnetic field magnitude across this interface is

$$b_x = b_0 \cos(\pi y/2L) \quad (2a)$$

$$b_y = 0 \quad (2b)$$

$$b_z = b_0 \sin(\pi y/2L) \quad (2c)$$

with b_0 being the asymptotic value of the magnetic field and L being the half thickness of the magnetopause. Equations of system (2a-2c) are valid for $-L < y < +L$. For $y < -L$ (respectively $y > +L$), $b_z = -b_0$ (respectively $b_z = +b_0$), with $b_x = b_y = 0$. The vector potential associated to this magnetic field vector is

$$\vec{A} = \frac{2Lb_0}{\pi}[\cos(\pi y/2L)\hat{x} + \sin(\pi y/2L)\hat{z}] \quad (3)$$

with the Coulomb gauge. Calculations being less tedious using dimensionless coordinates, distances are normalized to the half thickness of the magnetopause L and time to the gyrofrequency $\Omega = qb_0/m$ of the particles of mass m and charge q. In the absence of an electric field the Lagrangian is thus given by

$$L = \frac{1}{2}(\dot{x}^2 + \dot{y}^2 + \dot{z}^2) + \frac{2}{\pi}[\dot{x}\cos(\pi y/2) + \dot{z}\sin(\pi y/2)]. \quad (4)$$

The three canonical momenta are thus

$$P_x = \dot{x} + A_x \quad (5a)$$

$$P_y = \dot{y} \quad (5b)$$

$$P_z = \dot{z} + A_z \quad (5c)$$

with $A_x = (2/\pi)\cos(\pi y/2)$ and $A_z = (2/\pi)\sin(\pi y/2)$. The Lagrangian does not depend on x and z, and as a result, P_x and P_z are constants of the motion ($d_t P_x = 0$ and $d_t P_z = 0$). Using the Legendre transformation $H = \mathbf{P}\dot{\mathbf{r}} - L$ (where $\mathbf{r}$ denotes the generalized coordinates), the Hamiltonian is

$$H = \frac{1}{2}[(P_x - A_x)^2 + P_y^2 + (P_z - A_z)^2] \quad (6)$$

that is also a constant of the motion ($d_t H = 0$) as it does not explicitly depend on time. A system with 3 degrees of freedom is known to be integrable if there are three

constants of the motion that are in involution, meaning that their Poisson brackets vanish [see, e.g., *Lichtenberg and Liebermann*, 1983]. It is easily verifiable that it is here the case. Hence there exists a frame in which H, P_x, and P_z are the new canonical momenta, the solution of the Hamilton's equations being trivial in this frame. Particle dynamics in a pure TD is thus regular and predictible.

The system described in this study can be compared to the one studied by *Speiser* [1965] and *Sonnerup* [1971] in a HS. In the absence of a small z component of the magnetic field normal to the neutral sheet, particle motion can be either adiabatic or super-adiabatic, whatever the value of κ_{BZ} (the higher κ_{BZ}, the thinner the super-adiabatic layer). The corresponding orbits are called noncrossing orbits and meandering orbits, respectively (see, e.g., Figure 2 of *Sonnerup* [1971]). However, in a pure HS, there is no phase space regions where one can find both adiabatic and super-adiabatic dynamics (involving transition regions) for the same orbit. In the same way, for a pure TD (no component of the magnetic field normal to the interface), particles initially far from the interface will never get close to it ($\mu = mV_\perp/qb_0$ being conserved) and particles initially close to the interface will never escape from it. However, annihilation of the magnetic field in the HS results in the existence of a super-adiabatic layer, whatever the value of the Hamiltonian, whereas this layer can vanish in the TD because of the absence of gradient in the total magnetic field magnitude. In the case where particles are close to the interface (in a TD), they can experience both meandering orbits (a constant of the motion $I_y = (2\pi)^{-1} \oint \dot{y} dy$ can be defined in the same way as in a HS as shown in section 4) or adiabatic orbits depending on their Hamiltonian value.

With the magnetic topology defined by (2a-2c), particle dynamics is regular and the associated Hamiltonian system is integrable. This conclusion is valid under the assumption that the electric field (not taken into account in this study) is also not able to drive particles close to the discontinuity. The convection and corotation electric field usually drive particles tangentially to the magnetopause, unless there exists some reconnection region. Thus the electric field can hardly be responsible for an evolution from noncrossing to meandering orbit.

In the magnetopause data a component of the magnetic field, even small, is generally observed in the direction normal to the interface. In a similar way to the tail configuration, this small component of the magnetic field can carry particles initially far from the discontinuity in its vicinity. Thus transient orbits in which particles experience a transition from noncrossing orbits to meandering orbits are expected. The equation (2b) is modified with $b_y = b_n$, where $\delta = b_n/b_0$ is small, to study the effect of such a small component of the magnetic field on particles dynamics. This topology is referred to as the modified TD.

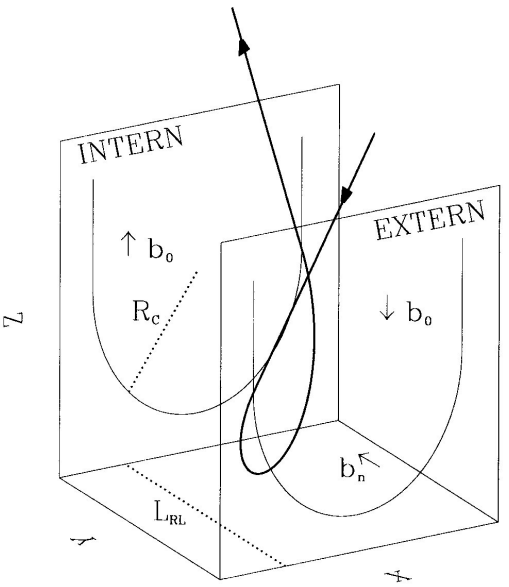

Figure 1. Solid thick line presents a magnetic field line in three dimensions. The arrow indicates the southward orientation of the magnetic field in the magnetosheath and its northward orientation in the magnetosphere. Dashed lines present the local curvature radius R_C and the characteristic scale length L_S.

It has to be noted that a rotational discontinuity has by definition a component of the magnetic field normal to the discontinuity of same magnitude in each side of the discontinuity (satisfying the Rankine-Hugoniot jump conditions). There is no assumption on its magnitude compared to the total magnetic field magnitude. To make a point that we consider in this study a normal component of the magnetic field of first order compared to the tangential magnetic field, we call this topology a modified TD as it is close to a pure TD. The resulting shape of the magnetic field lines is depicted in Figure 1. The solid thick line is a magnetic field line oriented southward for $y < -L$, and northward for $y > +L$. The two vertical planes are defined by $y = -L$ and $y = +L$, in which the solid lines are the projection of the magnetic field lines. This depicts the duskside of the magnetopause.

In this system the new vector potential then depends on the choice of the gauge. With the Coulomb gauge,

$$A_x = 2/\pi \cos[\pi y/2] + \delta z \quad (7a)$$

$$A_z = 2/\pi \sin[\pi y/2] \quad (7b)$$

The z coordinate is no longer cyclic, as the Lagrangian depends on z, and P_z is no longer a constant of the motion. However, knowing only two constants of

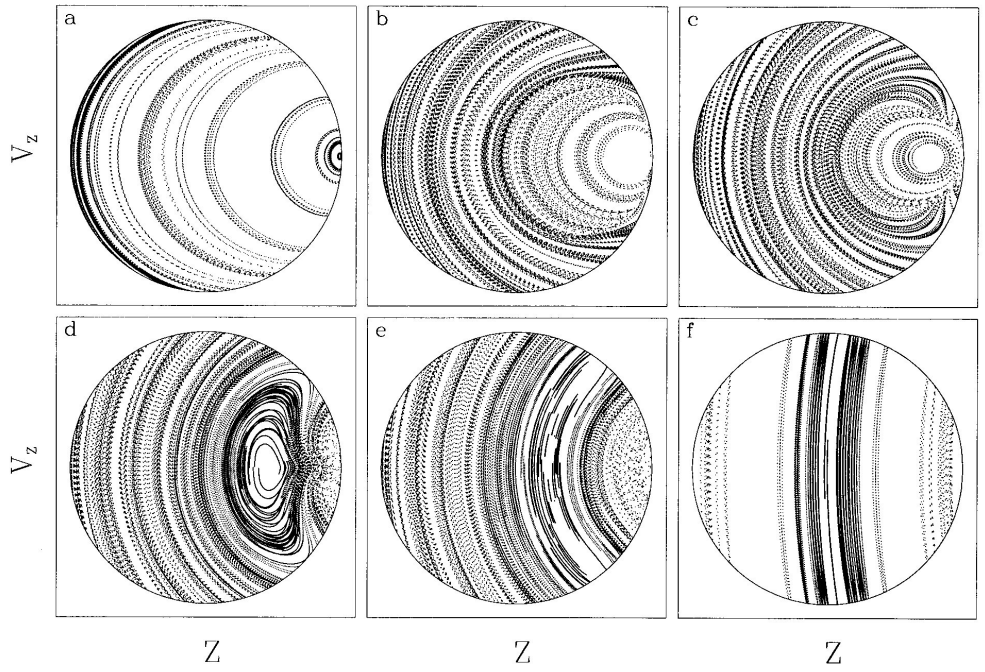

Figure 2. Poincaré surface of section in the $(z, \dot{z})$ plan: (a-f) obtained at $\kappa_{RL} = 0.3$, 0.8, 1.0, 1.2, 1.4, and 3.0, respectively.

the motion using elementary methods does not rule out the existence of a third (that can be in involution with the two others). The easier way to predict the integrability of the system is to compute Poincaré surfaces of section [see, e.g., *Lichtenberg and Liebermann*, 1983].

3. The κ_{RL} Parameter and the Poincaré Surfaces of Section Structures

The Poincaré SOS display the phase space position of a set of particles when crossing a given plane. The set of particles is chosen to cover the whole phase space, assuming that they all have the same values for the constants of the motion (H and P_x for a modified TD). The plane is generally chosen for its symmetric properties and the Poincaré SOS presented in this study are built in the $y = 0$ plane.

As different types of behavior are expected depending on the value of the normalized Hamiltonian, the new dimensionless parameter κ_{RL} is introduced

$$\kappa_{RL} = \left[\frac{L_{RL}}{\rho_{Lmax}}\right]^{1/2}, \tag{8}$$

where L_{RL} is the thickness of the reversal layer and $\rho_{Lmax} = mV/qb_0$ is the maximum Larmor radius. In the present case, $L_{RL} = L$, the half thickness of the magnetopause. As κ_{BZ} allows a classification of the different orbits depending on the importance of the curvature of the magnetic field lines, the κ_{RL} parameter is proposed to organize the possible orbits in topology with just a change of the magnetic field direction and no gradient of its total magnitude. In the modified TD case, $\kappa_{RL} = [Lqb_0/mV]^{1/2}$. Section 5 will be dedicated to the comparison between κ_{BZ} and κ_{RL}.

Figure 2 displays Poincaré SOS in the $(z,\dot{z})$ plan obtained for different values of κ_{RL}. These Poincaré SOS have been built with $P_x = 0$ and $\delta = 0.01$. The first Poincaré SOS in Figure 2a displays the phase space structure at $\kappa_{RL} = 0.3$. The computed crossing points draw curves (being the two-dimensional reduction of KAM surfaces). However, it can be seen that except at the very right part of the Poincaré SOS, those curves are not closed. The Poincaré SOS is just a collection of these arched curves. In order to understand these features a focus on the associated orbits is needed.

Figure 3 displays three particle orbits in a modified TD. The shaded region represents the $y = 0$ plan, and the solid and dotted thick lines represent the particle position for $y < 0$ and $y > 0$, respectively. Hence the particle position at $y = 0$ (on the shaded plane) are the one displayed in the Poincaré SOS. The orbit presented in Figure 3a is obtained at $\kappa_{RL} = 0.49$, which corresponds to $H = 10$, other parameters being set to

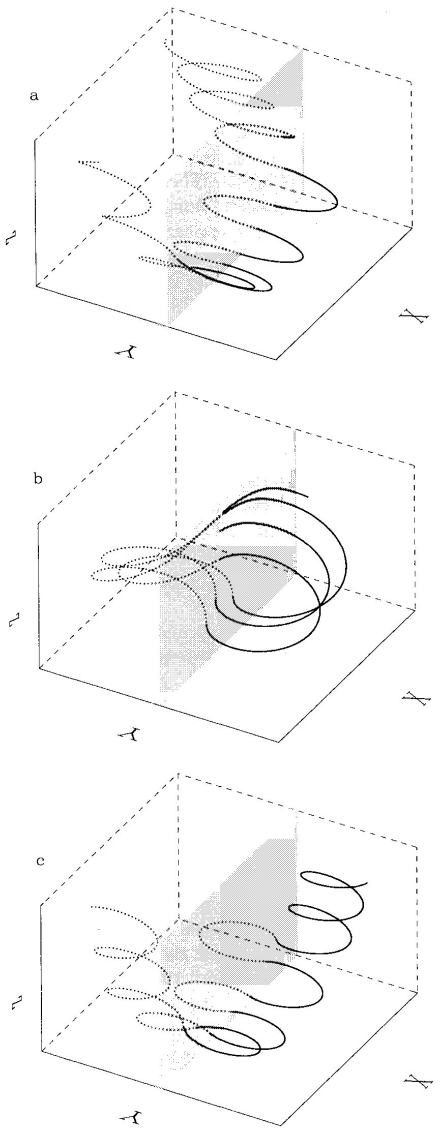

Figure 3. Particle orbits in a modified tangential discontinuity. The shaded region indicated the $y = 0$ plan, and the solid and dotted thick line indicate the particle position in the $y < 0$ and $y > 0$ region, respectively. (a) Nonescaping particle, (b) trapped particle, and (c) escaping particle.

$P_x = 0$ and $\delta = 0.1$ (the two other orbits of Figure 3 are obtained with the same values of κ_{RL}, P_x and δ). There is two adiabatic sequences for which the particle has a regular cyclotron motion around the magnetic field lines and a super-adiabatic motion for which the particle is meandering around the $y = 0$ plan. This type of orbit is somewhat similar to the Speiser orbits [see *Speiser*, 1965] in a modified HS. As the parameter δ is small, there is a clear decoupling between the fast oscillation in the y direction, owing to the reversal of the z component of the magnetic field in each sides of the $y = 0$ plane, and the slow gyration around the b_y component in the (x,z) plane.

This is on the origin of the arched curves in the Poincaré SOS. When getting close to the TD, z is decreasing as the magnitude of $\dot{z}$. Reaching the minimum value of z, $\dot{z}$ gets null, change its sign, and then its magnitude enhanced with the opposit sign while z is still increasing. A point that has to be noted here is that at $\kappa_{RL} = 0.3$, almost all these particles have this transient motion near the discontinuity. It is not the case for the marginal amount of particles that depict the small closed curves in the very right part of the Poincaré SOS of Figure 2.

Figure 2b depicts the Poincaré SOS computed for $\kappa_{RL} = 0.8$. Compared to the previous Poincaré SOS, the arched curves get fuzzy in the way that the crossing points are more dispersed than in Figure 2a and do not draw perfect lines. Furthermore, the closed features (at the right part of the plot) are developing in the phase space. As already mentioned at the begining of this section, KAM surfaces lies on the existence of 3 constants of the motion, for a system with 3 degrees of freedom. H and P_x being conserved, the third one is the action integral $I_y = (2\pi)^{-1} \oint \dot{y} dy$. We will show numerically in next section that I_y is conserved only when $\kappa_{RL} \ll 1$. The closed structures in Poincaré SOS were close to KAM surfaces for $\kappa_{RL} = 0.3$ as I_y was conserved but get fuzzy at $\kappa_{RL} = 0.8$ as I_y is not conserved anymore.

The origin of these closed structures lies on the existence of trapped orbits in the modified TD. Associated to the meandering motion in the y direction, the particle experience a slower gyromotion around the small y component of the magnetic field. Instead of experiencing half a turn around this small y component as in Figure 3a, trapped particles keep on gyrating around this component through the time. An example of this type of orbit is presented in Figure 3b. Even if just a fraction of the orbit is depicted for clearness, the particle stays trapped in the modified TD. The corresponding features in the Poincaré SOS are not closed curves as I_y is still not conserved but rather look like seashell. This spiral structure will become clearest in Figure 2c. The amount of trapped particles in the TD is increasing with κ_{RL}.

Figure 2c is the Poincaré SOS computed for $\kappa_{RL} = 1.0$. The two types of structures mentioned above are still present: the arched curves at the left part of the Poincarré SOS are still fuzzy, and the seashell-like structures are developing in phase space. The explanation for theses structures is the same as discussed above. But it has to be noted that the seashell-like structure

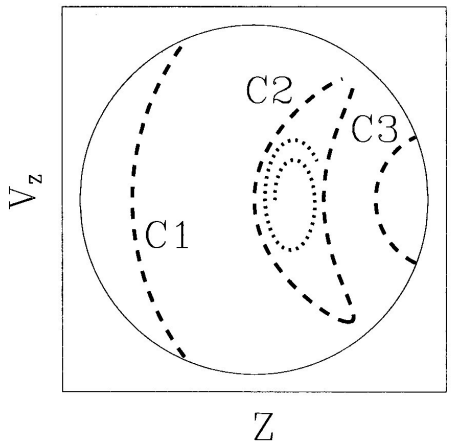

Figure 4. Schematic structure of a Poincaré surface of section in the $(z, \dot{z})$ plan. C1 and C3 regions (in dashed line) are associated to untrapped orbits, while C2 is associated to trapped orbits. The dotted line represent the seashell-like structure associated to weakly nonregular orbits.

is shifting to the left. Another point is that even if the arched curves are fuzzy, they still are arch shaped. That why we can not talk about chaos but rather on weak stochasticity.

Figure 2d is the Poincaré SOS computed for $\kappa_{RL} = 1.2$. As the κ_{RL} value is increasing, it is clear that the seashell-like structure is occupying more space in the whole phasespace. These structures stay localized at the large values of z and are now compressed on their right side. The very right part of the Poincaré SOS is then composed of new arched curves that are developing and shifting to small z values. These arched curves are very fuzzy but will become clearest at higher κ_{RL} value. This can be seen in Figure 2e, displaying the Poincaré SOS computed for $\kappa_{RL} = 1.4$. As the seashell-like structures are compressed, they get elongated in the $\dot{z}$ direction. These structures are thus not closed anymore and become arched curves as the tip of the seashell-like structures gets out of the Poincaré SOS. As κ_{RL} is increasing, seashell-like structures are opening. This means that increasing κ_{RL} results in detrapping of particles in the modified TD.

Figure 2f is the Poincaré SOS computed for $\kappa_{RL} = 3.0$. The seashell-like structure has been so compressed that they all became arched curves. This is the adiabatic regime for which particles' magnetic moment is conserved when interacting with the modified TD. The magnetic moment is now the third constant of motion, dynamic is regular, and the Poincaré SOS is just composed of KAM surfaces. It has to be said that the blank in the Poincaré SOS is due to the sampling of particles in order to make the plot clearest but could be filled with a different sampling.

The features discussed above are summarized in Figure 4. This is a schematic view of the Poincaré SOS. At low κ_{RL} value the Poincaré SOS is just made of arched curves as in structure C1. When increasing κ_{RL}, closed curves like in C2 appear at the very right part of the Poincaré SOS and shift to the left as κ_{RL} increases. At $\kappa_{RL} \sim 1$, seashell-like structures appear like the one enclosed in C2. Then as κ_{RL} continue to increase, C2 shift to the left, elongate in the $\dot{z}$ direction and get compressed by the appearing C3 structure that are also arched curves. Then the tips of C2 get out of the Poincaré SOS, and for $\kappa_{RL} > 3$, Poincaré SOS is just made of C1 and C3 structures.

There are several conclusions arising from the study of these Poincaré SOS:

1. The κ_{RL} is a new parameter that can organize particle dynamics in modified TD. When $\kappa_{RL} \gg 1$, particle motion is regular, the adiabatic moment being the third constant of motion (with H and P_x). When $\kappa_{RL} \ll 1$, particle motion is also regular, $I_y = (2\pi)^{-1} \oint \dot{y} dy$ being the new constant of motion associated to the meandering motion in the modified TD.

2. Depending on the κ_{RL} value, particles can be trapped in the modified TD: it happens for $\kappa_{RL} \sim 1$. This system is then chaotic.

3. The other particles experience just one interaction with the modified TD. This system is a chaotic scattering system.

The consequences of these conclusions will be discussed in section 6.

4. Separatrix Crossing

When particle dynamics is regular (either adiabatic or super-adiabatic), the third constant of the motion guarantees the existence of KAM surfaces in the Poincaré SOS (particle motion is thus predictible). Stochasticity arises at the transitions between different types of motion. This sequence is called the separatrix crossing [see, e.g., *Büchner and Zelenyi*, 1990].

Figure 5 (bottom) is the time evolution of the y position of a particle with $\kappa_{RL} = 0.45$, $P_x = 0$ and $\delta = 0.2$. Figure $I_y = (2\pi)^{-1} \oint \dot{y} dy$ and (dotted line) $\mu = mV_\perp/qb$, both in normalized units. The shaded regions are displayed to allow a comparison with Figure 6 and separate regions 1, 2, and 3. It is clear that in the adiabatic sequence (region 1), $\mu = mV_\perp/qb$ is the third constant of the motion, whereas in the superadiabatic sequence (region 3), $I_y = (2\pi)^{-1} \oint \dot{y} dy$ is the new one. The existence of this third constant of the motion vanishes during the switch between the two sequences (region 2). To emphasize the importance of region 2 and point out that it is on the origin of stochasticity in particle dynamics, a brief and qualitative analysis of the Hamiltonian equations is required.

Using (5a-5c) and (6), the first set of Hamiltonian's equations is

$$\ddot{x} = (\pi/2)\dot{y}A_z, \tag{9a}$$

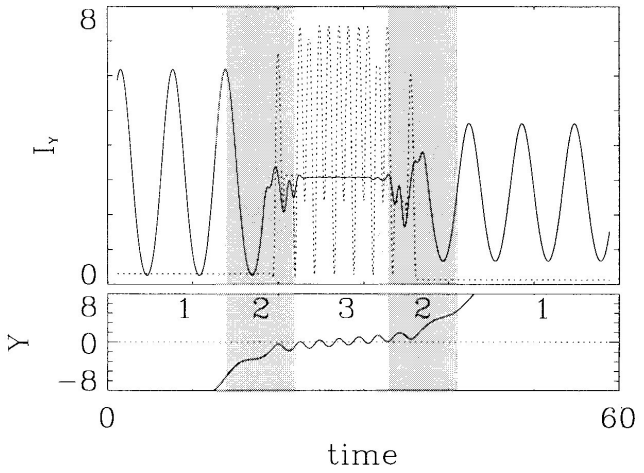

Figure 5. (top) (solid line) Action integral value and (dotted line) the magnetic moment evolution of the particle depending on time; (bottom) time evolution of the y position.

$$\ddot{y} = (\pi/2)\dot{z}A_x - (\pi/2)\dot{x}A_z, \quad (9b)$$

$$\ddot{z} = (-\pi/2)\dot{y}A_x. \quad (9c)$$

During the meandering sequence near the $y = 0$ plane the motion can be seen as the superposition of a fast oscillation in the y direction and a slow gyromotion in the (x, z) plane around the small b_y component. On the timescale of the fast oscillation, displacement due to the slow gyromotion in the (x, z) plan is of first order and thus has $z \sim C^{st}$ near $y = 0$. Using a Taylor series expansion near $y = 0$, (9b) is of the form

$$\ddot{y} = K\dot{x}y \quad (10)$$

(K being a constant). Defining $\tau_{\dot{x}}$ and τ_y as the timescale of variation of $\dot{x}$ and y, respectively, (10) will be nonlinear when $\tau_{\dot{x}} \sim \tau_y$, linear in $\dot{x}$ when $\tau_{\dot{x}} \ll \tau_y$ and linear in y when $\tau_{\dot{x}} \gg \tau_y$.

We computed at each time, t_i, the period of time, Δt, needed to get $\Delta\dot{x}_i/\dot{x}_i > \epsilon$ or $\Delta y_i/y_i > \epsilon$ (with $\Delta u_i = u(t_i+\Delta t) - u(t_i)$ and $\epsilon = 0.5$), Δt representing $\tau_{\dot{x}}$ and τ_y, respectively. We have thus defined the "Lorentz number" as

$$N_L = \frac{1}{\epsilon}\left[\frac{\Delta\dot{x}}{\dot{x}} + \frac{\Delta y}{y}\right], \quad (11)$$

which can be seen as the "order of the polynomial" in the right-hand side of (10). When N_L is ~ 1, (10) is a polynom of first order in $\dot{x}$ or in y (depending on the scaling between $\tau_{\dot{x}}$ and τ_y). When $\tau_{\dot{x}} \sim \tau_y$, (10) is nonlinear and can be seen as a second order polynom of a variable depending on $\dot{x}$ and y. We suspect emergence of stochasticity in regions where N_L reaches 2, whereas when N_L is close to 1, dynamics should be regular. Figure 6 depicts the evolution of this number (top) and the evolution of the y coordinate (bottom) over time for $\kappa_{RL} = 0.45$. This orbit is the same as the one presented in Figure 5.

Three different regions appear in Figure 6:

Region 1, where the particle motion is adiabatic, μ is conserved, N_L is close to 1 and the system is quite linear; Region 2 (indicated by the light gray rectangle) where the particles get close to the interface. In this transition region, between adiabatic motion and super-adiabatic motion, N_L reaches 2 and the system is nonlinear; Region 3, near the interface where the particle motion is super-adiabatic. I_y is conserved, N_L is close to 1 and the system is quite linear.

Region 2 in Figure 6 is a visual representation of the separatrix between adiabaticity and super-adiabaticity. When flowing through region 2, evolution of the phase space coordinates is stochastic.

The situation in the modified TD is quite different from the one in the modified HS. As in the modified TD the magnetic field magnitude is uniform, each particle experience just two crossings of the separatrix, each of them being associated to a chaotic scattering. In the modified HS the magnetic field gradient and the resulting bounce motion of particles leads to a succession of chaotic scattering. Furthermore, not only the number of chaotic scattering plays a role, but the nature of this scattering is different. This will be discussed in section 5. In this case, even if I_z is conserved during the meandering sequences, its value is not the same in each of the meandering sequences, because of its stochastic determination when crossing the separatrix. Hence the crossing points of the Poincaré SOS in the modified HS cannot draw any KAM curves. This is almost the case for the resonant energies (defined as the energies for which the magnetic moment is conserved after interacting with the modified HS) and the resulting Poincaré surfaces of

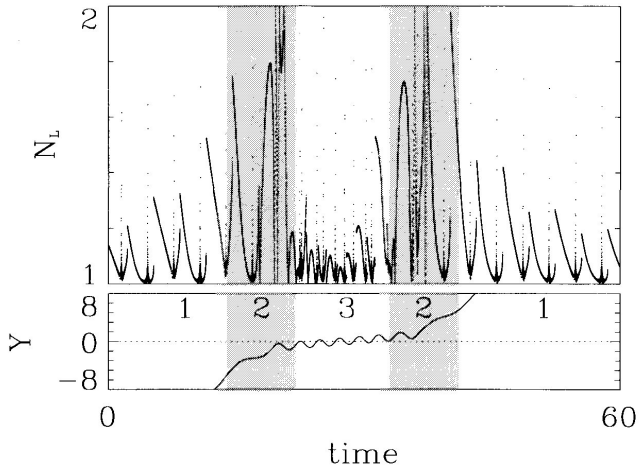

Figure 6. (top) N_L value (defined by (11)) and (bottom) y coordinate of the particle depending on time. In region 1 and 3 the system is weakly nonlinear (N_L is close to 1), and in region 2 indicated by light gray, the system is strongly nonlinear (N_L is close to 2).

section are more structured with the emergence of tentacles [see, e.g., *Chen and Palmadesso*, 1986].

Because there is only two separatrix crossings in the modified TD, the evolution of the particle position in phase space is weakly stochastic. At the first crossing the initial value of the action integral I_y is determined stochastically. As this value will not be the same for each particle, KAM curves cannot be obtained. However, the set of curves obtained from all the particles are close to one another, meaning that the different values of the action integrals are close. The phase space is well-organized, and the Poincaré SOS are not densely filled. Chaos cannot develop in modified TD, because of the limited number of interactions of the particles with the magnetic boundary.

5. Relation Between κ_{BZ} and κ_{RL}

There is a duality in the relative importance of magnetic field line curvature and finite size of the reversal layer effects between the modified HS and the modified TD. In the modified HS, $\vec{b} = b_0(z/L)\hat{x} + b_n\hat{z}$. The reversal layer thickness is $L_{RL} = L$ and the curvature radius of the magnetic field lines is $R_C = L\delta$, with $\delta = b_n/b_0$. Value δ being of the order of 0.1 or less in the tail, the curvature effects of the magnetic field lines will be dominant. In this topology, $\kappa_{BZ} = \delta\kappa_{RL}$ and particle dynamics will be essentially governed by the κ_{BZ} parameter. In the modified TD, $\vec{b} = b_0\cos[\pi y/2]\hat{x} + b_n\hat{y} + b_0\sin[\pi y/2]\hat{z}$. In this case, $L_{RL} = L$, and $R_C = L/\delta$ (δ being defined as in the former case). In Figure 1 the curvature radius and the reversal layer are indicated by thick dotted lines and labeled R_C and L_{RL}, respectively. Hence $\kappa_{BZ} = \delta^{-1/2}\kappa_{RL}$, and effects associated to the finite size of the reversal layer become dominant as $\delta \ll 1$. Thus we could expect a differentiation of the possible orbits depending on the κ_{RL} parameter value.

Several studies have been devoted to charged particle motion in a reversal magnetic field topology (like a HS or modified HS) in the presence of a shear field [see, e.g., *Karimabadi et al.*, 1990; *Büchner and Zelenyi*, 1991; *Zhu and Parks*, 1993; *Martin et al.*, 1994; *Holland et al.*, 1996]. Focusing on the magnetotail, this corresponds to a component of the magnetic field in the y direction of the order of the z component in quiet time, which become larger or dominant in flux ropes. *Büchner and Zelenyi* [1991] proposed the two parameter κ_n and κ_s associated to the normal and shear component of the magnetic field, respectively, and *Büchner et al.* [1991] investigated the consequences for the collisionless tearing mode instability. However, it has to be noted that in this type of magnetic configuration, there is a gradient of the magnetic field. Curvature of the magnetic field line plays a role in particle orbits but the gradient of the magnetic field magnitude has also a strong influence as the Larmor radius directly depends on it. These two effects cannot be decorelated in such magnetic topology. One of the aim of this study is to provide some insights in the relative importance of the finite size of the reversal layer and curvature effects for particle dynamics.

Figure 7 presents the ratio between final to initial magnetic moment of particles, after one interaction with the modified TD, depending on their initial pitch angle. Initial conditions are $P_x = 0$ and $\delta = 0.01$. When κ_{RL}

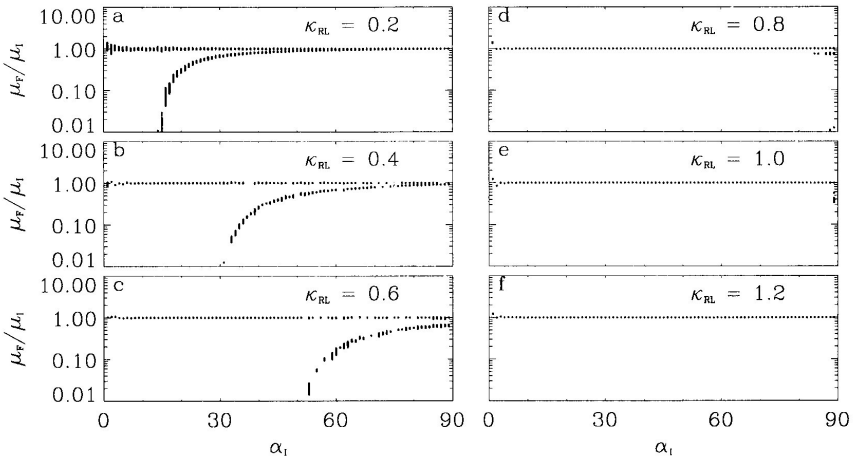

Figure 7. Ratio between final and initial magnetic moment after one interaction with the modified tangential discontinuity, depending on the initial pitch angle: (a-f) κ_S = 0.2, 0.4, 0.6, 0.8, 1.0, and 1.2, respectively.

is smaller than 0.3, κ_{BZ} is smaller than 3. As a result, both thickness of the reversal layer and curvature effects exist in this region. Conversely, when κ_{RL} is larger than 0.3, κ_{BZ} is larger than 3. *Sergeev et al.* [1983] demonstrated that above the limit $\kappa_{BZ} > 3$, there is no magnetic moment diffusion. The one observed in Figure 7 is only due to the finite size of the reversal layer. Figures 7a to 7f correspond to κ_{RL} = 0.2, 0.4, 0.6, 0.8, 1.0, and 1.2, respectively. The interval 0° - 90° of pitch angle and 0° - 360° of gyrophase are sampled with a 1° step. This display is similar to the one used by *Delcourt et al.* [1996] in their Figure 1 that they called the three branch pattern. Their study was conducted in a modified HS, for which κ_{BZ} is the parameter allowing to organize the different orbits. Figure 7 displays a horizontal branch at all pitch angle values, for which the magnetic moment is nearly constant and a skewed branch at higher pitch angle values, starting at a critical value α_C, for which the magnetic moment is damped. The position of the skewed branch drifts toward larger pitch angles when increasing the κ_{RL} value.

A major difference from the three branch pattern of *Delcourt et al.* [1996], is that for a given value of the pitch angle, the magnetic moment is either conserved or damped for $\alpha > \alpha_C$. However, the magnetic moment ratio can only reaches one of these two values, whereas the whole range of values between the limit can be reached in the three-branch pattern. In a modified HS topology, particle dynamics is chaotic, and the magnetic moment diffusion is strongly controlled by the particle's gyrophase. In the modified TD case the development of chaos is constrained, and the abscence of gradient in the total magnetic field magnitude is suspected to play a major role. Evolution of the particle magnetic moment is stochastic as after one interaction with the modified TD, the magnetic moment can be either damped or unchanged, this value strongly depending on the initial gyrophase of the particle. However, there is a kind of determinism in this scattering process as there exist only two possible values for the final magnetic moment, assuming that the initial pitch angle is larger than α_C. This is not the case in the modified HS as the whole range of magnetic moment bounded by the limits in the three branch pattern can be reached. The nature of the chaotic scattering is essentially different from the one in the modified TD. This is the meaning of "weakly chaotic."

Focusing on the particles' initial pitch angle α, it can be seen in Figure 7 that at small α values, particles are not scattered when crossing the modified TD. When increasing α, the damping occurs at the given value α_C (α_C being a function of κ_{RL}), the importance of the damping decreasing when α increases. As κ_{RL} increases, α_C increases and nearly vanishes at κ_{RL} = 1. The resulting orbits (not presented here) show that κ_{RL} = 1 is the limit between transient orbits (at $\kappa_{RL} < 1$) like the one presented in Figure 3, experiencing both adiabatic and super-adiabatic sequences, and purely adiabatic sequences (at $\kappa_{RL} > 1$). The population obtained after one interaction with the interface results in a mixing of initially low α value particles that are not scattered and high α value particles that are either damped or not damped during the interaction, depending on their initial gyrophase. It has to be noted that the gaps in each branch just depends on the pitch angle sampling, and could be filled with a better sampling. However a 1° step provides enough accuracy to get the form of the two branches. In the same way, a

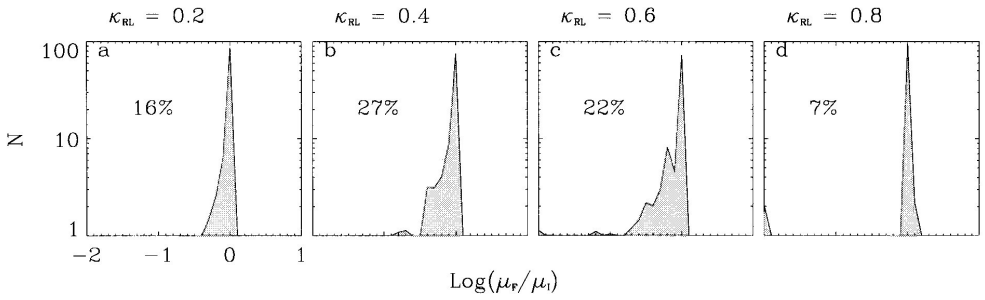

Figure 8. Magnetic moment (normalized to its initial value) after one interaction with a modified TD, depending on the κ_{RL} value.

better sampling in gyrophase does not modify the display as all the points for a given pitch angle are almost superposed in one of the branch.

Analyzing single particle orbits associated to each branch, a clear structure appears. Orbits like the one presented in Figure 3a are the one associated to the skewed branch. It can be seen that the particles stay in the same side of the modified TD before and after interacting with it. On the other hand, orbits like the one presented in Figure 3c escape from the modified TD on the other side than it entered it and are the one associated to the horizontal branch. Crossing particles will have a constant μ when interacting with the modified TD, whereas noncrossing particles will have a damped magnetic moment.

Figure 8 is rather similar to Figure 7 but using a different display. It depicts the amount of particles (in percentage) scattered after one interaction with the modified TD, depending on the logarithmic value of the ratio between final to initial magnetic moment. Figures 8a to 8d correspond to $\kappa_{RL} = 0.2$, 0.4, 0.6, and 0.8, respectively. The percentage in each windows correspond to the total amount of damped particles, whatever the value of the damping. It appears that for small values of κ_{RL}, $\sim 1/5$ to $1/4$ of the total initial population are damped when interacting with the modified TD.

Once could think that as the damped population is the one that does not cross the modified TD, no field-aligned population can be produced at the traversal of the modified TD. However focusing on a given value of κ_{RL}, all the small pitch angle particles will cross the modified TD without being damped, whereas just a fraction will cross at larger pitch angle (still in an undamped way) the other fraction being damped but noncrossing. This process is equivalent to a high pitch angle values filtering, resulting hence in a field aligned population. A qualitative description of this pitch angle distribution as the one associated to noncrossing particles is beyond the scope of this paper. The production of a field-aligned population is consistent with the observations of hot ions streaming, collimated along the magnetic field when crossing the magnetopause during flux transfer events [see, e.g., *Scholer et al.*, 1982].

6. Summary and Discussion

Because of its thickness, finite Larmor radius effects exist at the magnetopause. It is demonstrated that in a pure TD, when the IMF is southward, particle dynamics is regular. The addition of a small component of the magnetic field, normal to the interface (in the y direction), breaks down the regularity of motion resulting in a weakly stochastic dynamics. This is analogous to tightly curved magnetic field geometries, where the phase space can be structured with the κ_{BZ} parameter, defined by *Büchner and Zelenyi* [1989]. A new parameter, $\kappa_{RL} = [L_{RL}/\rho_{Lmax}]^{1/2}$ (where L_{RL} is the finite size of the magnetic field reversal layer) is proposed to fill the corresponding role in magnetic topology with a thin reversal layer. It is shown that particle motion is adiabatic for $\kappa_{RL} > 1$ and experience transient orbits for $\kappa_{RL} < 1$. Their magnetic moment is conserved at low pitch angle values, whereas it is damped at higher pitch angle values, leading to the production of a field-aligned population when crossing the magnetopause.

Other calculations, similar to those presented in Figure 7 and 8, have been carried out for different values of δ. We focused on the results obtained for $\kappa_{BZ} > 3$ to avoid all the curvature effects. In this way, the obtained magnetic moment damping can only be due to the finite size of the reversal layer. For whatever values of δ, smaller or larger than $\delta = 0.01$ as in Figure 7 and 8, the noncrossing particles are pitch angle damped when interacting with the modified TD at $\kappa_{RL} < 1$. The efficiency of this damping may slightly depend on the δ value, but the important point is that δ is not a critical parameter. It does not control the existence of the pitch angle damping and more generally the existence of the two branch pattern at low κ_{RL} value. Furthermore, the calcluations performed with different δ values show that κ_{RL} is unchanged, the obtained results are somewhat similar displaying also a two-branch pattern,

whereas κ_{BZ} depends on δ. By the way, κ_{BZ} cannot be used as an adequate parameter in such a magnetic topology as it depends on δ.

On the other hand, results are different if we consider different values for the polarization of the TD. The anisotropy, obtained after traversal of the magnetopause, disappears if we consider a rotation of 90° (IMF in the $-X$ direction). The magnitude of the magnetic shear is a controlling parameter for the flow direction resulting on the magnetopause traversal. A parametric study would be necessary to investigate the pitch angle distribution resulting from interaction with a modified TD at different magnetic shears. However, computation with a rotation of the magnetic field through the discontinuity of 175°, 170°, and 165° have been performed and a similar two-branch pattern has been obtained. The results obtained at 180° are not a singularity of the model. Pitch angle scattering obtained for different values of the magnetopause polarization could explain the production of bulk flow in particular directions [see, e.g., *Eastman and Frank*, 1982]. Another point to be raised is that the study presented in this paper is valid when $\delta = b_n/b_0$ is small, meaning that the discontinuity is essentially tangential. We suspect the results to be strongly modified if δ becomes close to or larger than one, as it can be the case for rotational discontinuity.

The results of this study can thus be summarized in the following four points.

1. Charged particle dynamics is regular in a tangential discontinuity and a constant of motion can be defined. This type of magnetic boundary does not allow any mass exchange.

2. In the same topology the addition of a small component to the magnetic field, normal to the interface, imply the loss of a constant of the motion and introduce a weakly stochastic behavior.

3. A new parameter $\kappa_{RL} = [L_{RL}/\rho_{Lmax}]^{1/2}$ (where L_{RL} is the size of the reversal layer) is proposed to organize the different possible orbits. When $\kappa_{RL} > 1$, particle motion is regular, and the magnetic moment $\mu = mV_\perp/qb$ is conserved. When $\kappa_{RL} < 1$, particle motion is weakly stochastic, and the magnetic moment is either conserved or damped, depending on the initial pitch angle and gyrophase.

4. The existence of a small component of the magnetic field, normal to the magnetopause, allows the particles to cross the magnetopause. In the southward IMF case, with a small component of the magnetic field normal to the magnetopause, particles are pitchangle scattered when crossing the magnetopause and the resulting population is mainly field aligned.

The existence of a small magnetic field component normal to the interface means that the magnetic field lines from magnetosphere and magnetosheath are connected. This results in breaking down the regularity of particle dynamics but implies the existence of a reconnection process which origin is still not elluded in collisionless plasma. For the Earth magnetopause the development of a Kelvin-Helmholtz instability or the existence of electrostatic turbulence could also lead to the existence of small scale lengths and modify the magnetic field topology. This would allow transition between adiabatic and super-adiabatic motion, giving rise to chaotic motions and traversal across the magnetopause. The efficiency of this process could also provide for mass exchanges at the magnetopause.

Acknowledgments. The author thanks Dominique C. Delcourt and Thomas E. Moore for useful discussions and suggestions. This work was performed while the author held a National Research Council-NASA/GSFC Resident Research Associateship.

Janet G. Luhmann thanks Lev Zelenyi and Richard F. Martin Jr. for their assistance in evaluating this paper.

References

Berchem, J., and C. T. Russell, The thickness of the magnetopause current layer: ISEE 1 and 2 observations, *J. Geophys. Res., 87*, 2108, 1982a.

Berchem, J., and C. T. Russell, Magnetic field rotation through the magnetopause: ISEE 1 and 2 observations, *J. Geophys. Res., 87*, 8139, 1982b.

Büchner, J., and L. M. Zelenyi, Regular and chaotic charged particle motion in magnetotaillike field reversals 1. Basic theory of trapped motion, *J. Geophys. Res., 94*, 11,821, 1989.

Büchner, J., and L. M. Zelenyi, The separatrix tentacle effect of ion acceleration to the plasma sheet boundary, *Geophys. Res. Lett., 17*, 127, 1990.

Büchner, J., and L. M. Zelenyi, Regular and chaotic particle motion in sheared magnetic field reversals, *Adv. Space Res., 11*, 177, 1991.

Büchner, J., M. Kuznetsova, and L. M. Zelenyi, Sheared field tearing mode instability and creation of flux ropes in the Earth magnetotail, *Geophys. Res. Lett., 18*, 385, 1991.

Burkhart, G. R., P. B. Dusenbery, and T. W. Speiser, Particle chaos and pitch angle scattering, *J. Geophys. Res., 100*, 107, 1995.

Chen, J., Nonlinear dynamics of charged particles in the magnetotail, *J. Geophys. Res., 97*, 15,011, 1992.

Chen, J., and P. J. Palmadesso, Chaos and nonlinear dynamics of single particle orbits in a magnetotaillike magnetic field, *J. Geophys. Res., 91*, 1499, 1986.

Curran, D. B., and C. K. Goertz, Particle distributions in a two-dimensional reconnection field geometry, *J. Geophys. Res., 94*, 272, 1989.

Curran, D. B., C. K. Goertz, and T. A. Whelan, Ion distributions in a two-dimensional reconnection field geometry, *Geophys. Res. Lett., 14*, 99, 1987.

Delcourt, D. C., R. F. Martin Jr., and F. Alem, A simple model of magnetic moment scattering in a field reversal, *Geophys. Res. Lett., 21*, 1543, 1994.

Delcourt, D. C., J.-A. Sauvaud, R. F. Martin Jr., and T. E. Moore, On the nonadiabatic precipitation of ions from the near-Earth plasma sheet, *J. Geophys. Res., 101*, 17,409, 1996.

Eastman, T. E., and L. A. Frank, Observations of high-speed plasma flow near the Earth's magnetopause: Evidence for reconnection?, *J. Geophys. Res., 87*, 2187, 1982.

Eckhardt, B., Irregular scattering, *Physica D, 33*, 89, 1988.

Harris, E. G., On a plsama sheath separating regions of oppositely directed magnetic field, *Nuovo Cimento, 23*, 115, 1962.

Holland, D. L., J. Chen, and A. Agranov, Effect of a constant cross-tail magnetic field on the particle dynamics in the magnetotail, *J. Geophys. Res., 101*, 24,997, 1996.

Karimabadi, H., P. L. Pritchett, and F. V. Coroniti, Particle orbits in two-dimensional equilibrium models for the magnetotail, *J. Geophys. Res., 95*, 17,153, 1990.

Landau, L. D., and E. M. Lifshitz, *Mechanics*, Addison-Wesley, Reading, Mass., 1960.

Le, G., and C. T. Russell, The thickness and structure of high beta magnetopause current layer, *Geophys. Res. Lett., 21*, 2451, 1994.

Lichtenberg, A. J., and M. A. Liebermann, Regular and Chaotic Dynamics, *Appl. Math. Sci.*, vol 38, Springer-Verlag, New York, 1983.

Martin, R. F., Jr., T. W. Speiser, and K. Klamczynski, Effect of B_y on neutral line ridges and dynamical source ordering, *J. Geophys. Res., 99*, 23,623, 1994.

Neff, J. E., T. W. Speiser, and D. J. Williams, Magnetosheath quasi-trapped distributions and ion flows associated with reconnection, *J. Geophys. Res., 92*, 1177, 1987.

Papamastorakis, I., G. Paschmann, N. Sckopke, S. J. Bame, and J. Berchem, The magnetopause as a tangential discontinuity for large field rotation angles, *J. Geophys. Res., 89*, 127, 1984.

Scholer, M., D. Hovestadt, F. M. Ipavich, and G. Glockler, Energetic protons, alpha particles, and electrons in magnetic flux transfer events, *J. Geophys. Res., 87*, 2169, 1982.

Sergeev, V. A., E. M. Sazhina, N. A. Tsyganenko, J. A. Lundblad, and F. Soras, Pitch-angle scattering of energetic protons in the magnetotail current sheet as the dominant source of their isotropic precipitation into the nightside ionosphere, *Planet Space Sci., 31*, 1147, 1983.

Sonnerup, B. U. Ö., Adiabatic particle orbits in a magnetic null sheet, *J. Geophys. Res., 76*, 8211, 1971.

Sonnerup, B. U. Ö., and L. J. Cahill, Magnetopause structure and attitude from Explorer 12 observations, *J. Geophys. Res., 72*, 171, 1967.

Speiser T. W., Particle trajectory in model current sheets, 1, Analytical solutions, *J. Geophys. Res., 70*, 4219, 1965.

Speiser T. W., Conductivity without collisions or noise, *Planet. Space Sci., 18*, 613, 1970.

Speiser, T. W., D. J. Williams, and H. A. Garcia, Magnetospherically trapped ions as a source of magnetosheath energetic ions, *J. Geophys. Res., 86*, 723, 1981.

Swift, D. W., and L. C. Lee, Rotational discontinuity and the structure of the magnetopause, *J. Geophys. Res., 88*, 111, 1983.

Williams, D. J., and T. W. Speiser, Sources for energetic ions at the plasmasheet boundary: Time varying or steady state?, *J. Geophys. Res., 89*, 8877, 1984.

Zhu, Z., and G. Parks, Particle orbits model current sheet with a nonzero B_y component, *J. Geophys. Res., 98*, 7603, 1993.

R. Smets, Centre d'étude des Environnements Terrestre et Planétaires, Centre National de la Recherche Scientifique, 78140 Vélizy, France.

(Received May 18, 1999; revised May 15, 2000; accepted June 5, 2000.)

— B —

On the incidence of Kelvin-Helmholtz instability for mass exchange process at the Earth magnetopause

R. Smets,

Laboratory for Extraterrestrial Physics (NASA/GSFC),

D. Delcourt, G. Chanteur,

entre d'étude des Environnements Terrestre et Planétaires,

T. E. Moore,

Laboratory for Extraterrestrial Physics (NASA/GSFC),

Anales Geophysicae

Vol. 20, pages 757 - 769 , 2002

Annales Geophysicae (2002) 20: 757–769

Annales Geophysicae

On the incidence of Kelvin-Helmholtz instability for mass exchange process at the Earth's magnetopause

R. Smets[1,2], D. Delcourt[3], G. Chanteur[2], and T. E. Moore[1]

[1]NASA/Goddard Space Flight Center, Greenbelt, MD, USA
[2]CETP/CNRS, Vélizy, France
[3]CETP/CNRS, Saint Maur des Fossés, France

Received: 26 February 2001 – Revised: 21 January 2002 – Accepted: 6 February 2002

Abstract. Due to the velocity shear imposed by the solar wind flowing around the magnetosphere, the magnetopause flanks are preferred regions for the development of a Kelvin-Helmholtz instability. Since its efficiency for momentum transfer across the magnetopause has already been established, we investigate its efficiency for mass transfer. Using nonresistive magnetohydrodynamic simulations to describe the magnetic field shape in the instability region, we use test-particle calculations to analyse particle dynamics. We show that the magnetopause thickness and the instability wavelength are too large to lead to nonadiabatic motion of thermal electrons from the magnetosphere.

On the other hand, the large mass of H^+, He^+ and O^+ ions leads to such nonadiabatic motion and we thus propose the Kelvin-Helmholtz instability as a mechanism for either magnetospheric ion leakage into the magnetosheath or solar wind ion entry in the magnetosphere. Test-particle calculations are performed in a dimensionless way to discuss the case of each type of ion. The crossing rate is of the order of 10%. This rate is anti-correlated with shear velocity and instability wavelength. It increases with the magnetic shear. The crossing regions at the magnetopause are narrow and localized in the vicinity of the instability wave front. As a Kelvin-Helmholtz instability allows for mass transfer through the magnetopause without any resistivity, we propose it as an alternate process to reconnection for mass transfer through magnetic boundaries.

Key words. Magnetospheric physics (magnetopause, cusp and boundary layers; MHD waves and instabilities) – Space plasma physics (numerical simulation studies)

1 Introduction

The origin of magnetospheric plasma has been extensively studied using both in situ observations, theoretical models and numerical simulations. The ionosphere and the solar wind represent the two possible sources, and their relative importance is still discussed. Several observations have demonstrated that the ionosphere supplies plasma to the Earth's magnetosphere (MSP) (e.g. Shelley et al., 1982; Chappell et al., 1987). Winglee (1998) revisited the concept of geopause proposed by Moore and Delcourt (1995) using 3-D multi-fluid simulations for different Interplanetary Magnetic Field (IMF) directions and showed that under southward IMF, the convection of ionospheric plasma out of the polar cap region is the major contribution to the plasma sheet population. The mass entry process from the solar wind can also supply magnetospheric plasma and many observations have been collected at the magnetopause (MP). The occurence of high-speed plasma flow has been interpreted as a signature of reconnection processes (e.g. Pashmann et al., 1979, 1986; Sonnerup et al., 1981; Gossling et al., 1982, 1991; Phan et al., 1996). Satellite crossings of the MP provided insights on its magnetic topology and on the particle distributions.

Using ISEE 1 and 2 measurements, Berchem and Russell (1982a) showed that the average thickness of the low-latitude dayside MP is about 800 km. Le and Russell (1994) obtained a lower value for high β (ratio of plasma pressure to magnetic pressure) in the magnetosheath (MSH). The average MP speed in the normal direction is a few tens of kilometers per second (e.g. Berchem and Russell, 1982a; Pashmann et al., 1993), and β is about 1, this value being larger (smaller) in the MSH (MSP) (e.g. Phan and Pashmann, 1996).

At the inner edge of the MP, the Low Latitude Boundary Layer (LLBL) was first defined by Eastmann et al. (1976) as the transition region between MSP and MSH (see also Mitchell et al., 1987). Using superposed epoch analysis of the AMPTE/IRM data, Phan and Pashmann (1996) found a thickness of the LLBL of 630 km that is uncorrelated with the β value in the MSH. Mitchell et al. (1987) found a correlation between the thickness of the LLBL and the IMF direction. The magnetic topology of the LLBL is still unclear. Song et al. (1993) found that under northward IMF, the inner (earthward) part of the LLBL is on closed magnetic field

Correspondence to: R. Smets (rsm@cetp.ipsl.fr)

lines, whereas the outer part could be composed of open and closed field lines. Fuselier et al. (1995) suggested that the LLBL could be on open field lines. A boundary layer is also observed at low latitudes in the MP flank (e.g. Eastmann and Hones, 1979). Mitchell et al. (1987) found that under northward IMF, this boundary is on closed field lines, but may lie on open or closed field lines for southward IMF.

The magnetic topology of the MP is of primary importance as it controls the mass loading process from the solar wind in the inner MSP. The first model of open magnetosphere proposed by Dungey (1961) invokes, at least locally, a component of the magnetic field normal to the MP. Examining EXPLORER 12 magnetic field measurements, Sonnerup and Cahill (1967) showed that in most MP crossings, the magnetic field component normal to the MP is very weak, and the magnetopause is thus essentially a tangential discontinuity (i.e. the magnetic field is always tangential to the MP). Studying the MP polarization, Berchem and Russel (1982b) also identified it as a tangential discontinuity, and showed a rotation of the magnetic field from its asymptotic value on both sides of the MP. Papamastorakis et al. (1984) obtained the same result for large field rotation angle and concluded that even for strong southward IMF (when reconnection is suspected to occur), the discontinuity is tangential and not rotational. Papamastorakis et al. (1984) concluded that the IMF direction is not the only parameter governing the reconnection process.

When MSP is closed, magnetic flux pile-up against MP – first predicted by Midgley and Davis (1963) – and the resulting plasma depletion layer are observed (e.g. Pashmann et al., 1993; Song et al., 1993). Absence of magnetic flux pile-up is thus also interpreted as a consequence of the open structure of the MP (e.g. Phan et al., 1994). A statistical study of these accelerated plasma flows by Scurry (1994) showed that they occur preferentially for southward IMF, for large magnetic shear, at low β value and in the subsolar region (see also Phan et al., 1996). Associated to these events, Phan and Pashmann (1996) found an enhancement of the parallel ion and electron temperatures when crossing the MP toward the LLBL.

Since the MP (and especially its flanks) is a preferred region for the development of Kelvin-Helmholtz (KH) instability, we investigate in this paper if nonadiabatic motion of charged particles in a KH instability can be at the origin of mass transfer through the MP. Therefore, we used 2 $D^{\frac{1}{2}}$ ideal MHD simulations to describe the magnetic field in the KH instability region, and test-particle computations to reconstruct the particle orbits. Considering the symmetry of the magnetic topology, the obtained results will be accounted and discussed as a mechanism for the escaping of ionospheric population from MSP to MSH, as the entry of solar wind in the MSP. Test-particle calculations are performed in a dimensionless way, and the results will be applied to both H^+, He^+ and O^+ ions. The basics of KH instability and its condition for occurence will be presented in Sect. 2. The methodology used to perform test-particle calculations will be described in Sect. 3. The obtained results will be generalized in Sect. 4 to a set of particles in order to derive macroscopic properties. Magnetospheric implications of these results will be discussed in Sect. 5.

2 The Kelvin-Helmholtz instability

The Kelvin-Helmholtz instability appears in a fluid flow in the presence of a shear velocity. In the classical hydrodynamic framework, there is no instability threshold for nonviscous fluid and a velocity shear is always unstable (e.g. Chandrasekhar, 1961). In magnetized plasmas, magnetic tension of the magnetic field lines tends to limit their bending and thus has a stabilizing effect. This yields an instability threshold (minimum value of the velocity shear) that depends on the initial conditions of the flow. It can easily be shown that, in the incompressible case, the wave vector of the instability in the direction normal to the interface is purely imaginary. The obtained perturbation is thus a surface wave localized at the interface.

Using the classical ideal MHD equations linearized at first order in the Fourier space (ω, $\boldsymbol{k}$), the stability condition for the interface (equating the total pressure on each side of the interface) is

$$\frac{\rho_1}{k_{N1}}\left[\omega_1^2-\left(\boldsymbol{k}\cdot\boldsymbol{v}_{A1}\right)^2\right]=\frac{\rho_2}{k_{N2}}\left[\omega_2^2-\left(\boldsymbol{k}\cdot\boldsymbol{v}_{A2}\right)^2\right], \tag{1}$$

where the subscripts 1 and 2 denote MSH and MSP, respectively; $\omega_i=\omega_a-\boldsymbol{k}\cdot\boldsymbol{v}_i$ is the Doppler shifted frequency in the media i moving at velocity v_i, and ω_a is the frequency in the absolute frame. ρ is the plasma density, $\boldsymbol{k}_N$ is the wave vector component normal to the interface and $\boldsymbol{v}_{Ai}$ is the Alfvèn speed in media i. Equation (1) is obtained for an infinitely thin boundary. We thus have $k_{T1}=k_{T2}$ (k_T being the tangential component of the wave vector). The full MHD dispersion equation is

$$\begin{aligned}\omega^4-\omega^2\left(k_T^2+k_N^2\right)\left(v_S^2+v_A^2\right)\\ +v_S^2v_A^2\cos^2\theta k_T^2\left(k_T^2+k_N^2\right)=0,\end{aligned} \tag{2}$$

where v_S is the sound speed and θ is the angle between the tangential component of the wave vector and the magnetic field (e.g. Southwood, 1968). Assuming an incompressible media, $v_S\to\infty$ and Eq. (2) reduces to $k_T^2+k_N^2=0$, i.e. $k_N=\pm i|k_T|$. We thus have $k_{N1}=-k_{N2}$ and Eq. (1) reduces to (e.g. Fejer, 1964),

$$\begin{aligned}\rho_1\left[\left(\omega-\boldsymbol{k}_T\cdot\boldsymbol{v}_1\right)^2-\left(\boldsymbol{k}\cdot\boldsymbol{v}_{A1}\right)^2\right]\\ +\rho_2\left[\left(\omega-\boldsymbol{k}_T\cdot\boldsymbol{v}_2\right)^2-\left(\boldsymbol{k}\cdot\boldsymbol{v}_{A2}\right)^2\right]=0.\end{aligned} \tag{3}$$

The flow will thus turn unstable when solutions of the second degree equation in ω are imaginary. Thus, the instability criterion is

$$\begin{aligned}\left(\boldsymbol{k}_T\cdot\Delta\boldsymbol{v}\right)^2>\left(\frac{1}{\rho_1}+\frac{1}{\rho_2}\right)\\ \left[\rho_1\left(\boldsymbol{k}_T\cdot\boldsymbol{v}_{A1}\right)^2+\rho_2\left(\boldsymbol{k}_T\cdot\boldsymbol{v}_{A2}\right)^2\right],\end{aligned} \tag{4}$$

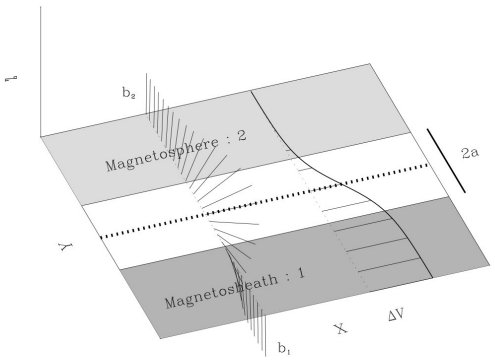

Fig. 1. The available TEC observations at 350 km altitude for a 15 min period.

where $\Delta \boldsymbol{v} = \boldsymbol{v}_1 - \boldsymbol{v}_2$ is the shear velocity. Solutions of Eq. (4) have been discussed for different magnetospheric cases by Talwar (1964). Let us just emphasize two particular cases: (i) when the magnetic field is normal to the velocity shear, the flow is unstable regardless the value of the shear, (ii) when the magnetic field is parallel to the velocity shear and densities are equal on each side of the interface, the instability criterion is $\Delta v > 2v_A$.

The above results are obtained assuming an incompressible flow and an infinitely thin boundary. The incompressibility hypothesis implies that $v_S \gg v_A$, i.e. $\beta \gg 1$. However, one has $\beta \sim 1$ at the magnetopause (e.g. Pashmann et al., 1978). Taking into account the plasma compressibility, Fejer (1964) concluded that it reduces the stabilizing effect of the magnetic field. Using perturbative calculations, Sen (1964) put forward a stabilizing effect of the compressibility at large values of the velocity shear. Pu and Kivelson (1983) solved this paradox by computing Eq. (1) with Eq. (2). For a given value of θ, they showed the existence of two solutions, namely quasi-slow and quasi-fast MHD modes (by analogy with the two MHD magnetosonic modes). At low values of the velocity shear an unstable mode thus appears, whereas the other mode is stabilized for high values of the shear (Eq. (1) impose a positive value of k_N^2 and the unstable surface wave evolves into a stable volume wave).

To take into account the thickness of the interface, the explicit form of the gradient in the normal direction has to be kept and the problem thus reduces to solving a second order differential equation (e.g. Walker, 1981). Miura and Pritchett (1982) studied the growth rate of the unstable mode depending on the wave vector k. In the incompressible case, Chandrasekhar (1961) showed that $\gamma \simeq k\Delta v$. Compressibility yields a bell-shaped curve, i.e. γ increases with k until a maximum value and then decreases to zero. Denoting a as the half thickness of the interface, γ is maximum for $2ka \simeq 1$. An enhancement of the plasma compressibility leads to a decrease of both the growth rate γ and the associated wave vector k.

Particle-like simulations have also been performed. Terasawa et al. (1992) used 2D hybrid simulations to issue the anomalous ion mixing in a KH instability. They showed that at the begining of the development of the KH instability, the mixing index (defined as the total area of the mixed cells normalized to the layer thickness) evolves as the square of time: t^2 phase. Then, the diffusion term due to the scattering of particles by the electric field (its non-electrostatic component) evolves as the square root of time. Thomas and Winske (1993) also used 2D hybrid simulations to put forward the inverse cascade (to longer wavelength) found in MHD and showed the existence of a small-scale structure (on the order of the ion larmor radius) that could be connected to flux transfer events or flux ropes. Two-dimensional Hybrid simulations used by Fujimoto and Terasawa (1994) showed that a large-scale mixing area develops at the corrugated interface. Three-dimensional hybrid simulations performed by Thomas (1995) showed results somewhat similar to 2D simulations and the strongly stabilizing role of the magnetic field is emphasized. It should be stressed here that in most particle-in-cell simulations, emphasis is placed on particle mixing so that crossing rates cannot be thoroughly assessed. This is why we focused in this paper on the crossing particles, and try to find a good criterion to identify them.

We used a 2 D$\frac{1}{2}$ MHD code (Belmont and Chanteur, 1989) to compute the magnetic field in the KH instability region. This code resolves the classical MHD equations with a polytropic law for the closure equation. Due to numerical resistivity, the magnetic Reynolds number R_M cannot be larger than 8000. The simulations used in this study were performed with $R_M = 2000$. Under southward IMF, the MP has the structure of a current sheet (e.g. Cahill and Amazeen, 1963, Berchem and Russell, 1982b). The initial geometry of the MP used for MHD simulations is sketched in Fig. 1. Subscripts 1 and 2 stand for MSH and MSP, respectively, and a is the MP half thickness. The X axis is along the Sun-Earth direction toward the tail (this direction being periodic); the Z axis is in the north-south direction toward the north, which is also the invariant direction, and the Y axis is in the dawn-dusk direction toward dawn. Figure 1 thus depicts the dusk side of the MP. We studied a rotation of 180° of the magnetic field which corresponds to a southward IMF. Even if systematic calculations have been performed in this case, different polarization of the MP will be discussed in Sect. 5. Defining $\chi = 0.5 \times [1 + \tanh((y - y_0)/a)]$, where y_0 is the position where the Z component of the magnetic field vanishes, we have $\alpha = \alpha_1 + \chi(\alpha_2 - \alpha_1)$ as the local direction of the magnetic field relative to the X axis. We define locally the initial density, velocity and magnetic field as

$$\rho = \rho_1 + \chi\,(\rho_2 - \rho_1)\,, \tag{5}$$

$$v = v_1 + \chi\,(v_2 - v_1)\,, \tag{6}$$

$$b_T = b_1 + \chi\,(b_2 - b_1)\,. \tag{7}$$

The three components of the magnetic field are given by $b_x = b_T \cos\alpha$, $b_y = 0$, and $b_z = b_T \sin\alpha$. We used a 512×512 grid in the X - Y plan. The simulation box size

is 2π in the X direction and π in the Y direction. Results are presented in normalized coordinates, namely lengths are normalized to ten times the MP thickness, velocities are normalized to the MSH Alfvèn speed and the magnetic field is normalized to the asymptotic magnetic field magnitude in the MSH.

With such an initialization of the MP structure, we do not take into account the inner part of the LLBL. Phan and Pashmann (1996) showed that for high magnetic shear, most of the magnetic field rotation occurs at the outer edge of the LLBL. The inner edge of the LLBL (bordering the MSP) is a region where both electron and ion temperatures can increase sharply, but the magnetic field weakly changes. In the following, we will focus on the magnetic field structure. This allows us to simplify the problem by decreasing the number of initial parameters.

Figure 2 presents the evolution of the magnetic pressure through time in the X - Y plane. Dotted lines in each panel represent the boundary between positive and negative Z components of the magnetic field. We will use this boundary as the definition of the MP position. The initial conditions in Fig. 2 are $\Delta v = 2v_{A1}$, $\beta_1 = 2$, $b_1 = b_2$, $\alpha_1 = 90°$, $\alpha_2 = 270°$, $\rho_1 = 1$, and $\rho_2 = 0.1$ The four panels present, from top to bottom, the magnetic pressure at $t = 10$, $t = 12$, $t = 14$ and $t = 19$, respectively. At the beginning of the simulations ($t = 10$), the interface is fairly stable, but the magnetic pressure strongly decreases in its vicinity (while it was initially uniform). At $t = 12$, the instability is fully developed and the wave front is quite steep. Even if the plasma is in a nonlinear state, the magnetic field is fairly structured. At $t = 14$, the wave front starts breaking and eddies merge together. At the end of the simulation ($t = 19$), one can see the result of an inverse cascade for which small eddies gather and give their energy to a larger one. The resulting dominant wavelength is larger than the one observed when the instability was rising at $t = 12$. The vortex pairing in the nonlinear evolution of the KH instability has already been pointed out in MHD simulation (see, e.g. Belmont and Chanteur, 1989), and studied recently by Miura (1999). Of course, this inverse cascade is limited by the size of the simulation box. Since boundary conditions are periodic, the KH instability wavelength cannot be longer than the X size of the simulation box. This is the limitation of all localized studies and cannot be resolved unless the instability is studied with a large-scale or global simulation. But this is not a limitation for this study, since the shear velocity barely modify the results. This point will be raised in Sect. 5.

These MHD results show that the development of the KH instability leads to a bending of the magnetic field lines in the vicinity of the interface. To explore the nonadiabatic regime of charged particles in the KH instability, one may compute the κ parameter defined by Büchner and Zelenyi (1989). However, detailed analysis of the particle orbits (see Sect. 3) reveals that nonadiabatic motion essentially arises from the small value of the MP thickness, rather than from the curvature of the magnetic field lines induced by the KH instability. This is emphasized by the vanishing of the magnetic field magnitude close to the MP, with the particle Larmor radius being inversely proportional to it.

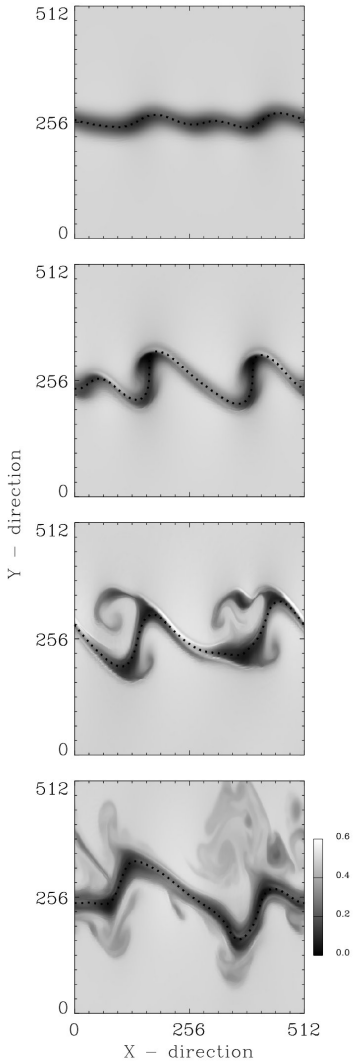

Fig. 2. Color-coded evolution of the magnetic pressure in the $X-Y$ plane from top to bottom: at $t = 10$, $t = 12$, $t = 14$, and $t = 19$.

Since the KH instability is a good mechanism to ensure momentum transfer from MSH to MSP (e.g. Miura, 1987), its efficiency for mass entry from the solar wind or escaping from MSP is investigated. Systematic calculations for electrons demonstrated that these particles behave most of the time adiabatically and that the KH instability is unable to induce nonadiabatic MP crossing of these particles. The

main reason is that, regardless of the KH instability state of development, the MP is too thick to break the adiabaticity of the electron motion and induce anomalous diffusion. Even if the magnetic pressure drastically decreases at the MP, the associated Larmor radii of electrons located in this region are small compared to the thickness of the magnetic field reversal layer. Furthermore, the evolution time scale for the instability is large compared to their gyroperiod. Thus, electrons verify the MHD hypothesis of low frequency and long wavelength. Due to the larger mass of H^+, He^+ and O^+ ions, they experience nonadiabatic motion in the vicinity of the KH instability. Thus, one may wonder whether the KH instability allows for a substantial crossing of these ions through the MP. Hereinafter, calculations are performed in a dimensionless way, allowing for a discussion of these different types of ions in Sect. 5.

3 Single-particle dynamics

Tracing particle orbits in MHD fields calls for a few cautions. Since the magnetic field is defined on each grid point, interpolation is needed to compute the field in between. In the following, we chose a bilinear interpolation in order to ensure $\nabla \cdot \boldsymbol{b} = 0$. The magnetic field is thus continuously defined, but not its gradient. Some numerical gradient drift can thus appear when the particles reach the edges of a cell. However, calculations reveal that this happens so seldom that it does not significantly affect the results. Quadratic interpolation may avoid such numerical artifacts, but the magnetic field divergence would then be nonzero.

Particles dynamics is also constrained by the fluid flow yielding to the electric field $\boldsymbol{e} = -\boldsymbol{v} \times \boldsymbol{b}$. Since the instability is nonstationary, as the position of the MP, a temporal interpolation is needed to describe the time evolution of the electromagnetic fields. This type of calculation has been performed and showed that the temporaly interpolated electric field gave rise to large numerical instabilities as the flow velocity and the magnetic field sharply reverse at the MP. Even small inaccuracies in the electric field values yield to large incorrect energy gains for particles. Focusing on the time scale needed for particles to cross the MP, it is small compared to the time scale of the instability evolution, since the KH instability phase velocity is small compared to the particle velocity. This point will be discussed in further detail in Sect. 5, but at this point we consider that the calculations can be performed by neglecting the time evolution of the instability without significantly impacting the results.

Systematic orbit calculations in the magnetic field topology obtained in the third panel from top of Fig. 2 ($t = 14$) were performed in a dimensionless way. The particle motion equation becomes $d_t \boldsymbol{v} = \boldsymbol{v} \times \boldsymbol{b}$ when the magnetic field is normalized to the asymptotic magnetic field in the MSH, where the time is the inverse of the gyroperiod and the length is ten times the MP thickness. This normalization is different from the one used for the MHD simulation and the ratio between the two, with normalized time and velocity, will be discussed in Sect. 5 on the basis of realistic values of magnetic field magnitude and density in the MSH.

Particle motion was computed over 50 gyroperiods (calculated using the asymptotic value of the magnetic field magnitude in the MSH). Particles were initially in the MSH and we focused on the one crossing the MP in order to end up in the MSP. Due to the symetry of the magnetic field topology, it was verified that the same type of dynamics was obtained for particles initially in the MSH and in the same proportion. This is also a consequence of conducting the calculations in the wave frame. The choice of 50 gyroperiods is large enough to ensure mass transfer through the MP and small enough for the steady state assumption to be valid. Increasing the maximum time for the simulation to 100 gyroperiods increases the rate of crossing particles, but not in a significant way. Transient crossings of the MP that last a few gyroperiods can be observed when following particle orbits for a long enough time. We then have to define when a particle can be considered as having crossed the MP and when it is just meandering in its vicinity. The criterion for a particle to be considered as a crossing one is to initially perform 3 cyclotron turns on one side of the MP, and 3 cyclotron turns as well once it has crossed the MP. This allows one to discard transient crossings of the MP associated with meandering motion in its vicinity. In the same way, increasing this minimum value of cyclotron turn, initially in the MSP and finally in the MSH, decreases the Crossing Rate (CR). These kinds of numerical constraints always play a role in computations and prevent any sort of sharp quantitative analysis. But the sensibility to these parameters is gentle enough to allow for a qualitative interpretation of the results, as presented below.

To investigate the dependence of the CR on the state of development of the KH instability, systematic computations have been performed using the MHD electromagnetic field at different times. These calculations were performed without any temporal interpolation, assuming that the MHD electromagnetic fields were stationary. These calculations have been performed with a given initial energy, namely 0.05, a given initial pitch-angle, namely 60° and a sampling of the whole $X - Y$ plan using a 80×80 grid. At each grid point (thus different from the grid used for the MHD simulations), the gyrophase domain is sampled with 6 different initial gyrophases uniformly distributed. Further test calculations reveal that a larger number of initial gyrophases does not change the results.

The computations were performed every half time step of the MHD simulations and the results are displayed in Fig. 3. The CR value is defined as the ratio between the number of crossing particles to the number of particles located at less than two Larmor radii from the MP position. As a matter of fact, particles that are initially too far from the MP will never reach it, since the magnetic field is uniform and unbended and thus, the particles have no chance of crossing the MP. To be significant, the crossing rate needs to be normalized to the number of particles that are potentially able (because they are close enough) to cross the MP. Until $t = 24$,

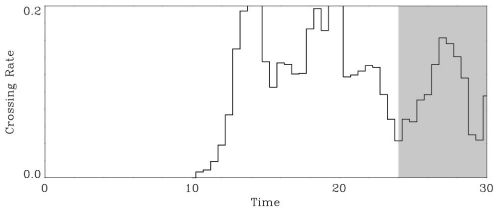

Fig. 3. Number of escaping particles depending on normalized time.

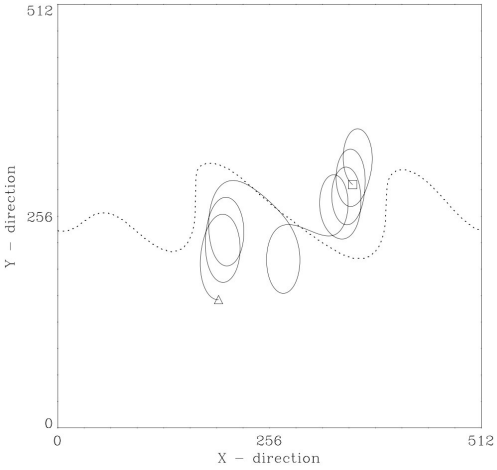

Fig. 4. Particle orbit crossing the interface in a nonadiabatic manner. The test particle starts in the MSP (square) and ends up in the MSH (triangle).

the average value of the CR is 12% and its standard deviation is 5%. We do not take into account the results obtained for $t > 24$ (shaded region in Fig. 3), because mass loss occurs at the Y boundaries and the MHD electromagnetic field becomes inaccurate. An important aspect is that the CR remains fairly constant, whereas the instability wavelength increases with time. Calculations with higher shear velocity (implying higher wave length) confirm this anti-correlation between the CR and the instability wave length. This point will be discussed in Sect. 5. Also, one has to notice that the use of a $2D^{\frac{1}{2}}$ code is justified, since particles remain close enough to the equatorial plane (at less than 3 R_E using standard values of the MP thickness for the normalization). A larger extension of the motion in the Z direction would call for a better description of the magnetic field lines bending at high latitude.

To illustrate the type of computed orbits, Fig. 4 depicts the one obtained for a positively charged particle launched with an energy of 0.05 and a pitch-angle of 60° from the MSP (indicated by a square) and ending up in the MSH (indicated by

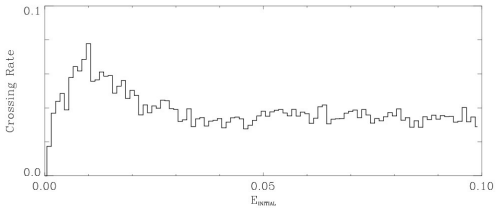

Fig. 5. Number of escaping particles depending on initial energy.

a triangle). The obtained orbit is representative of a general behavior. The particle has initially an adiabatic motion in the MSP. The steep gradient of the magnetic field magnitude at the MP brings forth strong deformation of the cyclotron turns. Then, the particle comes close enough to the MP and crosses it. Due to the magnetic field reversal at the MP, the gyromotion on the other side of the MP occurs in the opposite direction. Furthermore, since the magnetic field gradient is still steep, the gyromotion is highly distorded. But the three full cyclotron turns can be clearly seen in the MSH, thus satisfying the test to stop the computation. This orbit is representative of the one for which the crossing of the MP is brief, since the process occurs in less than 10 gyroperiods. Other orbits will be presented that exhibit transient motion at the MP before definitively crossing it.

Under the above assumptions, we can now examine the dependence of the CR with initial energy and pitch-angle. Since the convection electric field is not considered, the particle energy remains constant. The use of a 4th order Runge-Kutta scheme (for the particle motion integration) provides enough accuracy for the artificial energy variation due to the fact that the numerical technics are smaller than 0.01%. Figure 5 presents the variation of the CR with initial energy. The CR increases with energy to reach its maximum value at $E = 0.01$. Then, it decreases until $E = 0.02$, to reach CR = 0.04. After this threshold, the CR is somewhat constant regardless of the initial energy of the particles. The importance of the normalization technics needs to be discussed. As mentioned above, the CR is calculated using a normalization to the number of particles initially located at less than 2 Larmor radii from the MP. Since the Larmor radii depend on the particle energy, the size of this nonadiabatic sheet will decrease with energy. The population or depletion of this nonadiabatic sheet would need to resolve the plasma motion upstream of the MP.

As mentioned above, the calculations presented in this paper have been performed by neglecting the fluid velocity compared to the particle velocity. Since the associated $\boldsymbol{v} \times \boldsymbol{b}$ electric field is also neglected, the particle energy remains constant. Hence, all crossing particles will carry their momentum themselves. The CR equal to 0.04, obtained in Fig. 5, is thus also an estimation of the momentum transfer. It is interesting to notice that it is somewhat the same as the one obtained by Miura (1987), even if the physical

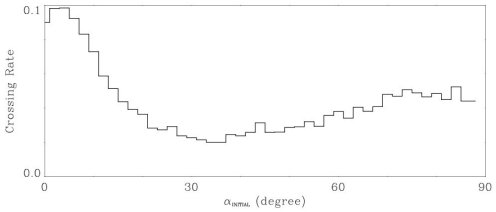

Fig. 6. Number of escaping particles depending on initial pitch-angle.

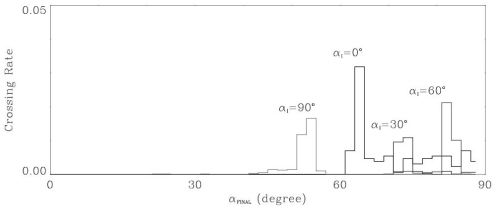

Fig. 7. Number of particles crossing the MP depending on final pitch-angle at the observation point. The four curves correspond to the initial pitch-angles that are labeled.

process is somewhat different. In the work of Miura (1987), the anomalous (eddy plus magnetic) viscosity is responsible for this momentum transfer by enhancing the initially null particle velocity at the discontinuity. In the present study, the crossing of the particles is responsible for the transfer. It must also be noted that this rate is calculated with a very different method of normalization, since Miura (1987) calculated the peak of the spatial average over one wave period of the tangential velocity. This also raises the difficulty of having a crossing rate integrated over the whole cross section of the magnetosphere, unless one uses a global simulation.

Figure 6 presents the evolution of the CR with the initial pitch-angle value α. These calculations are conducted using an initial energy of 0.05. For initially field-aligned particles, the CR decreases as the initial pitch-angle increases, until it reach 30°. The CR is thus at its minimum value, namely 0.02 and then from 30° to 90° of initial pitch-angle value, the CR increases until about 0.04. There exists a smooth dependence of the CR with the initial value of the pitch-angle. But this value does not drastically evolve, and furthermore, the profile obtained in Fig. 6 becomes flatter and less pronounced when using a larger value for the minimum number of cyclotron turns. For the calculations presented below, $\alpha = 60°$ will be used as the initial value. On the other hand, these particles will be pitch-angle scattered when crossing the MP. The consequences of this individual behaviour for a large collection of particles is discussed in the next section.

4 Macroscopic implications

Figure 5 showed that the CR is somewhat constant depending on the initial energy of the particles. But since this rate is normalized to the number of particles located at less than 2 gyroradii from the MP, the number of concerned particles decreases with their initial energy. Even if some process can account for bringing particles close to the MP, the distribution function resulting from the crossing particles is expected to have a weaker density at low energy compared to that at higher energy; hence, there is a build-up of a high energy tail distribution, which is beyond the scope of this paper and would need to take into account the energy gain of the particles via the electric field.

On the other hand, pitch-angle scattering upon crossing of the MP leads to a clear structuring of the phase space. This can be appreciated in Fig. 7, which presents the CR depending on the pitch-angle at the observation point after crossing the MP. These computations was performed by sampling the whole initial pitch-angle domain with a step of 2°. In order not to cloud the results, only 4 curves, corresponding to 0°, 30°, 60° and 90° initial pitch-angle (indicated by the text and different levels of grey), are displayed. As the magnetic field magnitude is constant across the MP, the projection of the particle pitch-angle on an asymptotic magnetic field is not a problem. Furthermore, the test described in Sect. 3 ensures that particles are in an adiabatic sequence when the orbit tracking is interrupted so that the pitch-angle can be accurately defined.

Focusing on one of these curves, it is clear that the obtained distribution is highly collimated along a specific direction, which depends on the initial pitch-angle. For zero initial pitch angle, the distribution obtained after interaction with the MP will be collimated at about 60° from the magnetic field direction. As the initial pitch-angle increases, the angle formed by the obtained beam with the direction of the magnetic field will also increase, until it reaches 90° for the initial distribution at approximately 75°. Then the obtained beam is located at 50° and continues to drift until 60° as the initial pitch-angle of the distribution reaches 90°. As displayed in Fig. 6, the CR depends on the initial pitch-angle. This is the reason why 4 peaks are obtained in Fig. 7.

There exists a clear bijective relation between the initial and final particle pitch-angles after crossing the MP. To illustrate the pitch-angle distribution obtained from an initially isotropic population, Fig. 8 shows the average of the curves presented in Fig. 7 (using the wholes curves obtained with a 2° step). Since the distributions obtained in Fig. 7 are sharply collimated, a good sampling is needed to smooth the obtained peaks. Figure 8 clearly depicts the emergence of a population mainly in the direction perpendicular to the magnetic field. A better sampling would certainly smooth the contours, but will not change the overall direction of this distribution. Particle interaction with a KH instability is thus an efficient mechanism to pitch-angle scatter an initial population in a specific direction, producing for a 180° magnetic shear a population in the direction perpendicular to the

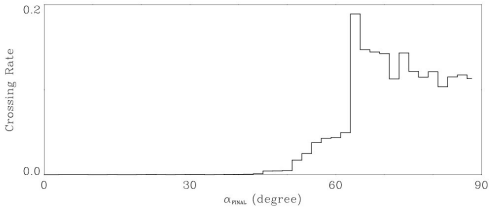

Fig. 8. Number of particles crossing the MP depending on final pitch-angle and assuming an initially isotropic distribution.

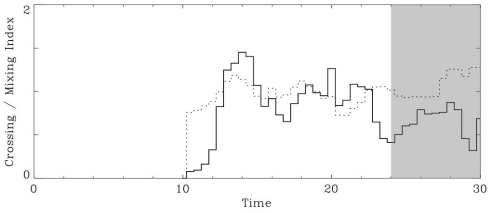

Fig. 10. (Solid line) crossing index and (dashed line) mixing index depending on normalized time.

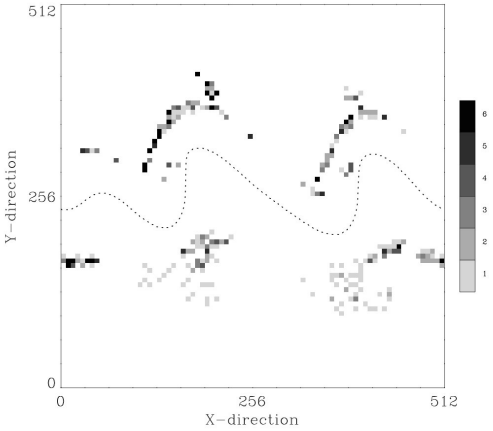

Fig. 9. Color-coded number of particles crossing the MP. Initial and final position in the X - Y plane is depicted.

magnetic field.

This structuring in velocity space goes together with structuring in position space. This can be appreciated in Fig. 9 which presents the initial and final positions of the crossing particles. As mentioned above, for each grid point the orbit of 6 particles is computed by sampling the whole initial gyrophase space.

Figure 9 shows the number of particles crossing the MP. The color-code used depicts the number of particles (from 1 to 6) that cross the MP while their location, both initial and final, is represented by each pixel position. Remembering that particles initially start in the MSP side of the MP, the points displayed at large Y values are the initial positions and the parts displayed at low Y values represent their coresponding final positions. In this figure, one can clearly see islands of escaping particles localized near the edge of each wave front, while they end up narrowly localized near the steep part of the wave profile on the other side of the MP.

The feature displayed in Fig. 9 Triggers the question of the time evolution of the escaping regions. Terasawa et al. (1992) put forward the existence of a t^2 phase, describing the time evolution (at the early stage of the instability) of the mixing layer. Their mixing index (representing the size of the mixing region with a suitable normalization) showed a quadratic evolution with time. In order to compare our results with this one, we computed in Fig. 10 the time evolution of the crossing index (solid line) and the mixing index (dashed line), using the same normalization. For the clarity of the figure, the mixing index is divided by 10. The mixing index is the size of the mixing layer. In a like manner to Terasawa et al. (1992), we consider that a cell is mixed if the fraction of ions that cross it is at least equal to 0.25. The crossing index is the same one with the constraint on each ion to stay at least 3 gyroperiods in the MSP after crossing. It is clear that neither of these curves depict a t^2 phase. Thomas and Winske (1993) found a linear phase that was also different from the t^2 phase, and argued that the different initial topologies used are based on the origin of this discrepency. This argument certainly holds also in the case of this paper, as we considered gradients in density, magnetic field magnitude and magnetic field direction.

The evolution of the curves displayed in Fig. 10 are also quite different from the regular and smooth evolution obtained in the two papers cited above. In test-particle simulations, all particles have a different time-of-flight, which is different from the case of self-consistent, particle-like simulations. To build a map of mixing regions would thus be meaningless in test-particle calculations and the dashed line in Fig. 10 can hardly be compared to the results of Terasawa et al. (1992). On the other hand, the crossing index depicted by the solid line provides some new insights on the mass transfer induced by KH instability. The difference in the particles' time-of-flight is not a problem, since all the crossing particles reach a stationary state in the sense that they stay on the MSP side of the MP. Such a conclusion could not be reached from a snapshot of the mixing region at a given time. Indeed, self-consistent particle-in-cell simulations generally display instantaneous fields contrained by the existence of a $t = 0$ time. The curves displayed in Fig. 10 thus lead to a conclusion: there is about one order of magnitude between the crossing rate and the mixing rate, meaning that most of the particles trapped at the boundary never cross the MP in a definitive way.

The localization of the entry regions depicted in Fig. 9 is of primary importance for the observation of such a population.

This means that in addition to the signature associated with the magnetic field structure, there also exists a signature in the particle distribution. The crossing particles, regardless of the direction of the crossing, are located in the close vicinity of the wave front associated with the KH surface wave. Even if the large-scale motion of plasma is suspected to smooth and merge these bubbles, the stationarity of the process maintains their structure. For a spacecraft traversing the MP under KH instability, the spatial localization of escaping points in the MSH suggests the occurence of particle bursts near the interface. For a spacecraft orbit tangent to the MP, observation of such bursts should provide the location of the steepened part of the profile. On the other hand, crossing of the MP in the transverse direction, far from the wave front, will not allow for observation of such bursts.

To conclude this section, there exists a clear structure of the plasma in the vicinity of a KH wave. The efficiency of the process does not depend on the initial energy of the particles and the number of particles concerned increase with their energy. The larger the particle energy is, the larger the number of particles crossing. Even if the structure of the distribution function cannot be issued, this process leads to the build-up of a high energy tail distribution. On the other hand, there is a clear structure in the pitch-angle distribution. The particles crossing the MP are mainly in the perpendicular direction after their crossing of the MP. This result is limited to the 180° magnetic shear case. The crossing particles are initially located at the edge of the wave front and after crossing of the MP, end up at the edge of the KH wave on the other side.

5 Discussion

Examination of crossing particle orbits allows us to better understand the escape process. Figure 11 depicts the orbit of an ion initially in the MSP (position indicated by the square) and then entering into the MSH (indicated by the triangle). One can identify two adiabatic sequences at the beginning and at the end of the orbit, a meandering sequence near the interface and transition sequences in between. Meandering sequences are somewhat similar to those predicted by Speiser (1965). Due to the sharp field reversal across the interface on a length scale comparable to the particle Larmor radius, particles execute about half a cyclotron turn on each side of the MP. These turns occur in opposite directions due to the antiparallel geometry of the magnetic field. In a recent paper, Smets (2000) discussed the nonlinear dynamic of charged particles in such magnetic topology, and put forward the similarities and differences between a Harris sheet and a tangential discontinuity.

The orbit of Fig. 11 exhibits a sequence (around $X = 128$) where the particle experiences a nearly full cyclotron turn on each side of the MP. The resulting figure eight-like orbit looks similar to the one discussed by Sonnerup (1971) (see, e.g. Fig. 2 of Sonnerup, 1971). This type of orbit follows from the sharp field reversal at the interface. Near $X = 256$, Fig. 11 also exhibits a sequence where the particle experiences just half a cyclotron turn on each side of the MP. The resulting Speiser-like orbit resembles the one discussed by Speiser (1965) in a Harris sheet. It has to be noted, however, that without any KH instability, these types of orbits are regular. As a matter of fact, it has been shown numerically by Smets (2000) that the action integral $I_z = \int \dot{z} dz$, where z is the direction of fast oscillation, is conserved during such a motion. In a similar manner to dynamics in a Harris sheet, each particle orbit may have crossing (meandering at the MP) or non-crossing sequences, depending on the initial position in phase space.

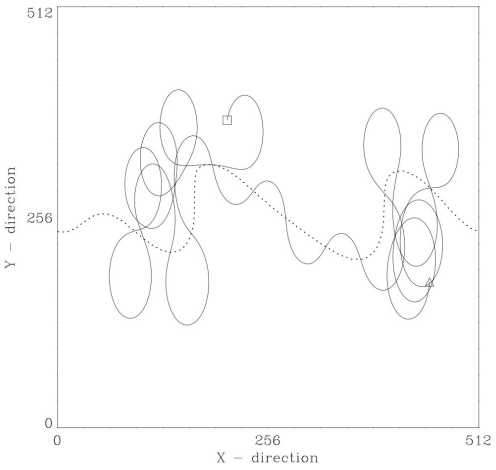

Fig. 11. Particle orbit crossing the interface. The particle starts in the MSP (square) and ends up in the MSH (triangle). Both Speiser-like and figure eight-like sequences can be observed.

For non-crossing (crossing) sequences, a magnetic moment (action integral) will be conserved and the particle motion is regular. On the other hand, it has been shown that in a modified Harris sheet, chaos arises when a small component of the magnetic field normal to the current sheet is added (see, e.g. Chen and Palmadesso, 1986). Such a normal component does not exist in the present case, since the discontinuity is tangential and it remains tangential throughout the development of the KH instability. However, bending of the magnetic field lines produces similar chaotic consequences for the particle dynamics and allows for a transition between different regimes.

The top panel of Fig. 12 presents the three different possible orbits in a tangential discontinuity before the developement of a KH instability. We consider a magnetic field topology defined by (7) with y_0 = const in the expression of χ. Orbit 1 corresponds to the adiabatic case, far from the discontinuity, for which the gyromotion is regular and the magnetic moment is conserved. Orbit 2 is also regular, with the integral action being conserved. Orbit 3 is somewhat similar to orbit 2, except that it is characterized by a nearly full

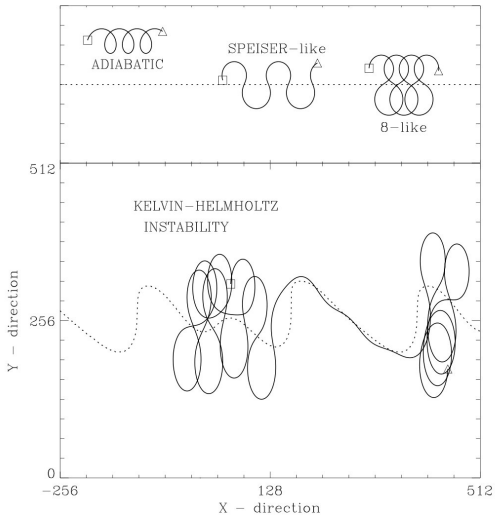

Fig. 12. Different orbit types in a tangential discontinuity: (1) adiabatic, (2) Speiser-like and (3) figure eight-like (upper panel). KH instability essentially allows transition between these d ifferent types of motion (lower panel).

cyclotron turn in each side of the MP. In the absence of KH instability, particles may exhibit all three behaviors, but retain this character throughout the motion. In contrast, the bottom panel of Fig. 12 shows that the development of a KH instability and resulting bending of the magnetic field lines results in transitions between these different motions. The mechanism we envision for ions to cross the MP is that the KH instability enforces transition between different possible regimes in the sharp field reversal region.

As mentioned in Sect. 3, test-particle calculations have been performed in a dimensionless way. The leakage or mass entry process associated with each type of ion needs to be discussed in physical units using realistic values for the MP thickness and the magnetic field magnitude and density in the MSH. With an MP thickness of $0.1\,R_E$, $B_0 = 10\,\mathrm{nT}$ and $n_0 = 10^7\,\mathrm{m}^{-3}$ in the MSH, the Alfvén speed is $v_A = 7 \times 10^4\,\mathrm{m.s}^{-1}$. Distances are thus normalized to $1\,R_E$, velocity to v_A and time to $\sim 100\,\mathrm{s}$. With the same values for test-particles calculations, distances are also normalized to $1\,R_E$, time to $\omega_c^{-1} = 1\,\mathrm{s}$ and velocity to $6 \times 10^6\,\mathrm{m.s}^{-1}$.

Most of the calculations were done with $E = 0.05$. For H^+ ions this corresponds to an energy of 18 keV. The associated velocity is $1800\,\mathrm{km.s}^{-1}$ and the 50 gyroperiods used as the maximum time allowed for the particles to cross the MP correspond to a time-of-flight of 50 s. The shear velocity $\Delta v = 2v_A = 140\,\mathrm{m.s}^{-1}$ is one order of magnitude smaller than the particles' velocity and performing the test-particle calculations in the wave frame is thus relevant. Furthermore, since the time-of-flight is smaller than 50 s, the stationary hypothesis is valid as the MHD electromagnetic field weakly evolves on a time scale of 100 s. The assumptions used for the test-particle calculations are justified for H^+ ions of high energy. Even if Fig. 5 shows that the crossing rate for particles with an initial energy of the order of 0.01 is also of a few percentage points, the results discussed above mainly concern the high energy tail of the H^+ ion distributions.

When the mass of the particles is increasing, the time normalization increases proportionally to the mass ratio, and the velocity and energy normalization decrease proportionally to the inverse of the mass ratio. This means that the time-of-flight increases with particle mass and the velocity decreases. The dimensionless test-particle calculations can also be applied to He^+ ions. Performing these calculation in the wave frame under the stationary hypothesis is still valid and instead of concerning the high energy tail, it concerns a population closer to the thermal one.

The case of O^+ ions is different. Considering their large mass, $E = 0.05$ corresponds to the thermal population (with an average temparature of 2 keV (see, e.g. Gloeckler and Hamilton, 1987). But then their velocity is about the same as the surface wave and the time-of-flight is about the same as the time scale evolution of the MHD fields. A deeper investigation of the O^+ ions' case would thus need to take care of these problems, since the temporal evolution of the instability could be important.

Several studies have reported evidences of KH instability at the Earth's magnetopause since the early observation by Lepping and Burlaga (1979). These authors developed a method to infer the amplitude and the wavelength of the KH instability. Using VOYAGER 1 data, they found an average amplitude of 2100 km and a wavelength of 47 000 km. These observations thus yield a larger value for the KH instability wavelength, as compared to the one obtained in our simulations. This result is fairly general in numerical simulations of the KH instability. The inverse cascade we observed in the simulations could be one of the reasons for such a disagreement. However, this is of minor importance, since the number of escaping particles per wavelength is somewhat independent of the KH instability wavelength.

In order to explore the dependence upon velocity shear, we performed calculations with $\Delta v = 3v_A$. After development of the KH instability, we obtained four wavelengths in the simulation box, that merged into two wavelengths at the end of the simulation. The average value of the CR is 14%, and its standard deviation is 9%. Keeping in mind that with $\Delta v = 2v_A$, one has a CR of 12%, with a standard deviation of 5%, we can conclude that the wavelength of the KH instability is not a predominant parameter. Therefore, it appears that with a velocity shear large enough to ensure the development of a KH instability, the escaping particle number is anti-correlated with the instability wavelength and the shear velocity.

The results presented above were performed with a high magnetic shear of 180° that corresponds to a southward IMF. Since MHD simulations require a lot of computer resources, we cannot perform a systematic analysis of the magnetic

shear influence. Only the 90° and 135° magnetic shear cases were considered. It should be noted here that the X component of the magnetic field is important because it has a stabilizing effect for the development of a KH instability. When the magnetic field is in the same direction as the shear velocity, magnetic tension tends to oppose its bending and thus, has a stabilizing effect. On the other hand, when the magnetic field is normal to the shear velocity, the KH instability can develop like in a neutral fluid.

In the 90° magnetic shear case, KH instability does not develop until the shear velocity reaches $\Delta v = 3\,v_A$. Accordingly, the KH instability cannot drive any substantial MP crossing. From a general point of view, higher values of the velocity shear quickly turn unstable. For a magnetic shear of 135°, the KH instability appears from $\Delta v = 3\,v_A$. The corresponding crossing rate is of a few tenths of percent. This very small value of the crossing rate is due to the nonzero X component of the magnetic field. This component drives the particles along the interface and is responsible for transition toward meandering motion. When the X component of the magnetic field becomes negligible as compared to the Z component, particles that cross the MP have a gyromotion essentially in the X - Y plan and flow along the Z direction. This limits accordingly the number of transient orbits and increases the escape rate.

6 Conclusion

Observations of high-speed plasma flows at the MP are generally interpreted as a signature of reconnection. As the outflowing plasma carries substantial magnetic flux, this implies the existence of a magnetic field component (even small) normal to the interface. But under southward IMF, high-speed plasma flows can be observed for which the MP has the structure of a rotational discontinuity (e.g. Sonnerup, 1967; Pashmann et al., 1979; Sonnerup et al., 1981). However, under normal conditions, MSP is closed and MP has the structure of a tangential discontinuity. Considering such a tangential discontinuity, we have shown that the development of a KH instability at the flanks of the MSP is unable to sufficiently bend magnetic field lines to induce nonadiabatic motion of electrons.

Due to their larger mass, ions are subject to nonresistive diffusion through the MP. The development of a KH instability breaks the regularity of their motion and allows for a net outward flow of these ions. KH instability thus appears as a possible mechanism for the leakage of ions in the MSH or entry of solar wind ions in the MSP. Since the proportion of the concerned population is of a few percentage points, the mass exchange process is not associated with a significant transfer of magnetic flux through the MP.

We have shown that MP crossing does not depend on the velocity shear and leads to a structuring of the escaping population:

1. The escaping rate is barely invariant with the initial particle energy. But the number of particles embeded in the nonadiabatic sheet increases with their energy, and this leads to an outgoing distribution with a high energy tail.

2. The escaping rate depends slightly on the initial pitch-angle. However, after crossing of the MP, the outgoing population is peaked in the perpendicular direction.

3. The crossing process is not uniform, and some preferential regions localized at the edge of the wave front of the KH instability exist.

For a normalized energy of 0.05, we obtain a crossing rate of 12%; this rate is somewhat independent of the initial energy. The exact value of the crossing rate is meaningless due to the influence of the numerical constraints, but we would like to emphasize that about 1 ion in 10, located in the nonadiabatic sheet (defined above), cross the MP. At this stage, we would like to be able to give an evaluation of the total net mass transfer across the whole MP that results from nonadiabatic motion in a KH instability. We cannot offer this evaluation for essentially two reasons:

- Since the MSH plasma flow is essentially tangential to the MP, it cannot be responsible for bringing particles close to it. Longer time processes (like gradient or curvature drift) can supply particles close to the MP, but the implications of such processes would need relevant calculations or simulations that are far beyond the scope of this paper. On the other hand, large-scale simulations (e.g. Winglee, 1998) that could answer such a problem could not deal correctly with the local effects on particles, such as their nonadiabatic motion.

- Depending on the part of the MP studied, the magnetospheric magnetic field changes in direction and magnitude. Since it is a crucial parameter for the development of a KH instability, we can definitively not expect that the KH instability would occur on the whole surface of the MP. Once again, unless there is the use of global treatment of the whole MP, it seems unrealistic to evaluate a global mass transfer integrated over the whole cross section surface of the magnetosphere.

Other simulations performed with 90° and 135° magnetic shear reveal that the escape rate strongly depends upon the magnetic shear. More specifically, there exists a minimum threshold for the magnetic shear (its value depending on velocity shear) above which a KH instability can develop. Nonresistive diffusion at the MP then occurs due to the nonadiabatic motion of the particles.

Acknowledgements. Part of this work was performed while the first author held a National Research Council-NASA/GSFC Research Associateship. The MHD simulations were done on the Cray C-90 at IDRIS Laboratory, the supercomputing center of CNRS/FRANCE.

The Editor in Chief thanks D. Winske and another referee for their help in evaluating this paper.

References

Belmont, G. and Chanteur, G.: Advances in magnetopause Kelvin-Helmholtz instability studies, Phys. Scripta, 40, 124, 1989.

Berchem, J. and Russell, C. T.: The thickness of the magnetopause current layer: ISEE 1 and 2 observations, J. Geophys. Res., 87, 2108, 1982a.

Berchem, J. and Russell, C. T.: Magnetic field rotation through the magnetopause: ISEE 1 and 2 observations, J. Geophys. Res., 87, 8139, 1982b.

Büchner, J. and Zelenyii, L. M.: Regular and chaotic charged particle motion in magnetotaillike field reversals 1. Basic theory of trapped motion, J. Geophys. Res., 94, 11 821, 1989.

Cahill, L. J. and Amazeen, P. G.: The boundary of the geomagnetic field, J. Geophys. Res., 68, 1835, 1963.

Chandrasekhar, S.: Hydrodynamic and hydromagnetic stability, Dover Publication, 1961.

Chappell, C. R., Moore, T. E., and Waite, Jr., J. H., : The ionosphere as a fully adequate source of plasma for the Earth's magnetosphere, J. Geophys. Res., 92, 5896, 1987.

Chen, J. and Palmadesso, P. J.: Chaos and nonlinear dynamics of single particle orbits in a magnetotaillike magnetic field, J. Geophys. Res., 91, 1499, 1986.

Dungey, J. W.: Interplanetary magnetic field and the auroral zone, Phys. Rev. Lett., 6, 47, 1961.

Eastmann, T. E., Hones, Jr., W., Bame, S. J., and Asbridge, J. R.: The magnetospheric boundary layer: site of plasma, momentum, and energy transfer from the magnetosheath to the magnetosphere, Geophys. Res. Lett., 3, 685, 1976.

Eastmann, T. E. and Hones, Jr., W.: Characteristics of the magnetospheric boundary layer and magnetopause layer as observed by IMP 6, J. Geophys. Res., 84, 2019, 1979.

Fejer, J. A.: Hydromagnetic stability at a fluid velocity discontinuity between compressible fluids, Phys. Fluids, 7, 499, 1964.

Fujimoto, M. and Terasawa, T.: Anomalous ion mixing within and MHD scale Kelvin-Helmholtz vortex, J. Geophys. Res., 99, 8601, 1994.

Fuselier, S. A., Anderson, B. J., and Onsager, T. G.: Particles signatures of magnetic topology at the magnetopause: AMPTE/CCE observations, J. Geophys. Res., 100, 11,805, 1995.

Gloeckler, G. and Hamilton, D. C.: AMPTE ion composition results, Phys. Scripta, T18, 73, 1987.

Gosling, J. T., Asbridge, J. R., Bame, S. J., Feldman, W. C., Paschmann, C., Sckopcke, N., and Russell, C. T.: Evidence for quasi-stationary reconnection at the dayside magnetopause, J. Geophys. Res., 87, 2147, 1982.

Gosling, J. T., Thomsen, M. F., Bame, S. J., Elphic, R. C., and Russell, C. T.: Observation of reconnections of interplanetary and lobe magnetic field lines at the high latitude magnetopause, J. Geophys. Res., 96, 14 097, 1991.

Le, G. and Russell, C. T.: The thickness and structure of high beta magnetopause current layer, Geophys. Res. Lett., 21, 2451, 1994.

Lepping, R. P. and Burlaga, L. F.: Geomagnetopause surface fluctuations observed by Voyager 1, J. Geophys. Res., 84, 7099, 1979.

Midgley, J. E. and Davis, L.: Calculation by a moment technique of the perturbation of the geomagnetic field by the solar wind, J. Geophys. Res., 68, 5111, 1963.

Mitchell, D. G., Kutchko, F., Williams, D. J., Eastman, T. E., Franks, L. A., and Russell, C. T.: An extended study of the low-latitude boundary layer on the dawn and dusk flanks of the magnetosphere, J. Geophys. Res., 92, 7394, 1987.

Miura, A. and Pritchett, P. L.: Nonlocal stability analysis of the MHD Kelvin-Helmholtz instability in a compressible plasma, J. Geophys. Res., 87, 7431, 1982.

Miura, A.: Simulation of the Kelvin-Helmholtz instability at the magnetospheric boundary, J. Geophys. Res., 92, 3195, 1987.

Miura, A.: Self-organization in the two-dimensional magnetohydrodynamic transverse Kelvin-Helmholtz instability, J. Geophys. Res., 104, 395, 1999.

Moore, T. E. and Delcourt, D. C.: 'The Geopause', Rev. Geophys., 33, 175, 1995.

Papamastorakis, I., Paschmann, G., Sckopke, N., Bame, S. J., and Berchem, J.: The magnetopause as a tangential discontinuity for large field rotation angles, J. Geophys. Res., 89, 127, 1984.

Paschmann, G., Sonnerup, B. U. Ö., Papamastorakis, J., Bame, S. J., Asbridge, J. R., Gosling, J. T., Hones, Jr., E. W., and Tech, E. R.: ISEE plasma observations near the subsolar magnetopause, Space Sci. Rev., 22, 717, 1978.

Paschmann, G., Sckopke, N., Haerendel, G., Papamastorakis, I., Sckopke, N., Haerendel, G., Bame, S. J., Asbridge, J. R., Gosling, J. T., Russell, C. T., and Elphich, R. C.: Plasma acceleration at the Earth's magnetopause: evidence for magnetic reconnection, Nature, 282, 243, 1979.

Paschmann, G., Papamastorakis, J., Baumjohann, W., Sckopke, N. K., Carlson, C. W., Sonnerup, B. U. Ö., and Lühr, H.: The magnetopause for large magnetic shear: AMPTE/IRM observations, J. Geophys. Res., 91, 11 099, 1986.

Paschmann, G., Baumjohann, W., Sckopke, N. K., Phan, T. D., and Lühr, H.: Structure of the dayside magnetopause for low magnetic shear, J. Geophys. Res., 98, 13 409, 1993.

Phan, T. D., Paschmann, G., Baumjohann, W., Sckopke, N., and Lühr, H.: The magnetosheath region adjacent to the dayside magnetopause: AMPTE/IRM observations, J. Geophys. Res., 99, 121, 1994.

Phan, T. D. and Paschmann, G.: Low-latitude dayside magnetopause and boundary layer for high magnetic shear 1. structure and motion, J. Geophys. Res., 101, 7801, 1996.

Phan, T. D., Paschmann, G., and Sonnerup, B. U. Ö.: Low-latitude dayside magnetopause and boundary layer for high magnetic shear 2. occurence of magnetic reconnection, J. Geophys. Res., 101, 7817, 1996.

Pu, Z. Y. and Kivelson, M. G.: Kelvin-Helmholtz instability at the magnetopause: solution for a compressible plasma, J. Geophys. Res., 88, 841, 1983.

Scurry, L., Russell, C. T., and Gosling, J. T.: A statistical study of accelerated flow events at the day side of the magnetopause, J. Geophys. Res., 99, 14 815, 1994.

Sen, A. K.: Effects of compressibility on a Kelvin-Helmholtz instability in a plasma, Phys. Fluids, 7, 1293, 1964.

Shelley, E. G., Peterson, W. K., Ghielmetti, A. G., and Geiss, J.: The polar ionosphere as a source of energetic magnetospheric plasma, Geophys. Res. Lett., 9, 941, 1982.

Smets, R.: Charged particle dynamics in a tangential discontinuity, J. Geophys. Res., 105, 25 009, 2000.

Song, P., Russell, C. T., Fitzenreiter, R. J., Gosling, J. T., Thomsen, M. F., Mitchell, D. G., Fuselier, S. A., Parks, G. K., Anderson, R. R., and Hubert, D.: Structures and properties of the subsolar magnetopause for northward IMF: multiple-instrument observations, J. Geophys. Res., 98, 11 319, 1993.

Sonnerup, B. U. Ö.: Adiabatic particle orbits in a magnetic null sheet, J. Geophys. Res., 76, 8211, 1971.

Sonnerup, B. U. Ö., and Cahill, L. J.: Magnetopause structure and attitude from Explorer 12 observations, J. Geophys. Res., 72, 171, 1967.

Sonnerup, B. U. Ö., Paschmann, G., Papamastorakis, I., Sckopke, N., Haerendel, G., Bame, S. J., Asbridge, J. R., Gosling, J. T., and Russell, C. T.: Evidence for magnetic reconnection at the Earth's maghnetopause, J. Geophys. Res., 86, 10 049, 1981.

Southwood, D. J.: The hydromagnetic stability of the magnetospheric boundary, Planet. Space Sci., 16, 587, 1968.

Speiser, T. W.: Particle trajectory in model current sheets, 1, Analytical solutions, J. Geophys. Res., 70, 4219, 1965.

Talwar, S. P.: Hydromagnetic stability of the magnetospheric boundary, J. Geophys. Res., 69, 2707, 1964.

Terasawa, T., Fujimoto, M., Karimabadi, H., and Omidi, N.: Anomalous ion mixing within a Kelvin-Helmholtz vortex in a collisionless plasma, Phys. Rev. Lett., 68, 2778, 1992.

Thomas, V. A.: Three-dimensional kinetic simulation of the Kelvin-Helmholtz instability, J. Geophys. R., 100, 19 429, 1995.

Thomas, V. A. and Winske, D.: Kinetic simulation of the Kelvin-Helmholtz instability at the magnetopause, J. Geophys. Res., 98, 11 425, 1993.

Walker, A. D. M.: The Kelvin-Helmholtz instability in the low latitude boundary layer, Planet. Space Sci., 29, 1119, 1981.

Winglee, R. M.: Multifluid simulations of the magnetosphere: the identification of the geopause and its variation with IMF, Geophys. Res. Lett., 25, 4441, 1998.

— C —

Diffusion at the Earth magnetopause : enhancement by Kelvin-Helmholtz instability

R. Smets, G. Belmont, D. Delcourt, L. Rezeau,
Centre d'étude des Environnements Terrestre et Planétaires,

Annales Geophysicae
Vol. 25, pages 271 - 282, 2007

Ann. Geophys., 25, 271–282, 2007
www.ann-geophys.net/25/271/2007/

Annales Geophysicae

Diffusion at the Earth magnetopause: enhancement by Kelvin-Helmholtz instability

R. Smets[1], **G. Belmont**[1], **D. Delcourt**[2], **and L. Rezeau**[1]

[1]CETP/CNRS/UVSQ/UPMC/IPSL, 10–12 Avenue de l'Europe, 78140 Vélizy, France
[2]CETP/CNRS/UVSQ/UPMC/IPSL, 4 Avenue de Neptune, 94107 Saint Maur des Fossés, France

Received: 18 April 2006 – Revised: 18 December 2006 – Accepted: 22 January 2007 – Published: 1 February 2007

Abstract. Using hybrid simulations, we examine how particles can diffuse across the Earth's magnetopause because of finite Larmor radius effects. We focus on tangential discontinuities and consider a reversal of the magnetic field that closely models the magnetopause under southward interplanetary magnetic field. When the Larmor radius is on the order of the field reversal thickness, we show that particles can cross the discontinuity. We also show that with a realistic initial shear flow, a Kelvin-Helmholtz instability develops that increases the efficiency of the crossing process. We investigate the distribution functions of the transmitted ions and demonstrate that they are structured according to a D-shape. It accordingly appears that magnetic reconnection at the magnetopause is not the only process that leads to such specific distribution functions. A simple analytical model that describes the built-up of these functions is proposed.

Keywords. Magnetospheric physics (Magnetopause, cusp, and boundary layers; Magnetosheath; Solar wind-magnetosphere interactions)

1 Introduction

Since the open magnetosphere concept has been proposed by Dungey (1961), possible mechanisms to ensure mass loading of the magnetosphere from the shocked solar wind are highly debated. Magnetic reconnection plays a central role in this paradigm to explain the in situ observed coupling between magnetosphere and solar wind. The exact way magnetic reconnection develops is still controversial, the main reason being that large (MHD) scales have to be coupled with small (electron) scales, which is hardly achieved in numerical studies (a same kind of problem occurs in turbulence, see e.g. Frisch, 1995).

Magnetized plasmas consist of particles gyrating around convecting magnetic field lines. When magnetic reconnection occurs, plasma travels in the newly connected regions that were prohibited prior to reconnection. An alternative way to transfer matter across a magnetic boundary is diffusion. The topology of the magnetic field lines is preserved, but because of diffusion, particles can jump from one magnetic field line to another. Because of the collisionless nature of the plasma, the origin of diffusion cannot be classical viscosity, and many studies (see e.g. Winske et al., 1995; Treumann et al., 1995) have been dedicated to diffusion processes in collisionless plasma. On the whole it is commonly admitted that diffusion is less efficient than magnetic reconnection to ensure mass loading of the inner magnetosphere from the shocked solar wind (see Phan et al., 2005).

The physical process at work at the magnetopause is related to the nature of the magnetic discontinuity: in a tangential discontinuity there is no connection between upstream and downstream plasmas. In contrast, in a rotational discontinuity, a normal component of the magnetic field exists that connects both sides. Although the theoretical distinction is clear, experimental evidences are far more complicated because the measurement of a small component of the field is technically difficult. This difficulty is not due to the instruments, but to the uncertainty in determining the normal, the planarity of the discontinuity, ... Tests have been developed to check the Rankine-Hugoniot relations and demonstrated that the magnetopause sometimes is a rotational discontinuity (Paschmann et al., 1979). In other instances, the magnetopause is assumed to be a tangential discontinuity (Papamastorakis et al., 1984). Recent observations with Cluster (Paschmann et al., 2005) lead to the first statistical studies on the nature of the discontinuity with precise multipoint observations, showing that on the same day both situations can be observed.

Correspondence to: R. Smets
(rsm@cetp.ipsl.fr)

Published by Copernicus GmbH on behalf of the European Geosciences Union.

Using hybrid simulations, we show that finite Larmor radius (FLR) effects are responsible for anomalous diffusion, due to the thickness of the magnetopause (MP), on the order of the ion Larmor radius (see e.g. Eastmann et al., 1996). Furthermore, at the Earth MP, the shear velocity between the solar wind flowing in the anti-solar direction and the quasi stagnant plasma of the inner magnetosphere can trigger the Kelvin-Helmholtz instability (KHI). The development of such KHI can amplify the diffusion process. The kinetic properties of the plasma are investigated, and compared to the classical structures observed during magnetic reconnection.

In the case of a neutral fluid, Chandrasekhar (1961) showed that KHI develops, regardless of the shear velocity magnitude. Talwar (1964) showed that when there is a component of the magnetic field tangential to the flow, the stabilizing effect of the magnetic tension results in a threshold for the instability development. The threshold as well as the growth rate of the instability is modified by the plasma compressibility (see, e.g. Miura and Pritchett, 1982; Pu and Kivelson, 1983).

Using compressible 2-D MHD code, Miura (1984) showed that up to 2% of the energy flux can cross the magnetic boundary. Miura (1987) also showed that the anomalous tangential stress associated with the instability ensures a momentum transport across the discontinuity that can reach a few percents. Still in the MHD interpretation framework, development of KHI can lead to plasma blobs (a direct consequence of mass transport, but not the only one) because of resistivity (Nykiri and Otto, 2001), electron inertial effects (Nakamura et al., 2004), or finite Larmor radius effects Huba (1996). KHI may also trigger turbulence (Matsumoto and Hoshino, 2004), and vice-versa, Shinohara et al. (2001) showed that kinetic instability (namely the low hybrid drift instability and the current sheet kink instability) can cascade in KHI.

Using 2-D hybrid simulations, Terasawa et al. (1992) studied the time evolution of a mixing index, providing insights on the total surface close to the instability where particles, initially from both sides of the discontinuity, are mixed. Thomas and Winske (1993) also used 2-D hybrid simulations to demonstrate the existence of small-scale structures (on the order of the ion Larmor radius) possibly related to such flux transfer events (see e.g. Southwood et al., 1988, for flux transfer observations). Fujimoto et al. (1994) extended this investigation and focused on mass transport, showing that mixing is quicker and larger than that due to finite Larmor radius overlapping at the interface. Thomas (1995) obtained similar results with 3-D hybrid simulations for the same geometry, but showed that a rotation of the magnetic field stabilizes the system, and leads to a less efficient mass transport.

Recently, clear observations of the KHI have been reported by Hasegawa et al. (2004) using the four spacecrafts of the Cluster 2 mission. Furthermore, this paper provided evidences of plasma penetration from the magnetosheath into the inner magnetosphere. Interestingly, this paper quotes: "... we could rule out local reconnection because... we did not find signatures of plasma acceleration due to magnetic stresses and D-shaped ion distribution characteristic of reconnection". Conversely, one may wonder whether D-shaped distribution functions provide unambiguous signatures of magnetic reconnection. We show in this paper that such distribution can actually be observed in the vicinity of a KHI.

In this paper, we will not study in details the development of the KHI, that is, the possible stabilization by Landau damping as demonstrated by Ganguli (1997), the vortex pairing or inverse cascad as put forward by Belmont and Chanteur (1989), or the coupling with smaller scales process (see e.g. Shinohara et al., 2001; Matsumoto and Hoshino, 2004). We use hybrid simulations of the KHI to study the mass transport across the magnetic boundary. Electrons being considered as a massless fluid, we do not resolve electron frequencies. Instabilities like Electron-Ion-Hybrid instability (see Ganguli, 1997; Romero and Ganguli, 1993, 1994) can then not be addressed. In Sect. 2, we describe the hypotheses inherent to hybrid simulations. In Sect. 3, we present the model of the initial tangential discontinuity. In Sect. 4, we discuss the development of the KHI. In Sect. 5, we examine the structure of the ion distribution function, and discuss the possible occurence of reconnection. In Sect. 6, we focus on particle dynamics to understand the origin of D-shaped ion distribution functions. In Sect. 7, we exhibit the microscopic process and the implications for spacecraft observations.

2 Simulation model

The calculations are carried out using a hybrid code (ions treated as particles and a massless electron fluid) with two spatial dimensions and three velocity dimensions. Details of the simulation algorithm are given by Winske and Quest (1986). Distances are normalized to the ion inertial length (c/ω_{Pi}), time is normalized to the inverse of the ion gyrofrequency (ω_{Ci}^{-1}), mass is normalized to the ion mass, and density and magnetic field are normalized to their asymptotic values (the same on each side of the discontinuity), n_0 and B_0 , respectively. The size of the simulation box is X_m in the x-direction and Y_m in the y-direction. We use n_x=256 grid points in the x-direction, and n_y=128 grid points in the y-direction, X_m=80 and Y_m=40 (size of the box in x- and y-direction), 100 macroparticles per cell and a time step Δt=0.005.

In the calculation of the electric and magnetic field, we neglected the displacement curent in the Maxwell-Faraday equation. Such an assumption prevents the development of high frequency modes. Ohm's law is then needed to define the electric field. Taking into acccount the Hall term, the

electron pressure term and a resistivity, we have

$$\mathbf{E} = -\mathbf{V}_i \times \mathbf{B} + \frac{1}{qn}(\mathbf{J} \times \mathbf{B} - \nabla P_e) + \eta \mathbf{J} \quad (1)$$

where $\mathbf{V}_i$ is the ion fluid velocity, $\mathbf{J}$ the current density, P_e the scalar electron pressure, η the resistivity, and n_e=n_i is the electron (ion) density (noted n hereinafter). We also need a closure equation for the electron fluid. As the development of the KHI is a low frequency process, we used an isothermal equation P_e=$n_e k_B T_e$ with a constant value of the electron temperature T_e, k_B being the Boltzman constant.

We used a small resistivity in these calculations, mainly because of its stabilizing effect on the results, and chose η=0.0001. With this value, the diffusion time is τ_D=40 000. The Alfvén time τ_A being 2, the growth time of the resistive tearing mode is τ_r=$\sqrt{2\tau_D \tau_A}$=400. We will see in the next section that the simulations are all performed over a total time T=400. Furthermore, KHI starts its linear growth phase at $t\sim$100, and the penetration process starts at the very begining of the simulations. We can thus suspect that there is no magnetic reconnection due to anomalous resistivity that leads to the observed structures. This point will be detailed in Sect. 5 where we discuss the Walèn test.

The last classical hypothesis concern the boundary conditions. Because of the nature of the initial topology, we chose periodic conditions in the x-direction. This assumption cannot be made in the y-direction, because of the reversal of the magnetic field direction, and the bulk flow velocity. At Y=0 and Y=Y_m, we assumed that particles are specularly reflected, and E_X=E_Z=$d_Y E_Y$=0.

3 Initial topology

We focused on tangential discontinuities with a 180° rotation angle for the magnetic field. There is thus no normal component of velocity and magnetic field, and the only constraints for the tangential components are to satisfy the pressure balance. Such a geometry corresponds to the flanks of the MP when the interplanetary magnetic field (IMF) is southward. By definition, the rotation of the magnetic field is in a plane tangential to the discontinuity which we refer to as the XZ plane. As illustrated in Fig. 1, the magnetic field is in the +**Z** direction in side 1 of the discontinuity, and in the −**Z** direction in side 2. At the discontinuity, the rotation is such that the magnetic field is in the +**X** direction. The velocity profile is also represented, varying from $-V_0$ in side 1 to $+V_0$ in side 2.

We use a fluid equilibrium and consider the following profile

$$P_0(y) = P_1 + (P_2 - P_1)\chi \quad (2)$$

(with Φ=$(y - Y_0)/\lambda$, Y_0=$Y_m/2$, and χ=$(1+\tanh\Phi)/2$) for the magnetic field magnitude $B_0(y)$, the density $n_0(y)$, and the $\beta_i(y)$ and $\beta_e(y)$ parameter (β being the ratio between kinetic to magnetic pressure for ions and electrons, respectively). The tangential magnetic field is analytically described by

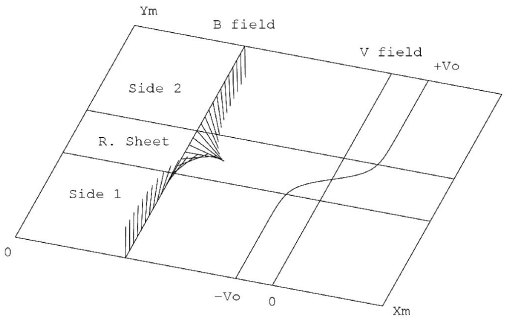

Fig. 1. Schematic view of initial magnetic field and velocity used in the simulations.

$$B_x = B_0 \sin(\alpha) \quad (3)$$

$$B_z = B_0 \cos(\alpha) \quad (4)$$

with α=$\pi(1-\chi)$. We first perform a reference run where the magnetic field magnitude, density, β_i and β_e parameters are unifom. We have V_0=$-V_1$=V_2=0.5, B_0=1.0, λ=1.0, n_0=1.0, β_i=1.0 and β_e=1.0. One remarks there is a gradient on the magnetic field direction, but not on its magnitude. As discussed later, ions are hence also magnetized in the field reversal region. Except when indicated, these values will also be used in the subsequent runs.

We did not consider any kinetic equilibrium because none of them are satisfactory in our case. Some provided an analytical solution for tangential discontinuities with no velocity shear and no magnetic shear (Channell, 1976; Mottez, 2003). Lee and Kan (1979) provided a semi-analytical solution of tangential discontinuities including a velocity shear and a small magnetic shear. Roth and DeKeyser (1996) described a large (though incomplete) class of solutions given as convolution between exponential and error functions. The common problem of these equilibriums is that the proposed solution may not be unique. The numerical equilibrium itself requires some time (even short) to adjust, either because of numerical uncertainties (inherent to semi-analytical solutions), or because the given equilibrium is not the most likely. This adjustment time is inherent to the problem and cannot be avoided. As a result, we used a fluid equilibrium and monitored the ion distribution functions to ensure that the equilibrium is reached before physical processes of interest occur.

To monitor the time evolution of the distribution function at the beginning of the simulation, we rebuilt the 10 independent components of the heat flux Q. We focus on the heat flux Q because fine structures play an increasing role in the

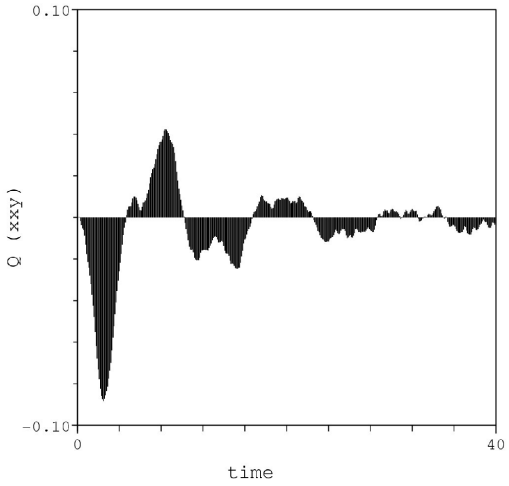

Fig. 2. Time evolution of the XXY component of the heat flux Q.

high order moments of the distribution functions. The integrale to build Q is made on the cells located at Y=Y_0, corresponding to an integral conducted along the x-direction, at the center of the discontinuity. Being at the center of the discontinuity, the distribution function strongly depends upon the kinetic equilibrium.

Figure 2 depicts the time evolution of the XXY component of the heat flux Q. This component of the heat flux is the only one that oscillates at the begining of the simulation, the others being approximately constant. The Q_{XXY} value oscillates with a period about 6, that is close to the gyroperiod (2π). After about 3 gyroperiods, the value of Q_{XXY} is close to zero. Though not represented here, this level is constant until T=400. Calculating the Q_{XXY} value at different Y positions, the level of these oscillations proves to be always lower, and reaches the noise level with the same caracteristic time. This suggests that a kinetic equilibrium is reached at $t\sim$20. As we will see hereinafter, the linear growth phase of the KHI starts at $t\sim$100. Hence, there is no overlapping between the phase during which the equilibrium is reached, and the begining of the KHI development.

Another requirement of this study is to identify the position of the boundary between side 1 and side 2, at whatever stage of the simulation. To do so, Nykiri and Otto (2001) calculated the z-component of the magnetic vector potential. In the present case, because of the rotation of the magnetic field, a simple definition can be used: we define the MP location as the location where the z-component of the magnetic field changes sign. Figure 3 depicts the z-component of the magnetic field at (a) t=120 (b) t=200 and (c) t=260. Figure 3a is the begining of the growing phase of the KHI, where the interface starts to ripple. Figure 3b shows the end of the linear growth phase of the KHI. In this figure, two wavelengths are noticeable at the interface. During the growing

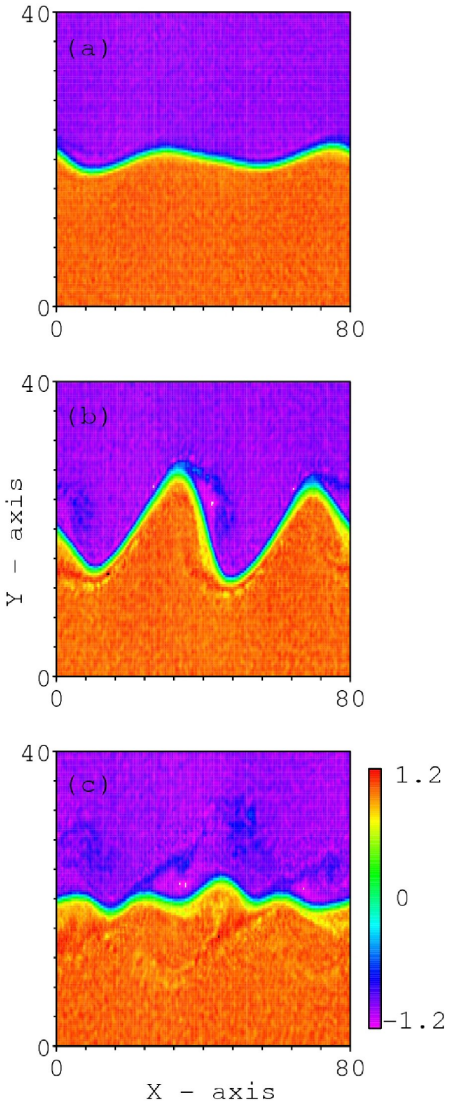

Fig. 3. Color-coded z-component of the magnetic field at **(a)** t=120, **(b)** t=200, and **(c)** t=260 in the x-y-plane.

phase, the wave fronts steepen until saturation. Thereafter, the two waves merge yielding new waves. The number of waves is not very clear in Fig. 3c. Fourier analysis presented later in the paper will help to picture the time evolution. After $t\sim260$, a new growing phase start, with the build up of 2 new waves fronts that grow until a new saturation. As discussed at the end of Sect. 1, inverse cascad occurence colsely depends on the size of the simulation box.

4 Development of the Kelvin-Helmholtz instability

We start our analysis with the reference run described above. As mentionned in Sect. 3, there is an initial velocity shear and reversal of the magnetic field, with no gradient in density, temperature and magnetic field magnitude. Prior to studying the ion distribution functions, we quantify the effect of the KHI on the mass transport across the discontinuity. We use the δZ value proposed by Thomas and Winske (1993), and defined by

$$\delta Z = \frac{N_T}{n_0 X_m} \tag{5}$$

where X_m is the system length in the x-direction, n_0 the initial ion density on each side of the boundary, and N_T the total number of ions crossing the interface (from side 2 to side 1) defined in Sect. 3. The crossing process being symetric, the N_T value computed considering particles crossing from side 1 to side 2 is statistically the same. Even if δZ is homogeneous to a distance, it has to be seen as the normalized number of particles crossing the MP from side 2 to side 1. The time evolution of this quantity is presented in Fig. 4. It should be noted here that at the begining of the simulation, particles close to the boundary may experience repeated excursions across it. To remove such behaviors from δZ calculated, the value of N_T (and thus δZ) is computed only with particles which remain at least one gyroperiod on the initial side of the discontinuity prior crossing. As a result, one has δZ=0 until t=2π.

In Fig. 4, δZ is strictly growing with time. Between $t\sim0$ and $t\sim160$, one observes a linear phase during which δZ evolves linearly with time. This demonstrates that the crossing process starts at the very begining of the simulation, when the KHI is not developed yet. Such a behavior was already obtained by Thomas and Winske (1993), and suggests that the crossing process is not directly triggered by the KHI. Between $t\sim160$ and $t\sim220$, a second linear phase is noticeable but with a higher slope value. This interval corresponds to the non-linear stage of the growing phase of the instability. Even though the crossing process is not directly triggered by the KHI, KHI clearly has an influence on this process and enhances it. Then, we observe a series of phases during which the slope of δZ increases and decreases.

To compare the time evolution of δZ with the stage of the KHI, we calculated the Fourier transform of the spatial series (in the x-direction) of the y-component of the magnetic field, averaged in the y-direction. In Fig. 5, we show the logarithm of this value (color-coded) as a function of time and K_X mode. We also calculated the time derivative of δZ. The obtained value being quite noisy (as usual with numerical derivative calculation), we filtered it with a gaussian window of 8 points width. The obtained result is multiplied by a normalization coefficient (to fit the K_X scale) and displayed with solid thick line in Fig. 5. At $t\sim100$, the KHI develops and grows until $t\sim200$. This can be seen in, Fig. 5 by the broadening of the B_Y spectra. At $t\sim200$, the instability reaches its saturation level after what, vortex coalescence is observed until $t\sim250$. This phase clearly corresponds to a lowering of the spectral width of B_Y. We then observe until t=400 two others saturation stages, preceded by a growing phase, and followed by a coalescence phase. One can note a good agreement between the time derivative of δZ and the spectral width of B_Y.

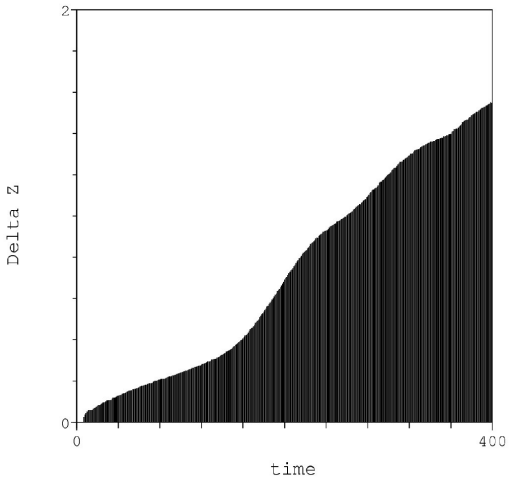

Fig. 4. Time evolution of the δZ=N_T/n_0X_m layer thickness.

For the sake of clarity, we introduce the following denomination for the particle orbits: we call "short crossings" particles that cross several times the discontinuity, with a time of flight between 2 crossings smaller than 2π, and "long crossings" particles that cross the discontinuity several times, with a time of flight between two crossings larger than 2π. We must also make a distinction between even number of crossings and odd number of crossing: odd values are associated to particles that change sides, whereas even values are associated to particles that end up on the same side of the discontinuity as they were initially.

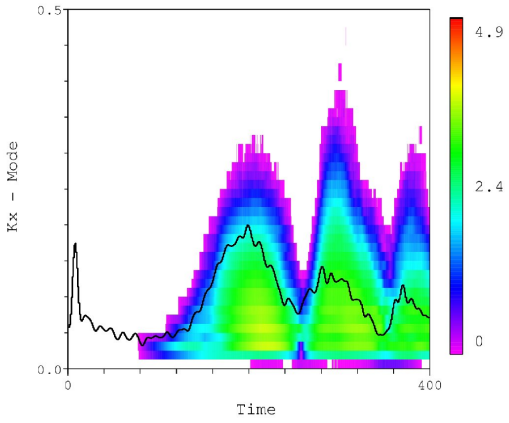

Fig. 5. Color-coded Y component of the magnetic field depending on the Kx mode (after spatial Fourier transformation) and time. The solid thick line is the time evolution of the derivative of δZ.

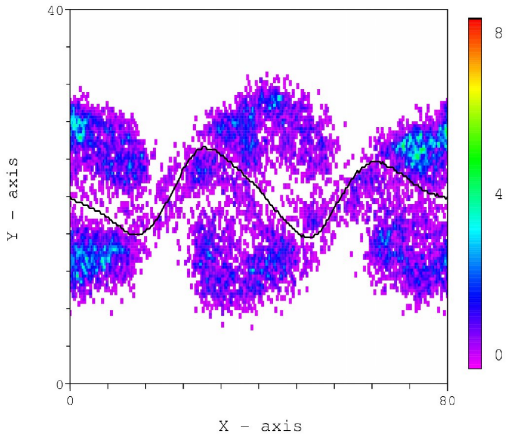

Fig. 6. Color-coded number of particles crossing once the discontinuity.

5 Ion distribution functions

In this section, we build the ion distribution functions associated with particles that cross the discontinuity. Building ion distribution functions requires to define a protocol. Indeed, with particle-like simulations, distribution function results from an average on a statistically representative population. In the same way as in Fig. 4, distribution functions correspond to particles that cross the discontinuity, with an initial time of flight prior to the first crossing at least equal to 2π.

Figure 6 displays the number of crossing particles color-coded in each cell (of size ΔX by ΔY), depending on their X and Y position at t=240. The solid line indicates the position of the MP identified by the sign change of B_Z. Figure 6 does not take into account "short crossing", but only particles that cross once the discontinuity. Hence, particles on sides 2 were initially on side 1 and vice-versa. One can clearly see that the crossing particles form islands located between the edges of the surface instability. Crossing particles being located in small regions, we build the distribution function associated with these 4 islands (2 on each side).

Figure 7 depicts the ion distribution functions at t=240 associated with particles that experience 2 crossings. Since we have very similar distribution functions in these 4 islands (whatever the side we consider), the one presented in Fig. 7 shows an average over all islands. The left and right panel of Fig. 7 show the color coded phase space density in the plane perpendicular to the local magnetic field and in the parallel – perpendicular velocity direction, respectively. The left panel of Fig. 7 reveals that the distribution is gyrotropic. This result is not unexpected: because of the constraints on the time of flight, the distribution functions correspond to particles that experience an adiabatic motion. The hypothesis of random gyrophases is thus satisfied. Furthermore, the computed value of the temperature is approximately the same as the one used for the initialization. No evidence of heating or cooling is noticeable.

In the right panel of Fig. 7, a D-shaped distribution can be seen, most particles having a positive value of their parallel velocity. One should note that the sign of the bulk flow associated to the D-shaped distribution (positive in Fig. 7) does not depend on the side of the MP where it is observed. As mentioned earlier, the particles considered here fly more than 2π after crossing the discontinuity. If this time of flight is increased the same overall pattern is observed, with just a slightly smaller number of particles. As discussed in the introduction, the build-up of such D-shaped distributions is often associated with magnetic reconnection when such D-shaped distribution is observed (see e.g. Cowley and Shull, 1983). We already saw that the numerical resistivity is supposedly too small to let resistive tearing occur. To explore this distribution further and rule out the occurence of magnetic reconnections, we perform Walèn test (see e.g. Sonnerup et al., 1981).

This test consists in comparing the fluid velocity to the Alfvén velocity (for both x- and y-components). To do so, we build at t=240, the components of the Alfvén and fluid velocity from the magnetic and fluid structures we computed along a virtual crossing, at X=25, and between Y=20.3 and Y=26.5. This arises from the position of the MP, located (at X=25) at Y=23.4 and corresponds to 20 cells (10 in each

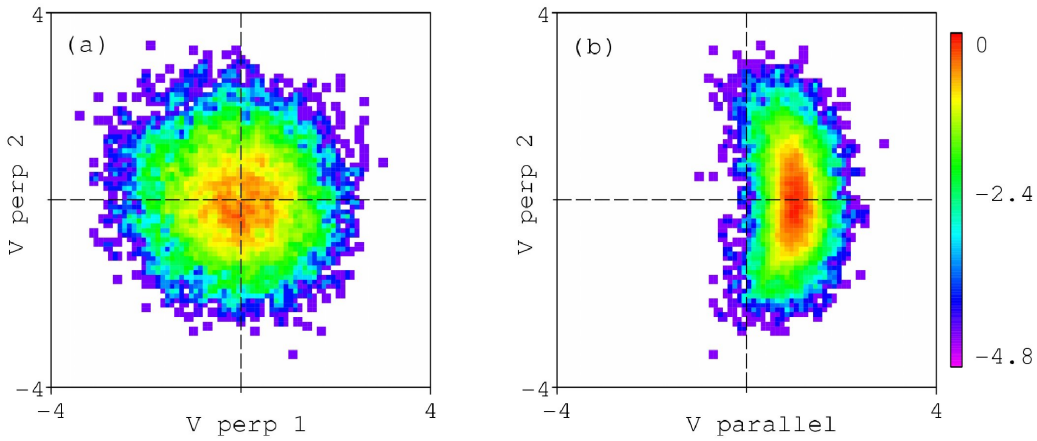

Fig. 7. Color-coded phase space density of crossing particles (see text): (left) in the perpeendicular plane (right) in the parallel-perpendicular plane.

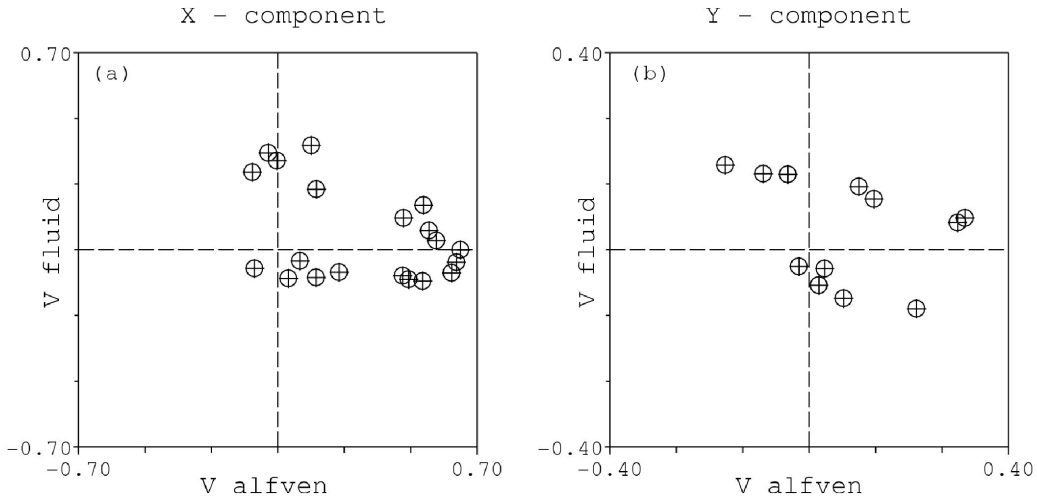

Fig. 8. (Left) normal and (right) tangential fluid velocity as a function of Alfvén speed.

sides of the MP) that gives 20 couples of Alfvén and fluid velocity (in both x- and y-direction). In Fig. 8, we show the distinct values of these couples (x-component on the left panel and y-component on the right panel) and check whether there exists a possible value of the deHoffmann-Teller frame velocity V_{HT} that can verify the test $V=V_{HT}\pm V_A$.

Figure 8 demonstrates that the Walèn test is not satisfied because there is no way to interpolate these points with a straight line having a slope equal to one. Similar calculations changing the localization and/or the stage of the KHI lead to the same conclusion. Accordingly, there is no magnetic reconnection in the present set of simulations. Starting from a tangential discontinuity, regardless of the stage of the KHI,

Table 1. Parameters used for different runs. λ is the initial half thickness of the discontinuity, V_0, B_0 and n_0 the initial asymptotic value of the fluid velocity, magnetic field magnitude and density, respectively, and β_i the ionic β parameter.

Run	parameters set
Run 1	reference
Run 2	λ=1.1, V_0=0.7
Run 3	λ=1.2, B_0=1.4
Run 4	λ=1.3, n_0=0.6
Run 5	λ=1.4, opposite polarization
Run 6	λ=1.6, β_i=2.0
Run 7	λ=1.8, β_i=2.0, B_0=0.7

the discontinuity never becomes rotational. To understand the building of the D-shaped distributions, one must consider the charged particles dynamics.

6 Particle dynamics

With the D-shaped distribution obtained in Fig. 7, we calculate the associated mean parallel velocity noted $V_\parallel$. A variety of runs were performed to characterize the conditions of occurence of such distributions, as well as the computed value $V_\parallel$. They are summarized in Table 1. As indicated in Sects. 2 and 3, we have for run 1, λ=1.0, V_0=0.5, B_0=1.0, n_0=1, β_i=1.0, β_e=1.0. We indicate for the other runs values that differs from these ones. This choice of parameters allows to explore differents values of the Alfvén velocity, of the shear velocity, of the thermal Larmor radius, and of the polarization of the discontinuity. For these 7 runs, we construct the ion distribution function as in Fig. 7. They are not depicted here, but in all cases, D-shaped structures are obtained. The efficiency of the penetration process can differ from one run to another by a factor of 2, which has (for our purpose) only consequences on the statistics to calculate $V_\parallel$.

We performed some other runs reversing the velocity shear direction and/or the direction of the asymptotic magnetic field, and obtained that it does not change the positive value of the mean parallel velocity in the D-shaped ion distribution function. The only way to achieve this is to reverse the sense of rotation of the magnetic field of the initial tangential discontinuity (being thus initially in the $-\mathbf{X}$ direction at the interface between side 1 and side 2). Other test runs showed that the magnitude of this mean parallel velocity only depends on the initial half thickness of the discontinuity λ and on the magnitude of the initial asymptotic magnetic field.

We computed the mean parallel velocity $V_\parallel$ and calculated the ζ value, defined as

$$\zeta = \frac{V_\parallel}{\Omega_C} \tag{6}$$

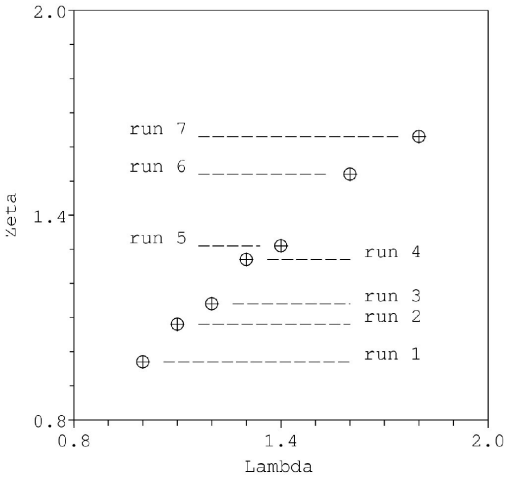

Fig. 9. Computed ζ value as a function of the initial half thickness λ.

where Ω_C is the gyroperiod with the asymptotic magnetic field magnitude. This is the average distance traveled along the magnetic field by the particle (forming the core of the D-shaped ion distribution function) during a cyclotron turn.

Figure 9 depicts the computed ζ value, depending on the initial λ value. It can be seen in this figure that a straight line with a slope close to one connects the various runs. Accordingly, the building of a D-shaped structure does not depend upon the magnitude of the Alfvén velocity or the shear velocity. We thus suspect the magnetic field rotation to play a role in this process. This idea is strenghtened by the fact that reversing the sense of rotation of the magnetic field changes the sign of the mean parallel velocity associated to distribution function. To examine this issue further, we examined test particle orbits.

Figure 10 shows the orbit of a particle in the time varying electric and magnetic field during T=200. This particle starts initially at $X\sim$4 and $Y\sim$22 on side 2. Following the shear velocity, this particle drifts in the +**X** direction. White triangles are drawn every ΔT=20. Around t=160, the particle crosses the discontinuity (indicated by the black triangle), and ends up on side 1 of the discontinuity until the end of the simulation. This type of orbit is representative of particles that compose the bulk of the D-shaped structure. In other words, these particles never exhibits short crossing, and seldom long crossing. Crossing always occurs on time scale on the order of the gyroperiod, with nearly-adiabatic sequences prior to and after this crossing. One can understand that, in view of Fig. 10, the structure of the magnetic field, even if corrugated through time, has a structure in the z-direction similar to the field reversal initially imposed.

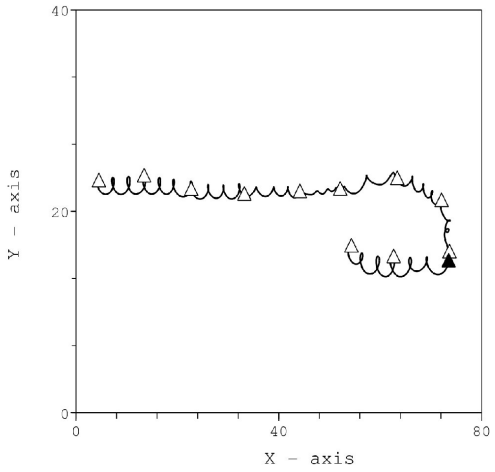

Fig. 10. Orbit of a crossing particle calculated self-consistently.

Such behaviors were already reported in Smets (2000). They are not due to the curvature of the magnetic field lines (the initial magnetic field lines being straight lines as indicated in Fig. 1), but to the scale of the field reversal. In a like manner to the adiabatic parameter κ_{BZ} defined by Büchner and Zelenyi (1989), Smets (2000) defined the κ_{RS} parameter (RS standing for Reversal Sheet) as the square root of the ratio between the thickness of the reversal sheet and the maximum Larmor radius. This study is hence done at $\kappa_{RS}\sim1$, and as predicted by Smets (2000), we never observe Speiser-like orbits and particle trapping at the interface, because of FLR effects. This type of non-linear dynamics has been reported by Smets (2002) using test-particle calculations in realistic magnetic topologies, obtained by MHD simulation of the KHI. But this work was done at $\kappa_{RS}\sim0.6$ which, as demonstrated by Smets (2000), allows particle trapping.

As we already saw in Fig. 4, penetration process starts at the begining of the simulation, before the KHI develops. We can suspect that this process is not directly linked to the occurence of the KHI, but rather to the magnetic topology of the discontinuity. The KHI just appears as a speeding up factor for the penetration process.

7 Microscopic process

A heuristic interpretation of the penetration process can be obtained with a rough picture of the magnetic field reversal. As a matter of fact, details of the magnetic profile (hyperbolic tangent in the present case) is not necessary and knowledge of the asymptotic value of the magnetic field in each side and

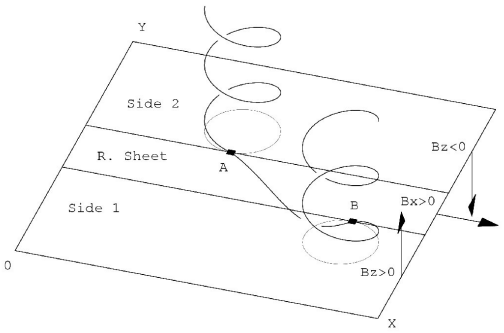

Fig. 11. Schematic view of the typical orbit followed by a particle crossing the magnetic field reversal.

at the center of the discontinuity is enough to drive the essential features. The associated process is depicted in Fig. 11. We considered side 1 and 2 with a magnetic field that is considered constant, in the $+\mathbf{Z}$ direction and $-\mathbf{Z}$ direction, respectively and we neglect the drift effect of the electric field: the associated fluid velocity being tangential to the discontinuity, it does not play a significant role in this process. At the interface, we consider also a constant magnetic field, in the $+\mathbf{X}$ direction that we call reversal sheet.

Let us consider a particle, initially on side 2, with a positive parallel velocity. Starting from an initial position with positive Z value, this particle, because of its parallel velocity, goes toward the Z=0 plane. Furthermore, because of the magnetic field and its perpendicular velocity, the particle gyrates around a magnetic field line, with a constant Larmor radius. With the appropriate initial position (as chosen in Fig. 11), this particle skims the interface between side 2 and the reversal sheet. When at the interface, because of magnetic noise, the particle can step aside, in the reversal sheet. This point is marked A in Fig. 11, and for simplicity, chosen to be in the Z=0 plane. To reach side 1 at point marked B, the Larmor radius in the reversal sheet has to be equal to the half thickness of the discontinuity λ. At point A, the perpendicular velocity needed in the calculation of the Larmor radius is in the $-\mathbf{Z}$ direction, that is the parallel velocity in side 2. Because there is no electric field, the kinetic energy of the particle is constant, and the parallel velocity in side 1 is equal to the parallel velocity in side 2 (that turns to be a perpendicular velocity in the reversal sheet).

The above explanation is based on geometric arguments, and does not depend upon the details of the discontinuity, provided it is tangential. This suggests that the analytical profile that we chose for the magnetic field is not critical. On the other hand, it is clear from Fig. 5 that magnetic field associated to high values of K_X plays an important role in this process. We computed the same figure as in Fig. 5 with the 3

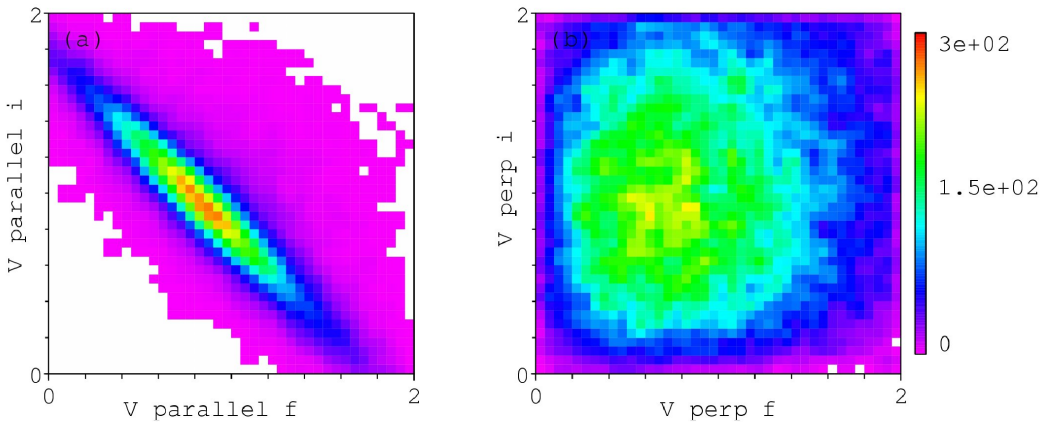

Fig. 12. Color-coded number of particles crossing the magnetic field reversal. Left panel depicts the final value of the parallel velocity, depending on its initial value, and right panel depicts the final value of the perpendicular velocity, depending on its initial value.

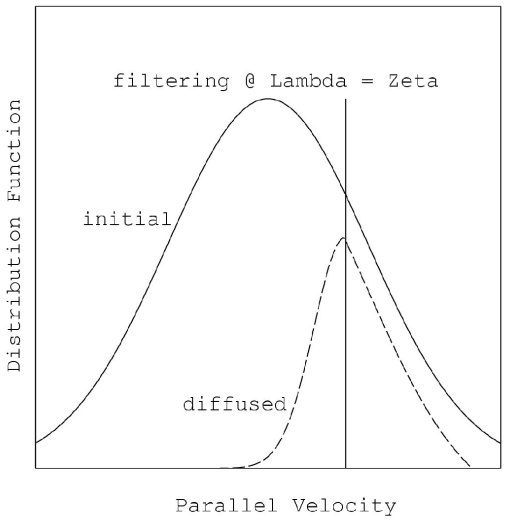

Fig. 13. Schematic view of the filtering effect acting upon the initial ion distribution function to produce a D-shaped one.

components of the electric field, and did not get any correlation between electric noise and enhancement of penetration process. It seems that magnetic noise is the essential source of penetration, even if ruling out the role of the electric noise would require us to perform some other runs with an appropriate low band filtering.

With the mechanism we just described, we explain easily why the crossing paticles are the one for which the computed ζ value is equal to λ. Further insights into this mechanism may be obtained from Fig. 12 that shows the initial particle velocity depending on its final value. Left panel of Fig. 12 is for parallel velocity, and right panel for perpendicular velocity. The first remark is that we have a clear symetry about the first bisector of the axis. In the left panel of Fig. 12, the largest number of particles crossing the interface is for both initial and final parallel velocity close to one, that is consistent with the mechanism discussed above. Furthermore, following the isocontour associated to the highest number of crossings, particles with a final parallel velocity larger than one have an initial parallel velocity smaller than one, and vice-versa. This is also consistent with the proposed mechanism. Going back to Fig. 11, let us consider a particle reaching point A with a parallel velocity giving a ζ value larger than λ. The Larmor radius in the reversal sheet being larger than λ, the particle will reach side 1 before achieving a complete half cyclotron turn. Thus, only a fraction of the perpendicular velocity in the reversal sheet will end-up in parallel velocity in side 1. This is the reason why crossing particles with large initial parallel velocity have a smaller one after crossing the discontinuity. This process being totally symetric, we explain in the very same way why particles with a small initial parallel velocity will have a larger one after crossing the discontinuity. In these two cases, initial parallel (perpendicular) velocity can transform in perpendicular (parallel) velocity after crossing the discontinuity, and vice-versa. This clearly explains the right pattern of Fig. 12.

8 Discussion

The process described here can be viewed as a filter for the crossing particles. Figure 13 shows a schematic view of the distribution function, depending on the parallel velocity. The solid line represents the initial distribution function, the dashed line represents the distribution function associated with the crossing particles. For simplicity, we neglect the mean value of the bulk velocity in the initial distribution function. The vertical line represents the parallel velocity for which we have $\zeta=\lambda$. Particles with a parallel velocity larger than this value are able to cross the discontinuity. The others can hardly achieve it.

The resulting D-shaped distribution is only associated with crossing particles. At a given point, there is no way to experimentally distinguish between crossing particles and non-crossing particles. This means that the observed distribution results from the superposition of a drifting maxwellian associated to the non-crossing particles, and a D-shaped distribution associated to crossing particles. Construction of realistic distribution is beyond the scope of this paper, but calculating the mixing index as suggested by Terasawa et al. (1992), we found that there exists regions where the proportion of crossing/non-crossing particles is half-half (at $t=400$). We claim that, even if fuzzed, D-shaped distribution should be observable in the vicinity of the MP, when the IMF is southward.

The spatial extension of the region in which such D-shaped distribution are observable around a tangential discontinuity is questionable. From Fig. 6, it appears that it is around the field reversal on a layer thickness of about 20 (even if it is not filled only by crossing particles). This layer may actually be much thicker since we have seen that the penetration process depends on the thickness of the discontinuity (only its efficiency depends on the KHI phase), ζ being a linear function of λ. The small value of δZ is clearly due to the fact that $\delta Z=0$ at $t=0$. As long as the thickness of the discontinuity remains constant (and we have no evidence of its enhancement) we will have penetration process. A proper answer to this question would need an asymptotic study of this behavior, on a time much larger than a few hundreds of ionic cyclotronic periods to reach a stationary state.

There also exists a density gradient at the MP. This gradient can be located at a different location from the magnetic field gradient that defines the boundary layer. We do not consider such a density gradient, and will explain why it is not a problem for our results. We computed two runs with a density gradient at the interface, one with a density ratio equal to 4, and another with a ratio equal to 10 (which is a quite realistic value at the MP, see e.g. Paschmann et al., 1978). We observe the same process of discontinuity traversal, and a D-shaped distribution. The relation between λ and ζ is still linear, but with a different value of the slope (depending on the density gradient). The diamagnetic drift associated with such a density gradient should then be considered in the explanation. But the important point however is that, looking at in situ observations, the density gradient can occur at a different location from the gradient of the magnetic field direction: density gradient and field reversal can then be decoupled (see e.g. Paschmann et al., 1978). Observations also show a thinner MP with a southward IMF than with a northward one, and a density gradient (considered as the MP thickness) thicker than the field reversal layer. The consequences of these remarks are that calculations with a realistic density gradient should not affect the build-up of D-shaped distribution if the density gradient is not located at the same position as the field reversal. If both density gradients and field reversal occur at the same location, this would only change the relation between λ and ζ, but not the overall structure of a D-shaped distribution.

9 Conclusions

The hybrid simulations performed demonstrate that in a tangential discontinuity as is the case in the flanks of the magnetosphere during southward IMF conditions, the KHI does not trigger the transport of matter across the MP but rather enhances and/or speed up it. The transmitted particles exhibit D-shaped distribution, the average parallel speed being controlled by the half thickness of the discontinuity and the asymptotic magnetic field magnitude. We hence conclude that there is no one-to-one relationship between magnetic reconnection and D-shaped distribution functions as is commonly postulated.

Acknowledgements. Part of this work was done while R. Smets held a grant from CNRS/JSPS # 12852 for a mid-term stay at University of Tokyo. R. Smets thanks M.. Hoshino, A. Miura, T. Terasawa, and Y. Matsumoto for fruitfull discussions, and M. Hesse for providing the hybrid code.

Topical Editor I. A. Daglis thanks G. Ganguli and another referee for their help in evaluating this paper.

References

Belmont, G. and Chanteur, G.: Advances in magnetopause Kelvin-Helmholtz instability studies, Phys. Scripta, 40, 124–128, 1989.

Büchner, J. and Zelenyi, L. M.: Regular and chaotic charged particle motion in magnetotaillike field reversal 1. Basic theory of trapped motion, J. Geophys. Res., 94, 11 821–11 842, 1989.

Chandrasekhar, S.: Hydrodynamic and hydromagnetic stability, Dover Publication, New York, 1961.

Channell, P. J.: Exact Vlasov-Maxwell equilibria with sheared magnetic fields, Phys. Fluids, 19, 1541–1545, 1976.

Cowley, S. W. H. and Shull Jr., P.: Current sheet acceleration of ions in the geomagnetic tail and the properties of ions bursts observed at the lunar distance, Planet. Space Sci., 31, 235–245, 1983.

Dungey, J. W.: Interplanetary magnetic field and the auroral zone, Phys. Rev. Lett., 6, 47–48, 1961.

Eastman T. E., Fuselier, S. A., and Gosling, J. T.: Magnetopause crossing without a boundary layer, J. Geophys. Res., 101, 49–57, 1996.

Frisch, U.: Turbulence, Cambridge University Press, 296 pages, 1995.

Fujimoto, F. and Terasawa, T.: Anomalous ion mixing within and MHD scale Kelvin-Helmholtz vortex, J. Geophys. Res., 99, 8601–8613, 1994.

Ganguli, G.: Stability of an inhomogeneous transverse plasma flow, Phys. PLasmas, 4, 1544–1551, 1997.

Hasegawa, H., Fujimoto, M., Phan, T.-D., Rème, H., Balogh, A., Dunlop, M. W., Hashimoto, C., and TanDokoro, R.: Transport of solar wind into Earth's magnetosphere through rolled-up Kelvin-Helmholtz vortices, Nature, 430, 755–758, 2004.

Huba, J. D.: The Kelvin-Helmholtz instability: Finite Larmor radius magnetohydrodynamics, Geophys. Res. Lett., 23, 2907–2910, 1996.

Lee. L. C. and Kan, J. R.: A unified model of the tangential magnetopause structure, J. Geophys. Res., 84, 6417–6426, 1979.

Matsumoto, Y. and Hoshino, M.: Onset of turbulence induced by a Kelvin-Helmholtz vortex, Geophys. Res. Lett., 31, L028071–L028074, 2004.

Miura, A. and Pritchett, P. L.: Nonlocal stability analysis of the MHD Kelvin-Helmholtz instability in a compressible plasma, J. Geophys. Res., 87, 7431–7444, 1982.

Miura, A.: Anomalous transport by magnetohydrodynamic Kelvin-Helmholtz instabilities in the solar wind-magnetosphere interaction, J. Geophys. Res., 89, 801–818, 1984.

Miura, A.: Simulation of the Kelvin-Helmholtz instability at the magnetospheric boundary, J. Geophys. Res., 92, 3195–3206, 1987.

Mottez, F.: Exact nonlinear analytic Vlasov-Maxwell tangential equilibria with arbitrary density and temperature profiles, Phys. Plasmas, 10, 2501–2508, 2003.

Nakamura, T. K. M., Hayashi, D., and Fujimoto, M.: Decay of MHD-scale Kelvin-Helmholtz vortices mediated by parasitic electron dynamics, Phys. Rev. Lett., 92, 145001-1–145001-4, 2004.

Nykiri, K. and Otto, A.: Plasma transport at the magnetospheric boundary due to reconnection in Kelvin-Helmholtz vortices, Geophys. Res. Lett., 28, 3565–3568, 2001.

Papamastorakis, I., Paschmann, G., Sckopke, N., Bame, S. J., and Berchem, J.: The magnetopause as a Tangential discontinuity for large field rotation angles, J. Geophys. Res., 89, 127–135,1984.

Paschmann, G., Sckopke, N., Haerendel, G., Papamastorakis, J., Bame, S. J., Asbridge, J. R., Gosling, T. J., Hones Jr., E. W., and Tech, E. R.: ISEE plasma observations near the subsolar magnetopause, Space Sci. Rev., 22, 717–737, 1978.

Paschmann, G., Sonnerup, B. U. O., Papamastorakis, I., Sckopke, N., Hearendel, G., Bame, S. J., Asbridge, J. R., Gosling, J. T., Russell, C. T., and Elphic, R. C.: Plasma acceleration at the Earth's magnetopause: evidence for reconnection, Nature, 282, 243–246, 1979.

Paschmann G., Haaland, S., Sonnerup, B. U. O., Hasegawa, H., Georgescu, E., Klecker, B., Phan, T.-D., Rème, H., and Vaivads, A.: Characteristics of the near-tail dawn magnetopause and boundary layer, Ann. Geophys., 23, 1481–1497, 2005, http://www.ann-geophys.net/23/1481/2005/.

Phan, T. D., Escoubet, C. P., Rezeau, L., Treumann, R. A., Vaivads, A., Paschmann, G., Fuselier, S. A., Atti, D., Rogers, B., and Sonnerup, B. U. O.: Magnetopause Processes, Space Sci. Rev., 118, 367–424, 2005.

Pu, Z. Y. and Kivelson, M. G.: Kelvin-Helmholtz instability at the magnetopause: solution for a compressible plasma, J. Geophys. Res., 88, 841–852, 1983.

Romero, H. and Ganguli, G.: Nonlinear evolution of a strongly sheared cross-field plasma flow, Phys. Fluids, 5, 3163–3181, 1993.

Romero, H. and Ganguli, G.: Relaxation of the stressedd plasma sheet boundary layer, Geophys. Res. Lett., 21, 645–648, 1994.

Roth, M., DeKeyser, J., and Kuznetsova, M. M.: Vlasov theory of the equilibrium structrure of tangential discontinuities in space plasmas, Space Sci. Rev., 76, 251–317, 1996.

Shinohara, I., Suzuki, H., Fujimoto, M., and Hoshino, M.: Rapid large-scale magnetic-field dissipation in a collisionless current sheet via coupling between Kelvin-Helmholtz and lower-hybrid drift instabilities, Phys. Rev. Lett., 87, 095001-1–095001-4, 2001.

Smets, R.: Charged particle dynamics in a tangential discontinuity, J. Geophys. Res., 105, 25 009–25 019, 2000.

Smets, R., Delcourt, D., Chanteur, G., and Moore, T. E.: On the incidence of the Kelvin-Helmholtz instability for mass exchange process at the Earth's magnetopause, Ann. Geophys., 20, 757–769, 2002, http://www.ann-geophys.net/20/757/2002/.

Sonnerup, B. U. O., Paschmann, G., Papamastorakis, I., Sckopke, N., Haerendel, G., Bame, S. J., Asbridge, J. R., Gosling, J. T., and Russell, C. T.: Evidence for magnetic field reconnection at the Earth magnetopause, J. Geophys. Res., 86, 10 049–10 067, 1981.

Southwood, D. J., Farrugia, C. J., and Saunders, M. A.: What are Flux Transfer events?, Planet. Space Sci., 36, 503–508, 1988.

Talwar, S. P.: Hydromagnetic stability of the magnetospheric boundary, J. Geophys. Res., 70, 2707–2713, 1964.

Terasawa, T., Fujimoto, M., Karimabadi, H., and Omidi, N.: Anomalous ion mixing within a Kelvin-Helmholtz vortex in a collisionless plasma, Phys. Rev. Lett., 68, 2778–2781, 1992.

Thomas, V. A. and Winske, D.: Kinetic simulation of the Kelvin-Helmholtz instability at the magnetopause, J. Geophys. Res., 98, 11 425–11 438, 1993.

Thomas, V. A.: Three-dimensional kinetic simulation of the Kelvin-Helmholtz instability, J. Geophys. Res., 100, 19 429–19 433, 1995.

Treumann, R. A., LaBelle, J., and Bauer, T. M.: Diffusion processes: an observational perspective, Geophys. Monograph, 90, 331–341, 1995.

Winske, D. and Quest, K. B.: Electromagnetic ion beam instabilities: Comparison of one- and two-dimensional simulations, J. Geophys. Res., 91, 8789–8797, 1986.

Winske, D., Thomas, V. A., and Omidi, N.: Diffusion at the magnetopause: a theoretical perspective, Geophys. Monograph, 90, 321–329, 1995.

— D —

Plasma diffusion in self-consistent fluctuations

R. Smets, G. Belmont, N. Aunai, L. Rezeau,
Laboratoire de Physique des Plasmas,

Physics of Plasmas
Vol. 18, pages 102310 - 102318, 2011

PHYSICS OF PLASMAS **18**, 102310 (2011)

Plasma diffusion in self-consistent fluctuations

R. Smets,[a] G. Belmont, N. Aunai, and L. Rezeau
LPP, UPMC, X, CNRS, route de Saclay, 91128 Palaiseau, France

(Received 1 March 2011; accepted 15 September 2011; published online 20 October 2011)

The problem of particle diffusion in position space, as a consequence of electromagnetic fluctuations is addressed. Numerical results obtained with a self-consistent hybrid code are presented, and a method to calculate diffusion coefficient in the direction perpendicular to the mean magnetic field is proposed. The diffusion is estimated for two different types of fluctuations. The first type (resulting from an agyrotropic initial setting) is stationary, wide band white noise, and associated to Gaussian probability distribution function for the magnetic fluctuations. The second type (resulting from a Kelvin-Helmholtz instability) is non-stationary, with a power-law spectrum, and a non-Gaussian probability distribution function. The results of the study allow revisiting the question of loading particles of solar wind origin in the Earth magnetosphere. © *2011 American Institute of Physics*. [doi:10.1063/1.3647558]

I. INTRODUCTION

This paper addresses the notion of particle diffusion in position space under fluctuating electromagnetic fields in collisionless plasmas. To make clear the distinction between diffusion in position space and diffusion in velocity space, we call diffusion the former, and scattering the latter. Particle scattering has been widely studied in the frame of quasi-linear theory.[1] This will not be discussed in this paper, even if one has to keep in mind that there is a relation between diffusion and scattering.[2]

Particle diffusion in collisionless plasmas is important for instance for cosmic ray modulation in interstellar media,[3] particle confinement in tokamaks,[4] or filling up the magnetosphere with solar wind's particles.[5] In the two first cases, the β value (ratio between kinetic and magnetic pressure) is very low, meaning that the self-consistency is not supposed to be important. As a consequence, most numerical studies have been conducted with test-particle computations. The field line random walk (FLRW) model[6] was the first analytical form of the diffusion coefficient, assuming that particles follow the magnetic field line and neglecting finite Larmor radius effects. The perpendicular diffusion coefficient is hence a quantification of how particles initially in a given fluid element can spread over time in the direction perpendicular to the mean magnetic field. When parallel diffusion is effective, the perpendicular transport is shown to be lowered[7] and can reach subdiffusive level.

An ansatz for the perpendicular diffusion coefficient was then proposed[8] (BAM from the names of its authors). In this model, the stochastic behavior of particles is contained in a single and self-explanatory parameter $\nu_\perp$: the perpendicular decorrelation time $\nu_\perp^{-1}$ (associated to the perpendicular velocity). The two models BAM and FLRW provide lower and upper limits, respectively, for the numerical results of test-particle simulations.[9] The non linear guiding center (NLGC) model[10] could be considered as an achievement of this task as suggested by the nice agreement between analytical model and test-particle simulations. It is worth noticing however that NLGC model needs 3 free parameters which can not be determined a priori. Another question raises from these studies; comparisons have always been done with test-particles simulations in magnetostatic turbulence. This questions the importance of self-consistency and the role of electric fluctuations (associated or not with the magnetic fluctuations).

The scope of this study is to revisit the calculation of a perpendicular diffusion coefficient in a collisionless plasmas using self-consistent numerical calculations. Such calculations have already been done in the context of mass transport across the Earth magnetopause.[11,12] In the former paper, the waves were associated to a two-stream instability, and the authors concluded that diffusion process is not likely to be a major effect at the magnetopause. In the latter, the authors reached the opposite conclusion when a Kelvin-Helmholtz (KH) instability develops, associated to the velocity shear between the solar wind flowing around the stagnant Earth magnetosphere plasma. We propose in this paper an alternative method to calculate a diffusion coefficient in self-consistent simulations, and emphasize the need to separate the fluid motion, that is taken into account in any complete fluid model, from the stochastic motion of the individual particles in the frame of this average motion. We only deal with the latter, whose consequences generally appear in fluid models under the form of a diffusive term. For this reason, we will have to subtract the fluid bulk velocity from the individual particle velocities to characterize their kinetic diffusion. Our results will allow to revisit the importance of the KH instability for diffusive transport of particles between the Earth magnetosphere and the solar wind.

In Sec. II, we present the numerical code we use, the two initial set-ups associated to different kinds of fluctuations, and the relevant boundary conditions. In Sec. III, we discuss the concept of diffusion in a magnetoplasma. In Sec. IV, we discuss the relevancy of two classical formalisms to infer the perpendicular diffusion coefficient, and the method we propose to compute it numerically in self-consistent calculations. In Sec. V, we present the numerical results for the

[a]Electronic mail: roch.smets@lpp.polytechnique.fr.

two kinds of fluctuations, and emphasize their similar behavior. In Sec. VI, we closely analyze the nature of the electromagnetic fluctuations associated to the two initial set-ups and emphasize their differences. In Sec. VII, we discuss the results, and question the importance of the KH instability for mass exchange process through the Earth magnetopause.

II. NUMERICAL APPROACH

The calculations are carried out using a hybrid code (protons are treated as macro-particles and electrons as a massless fluid) with two spatial dimensions and three velocity dimensions. The set of equations numerically solved is

$$d_t \mathbf{x}_p = \mathbf{v}_p, \tag{1}$$

$$d_t \mathbf{v}_p = q/m(\mathbf{E} + \mathbf{v}_p \times \mathbf{B}), \tag{2}$$

$$N(\mathbf{x}) = \Sigma_p q S(\mathbf{x} - \mathbf{x}_p), \tag{3}$$

$$\mathbf{V}_p(\mathbf{x}) = \Sigma_p \mathbf{v}_p S(\mathbf{x} - \mathbf{x}_p)/N(\mathbf{x}), \tag{4}$$

$$\partial_t \mathbf{B} = -\nabla \times \mathbf{E}, \tag{5}$$

$$\mathbf{J} = \nabla \times \mathbf{B}, \tag{6}$$

where $\mathbf{x}_p$ is the proton position, $\mathbf{v}_p$ the associated velocity, $\mathbf{E}$ the electric field, $\mathbf{B}$ the magnetic field, N the proton density (by hypothesis equal to the electron density), $\mathbf{V}_p$ is the proton fluid velocity, and $\mathbf{J}$ the current density. In these equations, $S(\mathbf{x})$ is the shape factor[13] associated to the concept of macro-particles. As usual for a particle-in-cell code, $S(\mathbf{x})$ is a triangle of 2 grid points width's and unitary surface. The electromagnetic fields are calculated self-consistently using a predictor-corrector scheme.[14] Distances are normalized to the proton inertial length (c/ω_P), times are normalized to the inverse of the proton gyro-frequency $\left(\omega_C^{-1}\right)$, masses are normalized to the proton mass and density and magnetic field are normalized to their initial uniform values. The size of the simulation box is $X_M = Y_M = 120$. We use $N_X = N_Y = 300$ cells, a time step $\Delta t = 0.005$ with 2×10^5 time steps and about 100 macro-particles per cell. This value is determined empirically from stability criteria depending on the numerical scheme. It has to be noted that the shape factor is not involved in Eqs. (1) and (2). The dynamic of macro-particles is strictly identical to the one of particles in the present case of a strictly collisionless plasma. The concept of macro-particle is only needed in Eqs. (3) and (4) to infer macroscopic moments from particles distribution.

The displacement current is neglected in the Maxwell-Faraday equation. Such an assumption prevents the development of high frequency modes. Ohm's law is then needed to compute the electric field. Taking into account the Hall term and the electron pressure term, the electric field is

$$\mathbf{E} = -\mathbf{V}_p \times \mathbf{B} + \frac{1}{qN}(\mathbf{J} \times \mathbf{B} - \nabla P_e), \tag{7}$$

where P_e the scalar electron pressure. We choose an isothermal closure equation for the electron fluid, which is a priori justified when studying processes with phase velocity smaller than electron thermal velocity:[15] $P_e = nk_B T_e$ with a constant value of the electron temperature T_e, k_B being the Boltzmann's constant.

All the runs presented in this paper are initially set with $\beta_p = 0.8$ and $\beta_e = 0.2$. Such values are typically observed at the Earth magnetopause.[16] The initial magnetic field is in the Z direction, perpendicular to the simulation plane. Because of self-consistency, we need to find the proper conditions to let some electromagnetic fluctuations develop and grow. For that issue, we conducted 2 series of runs: 1—the 2 beams (2B) runs for which the box is initially filled with particles from two Maxwellian beams, homogeneous in the simulation domain, with opposite bulk velocities V_B and $-V_B$ in the X direction and the same temperature, 2—the Kelvin-Helmholtz (KH) runs for which, half of the box is initially filled with a Maxwellian plasma with a bulk velocity V_B in the X direction, and the other half filled with particles of same temperature and a bulk velocity of same magnitude and opposite direction $-V_B$ (associated to a shear velocity of half-thickness equal 1 at the interface located at $Y = Y_M/2$). Both runs are periodic in X and Y directions. This is an important requirement for the calculation of particles displacement that might be underestimated by artificial reflections on the boundaries of the simulation domain. Hence, for KH runs, the box size is doubled in the Y direction to consider two velocity shears. The resulting size is large enough to prevent any coupling between the two surface waves. It has to be mentioned that 2B runs are not depicting the well-known two-beams instability, because the initial velocity of each beam, in the X direction, is perpendicular to the magnetic field. This just creates an initial agyrotropy at the origin of the development of electromagnetic fluctuations, as well as an enhancement in the perpendicular temperature.

III. WHAT MEANS "DIFFUSION" IN A MAGNETOPLASMA

The word "diffusion", although it can be defined in a quite general manner, can take, however, different meanings in different physical situations. This makes necessary to specify which kind of diffusion this paper focuses on, and why.

The concept of diffusion comes in when, in a medium, the scales larger than some characteristic scale λ_0 can be modeled in a closed way, the smaller scales being supposed sufficiently chaotic so that their effect on the large ones can be estimated correctly by their only statistically averaged properties, without any deterministic description of them. The basic notion of "molecular diffusion," invoked in hydrodynamics, can conveniently be taken as a reference, and the other types of diffusion extrapolated from it.

In molecular diffusion, the characteristic scale is the collisional mean free path λ_C. Taking averages over dimensions large with respect to it, and therefore over a large number of collisions, one can calculate the way the individual particles separate from each other in average because of them and the consequences this separation has on the mean flow, i.e., on the flow integrated over a large number of such particles. This leads to representing the medium by the only most probable 1-particle distribution function $f(v)$, and its moments, the collisions being not described finely but just

considered numerous enough to make equiprobable all the N-particle distributions corresponding to the same 1-particle distribution. Considering only the most probable $f(v)$, i.e., the one that maximizes the entropy, provides only a degraded information on the system, which is at the origin of the apparent irreversibility. This most probable distribution can be shown to be a distribution close to an isotropic Maxwellian, the small departure from it scaling as $k\lambda_C$ for a variation at scale k^{-1}. With respect to the fluid equations, the integration of this small departure provides all the transport coefficients, including the diffusion coefficient.

In hydrodynamic turbulence, the description is often further simplified by limiting the resolution of the models to scales larger than the correlation scale λ_T, which characterizes the turbulence. When analyzing variation scales much larger than this correlation length $k^{-1} \gg \lambda_T \gg \lambda_C$, a probabilistic hypothesis comparable to the above can be done and one can then derive a "turbulent diffusion" coefficient, scaling as $k\lambda_T$.

The present work concerns on the contrary scales that are much smaller than the mean free path since, in the space plasmas that we intend to describe, one deals with almost collisionless plasmas. In these conditions, one can nevertheless consider the so-called "MHD scales," which are the scales much larger than the "kinetic scales" λ_K, for instance the ion Larmor radius: $\lambda_C \gg k^{-1} \gg \lambda_K$. The question at stake is then whether, due to small scale turbulence or to any other phenomenon leading to some phase mixing at the particle gyration scale, the plasma description at MHD scales can also be simplified by some probabilistic argument, leading to similar diffusion phenomena.

For that issue, both velocity fluctuations and magnetic fluctuations can contribute to the diffusion process associated to the large scale MHD turbulence. In a recent study of the solar wind,[17] it was shown that the scaling exponent of the structure functions for the magnetic field and the velocity components are significantly different (the former following a Kolmogorov $-5/3$ scaling, and the latter a Iroshnikov-Kraichnan $-3/2$ scaling). The role of the magnetic fluctuations has already been extensively studied. When studying the magnetic field line diffusion[18] (organized in term of the Kubo number), one only considers the braided nature of the magnetic field lines. When performing test-particle calculations[19–21] in such magnetic field lines, other effects like finite Larmor radius effects can also be considered. But when considering a fluctuating velocity field, the calculation of a diffusion coefficient would need a special treatment. Because of the fluctuating velocity field, an initially small connected space will not stay as is for 2 different reasons: a "large scale" fluid velocity will eventually shift its barycenter, and a "small scale" fluid velocity will stretch, twist, and fold down this domain in a non-connected state.[7] Diffusion process can be associated to the latter effect, the former one resulting in a large-scale convection and associated ballistic motion.

Nevertheless, as emphasized above, the definition of a mean value in turbulent media depends on a characteristic length scale or time scale which is barely obvious. This happens to be critical for the calculation of a diffusion coefficient. If one considers the particle motion including the contribution of the mean fluid velocity, the associated "ballistic" motion will lead to an unrealistic superdiffusive behavior. As a simple picture, let us consider a drunkard on a speedwalk. His walk will look less confused for a motionless observer if the speedwalk motion is not subtracted from the drunkard motion. Because of this problem, we focus in this paper on the diffusion process associated to particle motion free of any fluid velocity defined at all scales, ranging from the grid size to the box size.

We will hence not consider in this paper the possibility of treating a MHD turbulence as a cause of larger scale diffusion. Even if there are indeed large scale fluctuations present in the simulations presented, they might not have, a priori, the necessary properties of stationarity that could justify this approach. These fluctuations are therefore modeled exactly, without probabilistic assumption. There is furthermore a more fundamental reason for not considering the possible diffusion due to the large MHD scales. As at these scales, each particle is known to remain on the same field line, whatever the more or less chaotic motion of this line, there will therefore not be any diffusion possible perpendicular to the magnetic field due to these scales. Since the main motivation we have in mind is the penetration of particles through the magnetopause tangential layer, all the large scale motions that respect an ideal Ohm's law can be disregarded since they are inefficient for that. On the contrary, the existence of small scales "microscopic" motions can introduce non ideal terms in the fluid equations, and allow some slipping of the particles with respect to the magnetic field line ideal motion.

IV. PARTICLE SPREADING IN POSITION SPACE

As described in Sec. II, the initial magnetic field is in the Z direction and the initial velocity V_B in the X direction. Hence, the initial electric field (given in Eq. (7)) is in the XY plane (no explicit gradients in the Z direction). As a consequence of the Maxwell-Faraday equation, the magnetic field will remain in the Z direction over time, and the electric field will also remain in the XY plane over time. This topology could be subject to a serious limitation that we must dissipate before presenting the results. It is analytically demonstrated[21] that if there is at least one cyclic coordinate, charged particle are tied to the convected magnetic field line at the frozen-in velocity $E \times B/B^2$, without possible cross-field diffusion. These results only hold in cases where the magnetic field direction is not in the same direction as the cyclic coordinate. In our computations, particles can freely diffuse since the magnetic field has only a Z component. To investigate particle diffusion in the perpendicular direction, we can focus on either X or Y direction. We present in this paper results obtained in the Y direction, but we will discuss (when needed) the differences between these two directions.

The diffusion coefficient can be calculated using the TGK formalism, from the names of its founders.[22–24] The perpendicular component of this tensor is defined as

$$K_\perp = \int_0^\infty R_{YY}(t)dt, \tag{8}$$

where $R_{YY}(t)$ is the canonical average of the particle velocity correlation tensor, defined as

$$R_{YY}(t) = \langle v_Y(0) v_Y(t) \rangle, \tag{9}$$

$v_Y(t)$ being the Y component of the particle velocity at time t, and the bracket associated to the canonical average over all particles. The numerical calculations of these coefficients are straightforward, but raise some difficulties. First, $R_{YY}(t)$ has to go asymptotically to zero for the integral (8) to converge. Second, (9) has to be independent of the time origin $t=0$. Third, X and Y direction should be equivalent. Depending on the case studied, these hypothesis might not be fulfilled and prevent to infer (8) from (9). Fig. 1 depicts (solid line) the time evolution of $R_{YY}(t)$ for a 2B run with $V_B = 1.0$. It also depicts (solid thick line) the root mean square exponential interpolation of the local maximums and minimums (on time scale ω_C^{-1}). The results can be compared with the ansatz formulation of the problem[8]

$$R_{YY}(t) = \frac{v^2}{3} \cos(\omega_C t) \exp(-\nu_\perp t), \tag{10}$$

$\nu_\perp^{-1}$ being a decorrelation time in the perpendicular direction and v the particle velocity. In this model, it is clear that the stochastic behavior of the particles is contained in the single parameter $\nu_\perp$. The oscillation at the gyrofrequency is clearly observed. The initial amplitude of the oscillation is 0.4, which is the Y component of the perpendicular thermal velocity of a plasma with $\beta_p = 0.8$ (the β_e value has no consequence on these results). The amplitude of these oscillations is exponentially decreasing with time in agreement with Eq. (10). Self-consistent calculations in this case agree with this simple model. Unfortunately for 2B runs with $V_B \gtrsim 1.4$ and most KH runs, stationarity and gyrotropy hypotheses were not verified, and the diffusive transport can then not be reduced to the single $\nu_\perp$ value.

TGK formalism is nice for analytical calculations because it involves the particles velocity, resulting from a single integral from Hamilton's equations. But from a numerical point of view, it has the disadvantage of involving $R_{YY}(t)$ that mathematically has a very high total variation, as illustrated in Fig. 1. Its numerical integration is hence sensitive to numerical rounding errors. The diffusion coefficient can also be calculated from the Fokker-Planck equation,[25] that we will call for convenience the FP formalism

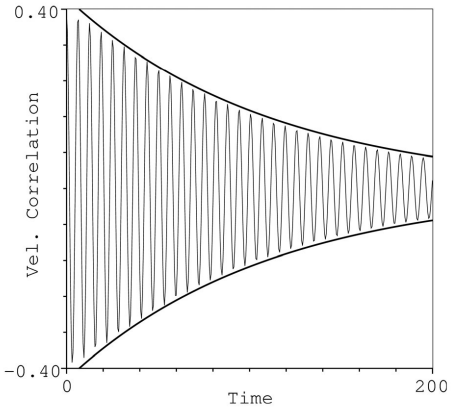

FIG. 1. Time evolution of the velocity correlation tensor $R_{YY}(t)$ for the 2B run. The envelope is an exponential fit of the local maximums.

$$\kappa_\perp = \frac{\langle \Delta Y^2 \rangle}{\langle 2\Delta t \rangle}, \tag{11}$$

where ΔY is the particle displacement in the Y direction during time Δt. We use a small $\kappa_\perp$ in Eq. (11) associated to FP formalism to make a distinction with the $K_\perp$ given by Eq. (8) associated to TGK formalism. FP formalism is more gentle for a numerical evaluation because it involves a root mean square linear interpolation of $\langle \Delta Y^2 \rangle$ (assuming it is linear to $\langle \Delta t \rangle$).

In a previous study,[9] three methods have been proposed for the calculation of $\kappa_\perp$, each leading to the same value. In this paper, computations will be done using the FP formalism (the same as experience 3 described in the Appendix of Ref. 9) as it is the only one that can be used in self-consistent simulations. For either formalism, one notes that calculations depend on the path in the position space (whole particle trajectory), which must be the case for irreversible process.

The perpendicular diffusion coefficient has already been calculated in self-consistent computation.[11,12] But with the FP formalism, ΔY can not be simply the difference of Y-position during Δt, because the particle displacement includes both bulk motion associated to large scale fluid motion and erratic motion associated to the kinetic diffusion. Hence, to properly calculate ΔY, one has to remove the contribution from the fluid velocity. To say it differently, ΔY is the difference in the particle position during Δt calculated in the local frame where the fluid is at rest. Of course, the definition of this frame is non-local and non-stationary.

Calling $V^\star(t)$ the fluid velocity at position $Y(t)$ at time t, the particle displacement free of large scale fluid motion ΔY during time $\Delta t = t$ is

$$\Delta Y = Y(t) - Y^\star(t) - Y(0), \tag{12}$$

where $Y^\star(t)$ is the position of the fluid particle at time t that was located at $Y(0)$ at $t=0$. It is obtained from the time integration of $d_t Y^\star(t) = V^\star(t)$ with the initial condition $Y^\star(0) = Y(0)$.

V. PARTICLE DIFFUSION COEFFICIENT $\kappa_\perp$

We compute the probability distribution function (PDF) of the displacement ΔY prior to calculate $\kappa_\perp$ with the caution detailed in Sec. IV. Fig. 2 exhibits the PDF obtained in the KH run with $V_B = 1.0$ measured at $t = 200$. The solid line indicates a Gaussian fit. This PDF is clearly Gaussian, even if the magnetic fluctuation δB has a non-Gaussian PDF (discussed in Sec. VI). This suggests that particles stagger across the magnetic field lines following a random walk process and rules out the possibility of any levy-flight motion.[26] To make this point stronger, one can also compute the PDF of ΔY in both 2B and KH runs (not shown in this paper). They are clearly Gaussian, whatever the value of V_B (between 0.0 and 4.0) and whatever the time of observation.

From the computation of $\Delta Y(t)$ for all particles at each time step, we compute the canonical average over all the

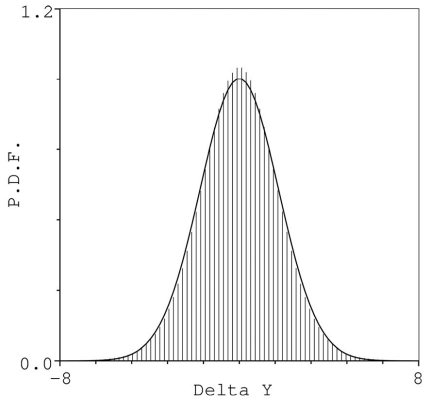

FIG. 2. Probability density function of ΔY in the KH run. The solid line is a Gaussian fit.

particles $\langle \Delta Y^2 \rangle$. Its time evolution is depicted in Fig. 3 for the 2B run with $V_B = 2.0$. The solid thick line is the root mean square linear interpolation. It is clear from this plot that $\langle \Delta Y^2 \rangle$ increases linearly in time, and that the stochastic motion of particles out of the fluid motion is a diffusion process. There is no superdiffusion as inferred by Fig. 2 (a superdiffusion process would be associated to a non-Gaussian PDF of ΔY). Note that in Fig. 3, we chose initially $B_0 = 0.4$ to emphasize the oscillation of $\langle \Delta Y^2 \rangle$ on the scale of the gyrofrequency. The amplitude of oscillation of $\langle \Delta Y^2 \rangle$ at the beginning is roughly the square of the thermal Larmor radius. Because of the magnetic fluctuations, the resulting phase mixing soften the oscillations of $\langle \Delta Y^2 \rangle$ with time. Different runs were performed varying the average number of macro-particles per cell. The results always exhibited a linear relation of $\langle \Delta Y^2 \rangle$ with time. Increasing the number of macro-particles per cell just results in lowering the level of electromagnetic fluctuations, and hence lowering the $\kappa_\perp$ value. Fig. 4 depicts the time evolution of $\langle \Delta Y^2 \rangle$ for a KH run with $V_B = 1.0$. As a general result, the linearity of $\langle \Delta Y^2 \rangle$ with time stands for both 2B and KH runs, whatever the value of V_B. Nevertheless, it has to be noted that, for KH

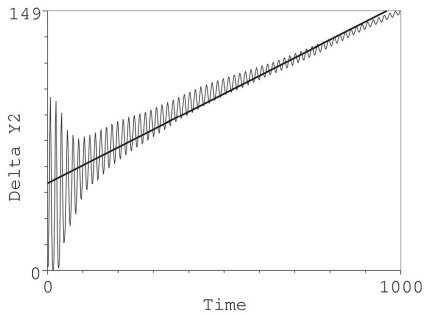

FIG. 3. Time evolution of $\langle \Delta Y^2 \rangle$ associated to the particle motion in the 2B run. Solid thick line is a linear fit.

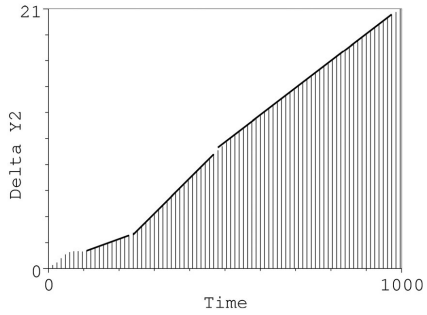

FIG. 4. Time evolution of $\langle \Delta Y^2 \rangle$ associated to the particle motion in the KH run. Solid thick lines are local linear fits.

runs, the general shape would be best fitted by several straight line (about 2 or 3) with slightly different slopes as indicated in Fig. 4. This is a consequence of the non-stationarity of the KH instability for which the 2 or 3 phases of vortex pairing (depending on the initial V_B value) results in such subtle change of the slope of $\langle \Delta Y^2 \rangle$. In either 2B or KH runs, the asymptotic regime sets in quickly. Previous studies[20] exhibited a transient behaviour at the beginning of the computation, not observed in these cases. As it will be detailed in Sec. VI, the nature of the magnetic fluctuations is different in 2B and KH runs, but it is worth noticing that they lead in both cases to a quick asymptotic regime. One can thus suppose the self-consistent electric field (neglected in previous studies) is important to explain the absence of transient stages.

From these numerical observations, it is clear that under the limitations coming from the geometry and the code, the particle displacement free of large scale fluid motion is of diffusive type. This clearly challenges previous results[12] and is a consequence of the different method adopted. We suggest that in the study of Ref. 12, the diffusion coefficients are over estimated because of the large scale fluid motion associated to KH instability. To emphasize this point, we performed computations with the same initial parameters, and get similar results (not shown). Furthermore, we performed runs with a simple drifting Maxwellian plasma (at velocity V_B), and calculated the diffusion coefficient without removing the large scale fluid motion. We obtained the same apparent superdiffusive behavior. In such a case, one should expect a behavior similar to the non-drifting case, as the β value and magnetic fluctuation level $\langle \delta B^2 \rangle$ are very comparable. This simple change of reference frame emphasizes the fact that one should calculate the diffusion coefficient in the frame of the "large scale" fluid motion.

The calculations presented in this paper results from an ensemble average on all particles. We did not studied the relative contribution of each particles velocity range to the $\kappa_\perp$ value depending on the velocity magnitude or the pitch angle because the self-consistent electric field is associated to a gain or loss of energy for each particles. This drastically complicates the picture and will be devoted to a forthcoming paper.

VI. NATURE OF THE ELECTROMAGNETIC FLUCTUATIONS

In this work, electromagnetic fields are calculated self-consistently. This has important consequences: 1—there is an electric field associated to the magnetic field (hence resulting in a fluid motion), 2—the kinetic energy of the particles can change, because of the work of the electric force, and 3—we have no control on the energy cascade, meaning that the slope of the power spectrum cannot be imposed.

A specific power law spectrum can be imposed at $t=0$, but there is no easy way to control the time evolution of the slope of the spectrum, as well as the injection, inertial and dissipation scales. The method we adopt is to use unsteady configurations as initial conditions that will lead to the growth of the electromagnetic fluctuations level.

With the initial set-up of 2B runs, parallel and perpendicular temperature are equal at $t=0$ for each beam. The initial bulk energy in $+X$ and $-X$ direction is rapidly converted in perpendicular temperature, as well as magnetic energy, because the particles initially phase-bunched, are rapidly spreading toward a uniform distribution of their gyrophases. This results in the enhancement of the perpendicular temperature as well as the level of magnetic fluctuations $\langle \delta B^2 \rangle$ (we use brackets for ensemble average, on all grid points). The same holds for KH runs. The initial bulk energy is converted (as the instability develops) in perpendicular thermal energy, and magnetic energy associated to the newly created electromagnetic fluctuations. The larger V_B, the larger the perpendicular temperature and magnetic fluctuation level. Nevertheless, a close look at the structure of the fields and particles show that the two initial set-up behave differently.

Using a 3D Fourier transform, Fig. 5 depicts the Z component of the magnetic field, depending on k_X and ω, at $k_Y=0$ for a 2B run. The darker the grey level, the higher the associated wave energy. We also traced the position of the Ion-Bernstein modes obtained in the same conditions by the WHAMP code.[27] The fluctuations generated in the 2B runs are seen to be essentially the first Ion-Bernstein modes, whatever the V_B value. The recovery of linear modes is essentially different from recent results of kinetic driven turbulence,[28] and is a consequence of the different nature of the driver of these electromagnetic fluctuations. These are actually the only modes provided by WHAMP in this configuration. The same question holds for KH runs, but has already been answered in numerous papers. The surface wave is of Alfvenic type. The time evolution of the instability is associated to the widening of the spectra and the feeding of smaller wave number from larger ones, until vortex pairing, destruction of the eddies, and recreations of new ones, eventually at smaller wave number (inverse cascade).

The second important difference between 2B runs and KH runs concerns their stationarity. For KH runs, the level of magnetic fluctuation is non-stationary, especially at the beginning of the simulation, when vortex pairing is effective. Later in the simulation, the shear velocity is lowered by perpendicular heating, and is thus less efficient to create new vortices. It is important to note that in Fig. 4, the time evolution of $\langle \Delta Y^2 \rangle$ is somewhat stationary, meaning that even if KH instability is non-stationary, the diffusion coefficient is almost time independent. The 2B runs behave differently: whatever the value of V_B, $\langle \delta B^2 \rangle$ reaches its asymptotic value in few cyclotron turns. Considering the time scale of the irreversible particle transport, the 2B runs can thus be considered as stationary.

The spectrum of the magnetic field also helps understanding the physics of these instabilities. Fig. 6 depicts in Log-Log the k_X spectrum of the Z component of the magnetic field, averaged in the Y direction. For a 2B run (dashed line) with $V_B=1.0$ and at $t=800$, the spectrum is flat (white noise) over about two decades, and then decreases at large k_X values. Some other runs with larger boxes indicate that the spectrum is always flat at small k_X values, until $k_X \sim 4$, where it starts decreasing. During the first cyclotron turns, because of the agyrotropy of the particle distribution function, fluctuations are created at all scales in the same proportion (there are no clear scale of injection). This prevents any cascade from large to small scales. As a consequence, the spectrum stays flat. At small wave-number ($k_X \sim 4$), there is some dissipation. The solid thick line indicates the position $k_X \rho_L = 2\pi$

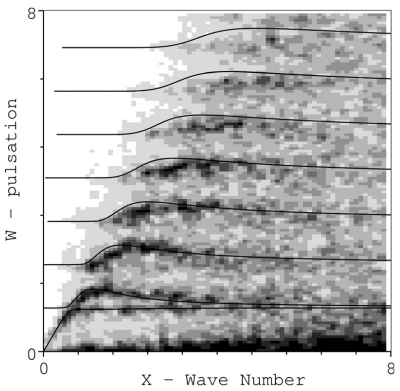

FIG. 5. Fourier transform of B_Z depending on k_X and ω, at $k_Y=0$. Solid lines are the Bernstein modes calculated by WHAMP.

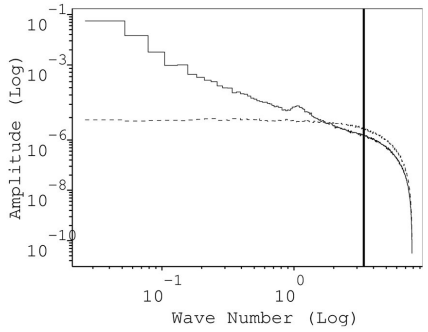

FIG. 6. k_X spectrum of B_Z, averaged in the Y direction for the 2B run (dotted line) and KH run (solid line). The solid thick line is located at $k_X \rho_L = 2\pi$.

where ρ_L is the thermal Larmor radius. It was recently shown[29] that at $k\rho_L \sim 2$, satellites data show a steepening of the slope of the power spectral density observed in the solar wind. We did not investigate this point in detail but we conjecture the process is similar. We rule out numerical reasons (associated to the grid size or the numerical resistivity) because the associated wave number values are much higher. Solid line in Fig. 6 depicts the results for KH runs (with $V_B = 1.0$ and at $t = 800$). The spectrum exhibits a clear slope, probably indicating a cascade from large scales (fed from the initial shear velocity and the large scale vortices) to small scales. There is also a dissipation range following the end of the inertial range, also observed at $k_X \sim 4$. In these two cases, the thermal Larmor radius values are very close.

The PDF of the electric or magnetic field components are also an important characterization of the nature of the electromagnetic fluctuations. For the 2B runs, whatever the V_B value and the time of observation, it always exhibit a clear Gaussian shape for both electric and magnetic components. The standard deviation of the magnetic component is equal to $\langle \delta B^2 \rangle^{1/2}$, and is thus the only parameter needed to characterize the level of magnetic fluctuation. The one associated to the KH runs are clearly non-Gaussian. Furthermore, because of the vortex pairing, those patterns are neither uniform nor stationary. This is expected to have important consequences on the diffusion process that will be discussed in the coming sections. The nature of the fluctuations in 2B and KH runs are also noticeably different. For 2B runs, fluctuations are stationary, mainly wide band white noise, and with Gaussian fluctuations, while for KH runs, they are non-stationary, with a decreasing spectrum and non-Gaussian fluctuations. As it will be further shown in Sec. VII, all these important differences in the fluctuations have few consequences on diffusion.

VII. DISCUSSION AND CONCLUSION

We have presented new results about the efficiency of particle diffusion in self-consistent electromagnetic fluctuations in collisionless magnetized plasma. Using hybrid simulations, we emphasized that, in such computations, the large scale motion of the fluid has to be considered to get a diffusion coefficient free of any bulk motion of the plasma. Our results exhibit diffusive process whatever the nature of the instability, its stationarity, the shape of its spectrum, the level of electromagnetic fluctuations and their associated PDF, in contradiction with previous results,[12] who exhibited a super-diffusive behavior. These differences are linked to the method and the definition of diffusion which has to be frame independent.

Finally, comparison can be done between the $\kappa_\perp$ values obtained in 2B and KH runs. Fig. 7 exhibit the $\kappa_\perp$ value depending on the value of $\langle \delta B^2 \rangle$ on the X-axis and the value of the perpendicular temperature $T_\perp$ on the Y-axis. The radius of the circles are proportional to the value of $\kappa_\perp$, white circles are associated to 2B runs and black circles are associated to KH runs. It is clear on this plot that KH instability does not seem to favor high values of $\kappa_\perp$ for comparable $\langle \delta B^2 \rangle$ and $T_\perp$ values in 2B runs. For the 4 upper circles (both black and white), they are associated to somewhat the same

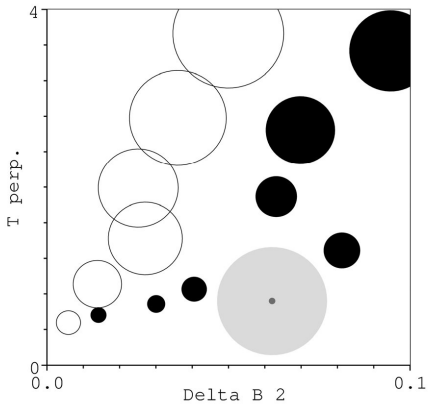

FIG. 7. $\kappa_\perp$ value depending on σ_B^2 on X-axis and $T_\perp$ on Y-axis. The radius of the circles are proportional to the values of $\kappa_\perp$. White circles are associated to 2B runs and black circles to KH runs. The light grey circle is associated to $\kappa_\perp = 10^9 \mathrm{m}^2 \cdot \mathrm{s}^{-1}$ and the dark grey circle is associated to $\kappa_\perp = 5 \times 10^7 \mathrm{m}^2 \cdot \mathrm{s}^{-1}$. They are located at an arbitrary position.

value of $T_\perp$, a larger value of $\langle \delta B^2 \rangle$ for KH runs than for 2B runs, and a smaller value of $\kappa_\perp$.

In the 2B runs, the initial bulk velocity in the $\pm X$ directions is very quickly transformed in thermal velocity, resulting in a situation for which the fluid velocity field appears to have a Gaussian PDF with a null mean value. In this case, as there is no artificial ballistic contribution of the mean velocity to the $\kappa_\perp$ value, the $Y^\star$ term in Eq. (12) could be omitted, to provide a value resulting from both magnetic and fluid velocity fluctuations. Hence, we also computed the time evolution of $\langle \Delta Y^2 \rangle = \langle (Y(t) - Y(0))^2 \rangle$ for the 2B runs. We got in all cases a linear evolution (associated to a diffusive behavior) with a $\kappa_\perp$ generally larger of a few tenth percents. This result suggests that the contribution of the velocity fluctuation to the $\kappa_\perp$ value is non negligible but remains small. This value should depend on the velocity fluctuations level $\langle \delta V^2 \rangle$, and a deeper study is needed to find the way to control (independently ?) the level of $\langle \delta B^2 \rangle$ and $\langle \delta V^2 \rangle$. By doing so in the KH runs, we got a $\langle \Delta Y^2 \rangle$ value evolving at a power of time larger than one. Part of this value is resulting from the fluid velocity fluctuations, but part (of ballistic type) is also the non-physical contribution of the "mean" fluid velocity.

The terms in the Ohm's law and the expression of the fluid velocity $V^\star(t)$ are also questionable for their consequences on the $\kappa_\perp$ value. In Eq. (12) the associated $V^\star(t)$ refers to the fluid velocity. By reference to an ideal Ohm's law, $V^\star(t)$ could also be the $E \times B$ drift. We calculated in both 2B and KH runs the $\kappa_\perp$ value considering $V^\star = E \times B$ (not shown) and also found a linear evolution with a $\kappa_\perp$ value smaller of a few tenth percents, depending on the V_B value. Non-ideal terms in Eq. (7) are indeed also associated to fluctuations (of the magnetic field and the density) and hence contribute to the diffusion process at small scales. This explains why the $\kappa_\perp$ value is smaller when they are neglected.

One of the important motivations for such diffusion studies is that KH instability is supposed to play a peculiar role in

mass loading from the solar wind into the magnetosphere.[30] This study clearly questions the importance of KH instability to fill the low-latitude-boundary-layer (the region adjacent to the inner side of the magnetopause, filled with plasma from solar wind origin) under diffusion processes. Diffusive transport results from the existence of electromagnetic fluctuations, and KH instability is just one way to make such fluctuations. These results suggest to revisit an old standing problem: what is the needed $\kappa_\perp$ value to fill the Low Latitude Boundary Layer (LLBL)? Using a simplified fluid approach[31,32] it was shown that a viscous-like interaction of the solar wind with the magnetosphere would need a kinematic viscosity of 10^9 m^2 s^{-1} to account for the observed momentum transfer. It was then argued that to fill the LLBL in the frame of a diffusive model, the associated mass flux needs the same value for the diffusion coefficient.[33]

We propose an alternative approach to the calculation of this coefficient using the Brownian motion of the particles and the associated diffusion coefficient. Consider the two-dimensional problem for simplicity, and call n_1 and n_2 the density in the LLBL and in the magnetosheath (the region filled with plasma of solar wind origin downstream of the bow shock). L is the length on which the diffusive transport is efficient (somewhat the length of the magnetosphere) and Δ the thickness of the LLBL. This is schematically depicted in Fig. 8. The number of particles in the LLBL is $N_1 = n_1 L\Delta$. The number of particles diffusing in the magnetosheath is $N_2 = n_2 L(1/2)\langle \Delta Y^2\rangle^{1/2} = n_2 L D^{1/2}\langle \Delta t\rangle^{1/2}$. By equating N_1 and N_2, and assuming $\Delta t = L/V_{sw}$ (V_{sw} being the speed of the solar wind), one gets

$$\kappa_\perp = \left(\frac{n_1}{n_2}\right)^2 \left(\frac{\Delta}{L}\right) \Delta V_{sw}. \tag{13}$$

With realistic experimental values, one gets $\kappa_\perp \sim 10^7 \mathrm{m}^2 \cdot \mathrm{s}^{-1}$.This threshold is two orders of magnitude smaller than the one proposed formerly.[33] It is not our goal to propose an alternative model, but just to suggest that the historical threshold for the diffusion coefficient to fill the LLBL should not be considered that sharply, and would need a more rigorous evaluation. In a realistic case, the density gradient should be considered[19] as well as the associated drift instability. Furthermore, finite Larmor radius effects associated to the thin current sheet located at the magnetopause acts as a filter on the particles that cross the magnetopause.[34] In Fig. 7, the light grey circle has a radius associated to $\kappa_\perp = 10^9 \mathrm{m}^2 \cdot \mathrm{s}^{-1}$, and the dark grey circle has a radius associated to $\kappa_\perp = 5 \times 10^7 \mathrm{m}^2 \cdot \mathrm{s}^{-1}$. The grey circles are depicted for a quantitative comparison with the numerical values computed for 2B and KH runs, and located at an arbitrary position. Our numerical results suggest that even if we do not observe any superdiffusion, diffusion process could play a significant role in filling the LLBL.

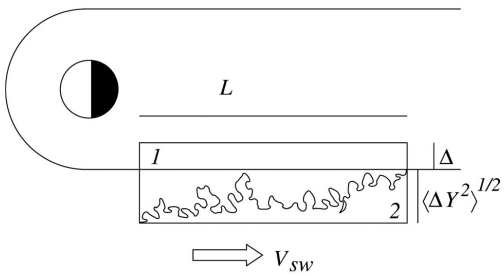

FIG. 8. Schematic representation for the diffusion process to fill the LLBL with solar wind's particles.

The four main conclusions that can be drawn from this work are: (1) a new method is proposed in the calculation of a perpendicular diffusion coefficient in self-consistent computation, to get a value free of any large scale fluid motion, (2) in the two-dimensional case with a magnetic field in the direction of invariance, irreversible transport is always diffusive, whatever the nature of the electromagnetic fluctuations, (3) the KH instability is not playing a specific role in mass transfer associated to diffusion other than generating magnetic fluctuations, and (4) the perpendicular diffusion coefficient computed could be large enough to fill the low-latitude-boundary-layer. These conclusions are drawn for the diffusion process, and does not rule out the possible role of KH instability to trigger magnetic reconnection and associated mass transfer.[35,36] The next step in this study is to identify the respective role of electric and magnetic fluctuation, as well as their coupling. A robust methodology to identify and subtract the mean fluid velocity would also allow to investigate the $\kappa_\perp$ value resulting from the magnetic and fluid velocity fluctuations separately. This problem should also be studied using a three-dimensional code, because the nature of the electromagnetic fluctuations can be different. The thin current sheet and the sharp density gradient at the magnetopause will have also to be considered, as previous studies[19] suggested an associated Lévy walk.

ACKNOWLEDGMENTS

The authors thank Amitava Bhattacharjee for fruitful discussions. This research is supported by ANR MAGNET.

[1]T. H. Stix, *Waves in Plasmas* (Springer-Verlag, Berlin, 1992).
[2]J. Minnie, W. H. Matthaeus, J. W. Bieber, D. Ruffolo, and R. A. Burger, J. Geophys. Res. **114**, 1102, doi:10.1029/2008JA013349 (2009).
[3]F. Casse, M. Lemoine, and G. Pelletier, Phys. Rev. D **65**, 023002 (2002).
[4]W. Horton, Rev. Mod. Phys. **71**, 735 (1999).
[5]R. A. Treumann, J. Labelle, and R. Pottelette, J. Geophys. Res. **96**, 16009, doi:10.1029/91JA01671 (1991).
[6]J. R. Jokipii, Astrophys. J. **146**, 480 (1966).
[7]A. B. Rechester and M. N. Rosenbluth, Phys. Rev. Lett. **40**, 38 (1978).
[8]J. W. Bieber and W. H. Matthaeus, Astrophys. J. **485**, 655 (1997).
[9]J. Giacalone and J. R. Jokipii, Astrophys. J. **520**, 204 (1999).
[10]W. H. Matthaeus, G. Qin, J. W. Bieber, and G. P. Zank, Astrophys. J. **590**, L53 (2003).
[11]D. Winske and N. Omidi, J. Geophys. Res. **100**, 11923, doi:10.1029/94JA02730 (1995).
[12]M. M. Cowee, D. Winske, and S. P. Gary, J. Geophys. Res. **114**, 10209, doi:10.1029/2009JA014222 (2009).
[13]C. K. Birdsall and A. B. Langdon, in *Plasma Physics via Computer Simulation*, edited by E. W. Laing (Institute of Physics Publishing, Bristol and Philadelphia, 1991).
[14]D. S. Harned, J. Comp. Phys. **47**, 452 (1982).
[15]T. Chust and G. Belmont, Phys. Plasmas **13**, 012506 (2006).

[16]J. de Keyser, M. W. Dunlop, C. J. Owen, B. U. Ö. Sonnerup, S. E. Haaland, A. Vaivads, G. Paschmann, R. Lundin, and L. Rezeau, Space Sci. Rev. **118**, 231 (2005).
[17]C. Salem, A. Mangeney, S. D. Bale, and P. Veltri, Astrophys. J. **702**, 537 (2009).
[18]P. Pommois, P. Veltri, and G. Zimbardo, Phys. Rev. E **63**, 066405 (2001).
[19]A. Greco, A. L. Taktakishvili, G. Zimbardo, P. Veltri, G. Cimino, L. M. Zelenyi, and R. E. Lopez, J. Geophys. Res. **108**, 1395, doi: 10.1029/2003JA010087 (2003).
[20]G. Qin, W. H. Matthaeus, and J. W. Bieber, Geophys. Res. Lett. **29**, 1048, doi: 10.1029/2001GL014035 (2002).
[21]J. R. Jokipii, J. Kota, and J. Giacalone, Geophys. Res. Lett. **20**, 1759, doi:10.1029/93GL01973 (1993).
[22]G. I. Taylor, Proc. London Math. Soc. **20**, 196 (1922).
[23]H. S. Green, J. Math. Phys. **2**, 344 (1961).
[24]R. Kubo, J. Phys. Soc. Jpn. **12**, 570 (1957).
[25]S. Chandrasekhar, Rev. Mod. Phys. **15**, 1 (1943).
[26]R. A. Treumann, Geophys. Res. Lett. **24**, 1727, doi: 10.1029/97GL01760 (1997).
[27]K. Rönnmark, "Waves in homogeneous, anisotropic multicomponent plasmas (WHAMP)," Tech. Rep., Kiruna Geophysical Institute Report No. 179, 1982.
[28]T. N. Parashar, S. Servidio, B. Breech, M. A. Shay, and W. H. Matthaeus, Phys. Plasmas **17**, 102304 (2010).
[29]F. Sahraoui, M. L. Goldstein, G. Belmont, P. Canu, and L. Rezeau, Phys. Rev. Lett. **105**, 131101 (2010).
[30]C. Foullon, C. J. Farrugia, A. N. Fazakerley, C. J. Owen, F. T. Gratton, and R. B. Torbert, J. Geophys. Res. **113**, 11203, doi:10.1029/2008JA013175 (2008).
[31]W. I. Axford, Planet. Space Sci. **12**, 45 (1964).
[32]T. Tsuda, J. Geophys. Res. **72**, 6013, doi:10.1029/JZ072i023p06013 (1967).
[33]B. U. Ö. Sonnerup, J. Geophys. Res. **85**, 2017, doi:10.1029/JA085iA05p02017 (1980).
[34]R. Smets, G. Belmont, D. Delcourt, and L. Rezeau, Ann. Geophys. **25**, 271 (2007).
[35]M. Faganello, F. Califano, and F. Pegoraro, Phys. Rev. Lett. **100**, 015001 (2008).
[36]M. Faganello, F. Califano, and F. Pegoraro, Phys. Rev. Lett. **101**, 105001 (2008).

— E —

Electric and magnetic contributions to spatial diffusion in collisionless plasmas

R. Smets, G. Belmont, N. Aunai,
Laboratoire de Physique des Plasmas,

Physics of Plasmas
Vol. 19, pages 102310 - 102309, 2012

PHYSICS OF PLASMAS **19**, 102309 (2012)

Electric and magnetic contributions to spatial diffusion in collisionless plasmas

R. Smets,[1,a)] G. Belmont,[1] and N. Aunai[2]
[1]*Laboratoire de Physique des Plasmas, UPMC-Ecole polytechnique-CNRS, France*
[2]*Space Weather Laboratory, Code 674, NASA Goddard Space Flight Center, Greenbelt, Maryland 20771, USA*

(Received 25 July 2012; accepted 3 October 2012; published online 25 October 2012)

We investigate the role played by the different self-consistent fluctuations for particle diffusion in a magnetized plasma. We focus especially on the contribution of the electric fluctuations and how it combines with the (already investigated) magnetic fluctuations and with the velocity fluctuations. For that issue, we compute with a hybrid code the value of the diffusion coefficient perpendicular to the mean magnetic field and its dependence on the particle velocity. This study is restricted to small to intermediate level of electromagnetic fluctuations and focuses on particle velocities on the order of few times the Alfvén speed. We briefly discuss the consequences for cosmic ray modulation and for the penetration of thermal solar wind particles in the Earth magnetosphere. © *2012 American Institute of Physics*. [http://dx.doi.org/10.1063/1.4762845]

I. INTRODUCTION

In a static and uniform magnetized plasma, the motion of a charged particle is completely determined by its gyropulsation ω_C and its Larmor radius ρ_L. When spatial and/or temporal fluctuations exist, the particle dynamics is modified, possibly leading to spatial diffusion. Noting ΔY the displacement in a given direction Y perpendicular to the local mean magnetic field during a time Δt and $\langle\cdots\rangle$ the average on all the particles, the quantity $\langle\Delta Y^2\rangle$ allows a quantization of how efficiently a population is spreading in space (in the Y direction). More specifically, if the ratio $\langle\Delta Y^2\rangle/2\Delta t$ has an asymptotic limit, it is called the diffusion coefficient in real space and will be noted $\kappa_\perp$. Similar ratios can be calculated in velocity space to evaluate diffusion in energy or pitch angle.

Particle diffusion in collisionless plasmas is important for cosmic ray modulation in interstellar media,[1] particle transport in tokamaks,[2] or filling up the magnetosphere with solar wind particles.[3] The first major analytical treatment of this problem by Jokipii[4] put forward the two possible contributions: particles can spread by following braided magnetic field lines or by departing from the magnetic field lines to which they were initially attached. The first mechanism can be studied focusing on the topological properties of the magnetic field lines.[5] When this is the only contribution, the particles follow the magnetic field lines like "beads on a string." This has been recently addressed[6] where the braided nature of the magnetic field lines is captured by the calculation of the magnetic field line diffusion coefficient $D_\perp$.[6] The perpendicular diffusion coefficient $\kappa_\perp$ linearly depends on $D_\perp$. This is the so-called field line random walk (FLRW) model. It should be emphasized that this mechanism cannot be responsible for the filling up of solar wind plasma on magnetospheric field lines without magnetic reconnection. The second mechanism needs a careful investigation of particle dynamics. It has been done up to now by using test-particles.

We focus on situations where a mean magnetic field B_0 is larger than the fluctuations and set its direction as Z in this paper. In the runs presented, the X and Y directions are equivalent and each can be used equally to calculate $\kappa_\perp$. We use here the Y direction. Different analytical models have been developed[7–9] involving different numbers of free parameters and successfully confronted with test-particle simulations. But up to now, few studies have been achieved with a self-consistent approach to study this problem.[3,10] Yet, when the plasma β (ratio between kinetic and magnetic pressure) is not small, it can be expected that the self-consistent nature of the electromagnetic fluctuations has to be considered since it can provide strong feedback of the particle dynamics on the electromagnetic fields. In addition, the electric component of the fluctuations might have important consequences for the diffusion process.

Using electric and magnetic data of the CLUSTER mission in the solar wind at ~1 AU, a recent study[11] has for instance confirmed the existence of electric field fluctuations with a $k^{-5/3}$ spectrum, agreeing the associated spectrum of the magnetic field fluctuations, their ratio being on the order of the Alfvén wave velocity. The associated diffusion in velocity space, which can be calculated in the frame of the quasi-linear theory, is suggested[12] to account for fluid-like behavior of the solar wind despite the near absence of collisions. Otherwise, conservation of adiabatic moments should build strong anisotropies.[13]

In this paper, we first aim to put forward the respective contributions of electric and magnetic fluctuations as well as their coupled effects, for the perpendicular diffusion coefficient $\kappa_\perp$. A second goal is to investigate the role of the fluid velocity fluctuations and investigate their relationship with the preceding. For each of these different contributions, we will investigate how the corresponding $\kappa_\perp$ values depend on the perpendicular particle velocity since it is of major theoretical and practical importance to know which particles in the distribution function are preferentially diffused. For all these issues, we use a self-consistent particle code to properly

a)Electronic mail: roch.smets@lpp.polytechnique.fr.

describe the time-evolving electromagnetic fluctuations and the associated proton motion of a hydrogen plasma.

In Sec. II, we give details on the simulation code and the associated assumptions. In Sec. III, we describe the way to compute the diffusion coefficient using either macro-particles or passive tracers, and why we do so. In Sec. IV, we study the respective roles of the electric and magnetic fluctuations for the particle diffusion as well as the coupling of these effects. In Sec. V, we address the role of the velocity fluctuations and the way they should be considered to compute a diffusion coefficient free of large scale fluid motion. In Sec. VI, we focus on the particle dynamics to suggest a qualitative explanation for the different features observed. These results are discussed in the conclusive Sec. VII.

II. SIMULATION MODEL AND INITIAL SETUP

The calculations are carried out using a hybrid code (protons are treated as macro-particles and electrons as a massless fluid) with two spatial dimensions X and Y and three velocity dimensions. Protons velocities and positions are solved by the time integration of

$$m d_t \mathbf{v}_p = q(\mathbf{E} + \mathbf{v}_p \times \mathbf{B}), \tag{1}$$

$$d_t \mathbf{x}_p = \mathbf{v}_p, \tag{2}$$

where $\mathbf{x}_p$ is the proton position, $\mathbf{v}_p$ is the associated velocity, $\mathbf{E}$ is the electric field, $\mathbf{B}$ is the magnetic field, q and m being the proton charge and mass, respectively. The magnetic field is calculated with the Faraday law

$$\partial_t \mathbf{B} = -\nabla \times \mathbf{E}. \tag{3}$$

Using the Darwin approximation, the Ampère's law reduces to

$$\mu_0 \mathbf{J} = \nabla \times \mathbf{B}, \tag{4}$$

where $\mathbf{J}$ is the current density. One hence needs an Ohm's law to set the electric field

$$\mathbf{E} = -\mathbf{V}_p \times \mathbf{B} + \frac{1}{qN}(\mathbf{J} \times \mathbf{B} - \nabla P_e), \tag{5}$$

where N is the electron density (equal to the proton density), $\mathbf{V}_p$ is the proton fluid velocity, and P_e is the scalar electron pressure. We choose an isothermal closure equation for the electron fluid, which is a priori justified when studying processes with phase velocity smaller than electron thermal velocity:[14] $P_e = N k_B T_e$ with a constant value of the electron temperature T_e, k_B being the Boltzmann's constant. N and $\mathbf{V}_p$ are calculated from the summation

$$N(\mathbf{x}) = \Sigma_p S(\mathbf{x} - \mathbf{x}_p), \tag{6}$$

$$\mathbf{V}_p(\mathbf{x}) = \Sigma_p \mathbf{v}_p S(\mathbf{x} - \mathbf{x}_p)/N(\mathbf{x}), \tag{7}$$

where $S(\boldsymbol{x})$ is the shape factor[15] associated with the concept of macro-particles. As usual for a particle-in-cell code, $S(\boldsymbol{x})$ is a triangle of 2 grid points width's and unitary surface.

These equations are integrated using a predictor-corrector scheme.[16] Distances are normalized to the proton inertial length (δ_p), times are normalized to the inverse of the proton gyropulsation (ω_C^{-1}), velocities are normalized to the Alfvén speed, masses are normalized to the proton mass, and density and magnetic field are normalized to their initial uniform values. The size of the simulation box is $X_M = Y_M = 300$. We use $N_X = N_Y = 300$ cells, a time step $\Delta t = 0.005$ with 2×10^5 time steps and about 200 macro-particles per cell. It has to be noted that the shape factor is not involved in Eqs. (1) and (2). The dynamics of macro-particles is identical to one of the particles in the case of a collisionless plasma. The concept of macro-particle is only needed in Eqs. (6) and (7) to infer macroscopic moments from the particles distribution.

The initial magnetic field is in the Z direction, perpendicular to the simulation plane. The runs are periodic in X and Y directions. This is an important requirement for the calculation of particles displacement that might be underestimated by artificial reflections on the boundaries of the simulation domain. For the initial setup, $\beta_p = 0.8$ and $\beta_e = 0.2$, p and e refer to protons and electrons, respectively. Such values are typically observed in the solar wind. Because of self-consistency, we need to find the proper conditions to let some electromagnetic fluctuations develop and grow. The box is initially filled with particles from two Maxwellian beams, homogeneous in the simulation domain, with opposite bulk velocities V_B and $-V_B$ in the X direction and the same temperature. This is the same initial setup as a recent study[10] (referred as paper 1 hereinafter): this initial agyrotropy leads to the development of electromagnetic fluctuations as well as an enhancement in the perpendicular temperature, but no bulk flow.

III. CALCULATION OF THE DIFFUSION COEFFICIENT

The diffusion coefficient can be calculated using the Fokker-Planck formalism

$$\kappa_\perp = \lim_{\Delta t \to \infty} \frac{\langle \Delta Y^2 \rangle}{2\Delta t} \tag{8}$$

or the Taylor-Green-Kubo formalism

$$K_\perp = \int_0^\infty \langle v_Y(t) v_Y(0) \rangle dt. \tag{9}$$

These 2 formalisms have recently been discussed[17] and provide the same result for parallel and perpendicular diffusion coefficients. Nonetheless, paper 1 outlined that Fokker-Planck formalism is better suited for numerical calculations because of its smaller sensitivity to numerical noise. We hence use this formalism in this study.

Prior to give details on the calculation of the diffusion coefficient $\kappa_\perp$, its definition has to be clearly enunciated. Fluid moments such as density, velocity, and higher moments are defined at a fluid scale l_F, meaning that they result from an average on a volume l_F^3. If some diffusion process takes place because of phenomena at scales larger than l_F, it can be classified as turbulent fluid diffusion and it can be fully described by the fluid equations without introducing any extra term. On the other hand, if some diffusion occurs because of phenomena at scales smaller than l_F, it cannot be described

by the ideal fluid theories and some non-ideal terms have to be added, involving in particular the diffusion coefficients. The way to estimate these extra-terms consists in first determining the probability distribution, i.e., the distribution function integrated over velocity space and divided by the total number of particles in the system. This distribution is indeed the organic link between the fluid term associated to dissipation and the value $\langle \Delta Y^2 \rangle$.[18] In this study, the fluid velocity is defined at a scale l_F equal the grid size. It is on the order of the proton inertial length which is close to the proton Larmor radius since $\beta \sim 1$. Hence, the diffusion coefficient $\kappa_\perp$ calculated in this paper is associated to irreversible transport due to the phenomena that are at scales smaller than the proton inertial length.

As a consequence, ΔY cannot be simply the difference $Y(t) - Y(0)$. A correction term $Y^\star$ has to be considered to get free of the fluid motion defined at a scale above the proton inertial length. As an illustration, the Kelvin-Helmholtz instability discussed in paper 1 was associated to large scale components of both electric and magnetic fields. The associated cross field drift corresponded to the large scale flows, the consequence of which cannot be considered as diffusion, neither at small scale nor at larger fluid scale since it concerns laminar flows and not random ones. This was referred as the speed-walk effect: the walk of a drunkard on a speed-walk looks less confused for a motionless observer if the speed-walk motion is not subtracted from the drunkard motion.

Such caution might be needed even in magnetostatic turbulence. If the magnetic field has spatial variations leading to gradient (or curvature) drifts, the consequences of these drifts for the $\langle \Delta Y^2 \rangle$ value should not be considered in the calculation of $\kappa_\perp$ since they are already described by the fluid equations. This will be discussed in Sec. V.

Calling $V^\star(t)$ the fluid velocity at position $Y(t)$ at time t, the particle displacement free of fluid motion ΔY during time $\Delta t = t$ is

$$\Delta Y = Y(t) - Y^\star(t) - Y(0), \tag{10}$$

where $Y^\star(t)$ is the position at time t of the fluid particle that was located at $Y(0)$ at time $t = 0$. It is obtained from the time integration of $d_t Y^\star(t) = V^\star(t)$ with the initial condition $Y^\star(0) = 0$. The probability distribution function (PDF) of ΔY has to be centered around zero by including the term $Y^\star(t)$ associated to $V^\star(t)$ in Eq. (10). Considering or not the $Y^\star$ term in Eq. (10) will allow to address the role of $\delta \mathbf{V}$.

We also want to address the respective roles of $\delta \mathbf{E}$ and $\delta \mathbf{B}$, separately or together. For this purpose, we add some passive tracers in the simulations (10^5 particles uniformly distributed in velocity for each kind detailed in Table I). Their motions are integrated using Eqs. (1) and (2) but have no contributions in Eqs. (6) and (7). These particles being not involved in the self-consistent process, one can set electric or magnetic fluctuations to zero for calculating their dynamics, and so studying their respective roles. Another advantage of the passive tracers is that their initial energies can be chosen freely. On the other hand, there is not enough of these passive tracers to calculate the fluid velocity needed in Eq. (10).

TABLE I. The first row is the type of particles, the second row is the electromagnetic fluctuations considered for their motion, the third row is the value of $V^\star(t)$ in Eq. (10), i.e., the velocity fluctuations, and the fourth row is the name of the population.

Part. type	E.M. fields	$V^\star$	Tag
Passive tracers	**B, E**	0	A
Passive tracers	**B**	0	B
Passive tracers	$\mathbf{B}_0$, **E**	0	C
Macro-particles	**B, E**	0	D
Macro-particles	**B, E**	$\mathbf{E} \times \mathbf{B}$	E
Macro-particles	**B, E**	$\mathbf{V}_p$	F

To investigate the role of the electromagnetic fluctuations and the importance of $Y^\star$ in the calculation of the perpendicular diffusion coefficient, we compute $\kappa_\perp$ with Eq. (8) and ΔY with Eq. (10) with different components of the electromagnetic fluctuations and different values of $V^\star(t)$. The different situations are detailed in Table I. The first row is the type of particles (macro-particles or passive tracers), the second row is the electromagnetic fluctuations considered for their motion, the third row is the value of $V^\star(t)$ used in Eq. (10), i.e., the velocity fluctuations and the fourth row is the name of the population. As an initial condition for all the runs of this paper, we have $V_B = \pm 2$ leading to a magnetic fluctuation level $\delta B \sim 0.11$. The results presented hereinafter are qualitatively the same for $\delta B \sim 0.21$ obtained with $V_B = \pm 5$.

As it is the case in paper 1, the PDFs of ΔY are Gaussian for all the runs of this paper, with a mean square deviation evolving linearly with time. This is thus a diffusive behavior for which a diffusion coefficient can be computed with Eq. (8). As an example, Fig. 1 is the time evolution of $\kappa_\perp$. In all the runs, an asymptotic behavior is reached in less than 400 ω_C^{-1}. To ease the comparison with observations, with a density $N = 6 \times 10^6 \mathrm{m}^{-3}$ and a magnetic field $B = 3$ nT (which are characteristic values observed in the solar wind at 1 AU), the normalized value of $\kappa_\perp$ has to be multiplied by 2.5×10^9 $\mathrm{m}^2\,\mathrm{s}^{-1}$.

IV. ELECTRIC AND MAGNETIC FLUCTUATIONS

Passive tracers can be injected in simulations without restrictions on their initial velocity as long as their motion is

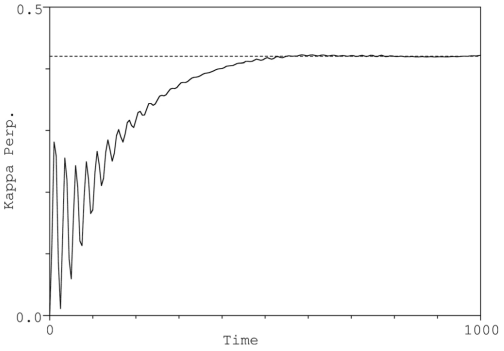

FIG. 1. Time evolution of $\kappa_\perp$. The dotted line is its asymptotic value.

correctly integrated. The time step being small enough to properly describe their gyromotion; there is no upper threshold for their initial velocity. We thus span the range from 0 to 8 Alfvén velocity for their initial velocity, which is large enough for the case of solar wind particles. As a first study case, $V^*(t)$ is set to zero in Eq. (10).

The diffusion coefficient $\kappa_\perp$ as the one depicted in Fig. 1 results from the average over all particles for the given distribution function. In addition, it is interesting to determine the dependence of the diffusion phenomenon on the particle velocity. To get this information, we computed $\kappa_\perp$ for each value of the perpendicular particle velocity $v_\perp$. Fig. 2 depicts the result for three particle populations: A (triangles, with magnetic, electric, and velocity fluctuations), B (circles, with magnetic and velocity fluctuations) and C (squares, with electric and velocity fluctuations). The mean square deviation of the time evolution of each passive tracers velocity is small enough so that a trend is clearly visible for each curve.

The curve for population B passes through the origin, its derivative at the origin is close to zero, grows with $v_\perp$, and at larger values is close to a linear relation. This emphasizes the point that $\kappa_\perp$ does not explicitly depend on a given power of $v_\perp$, even if it might be the case in some ranges of $v_\perp$. One can notice in particular that a linear model is better suited at low energy and a quadratic model at high energy. The simple analytical models where $\kappa_\perp$ is linear[4] or quadratic[7] with $v_\perp$ can therefore not adequately describe the diffusion coefficient for a large range of particle velocities. The linear models invoke a correlation length and the quadratic ones a correlation time. As shown in paper 1, these arguments cannot be general. It is worth recalling in particular that, in our numerical experiment, the magnetic fluctuation power spectrum is flat: according to the Wiener-Kintchin theorem, this corresponds to a coherence length close to zero (or to the grid size).

The results for population C are totally different. $\kappa_\perp$ reaches its maximum value for $v_\perp$ close to zero, decreases for increasing $v_\perp$ and goes to zero. The fact that the electric part of the Lorentz force does not depend on the particle velocity can qualitatively explain why $\kappa_\perp(0) \neq 0$.

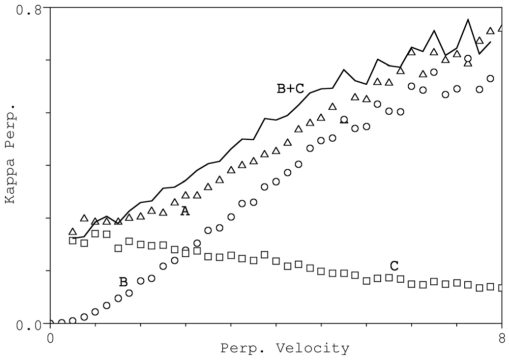

FIG. 2. Perpendicular diffusion coefficient $\kappa_\perp$ depending on the particle perpendicular velocity $v_\perp$. Triangles are associated to population A (magnetic, electric, and velocity fluctuations), circles to population B (magnetic and velocity fluctuations) and squares to population C (electric and velocity fluctuations). The solid line is obtained by summing B and C.

The result for population A is a mix between B and C: $\kappa_\perp$ is non-zero at $v_\perp = 0$ and grows with $v_\perp$. To facilitate the comparison, the sum of curves B and C is depicted in solid line in Fig. 2. The increase for curve A seems weaker than for curve B, but, apart from a slight overestimation, the addition of B and C is equal to A: electric and magnetic contributions to the diffusion coefficient are associated to very different mechanisms but act together in a very linear way. This supports the point that both contributions can be studied independently.

Because of the geometry of the simulation, B_x and B_y stay null during the simulation because there is no gradients in the Z direction in the Maxwell-Faraday equation. As a consequence, E_z calculated from the Ohm's law is also null. Hence, the growing modes have strictly perpendicular wave numbers. In such a situation, only ion Bernstein modes can develop. With an initial perturbation of the magnetic field in the XY plane, different fluctuations and associated modes could develop. But the close connection between the diffusion process and the precise nature of the fluctuations is beyond the scope of this study. We computed the 3D Fourier transform of the magnetic field and sliced it at $k_X = 0$. The resulting power spectral density displayed in Fig. 3 (without the DC components in each direction) depicts the wave dispersion relation in the $\omega - k_Y$ plane. Low energies are color coded in purple and high energies are color coded in black/red with a linear scaling. The dynamical range is small: as seen in paper 1, the k-spectrum is fairly flat. In addition with very low frequency fluctuations, the structure of the Ion Bernstein modes can be observed, even if they are less clear than in paper 1 (because the forcing is larger). This point has already been observed in a recent study[19] where an initial magnetic and velocity forcing using a 2D hybrid code exhibited Alfvén Ion Cyclotron and whistler waves with properties close to the linear ones. This conclusion is different from those drawn from a fluid simulation[20] or a hybrid one[21] where the authors used a forcing term on the magnetic field (and velocity field for the fluid study) over time and not only in the initial condition. The effect of a forcing therefore seems to strongly depend on its nature. Furthermore, the geometries of

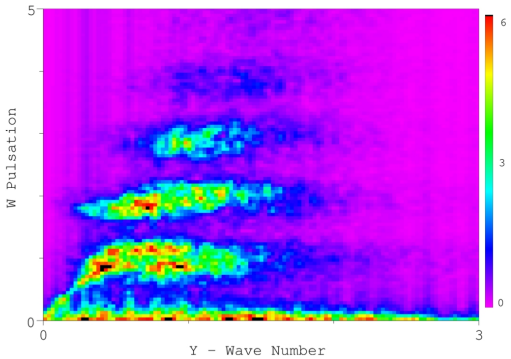

FIG. 3. Power spectral density in the "pulsation-wave number" plane for the Z component of the magnetic field. Low energies are color coded in purple and high energies are color coded in black/red with a linear scaling.

these studies are different, leading to different kinds of coupling between parallel and perpendicular directions.

To investigate the respective role of longitudinal and transverse electric field components, we computed the same Fourier transform as in Fig. 3 for each of them, separately. They look very similar except that for the transverse component of the electric field; there is no contribution at $\omega \sim 0$. It is noticeable that the electric field associated to ion Bernstein modes contains an electromagnetic component. These two points have recently been pointed out[22] as well as the absence of ion Bernstein modes close to $\omega \sim 0$. The mode observed at $\omega \sim 0$ in Fig. 3 can thus not be an ion Bernstein mode. Its identification would need some further work. This would be necessary for studies investigating the possible relationship between the diffusion coefficient and the precise nature of the modes that propagate the electromagnetic fluctuations. We also build curve C for each component. It clearly shows that only the longitudinal component of the electric field contributes to the diffusion process. Nevertheless, the level of fluctuations is $\delta E \sim 0.09$ for the longitudinal component and $\delta E \sim 0.05$ for the transverse part. This shows that the inefficiency of the transverse part of the electric field for the diffusion process does not lie in the small level of fluctuations. One can thus wonder whether this inefficiency results from the lack of energy at $\omega \sim 0$ or whether it lies in the intrinsic nature of this component. We have not yet investigated this point.

V. VELOCITY FLUCTUATIONS

The role of the velocity fluctuations for the diffusion process can be investigated by varying the term $V^\star(t)$ in Eq. (10). For this purpose, Fig. 4 depicts $\kappa_\perp$ depending on $v_\perp$ for population D (circles, with full velocity fluctuations), E (triangles, without the cross field part of the velocity fluctuations), and F (squares, without any velocity fluctuations). All these results involve both magnetic and electric fluctuations. The curve obtained for population D is very similar to the one obtained for population A.

Actually, the only difference with Fig. 2 is the velocity range that can be spanned: the passive tracers of population A can be chosen freely, while the macro-particles of population D were restricted to small perpendicular velocities, in agreement with the requirement $\beta \sim 1$. As a consequence, the points depicted in Fig. 4 cannot be obtained for perpendicular velocities up to 8 Alfvén velocities. To properly compute the $\kappa_\perp$ values and avoid statistical problems, only the points with at least 100 macro-particles by velocity bin (of width 0.2) are depicted.

One can observe that curve F, obtained with $V^\star(t)$ equal to the proton fluid velocity, is noticeably different from curve D obtained with $V^\star(t) = 0$. One can also note that $\kappa_\perp(0) \sim 0$ for curve F and that the slope increases with $v_\perp$. The curve E corresponds to an intermediate situation: it is calculated with $V^\star(t)$ equal to the cross field drift $(\mathbf{E} \times \mathbf{B})/B^2$. The result can be seen to be localized between curves D and F.

A striking point between Figs. 2 and 4 is the apparent similarities between the results obtained for populations B and F. To outline this point, Fig. 5 is the $\kappa_\perp$ value depending on $v_\perp$ for populations B (circles) and F (solid line). Both populations behave in a very similar way. The electric fluctuations therefore appear to contribute to the diffusion process in a similar way as the velocity fluctuations. To investigate this point, we focus on the particle dynamics.

VI. QUALITATIVE ANALYSIS

In this section, we analyze the three main features of the curves presented in Fig. 2: (1) the $\kappa_\perp$ associated to magnetic fluctuations is a growing function of $v_\perp$ with $\kappa_\perp(0) = 0$, (2) the $\kappa_\perp$ associated to electric fluctuations is non-null for $v_\perp = 0$, and (3) the $\kappa_\perp$ associated to both magnetic and electric fluctuations is somewhat the sum of the two preceding ones. The last issue (4), observed in Fig. 5, is that the contribution of the velocity fluctuations to $\kappa_\perp$ seems close to one of the electric fluctuations.

Answering these questions requires one to understand particle dynamics. Fig. 6 is an example of the *Y*-position of a

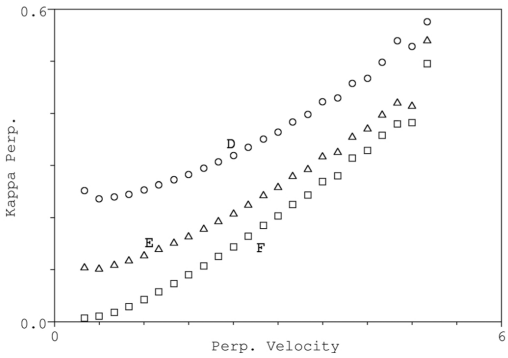

FIG. 4. Perpendicular diffusion coefficient $\kappa_\perp$ depending on the particle perpendicular velocity $v_\perp$. Circles are associated to population D (full velocity fluctuations), Triangles to population E (velocity fluctuations without their cross field part) and squares to population F (no velocity fluctuations).

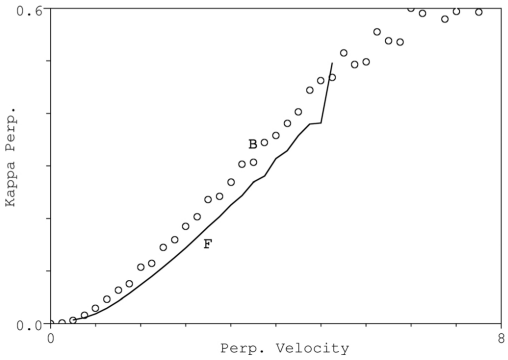

FIG. 5. Perpendicular diffusion coefficient $\kappa_\perp$ depending on the particle's perpendicular velocity $v_\perp$. Circles are associated to population B (magnetic and velocity fluctuations) and the solid line is associated to population F (magnetic and electric fluctuations).

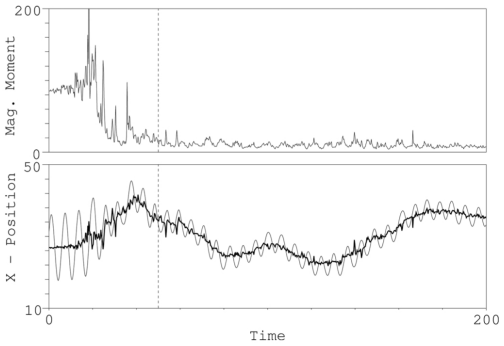

FIG. 6. Bottom panel displays the time-evolution of the X position of a particle (solid line) and its associated guiding center (solid thick line). Top panel displays the time evolution of the associated magnetic moment. The vertical dotted lines indicates the time at which the initial two beams are thermalized and the level of electromagnetic fluctuations gets stationary.

particle orbit (in a run where $\delta B \sim 0.21$). One can observe a clear gyromotion associated to a drift of the center of gyration. As a consequence, the ΔY displacement is closely connected to the drift of the center of gyration. The time evolution of the magnetic moment is also displayed in Fig. 6. After the time indicated by the dotted line, indicating the time at which the initial two beams are thermalized and the level of electromagnetic fluctuations gets stationary, the magnetic moment is rather well conserved. The small remaining spikes that can be observed result from magnetic fluctuations that are highly localized in space and time and weakly infer the global particle dynamic. As a coarse outline, although the scales of the fluctuations are not large with respect to ρ_L and ω_C^{-1}, we will investigate to what extent the simple quasi-adiabatic guiding center approximation can allow a physical interpretation of the results.

The guiding center motion is described in plasma textbooks. Several contributions can be exhibited.[23] Noting $\mathbf{b}$ the unit vector along the magnetic field (Z direction in our case) and $\mathbf{u}_E$ the cross field drift velocity ($\mathbf{u}_E = \mathbf{E} \times \mathbf{B}/B^2$), the perpendicular guiding center velocity (considering only zero and first order) is

$$\mathbf{v}_{GC\perp} = \mathbf{u}_E + \frac{\mathbf{b}}{\omega_C} \times \left[v_\perp^2 \frac{\nabla B}{B} + v_\parallel (\partial_t \mathbf{b} + v_\parallel \partial_Z \mathbf{b} + \mathbf{u}_E . \nabla \mathbf{b}) + (\partial_t \mathbf{u}_E + v_\parallel \partial_Z \mathbf{u}_E + \mathbf{u}_E . \nabla \mathbf{u}_E) \right], \tag{11}$$

which is needed to address the 4 issues listed here above.

First issue: Why is $\kappa_\perp$ associated to magnetic fluctuations a growing function of $v_\perp$ with $\kappa_\perp(0) = 0$? The second term is the well-known gradient drift velocity and is the only one playing a role for population B (other terms are either null or involve the electric field). Hence, for $v_\perp$ going to zero, the associated perpendicular guiding center drift is also going to zero as well as the associated $\kappa_\perp$. This is why for population B in Fig. 2, $\kappa_\perp(0) \sim 0$. The reason why $\kappa_\perp$ depends on $v_\perp$ is more indirect: it may come from the term $\mathbf{b} \times \nabla B$. This term actually depends on $v_\perp$ because the mean square deviation of the magnetic fluctuations seen by the particle depends on its Larmor radius.

Second issue: Why is $\kappa_\perp$ associated to electric fluctuations different from zero for $v_\perp = 0$? None of the terms of Eq. (11) associated to $\delta\mathbf{E}$ depend on $v_\perp$. Accordingly, curve C in Fig. 2 is such as $\kappa_\perp(0) \neq 0$. Nonetheless, second order terms in the expression of v_{GC} (not written in Eq. (11)) would involve both $v_\perp$ and $\delta\mathbf{E}$. This could explain why $\kappa_\perp$ is not constant but a decreasing function of $v_\perp$.

Third issue: Why is the diffusion coefficient associated to both magnetic and electric fluctuations somewhat the sum of the one associated to magnetic fluctuation and the one associated to electric fluctuations? All the terms involving the electric field actually depend on the term $\mathbf{u}_E$. At small level of fluctuations, $\mathbf{u}_E \sim (\delta\mathbf{E} \times \mathbf{b})/B_0$ (considering only the first order contributions) which does not depend on $\delta\mathbf{B}$. In the same way, terms involving $\delta\mathbf{B}$ are free of $\delta\mathbf{E}$. The linearity originates in the small level of fluctuations and the fact that the largest contributors to the guiding center velocity (and hence to $\kappa_\perp$) are first order terms.

Fourth issue: Why is the contribution of velocity fluctuations to $\kappa_\perp$ is close to one of the electric fluctuations? A particle velocity $\mathbf{v}_p$ is the sum of its guiding center velocity $\mathbf{v}_{GC}$ and the gyromotion $\mathbf{v}_\Omega$. If one averages these motion over several gyropulsations, one of course gets

$$\overline{\mathbf{v}_p} = \overline{\mathbf{v}_{GC}}, \tag{12}$$

which is illustrated in Fig. 6. But $\kappa_\perp$ depends on the square of this velocity,

$$\overline{v_p^2} = \overline{v_{GC}^2} + \overline{v_\Omega^2} + \overline{\mathbf{v}_{GC} . \mathbf{v}_\Omega}. \tag{13}$$

During few gyropulsations, $\mathbf{v}_{GC}$ is somewhat constant in both modulus and direction. Accordingly, the last term in Eq. (13) is null. Hence, the first term in the right hand side of Eq. (13) contains all the contributions of the electric fluctuations and only one of the magnetic fluctuations (the gradient drift). The second term depends only on the magnetic fluctuations (and on $v_\perp$). Hence, the contributions of the electric fluctuations are the same as the contributions of the fluid fluctuations if neglecting the gradient drift in the first term. This could explain why the role of electric fluctuations and velocity fluctuations is similar. If so, this means that the magnetic fluctuations mainly act through the second term of the right hand side of Eq. (13). These remarks are in agreement with explanations for the first and second issues. For the first issue, v_Ω depends on both $v_\perp$ and δB. The associated diffusion coefficient for population B is such as $\kappa_\perp(0) \sim 0$ and $\kappa_\perp$ grows with $v_\perp$. For the second issue, v_Ω does not depend on δE, meaning that this term has no contribution to $\kappa_\perp$ for population C.

VII. DISCUSSION AND CONCLUSION

We have estimated the perpendicular diffusion coefficient in a self consistent hybrid simulation and investigated its properties. The perpendicular diffusion coefficient $\kappa_\perp$ is calculated from an average over all the particles of the

associated distribution function. By comparison with the usual magnetostatic results, the electric field has been shown to decrease the slope of the $\kappa_\perp(v_\perp)$ relation and add a Y-intercept to it. Hence, there is no general answer whether the resulting $\kappa_\perp$ increases or decreases due to the electric fluctuations. For the runs presented in this study, with $\delta B \leq 0.2$, the $\kappa_\perp$ value is increased by about 25% the exact value depending on the range of $v_\perp$. If the average had been done spanning smaller velocities, the associated increase would have been larger. This could question the usual conclusions concerning the insufficient efficiency of such diffusion processes to allow solar wind particle penetration into the Earth magnetosphere. In the solar wind, the thermal proton velocity is close to the Alfvén velocity. In Fig. 2, averaging the $\kappa_\perp$ value on a Maxwellian population with a thermal velocity equal to 1 yields to a value that is twice the one obtained without the electric fluctuations.

In contrast, in the field of cosmic rays, particles are relativistic meaning that their velocities are large compared to the Alfvén velocity. Fig. 7 is the same as Fig. 2 for perpendicular velocities up to 32. This figure suggests that the role of the electric field (for Ion Bernstein modes) might be negligible for the diffusion process as curves A and B are very close. To emphasize this point, the same kind of calculation for other modes should be achieved, meaning the use of a 3D numerical code.

The term $Y^\star$ in Eq. (10) was suggested in paper 1 to properly compute the $\kappa_\perp$ value in situations where a mean fluid flow can exist. Omitting this term, the collective component of the particle motion results in an overestimation of $\langle \Delta Y^2 \rangle$ just because $\langle \Delta Y \rangle \neq 0$ (the so called "speed-walk effect"). In this paper, we put forward that even in the absence of a mean fluid flow at the largest scales, this term has to be taken into account, since its contribution is about the same as the one of the electric fluctuations. The reason lies in the existence of small scale (often turbulent) fluid motions, for instance related to the gradient drift motions of the guiding centers. It is worth noticing that these motions are already present in magnetostatic fluctuations. Of course, this contribution has to be set aside to properly evaluate the perpendicular diffusion coefficient. As a very simple example, consider a plane where the magnetic field (perpendicular to the plane) is linearly decreasing in half of the domain (in X direction) and linearly increasing in the second half. An associated gradient drift will exist in the $+Y$ direction in the first half, and $-Y$ in the second half. In such a situation, $\langle \Delta Y \rangle = 0$ but the associated PDF, even if Gaussian, would have a mean square deviation increasing faster than t. This is not a consequence of any super-diffusion even if it could look like it. This emphasizes the fact that the existence of mean flows, even in magnetostatic situations, has to be considered to avoid interpretations in terms of super-diffusion in situations where $\langle \Delta Y^2 \rangle$ is not secularly growing with time. This problem is in close connection with the discussion of Sec. III, where it is emphasized that the notion of fluid flow depends on the characteristic length it is defined. This question is usually not discussed in test-particle simulations and might need more caution.

The conclusion that can be drawn from this work is that at small to intermediate level of fluctuations, electric and magnetic fluctuations both contribute to the diffusion coefficient and their effects can be superposed almost linearly. Furthermore, the electric field fluctuations contribute to the perpendicular diffusion coefficient value in a similar way as velocity fluctuations do. This can be well interpreted as a consequence of the guiding center theory that can be applied for magnetic fluctuations up to $\delta B \sim 0.2$ in spite of the small scales of the fluctuations and of their fairly large amplitude. This study is restricted to the case of a bath of Ion Bernstein waves. In all the runs we performed, the particle behavior is diffusive, meaning that the associated diffusion coefficient can be considered in fluid equations using the usual second order derivative of the fluid velocity. A 3D study is now needed to study oblique and parallel modes. In such situations, one has to establish an adequate method to subtract the mean flows (that can be localized in space or time) to prevent from the computation of artificial super-diffusion.

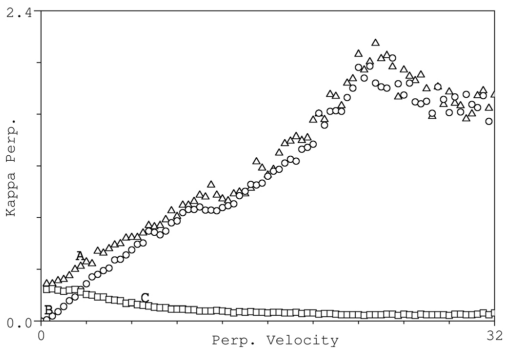

FIG. 7. Perpendicular diffusion coefficient $\kappa_\perp$ depending on the particle's perpendicular velocity $v_\perp$. Triangles are associated to population A, circles are associated to population B, and squares are associated to population C.

[1]A. Shalchi, *Nonlinear Cosmic Ray Diffusion Theories* (Springer, 2009).
[2]R. J. Bickerton, Plasma Phys. Controlled Fusion **39**, 339 (1997).
[3]D. Winske and N. Omidi, J. Geophys. Res. **100**, 11923, doi:10.1029/94JA02730 (1995).
[4]J. R. Jokipii, Astrophys. J. **146**, 480 (1966).
[5]P. Pommois, P. Veltri, and G. Zimbardo, Phys. Rev. E **63**, 066405 (2001).
[6]J. Minnie, W. H. Matthaeus, J. W. Bieber, D. Ruffolo, and R. A. Burger, J. Geophys. Res. **114**, A01102, doi:10.1029/2008JA013349 (2009).
[7]J. W. Bieber and W. H. Matthaeus, Astrophys. J. **485**, 655 (1997).
[8]W. H. Matthaeus, G. Qin, J. W. Bieber, and G. P. Zank, Astrophys. J. **590**, L53 (2003).
[9]A. Shalchi, Astrophys. J. **720**, L127 (2010).
[10]R. Smets, G. Belmont, N. Aunai, and L. Rezeau, Phys. Plasmas **18**, 102310 (2011).
[11]S. D. Bale, P. J. Kellogg, F. S. Mozer, T. S. Horbury, and H. Reme, Phys. Rev. Lett. **94**, 215002 (2005).
[12]P. J. Kellogg, Astrophys. J. **528**, 480 (2000).
[13]P. Hellinger, P. Trávníček, J. C. Kasper, and A. J. Lazarus, Geophys. Res. Lett. **33**, L09101, doi:10.1029/2006GL025925 (2006).
[14]T. Chust and G. Belmont, Phys. Plasmas **13**, 012506 (2006).
[15]C. K. Birdsall and A. B. Langdon, *Plasma Physics via Computer Simulation* (Institute of Physics Publishing, 1991).
[16]D. S. Harned, J. Comput. Phys. **47**, 452 (1982).
[17]A. Shalchi, Phys. Rev. E **83**, 046402 (2011).

[18]J. Klafter, A. Blumen, and M. F. Shlesinger, Phys. Rev. A **35**, 3081 (1987).
[19]D. Verscharen, E. Marsch, U. Motschmann, and J. Müller, Phys. Plasmas **19**, 022305 (2012).
[20]P. Dmitruk and W. H. Matthaeus, Phys. Plasmas **16**, 062304 (2009).
[21]T. N. Parashar, S. Servidio, B. Breech, M. A. Shay, and W. H. Matthaeus, Phys. Plasmas **17**, 102304 (2010).
[22]J. J. Podesta, J. Geophys. Res., [Space Phys.] **117**, A07101, doi:10.1029/2012JA017770(2012).
[23]T. Northrop, *The Adiabatic Motion of Charged Particles* (Interscience, 1963).

— F —

Proton acceleration in antiparallel collisionless magnetic reconnection: Kinetic mechanisms behind the fluid dynamics

N. Aunai, G. Belmont, R. Smets,

Laboratoire de Physique des Plasmas, Ecole Polytechnique,

Journal of Geophysical Research

Vol. 116, pages 9232 - 9244, 2011

JOURNAL OF GEOPHYSICAL RESEARCH, VOL. 116, A09232, doi:10.1029/2011JA016688, 2011

Proton acceleration in antiparallel collisionless magnetic reconnection: Kinetic mechanisms behind the fluid dynamics

N. Aunai,[1] G. Belmont,[1] and R. Smets[1]

Received 28 March 2010; revised 22 June 2011; accepted 6 July 2011; published 28 September 2011.

[1] This paper investigates the proton kinetic mechanisms leading to the formation of plasma jets in antiparallel magnetic reconnection. In particular, the interaction of the protons with the Hall electric field in the proton non-ideal region is discussed. The study, based on a two-dimensional hybrid simulation, details the important role of the proton pressure force in the acceleration process and its role in maintaining open and steady the proton outflow channel. When no fluid closure is assumed, it is found that this force arises from a strong anisotropy in velocity space which comes from kinetic effect. By analyzing the distribution functions and the individual particle dynamics, it is shown that the mixing of protons bouncing in a divergent electrostatic potential well associated to the Hall effect statistically couples the two in-plane velocity components of the particles. This coupling results, from the macroscopic point of view, in off-diagonal components of the pressure tensor.

Citation: Aunai, N., G. Belmont, and R. Smets (2011), Proton acceleration in antiparallel collisionless magnetic reconnection: Kinetic mechanisms behind the fluid dynamics, *J. Geophys. Res.*, *116*, A09232, doi:10.1029/2011JA016688.

1. Introduction

[2] Magnetic reconnection is a universal non-ideal plasma phenomenon allowing the breaking of the magnetic frozen-in constraint and the acceleration and heating of the plasma by releasing the energy stored in magnetic structures. It is thus considered to playa key role in many plasma environments, both in laboratory devices such as tokamaks and in astrophysical systems like the solar corona, solar wind, planetary magnetospheres or remote astrophysical objects like accretion disks [*Priest and Forbes*, 2000; *Yamada et al.*, 2010].

[3] It is now widely accepted that the Hall effect plays an important role in establishing a fast steady reconnection rate [*Birn et al.*, 2001]. As it is understood so far, the collisionless reconnection model involves two nested structures surrounding the magnetic X point, represented in Figure 1. The larger one is formed at the proton scale. At this scale, the protons decouple from the magnetic field motion and are accelerated away from the reconnection site up to a significant fraction of the upstream Alfvén speed. The smaller inner structure is at a tiny electron scale. At this scale, the kinetic behavior of the electrons creates the "dissipation" required to break the magnetic field line connectivity. When the magnetic reconnection process reaches a steady state [e.g., *Shay et al.*, 2007] it appears that the electron decoupling region is somehow playing a passive role regarding the reconnection rate, and adapts itself to a global dynamics imposed at the proton scale [*Hesse et al.*, 1999]. This may be different if reconnection is intrinsically unsteady, as observed by *Daughton et al.* [2006]. The classic Sweet-Parker analysis [*Sweet*, 1958; *Parker*, 1957; *Priest and Forbes*, 2000], linking the outflowing and incoming mass fluxes, teaches us that the reconnection rate is then fast for two reasons: firstly, when the Hall effect is allowed, we observe a wider channel for the outflowing plasma than in collisional models with high magnetic Reynolds number, and secondly because protons keep on flowing at an important fraction of the Alfvén speed through this channel. These two effects seem to be controlled at the microscopic proton scale and independent of the global system size. It is thus important to understand the physical mechanisms maintaining the channel open and accelerating the protons to this high velocity.

[4] Numbers of authors have shown that the protons are interacting with the Hall electric field located on the separatrices close to the reconnection site [e.g., *Hoshino et al.*, 1998; *Shay et al.*, 1998; *Pei et al.*, 2001; *Wygant et al.*, 2005; *Singh et al.*, 2010]. This electric field, and in particular its component along the downstream direction, has been said to be responsible for the proton acceleration up to the upstream Alfvén speed within a few proton inertial lengths from the X-line [*Shay et al.*, 1999]. However if the outflow is really Alfvénic in two-fluid simulations, it appears to be slower in kinetic models [*Shay et al.*, 2001; *Karimabadi et al.*, 2007]. The reconnection rates seem however quite similar because in the latter case the outflow channel is wider, thus leaving the outflowing mass flux approximately the same [*Shay et al.*, 2001]. One conclusion following from the observed differences would be that proton interaction with the electromagnetic fields in the decoupling region depends on the closure hypothesis chosen to model the plasma. Indeed, in collisionless plasmas, the macroscopic ("fluid") quantities such as density, velocity and pressure are just some global properties (low order moments) of the

[1]Laboratoire de Physique des Plasmas, Ecole Polytechnique, Palaiseau, France.

0148-0227/11/2011JA016688

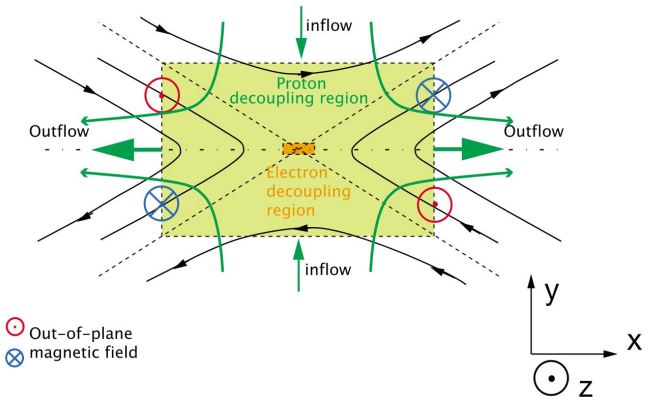

Figure 1. Sketch representing the characteristic features of the two-dimensional collisionless Hall model. The black lines represent the in-plane magnetic field lines. The green and orange rectangles represent the proton and electron decoupling region, respectively. The green arrows represent the proton fluid velocity in the inflow and outflow regions and the green curved lines the in-plane fluid trajectory from upstream to downstream of the proton decoupling region. The dash-dot line represent the mid-plane neutral line and the diagonal dashed line are the separatrices.

distribution function of particles in velocity space. Fluid simulations for collisionless systems are thus an incomplete description of the reality because they come with a closure of the large chain of moments of the distribution function at a certain order, which is often the second one (pressure).

[5] Within the context of magnetic reconnection, both kinetic simulations and satellite measurements in the terrestrial magnetosphere reveal the ubiquitous presence of highly structured proton distribution functions far from the Maxwellian shape [*Shay et al.*, 1998; *Hoshino et al.*, 1998; *Arzner and Scholer*, 2001; *Pei et al.*, 2001; *Nagai et al.*, 2001]. These distributions consist sometimes in the mixing of fast particles coming from the reconnection site with particles originating from upstream regions [*Hoshino et al.*, 1998; *Shay et al.*, 1998], or non-Maxwellian shapes related to some local acceleration mechanisms. Among these distributions, counterstreaming beams in the direction normal to the initial current sheet are often observed [*Shay et al.*, 1998; *Hoshino et al.*, 1998; *Arzner and Scholer*, 2001; *Pei et al.*, 2001; *Wygant et al.*, 2005]. These beams have been related to the acceleration of protons by the normal component of the Hall electric field both in simulations and in observations.

[6] Observing non-Maxwellian structures strongly suggests that a kinetic description is mandatory. Nevertheless, there is no clear understanding of what is the consequence of such distribution shapes, regarding the reconnection process, as seen from the macroscopic points of view. As an attempt to understand this, *Wygant et al.* [2005] proposed, from the analysis of Cluster spacecraft measurements, an interpretation of the acceleration mechanism both from the microscopic (particle) and macroscopic (fluid) point of view. The spatial appearance of counterstreaming beams in the jet region is related, from the particles point of view, to protons bouncing in a electrostatic potential well in the cross-current direction, and from the fluid point of view, to the rising of the kinetic pressure within the jet, maintaining pressure balance in this direction.

[7] In this paper, we are interested in understanding the proton acceleration in the vicinity of the Hall region surrounding the antiparallel symmetric reconnection site. This study aims to clarify the role of the kinetic mechanisms for the proton population regarding their interaction with the Hall electric field, as seen from the macroscopic, fluid, point of view. The second part of this paper will be dedicated to the description of our two-dimensional hybrid numerical model and the initial condition of our simulation. Then in section three, we will describe the interaction of the protons with the Hall fields from the fluid point of view. This step will reveal the importance of the pressure force in the fluid acceleration, and will show that it is the result of a kinetic mechanism. The appearance of off-diagonal terms in the proton pressure tensor will be shown to be consistent with the structure of the proton distribution functions in the fourth section, and will be understood by examining the underlying particle dynamics. The fifth section will summarize our results and discuss future possible related investigations.

2. Numerical Model and Initial Condition

[8] As we are interested in the proton dynamics, we will work with a hybrid code, in which protons are treated as macroparticles and electrons as a fluid. We assume the problem to be two-dimensional.

[9] The numerical scheme is close to those described by *Harned* [1982] and *Smets et al.* [2007]. The proton motion is calculated with equation (1), where $\mathbf{v}_{pi}$ is the particle velocity, m_i the proton mass, **E** and **B** are the electric and magnetic field, respectively. This equation is solved using the Boris algorithm [*Boris*, 1970] with a standard leapfrog scheme. We assume that at the scales we are interested in,

the quasi-neutrality holds, that is the electron density n_e can be considered to be everywhere and at all times equal to the proton density ($n_e = n_i \equiv n$). By neglecting consistently the displacement current in the Ampere's law (2), we obtain the total current **j** from the magnetic field **B**. Knowing the proton density n and fluid velocity $\mathbf{v}_i$ from equations (6) and (7), both the electron density and mean velocity $\mathbf{v_e}$ are known. We can therefore use the fluid momentum equation for electrons (3) to compute the electric field **E** consistent with all these assumptions (generalized Ohm's law). This implies the use of a closure hypothesis for the electrons, which in our case consists in treating the electrons as an isothermal fluid with an isotropic pressure P_e calculated with equation (5) where k_B is the Boltzmann constant and T_e is the electron temperature. This model for the electron pressure is of course an oversimplification of the complete electron dynamics and cannot for example model the physics taking place at the tiny electron decoupling region [*Divin et al.*, 2010]. Because equation (3) still retains the Hall term, it is expected to be qualitatively correct for understanding the ion acceleration mechanism. Full PIC simulations [*Drake et al.*, 2008] have recently revealed that a part of the electric field located on the separatrices is given by the divergence of the full electron pressure tensor. Because of our electron closure hypothesis, this effect cannot be seen in our simulation. Nevertheless, the simulation presented by *Drake et al.* [2008] shows that the electron ideal term, which is present in the hybrid model, is still the strongest. We can therefore reasonably assume that the electron kinetic physics is qualitatively not too important for the proton dynamics discussed in this paper. For numerical purposes mainly, we take the electron bulk inertia effect into account in the Ohm's law. This term is the last of equation (3), written with the Lagrangian viewpoint. Modeling the electron bulk inertia makes the whistler wave dispersion relation to saturate at the electron gyrofrequency $\Omega_{ce} = -eB/m_e$, where e and m_e are the elementary charge and electron mass, respectively. This effect prevents Courant-Friedrichs-Lewy (CFL) condition based on the whistler wave dispersion from constraining too much the time step value and thus allows us to have a higher spatial resolution. It is implemented following the method of the pseudo-fields [*Lipatov*, 2002; *Cassak*, 2006], the resulting additional equation is solved with the parallel PETSc library (http://www.mcs.anl.gov/petsc).

[10] The magnetic field is calculated from the electric field using the Faraday's equation (4). The electromagnetic fields are solved on two uniform cartesian staggered grids, discretized with a second order finite differences method and updated in time with a predictor-corrector scheme.

$$m_i \frac{d\mathbf{v}_{pi}}{dt} = e\left(\mathbf{v}_{pi} \times \mathbf{B} + \mathbf{E}\right) \tag{1}$$

$$\nabla \times \mathbf{B} = \mu_0 e n (\mathbf{v}_i - \mathbf{v}_e) \tag{2}$$

$$\mathbf{E} = -\mathbf{v}_i \times \mathbf{B} + \frac{1}{ne}(\mathbf{j} \times \mathbf{B} - \nabla P_e) - \frac{m_e}{e}\frac{D\mathbf{v}_e}{Dt} \tag{3}$$

$$\frac{\partial \mathbf{B}}{\partial t} = -\nabla \times \mathbf{E} \tag{4}$$

$$P_e = n k_B T_e \tag{5}$$

$$n = \int f(\mathbf{r}, \mathbf{v}_{pi}) d\mathbf{v}_{pi} \tag{6}$$

$$\mathbf{v}_i = \int \mathbf{v}_{pi} f(\mathbf{r}, \mathbf{v}_{pi}) d\mathbf{v}_{pi} \tag{7}$$

[11] The magnetic field and density are normalized to arbitrary values B_0 and n_0, which in this paper are the asymptotic values (*i.e.* far from the current sheet, in the uniform upstream region). Distances are normalized to the proton inertial length $\delta_i = c/\omega_{pi} = V_A/\Omega_{ci}$, where c is the speed of light in vacuum, $\omega_{pi} = \sqrt{n_0 e^2/m_i \epsilon_0}$ is the proton plasma frequency, $V_A = B_0/\sqrt{\mu_0 m_i n_0}$ is the Alfvén speed and $\Omega_{ci} = eB_0/m_i$ the proton gyrofrequency. Time is normalized to the inverse of the proton cyclotron frequency Ω_{ci}^{-1}. In these units, the simulation domain is a rectangle $(x_m, y_m) = (280,40)$ with $n_x = 1024$ and $n_y = 512$ cells in x and y directions. These directions can be compared with the x and z direction in the GSE coordinate system often used in the magnetotail studies. The time step is chosen to be $\Delta t = 0.005$, this value ensures a good sampling of the particle and wave dynamics and has been found to give good results regarding the numerical stability and conservation of invariants during the simulation which lasts $T = 175$. We set about 100 particles per cell initially, that is about 4000 particles per δ_i^2. The proton to electron mass ratio is set to $m_i/m_e = 50$, so that the electron inertial length is $\delta_e = 0.14\delta_i$. Perfect conducting boundary conditions are used at y borders and periodic in the x direction. It is well known that periodic boundary conditions can limit the time during which the simulation is valid (for astrophysical applications). The length of the box in the downstream direction has been chosen to be large enough so that the physics considered here is not coupled to the boundary conditions.

[12] The initial magnetic field profile is antiparallel (no guide field) and $\mathbf{B} = B_s \tanh((y - 0.5y_m)/\lambda)\mathbf{e}_x$ with the normalized half-width $\lambda = 1$ and the normalized asymptotic magnetic amplitude $B_s = 1$. In order to have one major X point in the simulation box, we impose a magnetic perturbation localized at the center of the domain. The normalized density is uniform with $n_s = 1$. The normalized electron temperature is uniform and set to $T_e = 0.005$. The total β of the plasma is set to 0.1 asymptotically in the y direction. The density and the magnetic field being chosen, this value determines the plasma temperature. The plasma is chosen to be rather cold asymptotically for mainly two reasons. The first is that it seems to be consistent with the reconnection of lobe plasma in the magnetotail [*Wygant et al.*, 2005]. The second is that the role of the particle dynamics in structuring the distribution function is easier to infer with cold asymptotic distributions, because of the statistical noise present in PIC simulations. Protons are loaded in a local Maxwellian distribution function, their temperature is chosen to balance the total pressure, using $\nabla(P + 0.5B^2/\mu_0) = 0$, where P is the total (electron plus protons) kinetic pressure. The asymptotic

normalized proton temperature is $T_i = 0.045$ and the sheet temperature is $T_i = 0.545$. For the sake of observational comparison, let's note that if one takes $B_0 = 15nT$, $n_0 = 0.25$ cm^{-3}, the proton temperature is 250 eV and 2.4 keV in the asymptotic region and sheet, respectively. This approximately corresponds to magnetotail lobe and plasma sheet plasmas. The electron to ion temperature ratio in the asymptotic region is 9 and increases within the sheet because of the isothermal hypothesis for electrons. This initial condition is not a Vlasov-Maxwell equilibrium and small amplitude waves are emitted from the current sheet at the very beginning of the simulation ($t < \Omega_{ci}^{-1}$). These waves are the consequence of the kinetic "relaxation" of the current sheet. They propagate in the y direction and are eventually reflected back to the sheet from the conducting walls at a time long compared to the X point dynamics ($\Delta t \Omega_{ci} \approx 50$). Let us note that using a kinetic equilibrium as an initial condition (for example the Harris equilibrium [*Harris*, 1962]) does not prevent from the emission of comparable waves as long as one uses an initial magnetic perturbation not calculated kinetically [*Fujimoto and Sydora*, 2008]. No coupling was found between the wave activity and the proton dynamics discussed in this paper.

3. Fluid Dynamics

[13] The formation of a plasma jet is one of the most remarkable features of the magnetic reconnection phenomenon. In the collisionless limit, it has been noticed that the outflow velocity scales as the Alfvén speed based on the upstream density and magnetic field values [e.g., *Shay et al.*, 2001]. The physical reason is that the fluid gains some of the energy stored in the magnetic shear and shares it between its thermal and convective kinetic energy. To understand the fluid dynamics, let us write the fluid momentum equation for the protons (8).

$$m_i n\left(\frac{\partial \mathbf{v}_i}{\partial t} + (\mathbf{v}_i \cdot \boldsymbol{\nabla})\mathbf{v}_i\right) = -\boldsymbol{\nabla} \cdot \mathbf{P}_i + ne(\mathbf{E} + \mathbf{v}_i \times \mathbf{B}) \quad (8)$$

[14] The Eulerian acceleration terms are on the left hand side. The right hand side terms are respectively the pressure, electric and magnetic forces felt by the proton fluid at a location (x, y). Note that the pressure force is the divergence of the full pressure tensor $\mathbf{P}_i$. The proton pressure tensor is defined by equation (9), where α and β indices represent the cartesian component x, y, z.

$$\mathbf{P}_{i\alpha\beta} = \int (\mathbf{v}_{pi\alpha} - \mathbf{v}_{i\alpha}) \otimes (\mathbf{v}_{pi\alpha} - \mathbf{v}_{i\beta}) f(\mathbf{r}, \mathbf{v}_{pi})\, d\mathbf{v}_{pi} \quad (9)$$

[15] We are interested in the acceleration within the Hall region, which can be identified in the Figure 2 as the area where the electric field is strong and localized on the separatrices. This electric field is mainly supported by the Hall term $\mathbf{j} \times \mathbf{B}/en$, and is consistent with the magnetic field motion frozen in the electron flow. It has a large y component ($E_y \sim 0.7 V_A B_0$), symmetric and directed toward the mid-plane and a small component in the outflow direction x ($E_x \sim 0.1 V_A B_0$). Further away, the electric field keeps its bipolar variation in the cross-current direction y, but is much weaker. There, the whole plasma, protons and electrons, becomes frozen in the magnetic field motion again [*Arzner and Scholer*, 2001; *Drake et al.*, 2008].

[16] Considering that the simulation domain is closed, the upstream magnetic energy reservoir is being emptied as the plasma is accelerated and heated. Because the reconnection rate depends on the actual value of the magnetic energy available, the whole process never reaches a true steady state and the rate keeps slowing down after reaching a maximum value. However, if one normalizes the reconnection rate by the characteristic electric field $V_{Ai}B_i$ in the inflow region (the i indice means that quantities are defined just upstream of the reconnection site) the rate appears steady. This confirms that the slow decay of the reconnection rate is the consequence of the limited energy supply rather than a local intrinsic evolution of the phenomenon. The data presented in this paper will be measured in the simulation during this pseudo steady phase at time $t = 105$.

[17] Figure 3 represents the calculated trajectories of fluid elements from the upstream region to the jet, based on the proton flow at this time, smoothed locally in areas of size ($\Delta_x = 2\delta_i$, $\Delta_y = \delta_i$) to avoid small scale fluctuations. All the terms of equation (8) are obtain from the self-consistent distribution of macroparticles in the simulation using equations (6), (7), and (9). One can firstly note that each trajectory is deviated in the separatrix region, where the Hall electric field is. It is likely that the fluid is taking its kinetic energy from this electric field, as already pointed out in the literature [e.g., *Shay et al.*, 1999]. To go further into details, one can measure the different terms of equation (8) projected in both in-plane directions, along the path of a fluid element. Figure 4 represents these forces along the path starting with the white point in Figure 3. The data necessary to calculate theses quantities has been averaged over $\Delta t_{av} = 10$. These plots reveal that the electric force felt by the fluid in both in-plane directions is indeed very important, in particular, it is accelerating the fluid toward the downstream region, as already suspected.

[18] One can also note, however, that the electric force is not the only force playing an important role. Both in the x and y directions, we notice a strong pressure force, located on the separatrices, and opposed to the electric force. The consequence is that the fluid is not as much accelerated by the electric field as it would be without the pressure force. Coming from the upstream regions from both sides of the current sheet, the frozen-in motion of the proton fluid stops at the separatrix region. Here the magnetic field is suddenly dragged in the out-of-plane (z) direction by a fast steady electron flow. Because of their high inertia, the protons cannot follow this suddenly fast motion and decouple from it. Decoupled from magnetic motion, the fluid elements nevertheless feel the associated electric field and are accelerated through the separatrices toward each other in the mid-plane. This effectively rises the pressure inside the jet so that the pressure difference with the upstream regions is able to dynamically balance the electric field force and maintain the structure open and steady. This pressure balance is consistent with the Hall effect and has to appear as soon as two-species effects are taken into account in the modeling.

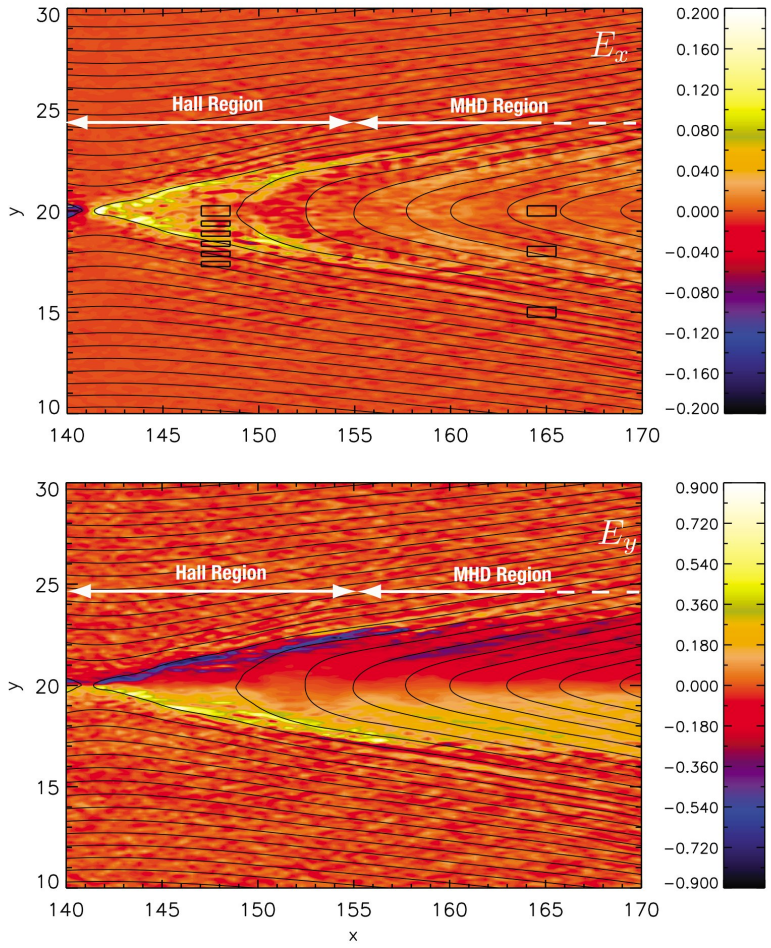

Figure 2. (top) E_x and (bottom) E_y electric field component at t = 105. Note that each component has a different color scale. The solid black line represent the in-plane magnetic field lines at that time. In Figure 2 (top), the small black boxes at x = 147 are from the bottom to the top the locations where the distributions A, B, C, D, E and F represented in Figure 6 are measured. The boxes at x = 165 are from bottom to the top the locations where the distributions G, H, and I in Figure 10 are measured.

However the microscopic physics responsible for the rising of the pressure inside the jet will depend on the model.

[19] In particular, if the kinetic behavior of the protons is retained, we can see from Figure 4 that the pressure force in the x direction on the separatrix almost entirely results from the off-diagonal part of the pressure tensor ($-\partial_y P_{ixy}$). This must come from an anisotropy of the proton velocity distribution, which will be shown to have a kinetic origin. In a fluid simulation where a closure is assumed and links the pressure to the density through some function, the pressure force has to be the consequence on the increase of the density in the jet and leads to a different steady width of the outflow channel as observed by *Shay et al.* [2001]. This could also lead to erroneous simulation-based predictions for future observational investigation in this region.

4. Pressure Tensor Structure and Particle Dynamics

4.1. Spatial Structure of P_{ixy}

[20] We will show in this section that a kinetic effect is at the origin of the observed pressure force. We aim to explain this effect, by analyzing the distribution functions and the underlying particle dynamics. Figure 5 represents the P_{ixy} component of the proton pressure tensor on the right side of the reconnection site at t = 105. Two regions can be iden-

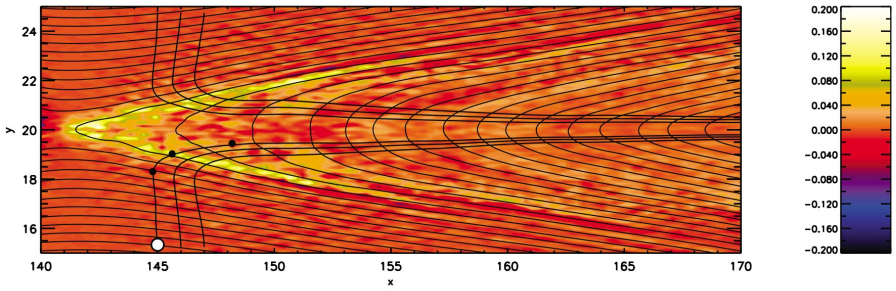

Figure 3. Trajectories of fluid elements calculated from the simulation results (black solid lines) and superposed to the E_x component of the electric field in color code. Figure 3 is made at $t = 105$. The white dot marks the trajectory that is being followed to investigate fluid forces represented in Figure 4 and the black dots identify the same locations as the black arrows in Figure 4. The black solid lines represent the in-plane magnetic field lines.

tified, each corresponds to a particular variation of P_{ixy} in the y direction. In the region labeled A, P_{ixy} is changing from positive to negative values as y increases, while it is the opposite in region B. Note that $P_{ixy} = 0$ outside of the jet. We will focus on explaining the variation in region A since it is here that the Hall electric field exists (Figure 2), but the reason for the variation in region B will also become clear later. So far, one can notice that the existence of these two different regions can serve as an observational proxy of spacecraft position relative to the X-line for *in-situ* measurements.

[21] Mathematically, the pressure tensor is an object that measures the statistical covariance between the velocity components of a set of particles. In a purely isotropic plasma, there is by definition no statistical correlation between the different components of the particle velocity so the off-diagonal terms are zero. The existence here of a particular structure of the P_{ixy} component of the pressure tensor is the consequence of an underlying kinetic mechanism which somehow statistically couples the v_x and v_y components of the particles. This correlation can be seen from the distribution functions, measured in the simulation and represented as projections of the particle density in the $v_x - v_y$ plane. Figure 6 shows these distributions inside the small boxes represented in Figure 2. Below the separatrix, in the upstream region, the plasma is roughly Maxwellian, but as soon as we probe the separatrix region, the distributions are deformed and look like two beams, one having a positive

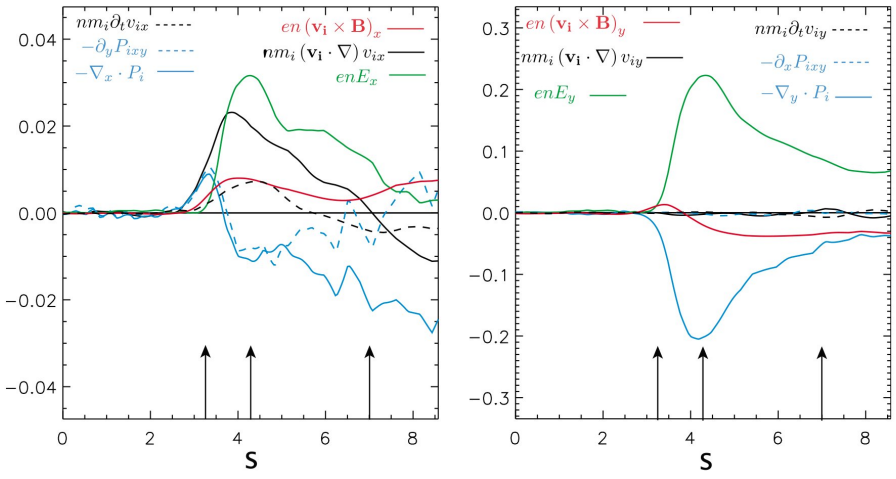

Figure 4. Forces felt by the fluid element represented by the white dot in Figure 3 along its motion (s is the curvilinear abscissa). Forces are projected in the (left) x and (right) y direction. The black arrows are specific locations identified by the black dots in Figure 3.

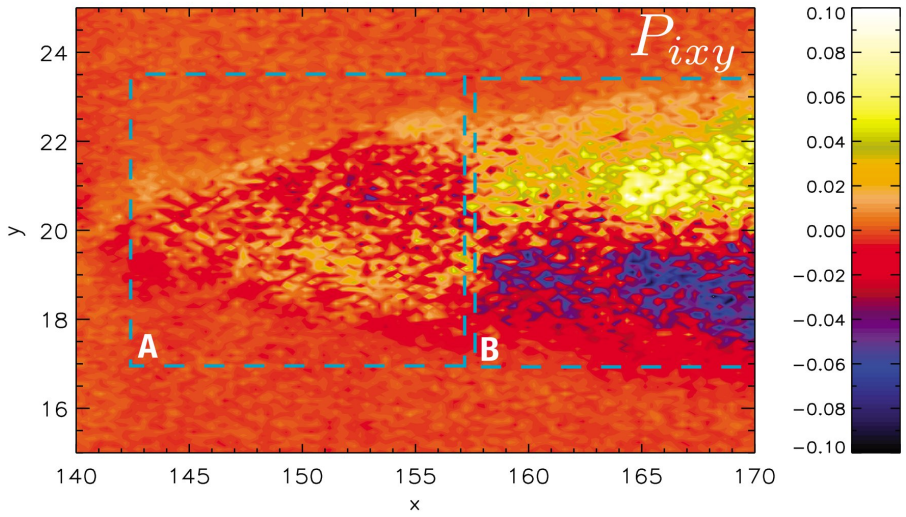

Figure 5. P_{ixy} component of the proton pressure tensor represented by a color contour at $t = 105$ on the right area of the reconnection site.

v_y velocity and the other a negative one. The appearance of these beams in the y direction explains the high pressure gradient seen in Figure 4, and is consistent with the proton distribution functions presented by *Wygant et al.* [2005] obtained from the analysis of the Cluster spacecraft measurements. Looking closer at distribution D and E, one can notice that statistically, the faster a particle is in the x direction, the faster it also is in the y direction. There is thus a positive statistical correlation between v_x and v_y, and this is exactly what summarizes the positive value of P_{ixy} at this location. At the center of the current sheet, the distribution (F) still consists of two beams, but as expected from the change of sign of P_{ixy}, there is no correlation and the beams are symmetric with respect to the $v_y = 0$ axis. From the outside (distributions A, B and C) to the inside of the jet (distributions D, E), the correlation goes from zero to positive values, there is thus a positive derivative $\partial_y P_{ixy}$, hence the negative pressure force in the x direction. The situation is of course symmetric above the line $y = 20$ and results in the bipolar variation observed in the y direction in Figure 5. As expected, the anisotropic pressure tensor, responsible for the force we observe is the result of the spatial evolution of the shape of the proton distribution function. The v_x and v_y components of the particles are not randomly distributed but some kinetic mechanism is ordering them. To further understand this underlying kinetic effect, one must now analyze the individual particle dynamics.

4.2. Particle Dynamics

[22] Let's pick a typical particle in the distribution F of Figure 6 and plot its trajectory projected in the simulation plane, superposed to the color coded E_x electric field at time $t = 105$. The result can be seen in Figure 7 (top). As for most of the other particles in this distribution (not shown), we can identify three distinct phases. The first and the last phases are characterized by a $\mathbf{E} \times \mathbf{B}$ drift motion of the particle, while the middle phase appears as a bounce motion. In this phase, most of the particles are reflected from the separatrices. This leads to the conclusion that the separatrices play a major role in particle dynamics. Note that this is ruling out the possibility of explaining these trajectories by a Speiser-like dynamics [*Speiser*, 1965], where the two-fluid effects are not taken into account and where the particle motion therefore does not depend on the separatrices location, but rather consists in oscillations due to the magnetic reversal.

[23] Of course, one immediately thinks about the electric field located on the separatrices, as the source of this bounce motion. To be sure about this assertion, one can plot the trajectory of a particle, again projected on the simulation plane, but this time we superpose the electric and magnetic forces felt by the particle at some times (Figure 7, bottom). Zooming on the bounce phase clearly reveals that it is indeed the electric force that is dominant and responsible for the bounce motion of the proton. What happens is that the proton comes from a region of high electric potential and fall inside a potential well [*Karimabadi et al.*, 2007]. As it falls inside the well, its potential electric energy is transferred to its kinetic energy until it reaches the other side of the well, bounces etc. Because the slope of the potential well is mainly in the y direction, the particle, as it is falling, mainly increases the v_y component of its velocity. The trick is that the potential walls are not parallel with each other, so at each bounce, the particle irreversibly transfers a bit of its velocity from the v_y component to the v_x one.

[24] This transfer may explain the elongated shape of each beam in the distribution F and their tilt in the (v_x, v_y) plane. A particle entering in the potential well first appears with a large $|v_y|$ as it falls into the bottom, and after each bounce appears at smaller $|v_y|$ but larger v_x at the bottom of the well.

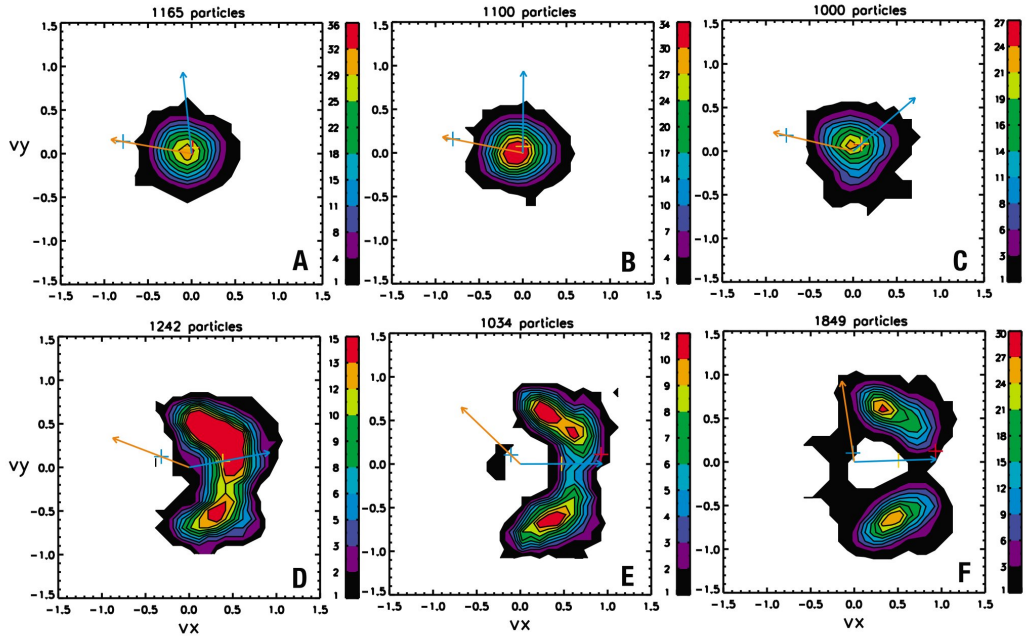

Figure 6. Projections of the proton distribution functions in the (v_x, v_y) plane. Distributions A, B, C, D, E, and F are measured within the small black boxes visible in Figure 2, from bottom to top at $x = 147$. The blue and orange arrows represent the in-plane direction of the bulk velocity and magnetic field, respectively. The blue, yellow and red crosses represent the in-plane Alfvén speed, bulk speed and $\mathbf{E} \times \mathbf{B}/B^2$ speed, respectively. For each distribution, the number of particles contributing to the distribution is indicated.

We can then assume that these elongated and tilted beams consist of particles that have experienced a different number of bounces before reaching our selection point. This assumption explains well the shape and tilt of each beam, and can be confirmed by counting, for each particle contributing to this distribution, the number of electric bounces it has experienced before reaching the selection point. The result of the counting is represented in Figure 8, where all particles have been placed at their position in the velocity space with a color flag coding the number of bounce they experienced. Clearly, this confirms our assumption: the spatial divergence of the potential well and the collisionless mixing of the bouncing protons structure the distribution function and built the in-plane pressure tensor components. Few particles (population 2) seem to have a different dynamics but have negligible contribution to the distribution. If the bounce mechanism can be inferred from spacecraft measurements [*Wygant et al.*, 2005], it seems difficult, because of their local character, to gain more detailed information such as the typical number of bounces a proton does. The numerical simulation comes here as a great complementary tool. As can already be seen in Figures 7 and 8, the protons seem not to bounce so many times. To have a better statistical insight, we have computed the histogram of the number of bounces for the distribution F and represented it in Figure 9. It appears clearly that most of the particles here have done, at this time, zero, one or two bounces, few particles have bounced three times and very few four times. In the mean time, the protons also feel the E_z electric field. However, because the bounce phase is short and the E_z field far weaker than the Hall field, they don't have the time to drift significantly in the z direction while in the bounce phase. The average drift distance in the z direction of all the particles in distribution F at $t = 105$ is $\overline{\delta}_z \approx 0.06$, and the standard deviation is $\sigma_z \approx 2.6$. Approximately 80% of these particles have drift less than σ_z, and the maximum drift distance is $\Delta_z \approx 18$ in the direction of the reconnection electric field. These numbers lead to the conclusion that our results concerning the proton bounce motion are not very sensitive to the two-dimensional hypothesis as long as three-dimensional variations do not significantly alter the Hall electric field structure at this scale.

[25] The proton bounce motion only exists in regions where there is a strong Hall electric field, therefore it ceases as we get away from the X-line. This is the reason why the pressure component P_{ixy} has the a different variation in region B of Figure 5 than in region A. In region A, P_{ixy} is positive and negative, below and above $y = 20$, respectively, and the signs are opposed in region B. The transition from region A to region B is consistent with position where the

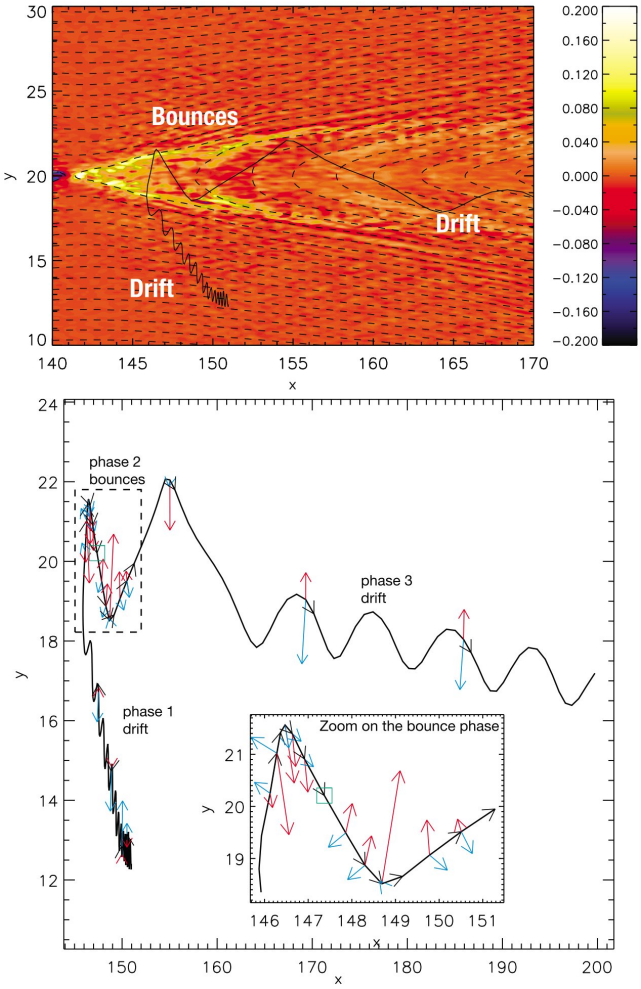

Figure 7. (top) Trajectory of a particle picked in distribution F in Figure 6 represented (solid black line) superposed to the E_x component of the electric field at time t = 105. Dashed black lines represent the in-plane magnetic field lines. (bottom) Trajectory of a particle picked in distribution F in Figure 6 (solid black line). The electric (red arrows) and magnetic (blue arrows) forces felt by the particles are represented at several times on the trajectory.

strong Hall electric field disappears, which can be seen in Figure 2. In region B, this part of the pressure tensor is no longer related to a bounce motion, but to another kinetic mixing effect already pointed out by *Shay et al.* [1998] and *Hoshino et al.* [1998]. This effect is illustrated in Figure 10, which represents the distribution functions in region B. Distribution G has a Maxwellian shape, as expected in the region upstream of the separatrix. Distribution I is located in the center of the current sheet at y = 20 and is consequently symmetric with respect to the v_y = 0 axis. This symmetry is consistent with the fact that P_{ixy} = 0 there. On the other hand, distribution H is located within the jet below the line y = 20. Consistently with the distribution presented by *Shay et al.* [1998, Figure 9a], it consists of a slow Maxwellian core made of protons coming from the upstream region and a bean-like shape distribution made of fast protons coming from the Hall region and accelerated by the bounce mechanism, as the typical trajectory in Figure 7. The symmetry of the distribution around the magnetic field, tilted in the (v_x, v_y) plane, is responsible for the sign of the P_{ixy} com-

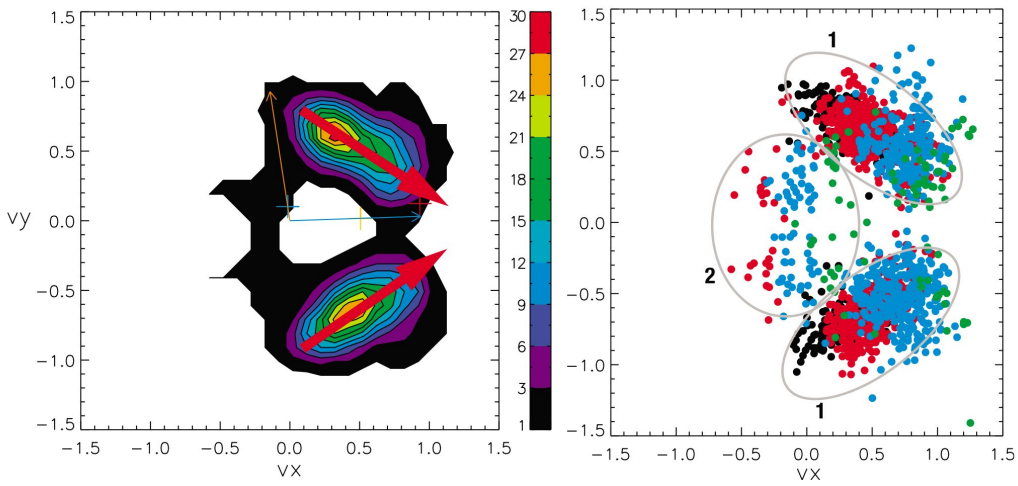

Figure 8. (right) Particles contributing to distribution F in Figure 6 are placed at their position in phase space at $t = 105$. Each particle is colored according to the number of bounces it has experienced between $t = 0$ and $t = 105$. Black, red, blue and green mean respectively 0, 1, 2 and 3 bounces. The two groups labeled "1" correspond to the particles that follow the bounce dynamics and spread in velocity space following the red arrows in Figure 8 (left). The particles labeled "2" appear not to follow the same dynamics but appear in a negligible number. (left) Distribution F in Figure 6 is reported with orange arrows indicating the "motion" in velocity space of the particles, bounce after bounce. This "motion" is confirmed in Figure 8 (right).

ponent of the pressure tensor here. By contributing to the pressure tensor, this mixing effect must also contribute to the local "heating" of the fluid plasma, which might thus not simply result from a local effect [*Drake et al.*, 2008]. At large distances from the X-line often observed in solar wind reconnection events however, the particles accelerated in the decoupling region have probably spread in space so that their contribution to local distributions should be insignificant. One must keep in mind that such distances are not present in simulation domains yet, which so far are still dominated by collisionless mixing effects, as also pointed out by *Lottermoser et al.* [1998].

5. Summary and Future Work

[26] Previous works on collisionless antiparallel magnetic reconnection have motivated us to understand the relationship between particle and fluid dynamics. It is well known that the Hall effect enables a high reconnection rate regime, but the role of the additional piece of physics coming with the kinetic description of the plasma is less understood. Concerning the reconnection dynamics, the proton bulk acceleration plays a central role and we have been interested in knowing to what extent the kinetic description for the protons would change the macroscopic point of view of this important feature. For this issue, we have chosen to use a two-dimensional hybrid code, treating the protons as macroparticles and assuming the electrons to be a fluid for simplicity. Our study have led to several important results:

[27] 1. Fluid dynamics: We have confirmed that the bulk acceleration in the proton decoupling region results from the interaction of the fluid with the Hall electric field, as already mentioned in previous studies [e.g., *Shay et al.*, 2001]. But we have also shown that the pressure force cannot be neglected for the jet formation. In both in-plane directions, this force is important and opposed to the electric field. It appears to maintain the outflow channel open by balancing the electric force. By opening a wider channel than in a fluid model with a polytropic closure [*Shay et al.*, 2001], the pressure is consistently more efficient in slowing the fluid down, resulting in a smaller jet velocity.

[28] 2. Kinetic mechanisms: We have shown, in the antiparallel case, that the pressure is built by a particle velocity anisotropy and thus results from an underlying proton kinetic effect. By analyzing the individual particle dynamics, we have found that each proton, from the upstream to the downstream region, falls into a divergent electrostatic potential well. The angular aperture of the well makes the particle to transfer the kinetic energy gained from the well from the v_y to the v_x component of its velocity over time. Along its trajectory, a particle falling in the well then follows a specific path in the velocity space over time. At a given time and spatial position, the mixing of many particles having experienced a different number of bounces thus appears as a statistical coupling of these velocity components, which, from the macroscopic momentum transport point of view, appears as a pressure force originating from the off-diagonal part of the pressure tensor.

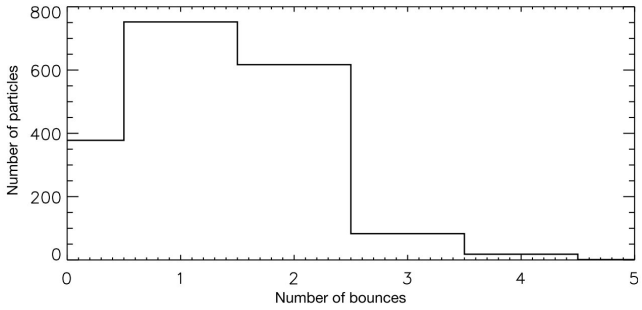

Figure 9. Histogram representing the number of particles versus the number of bounces detected for distribution F in Figure 6.

[29] 3. Observational proxy: We have shown the relationship between the proton dynamics as individual particles and the spatial structure of the in-plane off-diagonal component of the proton pressure tensor. This component is found to have a characteristic quadrupolar structure mapping the proton decoupling region and a different variation outside of it. The correlation of the temporal spacecraft measurement of this component of the pressure tensor with other characteristic quantities such as the proton bulk flow and the magnetic field components could be considered as a new additional proxy of this highly interesting region. This should be the subject of a future study.

[30] Let us now discuss the generality of our results. Several important points should be investigated in the future.

[31] 1. The symmetry: Both the pressure force and the underlying microscopic bounce mechanism rely on the symmetry of the Hall electrostatic potential well. We thus think that all the sources of asymmetry in the system may lead to an evolution toward another mechanism. Among these are of course the macroscopic asymmetry of the initial current sheet within which the magnetic reconnection develops. Asymmetric reconnection is still poorly understood in comparison to the extensively studied symmetrical case, but it has been pointed out many times that a density or magnetic field strength asymmetry results in asymmetric Hall fields [e.g., *Nakamura and Scholer*, 2000; *Mozer and Pritchett*, 2011, and references therein]. Besides, in initially asymmetric configurations, one should expect the distributions to be shaped not only because of the acceleration mechanism, but also because of the mixing of particle populations with different density and temperature. This will lead to an even more complicated kinetic/fluid relationship.

[32] Even if the initial current sheet is symmetric, the presence of an out-of-plane magnetic component (guide field) has also been known for a long time to lead to the asymmetry of the Hall fields [*Eastwood et al.*, 2010a]. It would be interesting to know the critical guide field amplitude regarding the existence of the bounce mechanism, and to know what is the fluid and kinetic behavior above this value.

[33] 2. Asymptotic temperature: The asymptotic plasma in our simulation was rather cold. This configuration may be relevant for magnetotail lobe reconnection [*Wygant et al.*, 2005] or solar wind reconnection [*Gosling*, 2011]. In a warmer configuration, the electrostatic potential well, whose

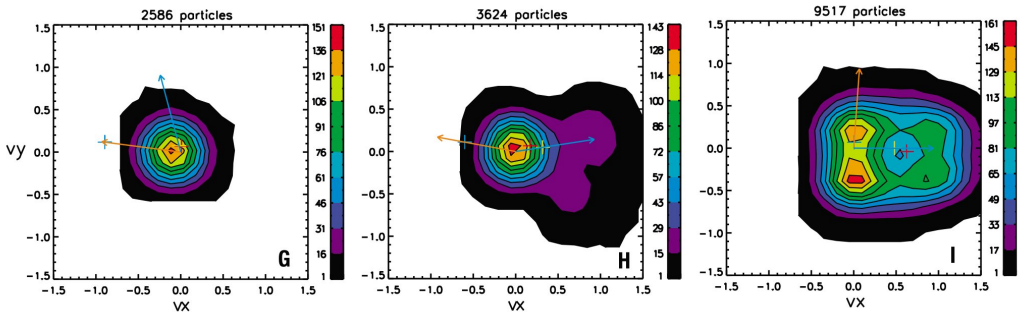

Figure 10. Projections of the proton distribution functions in the $t = 105$. Distributions G, H, and I are measured within the small black boxes visible in Figure 2, from bottom to top at $x = 165$. The blue and orange arrows represent the in-plane direction of the bulk velocity and magnetic field, respectively. The blue, yellow and red crosses represent the in-plane Alfvén speed, bulk speed and $\mathbf{E} \times \mathbf{B}/B^2$ speed, respectively. For each distribution, the number of particles contributed to the distribution is indicated.

depth is mainly determined by the magnetic field energy available, will not trap as many particles as in a cold plasma configuration. If the thermal kinetic energy exceeds the potential depth, one might thus expect to observe different particle behavior. This dependance on the asymptotic temperature should be investigated in future studies. Warmer asymptotic plasma may be relevant for magnetotail reconnection events accelerating the hot sheet plasma.

[34] 3. Electron kinetic physics: Our study initially assumes that the kinetic electron physics has no consequences regardingour results. This is a simplifying assumption that should be checked in the future. Anisotropic electron pressure tensors has been observed by *Drake et al.* [2008] in full kinetic simulations and prove that the electron fluid is not completely frozen in the electromagnetic field in the separatrix region, as explicitly assumed in our model. Recently, interesting yet still debated studies [e.g., *Daughton et al.*, 2006; *Shay et al.*, 2007] question the role of the kinetic electron behavior regarding the global steadiness of the reconnection process. If the tiny electron scale physics can lead to a bursty plasmoid formation, the steady reconnection rate as we present it would be more questionable.

[35] 4. Third dimension: Although the statistical properties of the spacecraft data seems to be consistent with classical two-dimensional reconnection model [*Eastwood et al.*, 2010b], the two-dimensionality of the simulation is still a quite big hypothesis. The protons studied in this papers do not drift significantly in the out-of-plane direction while in the bounce phase of their trajectory. It should be clarified in further studies if this scale is negligible compared to the characteristic self-consistent variations that would develop in a three-dimensional model.

[36] The relatively elementary situation resulting from our simplifications allowed us to study in detail the relationship between kinetic and fluid behaviors. This provides some guide toward understanding more complex configurations in future studies.

[37] **Acknowledgments.** This work has been partly funded by the A.N.R. MAGNET (http://magnet.ens.fr/).

[38] Philippa Browning thanks the reviewers for their assistance in evaluating this paper.

References

Arzner, K., and M. Scholer (2001), Kinetic structure of the post plasmoid plasma sheet during magnetotail reconnection, *J. Geophys. Res.*, *106*, 3827–3844, doi:10.1029/2000JA000179.

Birn, J., et al. (2001), Geospace Environmental Modeling (GEM) magnetic reconnection challenge, *J. Geophys. Res.*, *106*, 3715–3720, doi:10.1029/1999JA900449.

Boris, J. P. (1970), Relativistic plasma simulation-optimization of a hybrid code, paper presented at Fourth Conference on Numerical Simulation of Plasmas, Natl. Res. Lab., Washington, D. C.

Cassak, P. A. (2006), Catastrophe model for the onset of fast magnetic reconnection, Ph.D. thesis, Univ. of Md., College Park.

Daughton, W., J. Scudder, and H. Karimabadi (2006), Fully kinetic simulations of undriven magnetic reconnection with open boundary conditions, *Phys. Plasmas*, *13*(7), 072101, doi:10.1063/1.2218817.

Divin, A., S. Markadis, G. Lapenta, V. S. Semenov, N. V. Erkaev, and H. K. Biernat (2010), Model of electron pressure anisotropy in the electron diffusion region of collisionless magnetic reconnection, *Phys. Plasmas*, *17*(12), 122102, doi:10.1063/1.3521576.

Drake, J. F., M. A. Shay, and M. Swisdak (2008), The Hall fields and fast magnetic reconnection, *Phys. Plasmas*, *15*(4), 042306, doi:10.1063/1.2901194.

Eastwood, J. P., M. A. Shay, T. D. Phan, and M. Øieroset (2010a), Asymmetry of the ion diffusion region Hall electric and magnetic fields during guide field reconnection: Observations and comparison with simulations, *Phys. Rev. Lett.*, *104*(20), 205001, doi:10.1103/PhysRevLett.104.205001.

Eastwood, J. P., T. D. Phan, M. Øieroset, and M. A. Shay (2010b), Average properties of the magnetic reconnection ion diffusion region in the Earth's magnetotail: The 2001–2005 Cluster observations and comparison with simulations, *J. Geophys. Res.*, *115*, A08215, doi:10.1029/2009JA014962.

Fujimoto, K., and R. D. Sydora (2008), Whistler waves associated with magnetic reconnection, *Geophys. Res. Lett.*, *35*, L19112, doi:10.1029/2008GL035201.

Gosling, J. T. (2011), Magnetic reconnection in the solar wind, *Space Sci. Rev.*, *138*, 1–14, doi:10.1007/s11214-011-9747-2.

Harned, D. S. (1982), Quasineutral hybrid simulation of macroscopic plasma phenomena, *J. Comput. Phys.*, *47*, 452–462, doi:10.1016/0021-9991(82)90094-8.

Harris, E. G. (1962), On a plasma sheath separating regions of oppositely directed magnetic field, *Nuovo Cimento*, *23*, 115–121, doi:10.1007/s11214-010-9681-8.

Hesse, M., K. Schindler, J. Birn, and M. Kuznetsova (1999), The diffusion region in collisionless magnetic reconnection, *Phys. Plasmas*, *6*, 1781–1795, doi:10.1063/1.873436.

Hoshino, M., T. Mukai, T. Yamamoto, and S. Kokubun (1998), Ion dynamics in magnetic reconnection: Comparison between numerical simulation and Geotail observations, *J. Geophys. Res.*, *103*, 4509–4530, doi:10.1029/97JA01785.

Karimabadi, H., W. Daughton, and J. Scudder (2007), Multi-scale structure of the electron diffusion region, *Geophys. Res. Lett.*, *34*, L13104, doi:10.1029/2007GL030306.

Lipatov, A. S. (2002), *The Hybrid Multiscale Simulation Technology: An Introduction With Application to Astrophysical and Laboratory Plasmas*, Springer, Berlin.

Lottermoser, R.-F., M. Scholer, and A. P. Matthews (1998), Ion kinetic effects in magnetic reconnection: Hybrid simulations, *J. Geophys. Res.*, *103*, 4547–4560, doi:10.1029/97JA01872.

Mozer, F. S., and P. L. Pritchett (2011), Electron physics of asymmetric magnetic field reconnection, *Space Sci. Rev.*, *158*, 119–143, doi:10.1007/s11214-010-9681-8.

Nagai, T., I. Shinohara, M. Fujimoto, M. Hoshino, Y. Saito, S. Machida, and T. Mukai (2001), Geotail observations of the Hall current system: Evidence of magnetic reconnection in the magnetotail, *J. Geophys. Res.*, *106*, 25,929–25,950, doi:10.1029/2001JA900038.

Nakamura, M., and M. Scholer (2000), Structure of the magnetopause reconnection layer and of flux transfer events: Ion kinetic effects, *J. Geophys. Res.*, *105*, 23,179–23,192, doi:10.1029/2000JA900101.

Parker, E. N. (1957), Sweet's mechanism for merging magnetic fields in conducting fluids, *J. Geophys. Res.*, *62*, 509–520, doi:10.1029/JZ062i004p00509.

Pei, W., R. Horiuchi, and T. Sato (2001), Ion dynamics in steady collisionless driven reconnection, *Phys. Rev. Lett.*, *87*(23), 235003, doi:10.1103/PhysRevLett.87.235003.

Priest, E., and T. Forbes (2000), *Magnetic Reconnection*, Cambridge Univ. Press, Cambridge, U. K.

Shay, M. A., J. F. Drake, R. E. Denton, and D. Biskamp (1998), Structure of the dissipation region during collisionless magnetic reconnection, *J. Geophys. Res.*, *103*, 9165–9176.

Shay, M. A., J. F. Drake, B. N. Rogers, and R. E. Denton (1999), The scaling of collisionless, magnetic reconnection for large systems, *Geophys. Res. Lett.*, *26*, 2163–2166, doi:10.1029/1999GL900481.

Shay, M. A., J. F. Drake, B. N. Rogers, and R. E. Denton (2001), Alfvénic collisionless magnetic reconnection and the Hall term, *J. Geophys. Res.*, *106*, 3759–3772, doi:10.1029/1999JA001007.

Shay, M. A., J. F. Drake, and M. Swisdak (2007), Two-scale structure of the electron dissipation region during collisionless magnetic reconnection, *Phys. Rev. Lett.*, *99*(15), 155002, doi:10.1103/PhysRevLett.99.155002.

Singh, N., M. Yeladandi, T. Somarothu, and B. E. Wells (2010), Features of electron current layers: Comparison between three-dimensional particle-in-cell simulations and Cluster observations, *J. Geophys. Res.*, *115*, A04203, doi:10.1029/2009JA014601.

Smets, R., G. Belmont, D. Delcourt, and L. Rezeau (2007), Diffusion at the Earth magnetopause: Enhancement by Kelvin-Helmholtz instability, *Ann. Geophys.*, *25*, 271–282.

Speiser, T. W. (1965), Particle trajectories in model current sheets: 1. Analytical solutions, *J. Geophys. Res.*, *70*, 4219–4226, doi:10.1029/JZ070i017p04219.

Sweet, P. A. (1958), The neutral point theory of solar flares, in *Electromagnetic Phenomena in Cosmical Physics*, *Proc. IAU Symp.*, vol. 6, edited by B. Lehnert, pp. 123–134, Cambridge Univ. Press, Cambridge, U. K.

Wygant, J. R., et al. (2005), Cluster observations of an intense normal component of the electric field at a thin reconnecting current sheet in the tail and its role in the shock-like acceleration of the ion fluid into the separatrix region, *J. Geophys. Res.*, *110*, A09206, doi:10.1029/2004JA010708.

Yamada, M., R. Kulsrud, and H. Ji (2010), Magnetic reconnection, *Rev. Mod. Phys.*, *82*, 603–664, doi:10.1103/RevModPhys.82.603.

N. Aunai, G. Belmont, and R. Smets, Laboratoire de Physique des Plasmas, Ecole Polytechnique, F-91128 Palaiseau, France. (nicolas.aunai@lpp.polytechnique.fr)

— G —

Energy budget in collisionless magnetic reconnection : ion heating and bulk acceleration

N. Aunai, G. Belmont, R. Smets,
Laboratoire de Physique des Plasmas, Ecole Polytechnique,

Physics of Plasmas
Vol. 18, pages 122901, 2011

PHYSICS OF PLASMAS **18**, 122901 (2011)

Energy budgets in collisionless magnetic reconnection: Ion heating and bulk acceleration

N. Aunai,[a] G. Belmont,[b] and R. Smets[c]
Laboratoire de Physique des Plasmas (LPP), Ecole Polytechnique, Universite Pierre et Marie Curie, Universite Paris 11 Orsay, CNRS, route de Scalay, 91128 Palaiseau, France

(Received 15 July 2011; accepted 21 October 2011; published online 13 December 2011)

This paper investigates the energy transfer in the process of collisionless antiparallel magnetic reconnection. Using two-dimensional hybrid simulations, we measure the increase of the bulk and thermal kinetic energies and compare it to the loss of magnetic energy through a contour surrounding the ion decoupling region. It is shown, for both symmetric and asymmetric configurations, that the loss of magnetic energy is not equally partitioned between heating and acceleration. The heating is found to be dominant and the partition ratio depends on the asymptotic parameters, and future investigations will be needed to understand this dependence. © *2011 American Institute of Physics*. [doi:10.1063/1.3664320]

I. INTRODUCTION

Magnetic reconnection is a universal plasma phenomenon leading to the rapid change of the field line connectivity and to the transfer of a part of the magnetic energy stored in current sheets to the kinetic energy of particles. It plays a key role in many environments, ranging from laboratory devices to astrophysical systems.[1,2] The reconnection rate depends on the asymptotic upstream conditions: plasma density, temperature, magnetic field strength and orientation, etc. When these parameters are identical on both sides of the current sheet, one speaks about symmetric reconnection. Otherwise, reconnection is said to be asymmetric. Although the latter case has been less studied so far, both configurations have been analyzed with scaling arguments.[1,3–7]

Recent scaling laws for asymmetric systems have been proposed.[4] These laws are based on considerations about the energy transfer in the dissipation region. It was assumed that the pressure force does not play a significant role in the energy transfer and, thus, the enthalpy flux variations along the fluid motion was neglected. Simulation results show that half of the incoming Poynting flux was transferred to the bulk kinetic energy, indicating substantial increase of the enthalpy flux. This was observed independently of the upstream density and magnetic field strength. This scaling model of the reconnection rate was shown to be in agreement with MHD,[4,5] two-fluid,[6] full PIC simulations,[8] and even with global modeling of the magnetopause reconnection.[9]

More recently, a new scaling model for asymmetric reconnection was presented,[7] considering the plasma compressibility. Taking into account the enthalpy flux, the model extends the previous incompressible model[4] by including a dependence of the reconnection rate on the asymptotic $\beta = P_{kin}/P_{mag}$, where P_{kin} and P_{mag} are the kinetic and magnetic pressure, respectively. This dependence was found in agreement with MHD simulations. This model also leads to theoretical predictions regarding the energy transfer. In particular, it has been shown that the bulk kinetic energy gains only about one half of the incoming Poynting flux, and the other half of the magnetic energy being transferred to the outgoing enthalpy flux. Although this is still an order of magnitude estimate and cannot be considered as an exact prediction, this theoretical prediction is consistent with previous simulation results[4] and with the energy budget analysis which can be derived from the classic Sweet-Parker model,[3] although in this case, it is the Joule effect that is considered to be responsible for the heating of the plasma.[1] Whether it is compression, Joule heating, a kinetic effect, or a bit of everything, it is reasonable to think that a non-negligible part of the incoming magnetic energy is transfered to the thermal energy because of the approximate force balance in the cross current sheet direction.

In all these models, the ratio between the gain in thermal and bulk kinetic energy is supposed[4] or found[7] to be independent on the upstream condition. It is not *a priori* clear whether this should be the case. Measuring the different energy fluxes around the reconnection region of different MHD simulations, it was recently indeed found[7] that this ratio was not always the same: for symmetric low beta or weakly asymmetric systems, a strict equipartition was found; slight deviations were found in a symmetric and $\beta = 1$ run, or with large density asymmetries ($\rho_1/\rho_2 = 0.1$, $B_1/B_2 = 2/3$), where the lowercase indices 1 and 2 refer to the two different sides of the current sheet. However, it seems that the simulations with a large magnetic field asymmetry ($B_1/B_2 = 1/9$) are far from the equipartition during the simulation time. In all cases where no strict equipartition is observed, it is the enthalpy flux that is favored over the bulk kinetic energy flux. This discrepancy with the theoretical prediction was attributed to the presence of neglected pressure forces along the outflow direction, which balance in part the Laplace force.

The above results were obtained with single fluid simulations with collisional resistivity and closure. It is well

[a]Electronic mail: nicolas.aunai@lpp.polytechnique.fr.
[b]Electronic mail: gerard.belmont@lpp.polytechnique.fr.
[c]Electronic mail: roch.smets@lpp.polytechnique.fr.

known that retaining collisionless effects changes the physics of the reconnection process and in particular the plasma acceleration mechanism.[10–12] In this case, the plasma is accelerated up to a large velocity over a short distance from the X-line (around ten ion inertial lengths), because of the Hall electric field that develops on the separatrices in this region. It has been shown in particular, in the context of symmetric antiparallel reconnection that the pressure force plays an important role in the acceleration of the plasma away from the reconnection region.[11,12] It suggests that a (possibly important) part of the magnetic energy is transferred to the heating of the plasma at the expanse of its bulk acceleration. This study, therefore, aims to evaluate the energy transfers in collisionless magnetic reconnection. We use a hybrid code to model the reconnection process, therefore retaining both bi-fluid effects and the kinetic behavior of the ions, which have been shown to be important in antiparallel or weak guide field configurations.[13–15] Section II describes the model and initial condition of our simulations. Although more realistic than previously used simulation models, we shall see that the hybrid model chosen in our study will not allow electrons to gain energy from the magnetic field either. This assumption is very probably not valid in reality. The hybrid model also precludes the investigation of the production of energetic electrons, which seems to be an important actor of solar events[16] but might be related to a more complex and global mechanism than just be cause by local X point dynamics as investigated in this paper. Considering indeed that hybrid and full PIC simulations lead to similar ion heating and bulk acceleration, we can think that full kinetic electron physics is not dramatically important for the energy transfers, from the local reconnection mechanism point of view. Section III presents the methodology and results obtained for symmetric and asymmetric reconnection. We discuss the results in Sec. IV and describe future investigations.

II. NUMERICAL MODEL AND INITIAL CONDITION

For the sake of qualitative comparison with previous MHD results, we are mainly interested in the acceleration and heating of the ions. We, thus, address the problem in the more realistic but still simplified hybrid framework. Ions are, thus, treated as macroparticles and for this study are considered to be protons. Electrons are considered as a finite mass fluid. For simplicity, we consider an isothermal closure. This assumption, combined with the negligible electron mass, means that the electrons do not participate to the energy budget by varying their thermal or bulk kinetic energy. The heating of the electrons may have for consequences to lower the energy available for proton heating and acceleration, and its importance should be checked in future investigations. We further simplify our modeling by using 2D simulations, i.e., by neglecting the variations in the third dimension. Details regarding the physical equations solved in our hybrid code and their numerical implementation can be found in Ref. 12. The magnetic field and density are normalized to arbitrary values B_0 and n_0 which in this paper are the asymptotic values in the dense upstream region. Distances are normalized to the proton inertial length $\delta_p = c/\omega_p = V_A/\Omega_c$ and time to the inverse of the proton cyclotron frequency $\Omega_c^{-1} = m_p/qB_0$, where $V_A = B_0/\sqrt{n_0\mu_0 m_p}$ is the Alfvén speed, $\omega_p = \sqrt{n_0 e^2/m_p\epsilon_0}$ is the proton plasma frequency, and c is the speed of light in vacuum. The simulation plane is called (x, y), the ignorable coordinate being the z direction. The size of the domain is x_m and y_m in the x and y directions, respectively. The domain is periodic in the x direction and closed by perfect conducting boundaries in the y direction. The electron to ion mass ratio is set to $m_e/m_i = 1/50$.

This paper presents the results of two simulations. In both runs, the magnetic field is initially antiparallel, given by the step function $\mathbf{B} = B_s \tanh((y - y_0)/\lambda)$, where $y_0 = 0.5y_m$, $\lambda = 1$, and $B_s = 1$. In order to have one major X point in the simulation plane and to quickly reach a quasi-steady state regime, we impose initially a magnetic perturbation centered in the middle of the simulation domain. Table I summarizes the simulation parameters for both runs. The runs **A** and **B** are symmetric and asymmetric configurations, respectively. In the asymmetric run, the dense and cold side of the current sheet will be referred by the lowercase indice 1, while the indice 2 will be assigned to the other one. For the two runs, we choose the initial density profile analytically with the formula $n(y) = n_1 + 0.5(n_2 - n_1)(1 + \tanh((y - y_0)/\lambda))$ and calculate the proton temperature accordingly to satisfy the total pressure balance for a given asymptotic value of the plasma β and a constant electron temperature T_e. Note that in both cases, the magnetic field being symmetric, the plasma pressure and β are consequently symmetric too. Run **A** is the hybrid equivalent of the symmetric low beta run of Ref. 7 for which a strict equipartition is observed. Run **B** is close to their density asymmetric runs with a density gradient intermediate between theirs and a symmetric magnetic field.

Both simulations are run until a pseudo steady state is well established for few tens of Ω_c^{-1} and stopped when downstream or upstream boundary conditions begin to limit the physics either by recirculation effect or empty energy reservoir. Because the protons are initially loaded in local Maxwellian distribution functions, neither of the two initial conditions are steady solutions of the Vlasov-Maxwell system. So far, there has been, to our knowledge, no successful attempt in initializing a kinetic equilibrium for such asymmetric current sheets despite some theoretical work.[17] This should be the purpose of future studies. At the beginning of the simulation, the distribution functions within the current sheet are locally modified by protons coming from neighboring different distributions. This mixing effect leads to a slight and rapid reconfiguration of the sheet and emits waves

TABLE I. Parameters for runs **A** and **B**. B_1 and B_2 are the asymptotic magnetic field strength, n_1 and n_2 the asymptotic particle densities. β_p is the asymptotic proton beta, and T_e is the constant and uniform electron temperature. n_p is approximately the total number of macroparticles used for the simulations.

Run	n_1	n_2	β_p	T_e	(n_x, n_y)	(x_m, y_m)	n_p
A	1	1	0.1	0.005	(1024, 512)	(280, 40)	$\approx 5 \cdot 10^7$
B	0.25	1	1.0	0.005	(1024, 1024)	(300, 80)	$\approx 13 \cdot 10^7$

in the domain. These waves have been carefully monitored and do not have important consequences regarding the physics discussed in this paper. Their small effect will be visible in Sec. III. Figure 1 shows the modifications of the current sheet during the early times of the simulation. One can see that the density, uniform at first in the symmetric run, now has a small peak at the center of the current sheet. The panel C of Figure 1 presents the density and magnetic field profiles at $t = 10$ together. The perturbation created within the current sheet is seen to propagate on both sides. The propagation speed and the phase relationship between the two quantities indicate that the perturbation propagates as a fast magnetosonic mode. The same phenomenon appears in the asymmetric run (panels D, E, and F).

III. ENERGY BUDGET ANALYSIS

A. Methodology

For our study, it is necessary to split the total energy in three distinct contributions: the magnetic energy density $B^2/2\mu_0$, the bulk kinetic energy density $K_s \equiv 1/2 m_s n_s v_s^2$, and the thermal kinetic energy density $u_s \equiv 1/2\ Tr(\mathbf{P}_s)$ (where $\mathbf{P}_s$ is the full pressure tensor and $Tr()$ is the trace operator). In these expressions, the s indices stand for *species*, namely electrons and protons here. The Eulerian evolution of these quantities is governed by the following equations:

$$\frac{\partial B^2/(2\mu_0)}{\partial t} + \nabla \cdot (\Pi) = S_m, \tag{1}$$

$$\frac{\partial K_s}{\partial t} + \nabla \cdot (K_s \mathbf{v_s}) = S_{k_s}, \tag{2}$$

$$\frac{\partial u_s}{\partial t} + \nabla \cdot (\mathbf{q_s} + \mathbf{H}_s) = S_{u_s}. \tag{3}$$

Each of these equations has the same form. The left hand side consists of the local time evolution of the energy density and the local divergence of this energy density flux. On the right hand side, are the source terms, which result from the transfers between the different forms of energies. When summed over all plasma species and magnetic energy, all the source terms cancel out, because of the conservation of the total energy, hence $S_m + \sum_s (S_{k_s} + S_{u_s}) = 0$.

In Eq. (1), the magnetic energy is transported by the Poynting flux, defined as $\mathbf{\Pi} \equiv \mathbf{E} \times \mathbf{B}/\mu_0$, where $\mathbf{E}$ is the electric field and μ_0 is the vacuum magnetic permeability, respectively. The magnetic energy source term is $S_m \equiv -\mathbf{j} \cdot \mathbf{E}$,

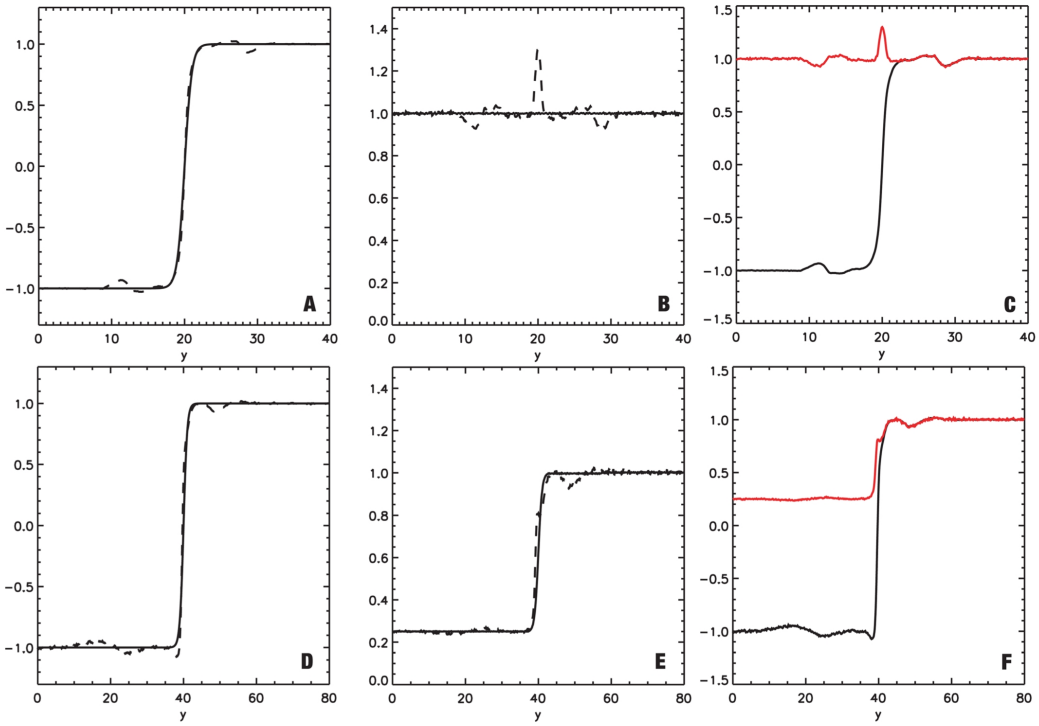

FIG. 1. (Color online) Initial modifications of the current sheet after $\Delta t = 10$. Solid lines are made at $t = 0$ while dashed line profiles are made are $t = 10$. Top panels present data from the symmetric run while bottom panels concern the asymmetric one. Panels A and D present the profiles of the magnetic field B_x. Panels B and E show the density profiles. Panels C and F show the density and magnetic field profiles together at $t = 10$ and reveals that both perturbations are in phase.

where **j** is the total current. In Eq. (2), the bulk kinetic energy density source term is $S_{k_s} \equiv nq_s \mathbf{v}_s \cdot \mathbf{E} - (\nabla \cdot \mathbf{P}_s) \cdot \mathbf{v}_s$, which represents the power of the electric force summed with the power of the pressure force exerted on the flow at velocity $\mathbf{v}_s$. Let us note that S_m is just the opposite of the first term of S_{k_s} summed over all particle species; it represents a link between magnetic and bulk kinetic energies. The second term of S_{k_s} appears to be the opposite of S_{u_s}, the pressure force thus represents the link between bulk and thermal energies. The thermal flux is the sum of the heat flux vector $\mathbf{q}_s$ and the enthalpy $\mathbf{H_s} \equiv u_s \mathbf{v}_s + \mathbf{P}_s \cdot \mathbf{v}_s$. Although these quantities play the same role regarding the heat transport as for a thermodynamical fluid, they are not simply related to lower moments of the distribution. Equations (1)–(3) are obtained from the Vlasov equation with no more assumptions and do not form a closed set of equations. All their terms can, however, be calculated locally as soon as one knows the distribution function of the particles.

For both simulations, we have evaluated the different terms of Eqs. (1)–(3) for the protons, by integrating them over a closed contour. Because quantities are now referring to protons, we drop the indices*s*. At each time, we know exactly the proportion of the different energy forms entering and leaving the contour and can thus measure the energy transfers. In the collisionless regime, it has been shown that the reconnection dynamics is determined in a key region surrounding the reconnection site, where protons are decoupled from the magnetic field.[18,19] In this so-called Hall region, electrons accelerated in a tiny region around the X-line create currents which drag very quickly the magnetic field in the out-of-plane direction while crossing the separatrices. The electron ideal electric field, which develops consistently with this magnetic motion, heats the protons and accelerate them in average to a velocity close to the upstream Alfvén speed. The above physics incites to choose a closed contour C having a rectangular shape surrounding the Hall region. The boundaries of the contour in the downstream direction are determined as the location where the Hall electric field equals the ideal MHD electric field. This location is found to coincide with the one where the proton jet velocity reaches the maximum value and stays approximately constant further away (not shown). Once the downstream boundaries are set, the width of the contour is chosen so that it is a bit larger than the proton jet during the whole simulation, i.e., the corners of our rectangle stay just upstream the separatrices. The top panel of Figure 2 illustrates this explanation, showing the closed contour used for the asymmetric run, superposed to the proton mean velocity projected in the x direction. The bottom panel reveals the extent of the Hall region by showing the E_z electric field where the Hall term is dominant. We call Γ_i the two inflow edges of C, and Γ_o the two outflow edges. In the asymmetric case, Γ_i can be split into Γ_{i1} and Γ_{i2} if one needs to separate the two different inflow edges. For both symmetric and asymmetric runs, we have slightly changed the size of the contour by a few proton inertial lengths and see only minor quantitative differences with the plot presented in Secs. III B and III C. In both cases, the proton decoupling region, as visualized on Fig. 2 for the asymmetric case, keeps more or less the same aspect ratio and slowly elongates as the reconnection rate decreases, certainly because of the closed upstream boundary condition.

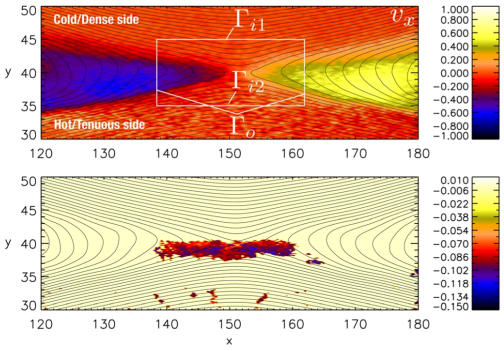

FIG. 2. (Color online) The two panels are made from the asymmetric run at $t = 105$. Top panel: The proton fluid velocity in the x direction is represented by a color code. The white rectangle is the contour chosen to evaluate the energy transfers. Upstream (Γ_{i1}, Γ_{i2}) and downstream (Γ_o) defined in Sec. III A are represented. Bottom panel: Color code representing the E_z electric field where the Hall term is larger than the ideal term, and 0 elsewhere. For both panels, the black lines represent the in-plane projection of the magnetic field lines.

B. Symmetric reconnection

The energy budgets for the symmetric run can be found in the left panels of Figure 3. We first consider the time evolution of the thermal and bulk kinetic energy gain $E_u(t)$ and $E_k(t)$, respectively. Then we look at the incoming (uppercase indice i) and outgoing fluxes (uppercase indice o) for bulk ($\phi_k^{i,o}(t)$) and thermal ($\phi_u^{i,o}(t)$) energies independently.

The first panel shows the time evolutions $E_k(t)$ and $E_u(t)$, calculated as follows:

$$E_u(t) = \frac{1}{|E_m(t)|} \int_{A_C} S_u(x, y, t) dx dy, \tag{4}$$

$$E_k(t) = \frac{1}{|E_m(t)|} \int_{A_C} S_k(x, y, t) dx dy, \tag{5}$$

$$E_m(t) = \int_{A_C} S_m(x, y, t) dx dy, \tag{6}$$

where A_C represents the area closed by the contour C. The normalization by the magnetic energy loss within the contour (Eq. (6)) allows to quickly visualize which part of this energy goes to the heat and which goes to the bulk energy. One can note first that, omitting rapid fluctuations related to wave activity or magnetic island creation, the energy transfer is approximately steady for times $t \approx 50\Omega_{ci}^{-1}$. The duration of the previous unsteady phase corresponds to the time necessary for the plasma bulge (related to the first reconnected field line) to leave the contour. Second, the two curves do not meet in average, meaning that the magnetic energy loss is not equally partitioned between the thermal and bulk kinetic energies, contrary to what is observed in the similar MHD case.[7] Here, the thermal energy is favored, taking as

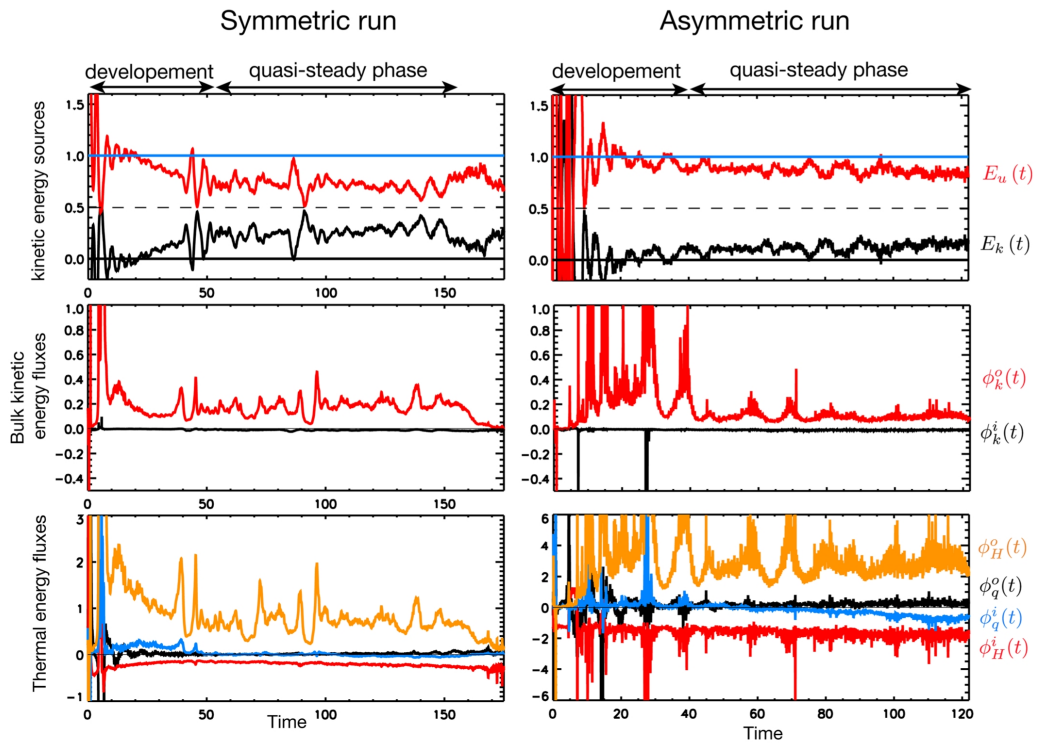

FIG. 3. (Color online) Energy budget for the run **A** (left) and **B** (right). Top panels: Time evolution of the bulk and thermal kinetic energies sources within the contour C. The blue (straight) line represents the total magnetic energy loss within the contour, and the black dashed line the equipartition. Middle panels: Time evolution of the incoming and outgoing bulk kinetic energy fluxes. Bottom panels: Time evolution of the incoming and outgoing enthalpy and heat fluxes.

much as roughly 75% of the magnetic energy loss. The bulk kinetic energy increases up to roughly the remaining 25%.

The second panel focuses on the time evolution of incoming and outgoing bulk energy fluxes. The two fluxes are normalized to the instantaneous incoming Poynting flux and calculated with the following equations:

$$\phi_k^{i,o}(t) = \frac{1}{|\phi_m(t)|}\int_{\Gamma_{i,o}} K(l,t)\mathbf{v}(l,t)\cdot\mathbf{dl}, \tag{7}$$

$$\phi_m(t) = \int_{\Gamma_i} \Pi(l,t)\cdot\mathbf{dl}. \tag{8}$$

As expected, we see that the incoming bulk kinetic energy flux is completely negligible. We logically find that outgoing bulk kinetic energy flux $\phi_k^o(t)$ is approximately equal to the production $E_k(t)$ of the energy density within the contour.

The last panel shows the time evolution of the heat flux and enthalpy flux at the upstream and downstream boundaries. Again, the fluxes are normalized by the instantaneous incoming Poynting flux, following the equation:

$$\phi_u^{i,o}(t) = \frac{1}{|\phi_m(t)|}\int_{\Gamma_{i,o}} (\mathbf{H}(l,t)+\mathbf{q}(l,t))\cdot\mathbf{dl}. \tag{9}$$

We define the enthalpy flux φ_H and the heat flux φ_q as the first and second term of Eq. (9). We can thus write

$$\phi_u^{i,o}(t) = \phi_H^{i,o}(t) + \phi_q^{i,o}(t). \tag{10}$$

The plot first reveals that the contribution of the heat flux vector can be neglected, i.e., $\phi_u^{i,o} \approx \phi_H^{i,o}$. The normalized incoming enthalpy flux is small, which is expected for a low beta plasma, and is greatly increased through the contour to match the high downstream value.

C. Asymmetric reconnection

The same quantities as for the symmetric simulation are presented for the asymmetric run in the right panels of Figure 3. The top panel indicates that during the steady phase, thermal energy increases much more than the bulk kinetic energy, taking roughly 85% of the magnetic energy loss. As for the symmetric run, the second panel confirms that the incoming bulk kinetic energy flux is negligible compared to the incoming Poynting flux. The last panel reveals that again the great majority of the thermal flux comes from the enthalpy flux, which is greatly enhanced between the upstream and downstream boundaries.

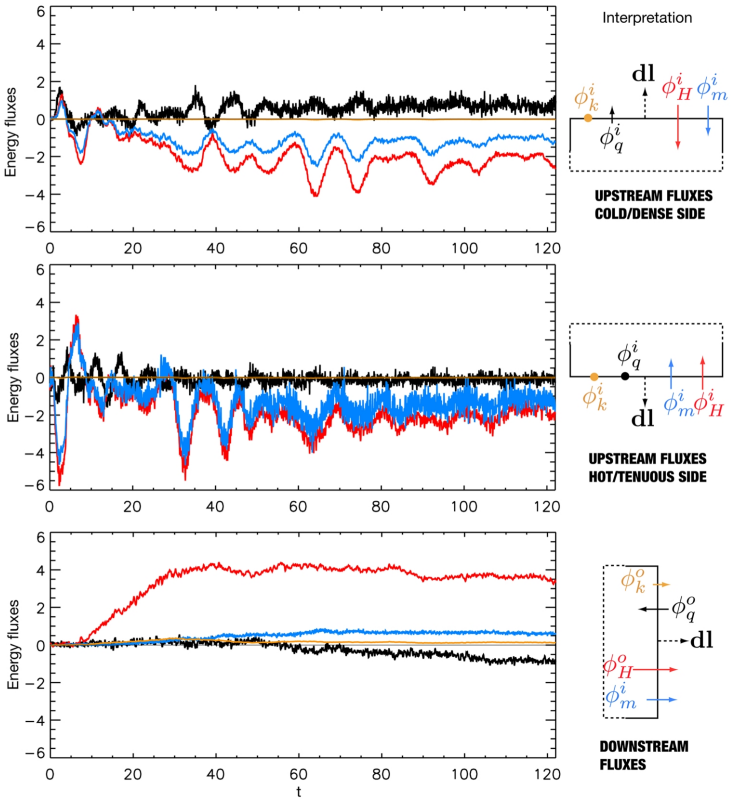

FIG. 4. (Color online) Time evolution of the different energy fluxes (not normalized by the Poynting flux) at the dense upstream side (top panel), tenuous upstream side (middle panel), and downstream side (bottom panel). A sketch is represented on the right of each panel to clarify the meaning of the curves. A color is attributed to each flux and the arrows have a length and direction indicating the relative amplitude of the corresponding flux and whether it is entering or leaving the contour. The surface vector **dl** indicates that positive fluxes are exiting the contour while negative fluxes are coming in.

Because the plasmas on both sides of the current sheet are different, it is interesting to look at their respective contribution to the above energy budgets. Figure 4 represents all the energy fluxes for both upstream boundaries (Γ_{i1} and Γ_{i2}) as well as for the downstream edges (Γ_o). At the upstream edges first of all, one can notice that both enthalpy and Poynting fluxes are roughly symmetrical (although the fluxes on the tenuous side are more noisy because of the smaller number of macroparticles on this side). The reason is that the plasma beta is symmetrical. However, there is a clear difference in the contribution of the heat flux vector. While it is zero on average at the tenuous edge, it has a clear positive contribution to the thermal flux on the dense edge, meaning that a small heat flux is going out of the contour, contrary to all other fluxes here. At the downstream boundary of the contour, the enthalpy flux is by far the most important. The bulk kinetic energy flux is even smaller than the outgoing Poynting flux. Note that there is also a small negative contribution of the heat flux vector, meaning that it is directed inward, again opposite to all other fluxes here.

The small contribution of the heat flux vector to the thermal flux can be understood by considering the collisionless mixing of the cold and comparatively hot proton populations. Figure 5 represents the time evolution of different locations in a cut through the X-line along the y direction. As previous studies, we notice the small but persistent shift between the X point and the stagnation point; the latter being on the tenuous side of the former. This measure is made in the simulation frame because no significant drift of the X-line was found during the simulation. Both points are embedded in the Hall region whose extension is roughly constant. One can then notice that the region where both proton species can be found (the mixing layer) is much larger than previous structures and asymmetric with respect to the X point. It extends further on the cold side than it does on the tenuous

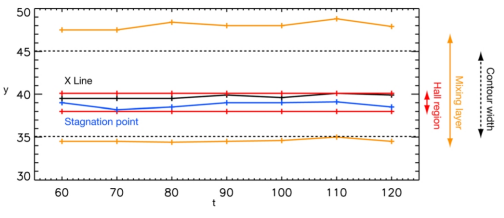

FIG. 5. (Color online) Time evolution of the main structures of the reconnection region along a cut in the y direction through the X-line for run **B**.

one because of the difference of energy between the two populations. This mixing effect has been reported before.[14] The position of our contour relatively to the boundaries of the mixing layer explains the small heat flux at the Γ_{i1} edge. This edge is indeed within the mixing layer while the edge Γ_{i2} is right at its boundary. The heat flux at the cold edge corresponds to the penetration of the hot plasma into the cold one. Similarly, the small inward flux observed at the downstream edge should correspond with the transfer of the hot plasma into the cold one along the field lines.

IV. SUMMARY AND FUTURE WORK

The observation of fast plasma jets, crucial for transporting the magnetic flux away from the reconnection region, often leads to the conclusion that the process dominantly transfers the incoming magnetic energy into bulk kinetic energy. It is however not *a priori* obvious that the gain of thermal energy is negligible, and not obvious either that the ratio between thermal and convective energy gains does not depend on the (possibly asymmetric) asymptotic plasma pressure and magnetic field strength. In this paper, we have used a two-dimensional hybrid numerical model to investigate the energy transfers within the proton decoupling region during the magnetic reconnection process. This model is more realistic than previous single fluid models that have investigated energy transfers because it retains both the Hall effect and the ion kinetic behavior. However, this study cannot discriminate the role of one and the other. A comparison between two-fluid and hybrid models would allow one to understand whether the kinetic behavior of the ions significantly changes the energy transfer. We have furthermore assumed an isothermal closure for the electron fluid for simplicity. If any, the role of the electron pressure force in the energy budget is expected to lower the proton energy increase, its importance should be investigated in future studies via full kinetic simulations. We have considered the case of antiparallel reconnection, with two different initial conditions: a cold symmetric current sheet and an asymmetric current sheet with symmetric plasma pressure. For both cases, it appears clearly that the magnetic energy entering in the ion decoupling region is mainly converted in thermal energy. This general dominance of the thermal flux over the bulk kinetic energy flux results from the important role of the pressure force in the cross current direction but also in the downstream direction, as previously pointed out in the MHD case[7] and in the kinetic case.[11,12] When kinetic behavior of the ions is retained, the microscopic origin of the thermal energy in this region is however not necessarily a compression (local increase of the density) but may be related to the individual proton dynamics or mixing effects appearing in the pressure tensor via the structuring of the distribution function.[12] In general, the heat flux vector can be neglected but can however be non-zero in the asymmetric case in regions where plasmas with different temperatures mix together. This study also shows that the ratio between the gain in bulk kinetic energy and the gain in thermal kinetic energy is not constant. A parametric study is therefore required to understand how it depends on asymptotic parameters.

ACKNOWLEDGMENTS

The authors wish to thank the ANR MAGNET (http://magnet.ens.fr/) for participating in the funding of this work.

[1]E. Priest and T. Forbes, *Magnetic Reconnection* (Cambridge University Press, Cambridge, UK, 2000), p. 612.
[2]M. Yamada, R. Kulsrud, and H. Ji, Rev. Mod. Phys. **82**, 603 (2010).
[3]E. N. Parker, J. Geophys. Res. **62**, 509, doi:10.1029/JZ062i004p00509 (1957).
[4]P. A. Cassak and M. A. Shay, Phys. Plasmas **14**, 2114 (2007).
[5]J. Birn, J. E. Borovsky, and M. Hesse, Phys. Plasmas **15**, 2101 (2008).
[6]P. A. Cassak and M. A. Shay, Geophys. Res. Lett. **35**, 19102, doi:10.1029/2008GL035268 (2008).
[7]J. Birn, J. E. Borovsky, M. Hesse, and K. Schindler, Phys. Plasmas **17**, 052108 (2010).
[8]K. Malakit, M. A. Shay, P. A. Cassak, and C. Bard, J. Geophys. Res. **115**, 10223, doi:10.1029/2010JA015452 (2010).
[9]J. E. Borovsky, M. Hesse, J. Birn, and M. M. Kuznetsova, J. Geophys. Res. **113**, 07210, doi:10.1029/2007JA012645 (2008).
[10]M. A. Shay, J. F. Drake, B. N. Rogers, and R. E. Denton, Geophys. Res. Lett. **26**, 2163, doi:10.1029/1999GL900481 (1999).
[11]N. Aunai, G. Belmont, and R. Smets, C. R. Phys. **12**, 141 (2011).
[12]N. Aunai, G. Belmont, and R. Smets, J. Geophys. Res. **116**, 09232, doi:10.1029/2011JA016688 (2011).
[13]R.-F. Lottermoser, M. Scholer, and A. P. Matthews, J. Geophys. Res. **103**, 4547, doi:10.1029/97JA01872 (1998).
[14]M. Nakamura and M. Scholer, J. Geophys. Res. **105**, 23179, doi:10.1029/2000JA900101 (2000).
[15]M. A. Shay, J. F. Drake, R. E. Denton, and D. Biskamp, J. Geophys. Res. **103**, 9165, doi:10.1029/97JA03528 (1998).
[16]J. A. Miller, P. J. Cargill, A. G. Emslie, G. D. Holman, B. R. Dennis, T. N. LaRosa, R. M. Winglee, S. G. Benka, and S. Tsuneta, J. Geophys. Res. **102**, 14631, doi:10.1029/97JA00976 (1997).
[17]M. Roth, J. de Keyser, and M. M. Kuznetsova, Space Sci. Rev. **76**, 251 (1996).
[18]J. Birn, J. F. Drake, M. A. Shay, B. N. Rogers, R. E. Denton, M. Hesse, M. Kuznetsova, Z. W. Ma, A. Bhattacharjee, A. Otto, and P. L. Pritchett, J. Geophys. Res. **106**, 3715, doi:10.1029/1999JA900449 (2001).
[19]J. F. Drake, M. A. Shay, and M. Swisdak, Phys. Plasmas **15**, 042306 (2008).

— H —

Kinetic equilibrium for an asymetric tangential layer

G. Belmont, N. Aunai, R. Smets,
Laboratoire de Physique des Plasmas, Ecole Polytechnique,

Physics of Plasmas
Vol. 19, pages 022108, 2012

PHYSICS OF PLASMAS **19**, 022108 (2012)

Kinetic equilibrium for an asymmetric tangential layer

G. Belmont,[a] N. Aunai, and R. Smets
Laboratoire de Physique des Plasmas (LPP), CNRS/Ecole Polytechnique/UPMC/Université Paris-Sud 11, Ecole Polytechnique, Route de Saclay, 91128 Palaiseau, France

(Received 27 September 2011; accepted 15 January 2012; published online 21 February 2012)

Finding kinetic (Vlasov) equilibria for tangential current layers is a long standing problem, especially in the context of reconnection studies, when the magnetic field reverses. Its solution is of pivotal interest for both theoretical and technical reasons when such layers must be used for initializing kinetic simulations. The famous Harris equilibrium is known to be limited to symmetric layers surrounded by vacuum, with constant ion and electron flow velocities, and with current variation purely dependent on density variation. It is clearly not suited for the "magnetopause-like" layers, which separate two plasmas of different densities and temperatures, and for which the localization of the current density $\mathbf{j} = n\delta\mathbf{v}$ is due to the localization of the electron-to-ion velocity difference $\delta\mathbf{v}$ and not of the density n. We present here a practical method for constructing a Vlasov stationary solution in the asymmetric case, extending the standard theoretical methods based on the particle motion invariants. We show that, in the case investigated of a coplanar reversal of the magnetic field without electrostatic field, the distribution function must necessarily be a multi-valued function of the invariants to get asymmetric profiles for the plasma parameters together with a symmetric current profile. We show also how the concept of "accessibility" makes these multi-valued functions possible, due to the particle excursion inside the layer being limited by the Larmor radius. In the presented method, the current profile across the layer is chosen as an input, while the ion density and temperature profiles in between the two asymptotic imposed values are a result of the calculation. It is shown that, assuming the distribution is continuous along the layer normal, these profiles have always a more complex profile than the profile of the current density and extends on a larger thickness. The different components of the pressure tensor are also outputs of the calculation and some conclusions concerning the symmetries of this tensor are pointed out. [doi:10.1063/1.3685707]

I. INTRODUCTION

Thin current layers are ubiquitous in space plasmas. In the absence of magnetic reconnection, they occur a priori to be tangential whenever they are formed at the interface between two magnetized plasmas of different origins that are pushed against each other. The terrestrial magnetopause, which lies between the solar wind plasma and the magnetospheric one, is a typical and well-documented example of such a boundary. Its stability with respect to the so-called "tearing instabilities,"[1,2] and more generally to any instability implying reconnection, is a question of prime importance. Most of the magnetospheric processes, in particular the magnetic substorms and the consecutive auroras, originate in the penetration of solar wind magnetic flux and matter inside the magnetosphere through the boundary. The reconnection allowing this penetration is likely to occur preferentially at the places on the magnetopause where the magnetic field reverses. The most favorable configuration is even when the magnetic field reverses in a coplanar manner, without guide field nor rotation, i.e., going through a strictly null value.[2,3] We will focus on this case hereafter.

As far as different equilibria do exist for a magnetopause-like current layer, their stability is likely to strongly depend on their plasma and field profiles along the normal. From a "fluid" point of view, many different equilibria can actually easily be built, which has allowed for many magnetohydrodynamic (MHD) stability studies (see for instance Refs. 4 or 5). For 1D equilibria, the only constraint is that the total pressure $P + B^2/2\mu_o$ be constant all along the layer normal. In contrast, the problem is much more complex when the layer thickness becomes of the order of the ion Larmor radius or thinner, making necessary a kinetic description. In this case, not only the macroscopic moment profiles have to be known but also the complete distribution functions do as well. Much fewer equilibria of this kind exist in the literature.[6–11] Yet, it is clear that any stability analysis is questionable as long as the profiles cannot be known since the stability of an equilibrium depends, in general, not only on the asymptotic distributions on both sides but also on the distribution variation profiles between them.

In kinetic simulation studies, full PIC (Particle In Cell), hybrid PIC, or Vlasov, this problem arises in the choice of an initialization. For magnetopause-like layers, most authors usually start with Maxwellian distributions, with just appropriate moments to fulfill the pressure balance condition. This is not a kinetic equilibrium and the system is actually not stationary in this case: waves are emitted from the layer from the very first time steps, which can eventually be reflected back in the system, depending on the boundary conditions.

[a]Electronic mail: gerard.belmont@lpp.polytechnique.fr.

If magnetic islands develop, one does not know to what extent the conditions of their formation is independent of this initial non equilibrium. It is indeed possible, as often argued, that the system could naturally converge rapidly to a kinetic equilibrium before the tearing instability develops. However, this is never guaranteed. Even in this case, one cannot control the equilibrium in which the instability develops; therefore, studying the stability as a function of the equilibrium profiles is not possible.

The most famous kinetic equilibrium in the literature is the so-called "Harris equilibrium."[6] This equilibrium consists of ions and electrons drifting at a constant velocity everywhere, so that the current density is localized in the layer only because the density itself is localized. Such a layer, which is by nature symmetric and surrounded by vacuum, has been frequently used, with different generalizations, for mimicking layers such as the plasma sheet of the terrestrial magnetotail. On the contrary, it is obviously not suitable for modeling the magnetopause-like layers, since these layers separate two media with different densities and different temperatures and since the localization of the current density $\mathbf{j} = n\delta\mathbf{v}$ comes from the cancellation of the electron-to-ion velocity difference $\delta\mathbf{v}$ on both sides and not from the cancellation of the density n. It can be reminded that a rather trivial modification of the original Harris equilibrium consists in adding a constant, Maxwellian population everywhere, with a given temperature. It indeed provides a new equilibrium, but (1) it remains symmetric and (2) it has a very special—and unrealistic—distribution function: since the new population does not carry any current, it introduces a new peak in $v = 0$, which is superposed with the original Harris population, which has a peak at $v \neq 0$. This may even cause a kinetic instability not related to the tearing mode.[12,13] Controlling the shape of the velocity distribution function, with the possible associated instabilities, is one of the important issues in the present study.

In this paper, as said above, we investigate the most basic case of a coplanar layer with a null sheet, when the magnetic field reverses without guide field or rotation, as in the Harris sheet. The introduction of a constant guide field or of a rotation should be possible without difficulty following the principles presented here, but these extensions are kept for future works. The configuration considered is the most favorable for reconnection and does actually correspond to many of the simulations of this phenomenon. In this configuration, the magnetic pressure variation is balanced by the normal component of the particle pressure tensor (and/or by an electrostatic force, see next paragraph). It is worth noticing, however, that the hypothesis used here of a coplanar layer is quite different from those of the papers that consider force-free equilibria, such as Ref. 11. In these models, neither the magnetic pressure nor the normal particle pressure varies: the magnetic field just rotates without changing its modulus.

The value of the electrostatic field makes another important difference between the models. Contrary to most of them, we suppose here that the electrostatic field is zero (as in Harris layer). Having in mind sketches inspired by some of the first pioneer plasma works in the field,[14] popularized by Ref. 15 and often reproduced (e.g., Ref. 16), this choice may appear surprising as one may think that the self-consistent magnetopause equilibrium is essentially based on this electrostatic field, due to a space charge raising from the difference in Larmor radius between ions and electrons. In these sketches, the particle trajectories are drawn in the hypothesis of an infinitely sharp magnetic boundary while the found trajectories actually imply a thick current layer. This certainly makes quite questionable the classical image of an electrostatic field necessary to maintain quasi-neutrality. It is worth recalling more generally that the role of the electrostatic field to limit the charge separation, when considering a direction perpendicular to the static magnetic field, cannot be invoked as simply as it can be for the parallel direction (or in the absence of magnetic field). In the case of a charge separation on a scale larger than the Larmor radius, in particular, it is well-known that the most important effect of the electric field is to drive a particle drift perpendicular to the direction of the original charge separation, which is clearly quite unable to limit it. It is true, nevertheless, that many recent models and simulations do show strong electric fields forming near the current layer. The reasons for the presence of these electric fields are probably diverse. For PIC simulations (see particularly, Ref. 17), this may be understood by a simple argument: when a simulation is not initialized with a kinetic equilibrium, the quasi-neutrality that is ensured in the initial distributions becomes violated after half a gyroperiod, because of the different gyroradii of ions and electrons. This may lead to a strong—and a priori unphysical—electric field. A similar argument holds for the theoretical models: the electric field is indeed self-consistent in all the most recent of them, but its value strongly depends on the analytical forms chosen for the two velocity distributions (ions and electrons). As long as these choices remain arbitrary, the behaviors they imply for both populations are different and uncontrolled. This can also lead to unrealistically large electrostatic fields. Keeping the electrostatic field at a reasonable value would mean that one is able to find conditions on the two-species distributions to remain close to quasi-neutrality, even in the absence of electric field. This is a difficult problem. It is worth noticing that quite similar problems (in toroidal geometry) are investigated in fusion studies. Initialization of gyrokinetic codes such as GYSELA with local Maxwellian distributions also gives rise to spurious electric fields. Finding kinetic equilibria is, therefore, also necessary to bypass this difficulty, and this determination demands special care to avoid charge separation that is too large.[18,19] The question of the electrostatic field is different in hybrid simulations where quasi-neutrality is assumed in the basic equations that are solved. In this case, the profile of the electric field seems to be an independent function, which can be fixed arbitrarily. The only constraint is that the two asymptotic values (in the right frame) are zero if there is no velocity shear between the two media. For the real magnetopause, which is neither perfectly 1-D nor perfectly stationary, this function could be fixed by the history of the layer or by remote boundary conditions in the tangential directions. Even if our hypothesis of no electrostatic field at all may seem simplistic and arbitrary, we think that it is not fully unrealistic and that it has the advantage of being physically

explicit. This also allows us to demonstrate that asymmetric equilibria can indeed be found without electrostatic field, which was not obvious hitherto. The limits of this assumption should be investigated in future simulation studies.

The general method for finding kinetic equilibria is to express the particle distribution functions $f_\alpha(\mathbf{v},\mathbf{r})$ of the different species α as functions of the particle invariants of motion $f_\alpha(\mathbf{r},\mathbf{v}) = g_\alpha(\mathbf{I})$ (see for instance Ref. 8 for a review dating from 1995). Whatever the functions g_α chosen, the Vlasov equation grants that the distributions are constant in time and, therefore, that an equilibrium has indeed been found. This same basic principle has been used to construct the Harris equilibrium and all the other existing ones, including the present work. The most famous paper is Ref. 20, who could exhibit several particular solutions, corresponding to different functions g_α. He showed how linear combinations of these particular solutions can provide further solutions to the system. These may be more realistic and possibly closer to practical applications. In Ref. 10, the author generalized the preceding work by replacing the linear combination of a discrete set of particular solutions by a continuous integral of them, so obtaining a larger class of particular solutions. The same author, in Ref. 21, even investigated the pressure nongyrotropy of his solutions, which is an interesting problem on which we will come back in the present paper.

Even if the above general principle for finding kinetic equilibria is well-known, its implementation generally runs into difficulties, when one has to choose the g_α functions for a practical application. The main limitations include the following:

(1) If the "direct problem" is easy, i.e., determining the profiles for all macroscopic parameters (current, pressure, density,.) from given functions g_α, the "inverse problem", i.e., determining the g_α functions in order to prescribe some macroscopic profiles, is still not generally solved. Of course, the"inverse problem" is much more interesting from the modeling viewpoint.
(2) For symmetric **B** profiles (with $B=0$ at the center) and in the absence of electrostatic field, all the usual choices for the g_α functions (single-valued) unavoidably lead to symmetric plasma profiles: we will show that any asymmetry demands multi-valued functions that have not been considered hitherto. All the asymmetric plasma profiles existing in the literature have actually been based on different hypotheses: asymmetric current density or existence of an electric field.
(3) The functions g_α have to be chosen separately for the different species. This makes the choice still more difficult to manage, especially with respect to the question of charge separation and electrostatic field explained just above. Taking, as usual, the two functions identical is quite arbitrary, since the finite Larmor radius (FLR) effects should appear at quite different scales for ions and electrons.

All these difficulties explain, for a large part, why the theoretical kinetic equilibria existing in the literature are almost never practically used for initializing simulations (except for a few gyrokinetic studies in fusion[18,19]).

In Sec. II, the general method using the invariants of motion will be recalled, and it will be shown how the concept of accessibility demands to generalize it to multi-valued functions. Then, the practical method that we propose for constructing an asymmetric equilibrium will be presented in Sec. III. As this method yields an infinity of solutions, we will explain in Sec. IV how one can manage to select some of them thanks to a little analytical model close to exact kinetic solutions. The main characteristics of the solutions will then be presented in Sec. V, before a short discussion and a summary of the conclusions.

II. INVARIANTS AND THE CONCEPT OF ACCESSIBILITY

The general method for constructing a 1-D kinetic equilibrium consists of imposing that the distribution function $f(\mathbf{v},\mathbf{r})$ of each particle species depends on the three velocity components $\mathbf{v} = (v_x, v_y, v_z)$ of the particles only via their invariants of motion. In this paper, we consider a current layer without an electric field (in the given reference frame), with a normal in the y direction and a magnetic field always in the x direction. One imposes that $f(\mathbf{v},\mathbf{r}) = g(E, p_z, p_x)$, where $E = m(v_x^2 + v_y^2 + v_z^2)/2$ is the energy, $p_z = mv_z + qA_z$ is the z generalized momentum, A_z being the z component of the vector potential, and $p_x = mv_x$ is the x momentum. This reduces a priori the dimension of the variable space (velocity + configuration) from six to three and grants the stationarity of the result, whatever the function g chosen. The third invariant p_y will actually be ignored in this paper, i.e., the functions g will be supposed independent of it. When looking to a 1-D localized current layer as we do here, the dependence on p_x is indeed fully determined by the assumed asymptotic states. Whenever these states are supposed isotropic, i.e., depending only on the energy E, the independence on p_x remains valid everywhere in the layer (since g does not depend on y). This allows diminishing the dimension of the variable space of one unit more.

From basic local physics, very few properties are actually imposed for the function g. The distribution function itself $f(\mathbf{v}, y)$ can reasonably be supposed a continuous and single-valued function of $\mathbf{v}$ for each y-value along the normal. But it does not automatically imply that the g function, which does not explicitly depend on y, has the same properties. The reason lies in the notion of particle accessibility, which has been put forward in Ref. 22 and used for instance in Ref. 23. The principle is sketched in Fig. 1. At a given position, y, along the normal, the distribution function of the entire $\mathbf{v}$ space corresponds to the interior of the parabola in the (E, p_z) plane. This is simply because the energy is always larger than $mv_z^2/2$, which writes $E > (p_z - qA_z)^2/2m$. The parabola has its apex in $p_z = qA_z$, which is a function of y. This demonstrates how the distribution function depends on y while g does not. When varying y, one varies A_z and the parabola is displaced. In so doing, different regions of the g function are explored in the (E, p_z) plane. The existence of these parabolas has actually already been pointed out in the early sixties in the pioneer works on this issue such as Refs. 24

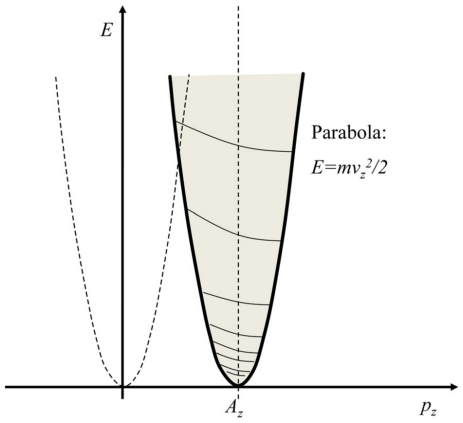

FIG. 1. (Color online) For each value of the normal coordinate y, the distribution function $f(\mathbf{v})$ is determined in the entire $\mathbf{v}$ space by the value of the function $g(E,p_z)$ in the only part of the (E,p_z) plane that is inside the drawn parabola. This parabola has its apex in $p_z = A_z(y)$ and, therefore, moves with y. The distribution function can thus vary in y, since the parabola explores different regions of the (E,p_z) plane.

and 25 (with a vertical displacement in addition, since the electrostatic field is not assumed null).

Turning to real space, the accessibility effect can be told in a more intuitive manner. If the distribution function is known at one y point, its value in the vicinity is imposed by the Vlasov equation (and the given magnetic field) only in a region limited by the individual particle trajectory extension, i.e., of the order of the Larmor radius. When going from y to $y + dy$, this means that the distribution function at the second point is constrained by the first one only for the particles that have a Larmor radius larger than $dy/2$. It can vary freely for all others, since none of them has a trajectory joining the two points. If all the particles present in the magnetopause were supposed to have a part of their trajectory in one of the two asymptotic sides (i.e., assuming a layer thinner than all the Larmor radii), one single profile could be determined, if any. Such assumptions were used until the 70's (sometimes leading to the false conclusion that kinetic equilibria of magnetopause-like layers don't exist), before it was realized that they cannot be realistic (see Ref. 26). In the distribution function, there are always particles inside the layer that don't pass by any of the asymptotic sides because of their small Larmor radii. Ignoring the accessibility problem amounts to disregarding these particles, which much biases the conclusions.

Even if the concept of accessibility is often forgotten in the context of the magnetopause-like layers, the necessity of dealing with it has, however, been known for long in different contexts. For example, particle trapping by an electrostatic or gravitational potential can lead to such limited accessibility. This is the case for instance in BGK (Bernstein-Green-Kruskal) equilibria,[27] for the solar wind expansion[28] or for the terrestrial polar wind.[29] For the magnetopause-like layers that we are dealing with, the accessibility question just arises from the only Larmor radius effect, without any external potential. Using the word "trapping" in this case (as sometimes done) would, therefore, be misleading. It is worth noticing, in particular, that the MHD results can be retrieved from the kinetic ones when the magnetopause gradients are much larger than all the Larmor radii. All particles should, therefore, be labeled as "trapped" in these conditions if this vocabulary was used. Contrarily, all the simplest theories consider that the trapped particles, if any, represent a minority component of the population.

Let us investigate now to what extent the single-value of f implies, or not, that g is also single-valued. In other words, we know that $f(\mathbf{v},y)$ has one single value for each given value of $\mathbf{v}$ and y, but does $g(E,p_z)$ also always have a single value, whatever the position y? Let us consider (Fig. 2) a magnetic field varying in y as a tanh function and, therefore, a current density varying as $1/\mathrm{ch}^2$ and a vector potential varying as ln(ch).

In the left ($y < 0$) side, A_z is a monotonic decreasing function of y. The functions $g(E,p_z)$ are then bound to be single-valued, as the distribution function $f(\mathbf{v},y)$ is. It can easily be understood. For a given y, the single-value of g inside the local parabola is a trivial consequence of that of f. Increasing y then amounts to displacing the parabola toward the left (smaller A_z), covering new parts of the (E,p_z) plane. In the part of the new parabola common with the previous one, g is already known and cannot change. It corresponds to particles with Larmor radii large enough to access the two locations. In the part newly covered, corresponding to particles that did not access the previous location but appear at the new one, g can be any new value but remains single-valued for the same reason as previously. The part newly uncovered corresponds to the particles that cannot access to

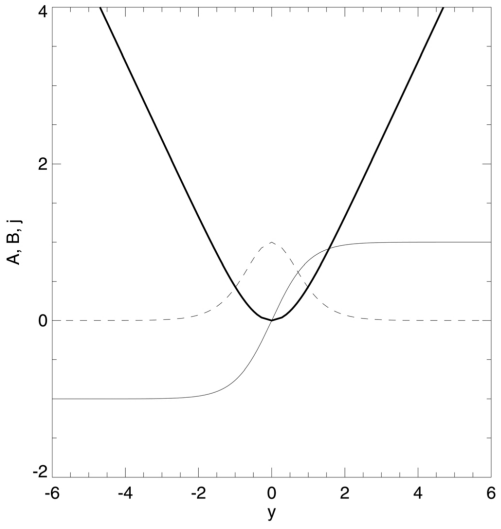

FIG. 2. Assumed variations for the vector potential A_z (bold), the magnetic field B, and the current density j (dashed) as functions of the normal coordinate y.

the new y and, therefore, have no influence on the distribution function at this point and further away.

The same argument holds for the right side ($y > 0$), where A_z is a monotonic increasing function of y. However, when considering the whole current sheet, i.e., the two sides of the $y = 0$ point simultaneously, A_z is no longer monotonic, and the notion of accessibility has an important consequence. When going from $y < 0$ to $y > 0$, the parabola goes first from the right to the left, till $y = 0$. It then goes back toward the right and covers again parts of the (E, p_z) plane, which have already been successively covered and uncovered in the $y < 0$ part. Uncovering parts actually means that the corresponding information has physically been lost. On the right side, the same invariants now correspond to different particles, independent of those on the left, which can, therefore, correspond to different values of g. In this way, one can get a double-valued function, g, of the invariants. One value corresponds to the left side and the other to the right side.

Thus, the distribution function depends on y only through the y dependence of A_z. It is important to understand that, with the assumptions done, the only way of getting distributions that are not symmetric in y when $A_z(y)$ is symmetric is for g to be double-valued. Because of the back and forth motion of A_z when y varies from $-\infty$ to $+\infty$, the distribution function necessarily has purely symmetric variations when g is single-valued in the (E, p_z) plane. Again, this is because the same parts of g are explored symmetrically in the two sides of the layer. Looking beyond the simplifying assumptions of this paper, this result can easily be generalized. If the magnetic field configuration implies some rotation, this brings the additional invariant p_x and, therefore, the component A_x of the vector potential. Similarly, if an electrostatic potential ϕ is present, it modifies the expression of the energy invariant. The equilibrium distribution thus depends in general on y through the three potentials A_z, A_x, and ϕ. An asymmetric equilibrium can then easily be found, even with single-valued functions g, when at least one of these potentials is not symmetric in y. The pressure is then modified by a diamagnetic effect on a single population. For this reason, the possibility of getting double-valued functions g has been disregarded in the literature hitherto.[7,11] However, adding the constraint that these two potentials are zero makes necessary to consider this important possibility (although it is not limited to this case). This has the big advantage of putting forward the main feature we are interested in: the existence of two populations of different origins on both sides of the tangential layer.

We have thus shown that using double-valued functions indeed allows asymmetric solutions to be constructed in any case, even with $A_x = 0$ and $\phi = 0$. In this case, it is worth noticing that, as will be seen in the results, a local symmetry around $y = 0$ is unavoidable, whenever one assumes the continuity of the distribution function and its first derivatives around the central parabola. The combination of this local symmetry and the global asymmetry will lead to density profiles which are never simple and monotonic. These profiles nevertheless seem to be close to the pseudo equilibria reached after about one gyroperiod when initializing a kinetic simulation with local Maxwellians. This point will be discussed in detail in a forthcoming paper.

III. METHOD

The goal of this paper is to construct a 1-D ion kinetic equilibrium with a localized current sheet. As a demonstration of feasibility, we simply assume that there is no electrostatic field (and therefore no ion bulk velocity shear between the two sides of the sheet) nor magnetic rotation. The method is semi-analytical.

We impose first the magnetic field profile as $B_x = \tanh(y/2)$. This analytical form provides simple expressions for the magnetic pressure, which can be expressed as well as a function of y or a function of the vector potential A_z, since:

$$B_x^2 = \tanh^2(y/2) = 1 - e^{-A_z}. \tag{1}$$

In these equations as in all the following, we work with normalized quantities: B_x stands for B_x/B_∞, y for y/λ, and A_z for $A_z/\lambda B_\infty$, where B_∞ is the magnetic field at infinity on both side (the magnetic field is supposed symmetric) and λ is the layer width. Similarly, the pressures, P and $B_x^2/2\mu_0$, will be normalized by B_∞^2/μ_0. The momentum p_z will also be consistently normalized as qA_z, the energy as p_z^2/m, and the temperature as E/k_B.

The current and vector potential profiles are thus imposed consistently, and we look for the ion distribution profiles that are consistent with these field data. For that, we have to make an assumption about the part of the current that is carried by the ions. In Harris sheet, the ratio between electron and ion currents is constant and equal to the electron-to-ion temperature ratio. In the hypotheses done for this equilibrium (drifting Maxwellian distributions for both ions and electrons, constant drift velocities, and no electrostatic field), this property just results from the quasi-neutrality condition. For the sake of simplicity, we here simply assume that the ions carry the whole electric current, which would also be the case, in the absence of electrostatic field, for perfectly cold electrons. Treating the more general case, with a non null electron current, hot electrons, and an electrostatic field, is kept for further works. It would demand *a priori* to apply the same method presented here to both species. It is worth noticing, however, that at the ion scales, the finite current carried by the electrons could probably be correctly calculated via a simple closure equation (a priori isothermal), as done in the numerical hybrid codes; the main difference with complete kinetic calculations, if any, would then likely be confined in very thin sub-layers, at the electron scales.

With the hypotheses done, the total plasma pressure is imposed to be

$$P = P_\infty + 1/2e^{-A_z}. \tag{2}$$

To reach the goal defined above, we use the same general method as usual, i.e., we write the ion distribution function under the form:

$$f(\mathbf{v}, \mathbf{r}) = g(E, p_z). \tag{3}$$

For the sake of simplicity and likelihood, the function g is supposed continuous, with continuous derivatives. As explained

above, g is supposed different on both sides of the layer, with two functions $g = g_l$ for $y < 0$ and $g = g_r$ for $y > 0$, respectively. The asymptotic states, for $p_z \to \infty$, are supposed Maxwellian on both sides, with temperatures T_1 and T_2: $g_l(E,\infty) = g_{l\infty}e^{-E/T_1}$ and $g_r(E,\infty) = g_{r\infty}e^{-E/T_2}$.

Between the two asymptotic states, i.e., for all values of y between $-\infty$ and $+\infty$, we choose the distribution to be made of two populations, labeled 1 and 2, in relation with the asymptotic temperatures T_1 and T_2 (in the example presented hereafter, the normalized temperatures are $T_1 = 0.5$ and $T_2 = 0.125$, corresponding to $p1 = p2 = 0.5$ and $n_1 = 1$, $n_2 = 4$). The general form chosen for the functions g_l and g_r is

$$g_s = g_{1s}e^{-E/T_1} + g_{2s}e^{-E/T_2}, \tag{4}$$

where s indicates the side and stands for l or r. The four functions g_{1l}, g_{2l}, g_{1r}, and g_{2r} can be in general functions of p_z and E. We will here take them as functions of $\delta p_z = p_z + \sqrt{2mE}$, which is the distance in p_z of a point (E, p_z) with the left boundary of the central parabola. Choosing them as functions of only p_z would also possible (and simpler), but our choice is guided by a reason of numerical accuracy, which will be explained just after.

In order to get functions with the right asymptotic behaviors and to have a sufficient number of free parameters to impose easily the desired constraints, all these functions are chosen of the form:

$$g_{ps} = g_{ps\infty} + \sum_{i=1}^{N} g_{psi}e^{-k_{si}\delta p_z}. \tag{5}$$

The $4N$ values of the parameters g_{psi} are the unknown to be determined. The subscript p indicates the population considered, 1 or 2, and the subscript i indicates the different components and runs from 1 to N (corresponding to the N values of k_{si}, with $k_{si} > 0$). In the example given hereafter, we choose $N = 10$. The values $g_{ps\infty}$ are the imposed values of g_{ps} for p_z infinite; these values derive directly from the asymptotic densities: the left density for $g_{1l\infty}$, the right density for $g_{2\gamma\infty}$, and zero for the two others. This means that the whole distribution is carried asymptotically by population 1 on the left side and population 2 on the right side, each population decreasing to zero on the opposite side.

The previous analytical form has the great advantage that all moments of the distribution functions have exactly the same formal expression in function of the potential vector, which allows the semi-analytical treatment. For the pressure component P_{yy}, which is involved in the pressure balance equation and which will be simply noted P here for simplicity, we have in particular:

$$P_{ps} = P_{ps\infty} + \sum_{i=1}^{N} g_{psi}P_{psi}e^{-k_{si}A_z}, \tag{6}$$

where each coefficient P_{psi} is the centered second order moment of the ith component of the distribution function of population p. All of these coefficients need to be calculated only once at the beginning of the program, by integrals over E and p_z of the given function.

As the sum of the two partial pressures must equal the total pressure imposed by (2), it is clear that

- the two population distributions have to contain the variation rate $k_1 = 1$ on both sides.
- the other terms have to cancel two by two, which explains why the variation rates k_{si} can depend on the side but not on the population.

The values of the other k_{si} rates can be chosen more or less arbitrarily, without noticeable influence on the result (in some limits). In the results presented hereafter, they have empirically been chosen all between 0.5 and 3. A special caution has to be taken anyway: all the rates, except the k_{s1}, must be different on each side to avoid getting an ill-determined system, the system solved hereafter having a zero determinant.

The constraint concerning the total pressure writes

$$\begin{aligned} g_{1s1}P_{1s1} + g_{2s1}P_{2s1} &= B^2/2\mu_o, \\ g_{1si}P_{1si} + g_{2si}P_{2si} &= 0. \end{aligned} \tag{7}$$

The subscript i runs from 1 to N, but the first equation, which involves a RH side, has been isolated. Because of the identity of the first rates k_{s1} on both sides, it is worth noticing that the corresponding pressure terms are also identical for the two populations: $P_{1l1} = P_{1r1}$ and $P_{2l1} = P_{2r1}$.

The second constraint to be taken into account is that the functions g_{1s} and g_{2s} are identical in the central parabola for $s = l$ and $s = r$. They are, furthermore, supposed continuous, with continuous derivatives. This is done, with a tunable accuracy, by imposing that g_{1s} and g_{2s} have identical expansions in δp_z around $\delta p_z = 0$ for $s = l$ and $s = r$, at the some order M ($M = 4$ in the example hereafter). This second constraint writes

$$\begin{aligned} (g_{pl1} - g_{pr1}) + \sum_{i=2}^{N}(g_{pli} - g_{pri}) &= g_{pr\infty} - g_{pl\infty}, \\ k_1^d(g_{pl1} - g_{pr1}) + \sum_{i=2}^{N}(k_{li}^d g_{pli} - k_{ri}^d g_{pri}) &= 0. \end{aligned} \tag{8}$$

The order of derivation d extends from zero to M, but the zero order, which has a non null RH side, has been isolated as above. The component 1 has also been isolated in each equation, the remaining sums, therefore, extending from $i = 2$ to N (in order to evidence that only the rate $k_1 = 1$ is the same on both sides, l and r).

The advantage of using δp_z instead of p_z is not major but can now be explained: using p_z would identify exactly the two functions in $p_z = 0$ and their values would be slightly different (depending on the expansion order) near the two edges of the central parabola. Taking into account the numerical results found, the difference shows actually to be larger on the left side than on the right one. The global error is thus smaller by equating the two functions on the left side and letting the small difference arise on the right one.

The problem being posed in these terms, let us describe finally the way of solving it. The imposed total pressure

profiles on both sides impose $2N$ relations. The identity of the expansions at order M on both sides for the two populations imposes $2M+2$ other ones. The number of variables is $4N$, since N coefficients have to be determined for each of the 4 functions. We, therefore, deal with a linear system with $2N+2M+2$ equations and $4N$ variables. For a given order M, this fixes a priori a minimum number of components $N=M+1$, since the number of equations to be verified would, otherwise, be larger than the number of variables to be determined. This minimum number would lead to a square matrix $(4N*4N)$ to be inverted, but the corresponding determinant would actually be zero because of the identity of k_{l1} and k_{r1} and that of P_{pl1} and P_{pr1}, which make the equations non independent. This means that only $4N-1$ independent variables could be determined by this way, one variable being left to a free choice. This is, however, a rather limited choice and does not allow a large variety of solutions.

We here prefer to choose $N=2(M+1)$, which gives much more freedom for choosing the resulting profiles. Practically, it is done by imposing the g profile of the first population on the left side, i.e., putting the N variables g_{1li} in the second member and solving the $3N*3N$ remaining system as a function of these N variables. Then, these N variables are chosen by minimizing the distance to some extra-condition. The nature of this extra-condition is now rather preliminary and may call for further studies. However, the choice that has been done in the present paper will be shown to yield satisfactory results, and it is explained in the next section.

IV. EXTRA-CONDITION: CHOICE OF A SIMPLE MODEL

As explained in the previous section, the method proposed in this paper provides one with an infinity of solutions, corresponding to N free parameters. Almost all of these solutions are physically admissible, since they all correspond to the imposed current profile and to the imposed asymptotic values for the ion distribution, and all verify the stationary Vlasov equation, granting a well verified pressure balance. The only restriction that has to be checked a posteriori is the strict positiveness of the distribution function for all velocities and all positions. Whenever this condition is verified, there is, indeed, no clear argument for choosing one solution rather than another, and one is free of selecting those which appear more convenient than others ("realistic," close to data, simple, likely, easily usable, or anything else).

Using arbitrary values for the N parameters yields various forms for the solutions, but all are observed to verify robust characteristics, concerning in particular the shape of the density profile, which is always thicker than the current density profile, and always displays an extremum in $y=0$ with one or more bounces of the curve outside. We will come back on these features later, but we have good confidence in that they are indeed physical properties of this kind of configuration. In order to present a controllable set of solutions, our program uses a model for one of the output profiles (here, the pressure P_2 of the second population) and minimizes the distance of the kinetic solution to this model. The model is analytical, simple, and with few free parameters. To guide efficiently the convergence process, the model must be such as, for each choice of its free parameters, it resembles as much as possible one of the kinetic solutions and respect the above characteristics. As a minimum, it must verify, in addition to the imposed asymptotic values, the local symmetry of the profiles around $y=0$, which derives from the continuity of the distribution function, as already mentioned at the end of section II. One important role of this model choice is to guide the kinetic solution toward kinetic distributions that are strictly positive everywhere.

Here is the analytical form that we used, guided by our experience of the various kinetic solutions found:

$$P_2 = P_{step} + P_{peak}. \tag{9}$$

The first term P_{step} corresponds to the asymmetric evolution of the considered population (pop. 2), which goes from 0 on the left to P_∞ on the right. It is supposed to be a double step in the form of two hyperbolic tangents:

$P_{step}/P_\infty = \tilde{P}_s/2 - \tilde{P}_s/2\tanh[k_l(A_z - A_{zl})]$, on the left, and

$P_{step}/P_\infty = (1+\tilde{P}_s)/2 + (1-\tilde{P}_s)/2\tanh[k_r(A_z - A_{zr})]$ on the right.

This term has a normalized value approximately equal to $\tilde{P}_s$ in $A_z=0$ whenever the shifts A_{zl} and A_{zr} are large enough so that the hyperbolic tangents are approximately equal to their asymptotic values $+1$ and -1 at the origin. This condition is indeed necessary in order that the derivatives are approximatively zero in $y=0$ and remains consistent with the local symmetry needed around this point. This means that this step component, even if it contributes to the pressure, does not contribute to the current density (since $dP/dA_z = j$). The current density is, therefore, entirely carried by the second term:

$$P_{peak}/P_\infty = \tilde{P}_p e^{-A_z},$$

which is of course fully symmetric and is associated with the symmetric current density profile. It is worth noticing that the negative values of $\tilde{P}_p$ correspond to a current carried by population 2 opposite to the neat current, while $\tilde{P}_p > 1$ corresponds to the same inversion for population 1. Fig. 3 shows the kind of model used in this paper and from which the kinetic solutions presented are deriving. It has been done with the following parameters, which make the model quite close to the found kinetic solutions: $k_l = 1/2$, $k_r = 1/3$, $A_{zl} = 2.5$, $A_{zr} = 4.5$, $\tilde{P}_s = 0.2$.

The curve set is obtained by varying $\tilde{P}_p$ from -0.2 to 1.8, range which grants positive model pressures for both populations for the given value of $\tilde{P}_s$. The kinetic solutions deriving from this model have distribution functions that are also strictly positive everywhere, except in the extreme case $\tilde{P}_p = -0.2$, where the model predicts a null pressure for the population 2 at the origin and where the kinetic solution displays there a small negative part in the distribution function. The bold curves in Fig. 3 corresponds to $\tilde{P}_p = 0.3$, which is selected for presenting the main results in the next section. In the next section, the kinetic solutions will be chosen in

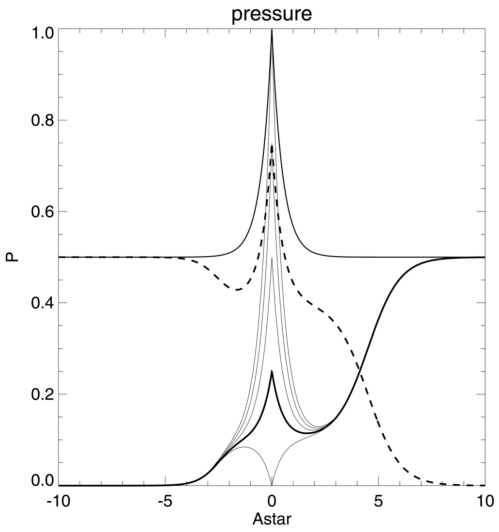

FIG. 3. Pressure of population 2 as produced by the simple model, in function of the symmetrized vector potential vector $A^* = A_z \text{sign}(y)$, for six values of the parameter $\tilde{P}_p$ (see text). The particular value marked by a thicker line corresponds to the value of $\tilde{P}_p$ used in the following results. The dashed line corresponds to the pressure of population 1 for the same particular $\tilde{P}_p$. The sum of both gives the total pressure (upper curve), which is imposed in all cases.

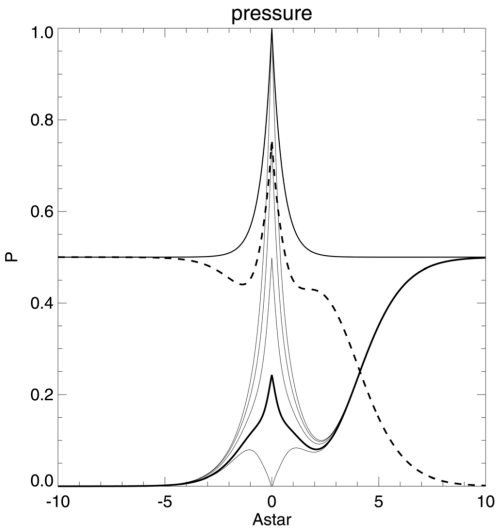

FIG. 4. Same format as Fig. 3, but for the kinetic solutions found. Its striking similarity with Fig. 3 proves that the simple model efficiently guides the convergence of the kinetic program.

minimizing the squared distance between it and the model, for the function itself and for its two first derivatives.

V. RESULTS

As explained above, all the kinetic solutions correspond to the same current density and the same total pressure P (let us recall that we have noted $P_{yy} = P$ by convenience). Contrary to the pressure, the density profile cannot be imposed and is a result of the calculation. It will thus be different for the different solutions. The same holds for the P_{xx} and P_{zz} components of the pressure tensor, which are also results of the calculation.

Let us first show that the simple model of the previous section resemble true kinetic solutions for the pressure function that has been chosen as a reference. Fig. 4 displays the same P_2 variations as Fig. 3, but for the true kinetic solutions found in minimizing their distance to the model. It can be checked that the two figures are very close to each other and that the choice of the model is, therefore, a satisfactory one. Other tries (not shown here) have proven that all the kinetic solutions have always properties that are quite close to these ones, with a maximum point in P_2 at the origin, a minimum one on one side, etc. If one starts with a very different model, the closest solution still keeps this kind of shape, but it is then quite difficult to control the output solution, for instance make the depth of the minimum vary. Fig. 5 shows the density profiles corresponding to the different kinetic solutions of Fig. 4. One can see that the profiles obtained can be different but that they all share some robust common characters:

- the density profiles are all more or less corrugated, but with always an extremum, more or less pronounced, at the center $y = 0$ of the layer.
- the effective thickness of the density profile is thicker and more complex than the current profile. It seems to always present a "depletion region" in the dense (right) side.

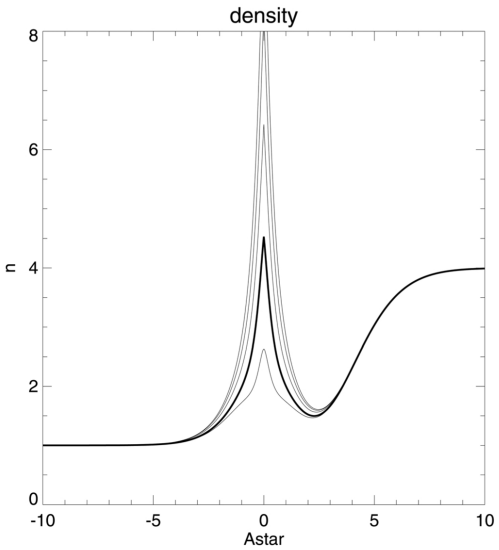

FIG. 5. Density profiles corresponding to the different P_2 profiles of Fig. 4. Same format as this figure.

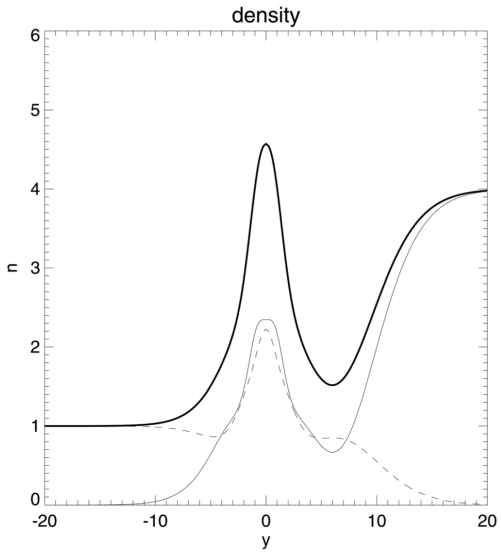

FIG. 6. Density profile as a function of the normal coordinate y. The thin lines show the contributions of the two populations, with T_1 (left temperature, dashed line) and T_2 (right temperature).

Let us now focus on the particular solution obtained with $\tilde{P}_p = 0.3$. Fig. 6 reproduces the same density profile as the bold curve of Fig. 5, but expressed as a function of the normal coordinate y instead of the vector potential. In addition, the partial densities of the two populations 1 and 2 are superposed as dashed lines to show what are their contributions on both sides.

Fig. 7 shows the distribution functions on both sides of $y = 0$ as functions of p_z. It can be checked that the two sides share the same function in the central parabola, but that they depart from each other when going to $-\infty$ or $-\infty$. It can be checked also that the variations are continuous with continuous derivatives on both sides.

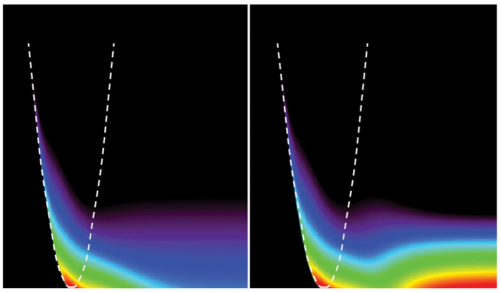

FIG. 7. (Color online) Distribution functions in the (E, p_z) plane. The left panel corresponds to the left side ($y < 0$) of the null sheet and vice versa. The central parabola ($y = 0$) is marked by dashed lines for reference on both panels. The two distributions must be identical in this parabola.

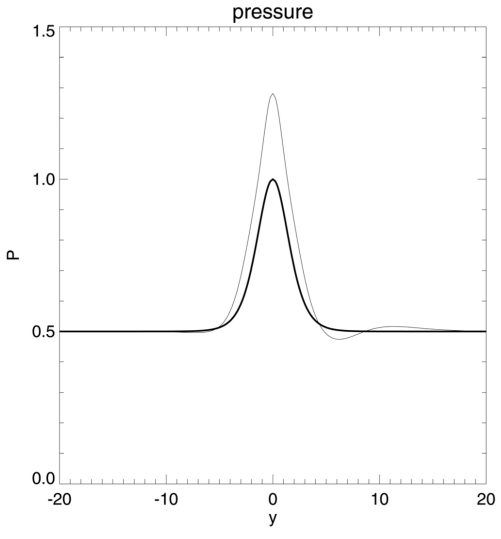

FIG. 8. Pressure components p_{yy} (bold) and p_{zz} as functions of y. The component p_{xx} is, by construction, equal to the p_{zz} one.

Looking finally at the pressure components, one gets the Fig. 8, where the profiles of the two components P_{yy} and P_{zz} are plotted. The first one is imposed directly by the current density, and one can see how the second departs from it in the current layer while both are supposed equal asymptotically. The P_{xx} component is equal to the P_{zz} one, and all the other components are zero. These symmetries can easily be understood. In particular, the identity of P_{xx} and P_{zz} directly derives directly from the fact that the functions g of the invariants are independent of p_x. As explained in Sec. II, this property itself comes from the fact that the distributions have been supposed isotropic and Maxwellian asymptotically on both sides. This unavoidably leads to this surprising "gyrotropy" around the direction z, which is not the direction of the magnetic field.

VI. DISCUSSION AND CONCLUSION

This paper provides one with a practical manner of constructing kinetic equilibria for a 1-D tangential geometry for the case of an asymmetric layer with a reversing magnetic field (magnetopause-like layers). For the sake of clarity, the paper focuses on the simplest geometry, with a pure B_x field varying from $-B_\infty$ to B_∞ in the normal y direction and, therefore, being strictly zero in the center of the layer, but the main results can be easily generalized.

The paper emphasizes that, in order to get an asymmetric layer, it is necessary that the ion distribution, expressed in terms of the motion invariants, be a double-valued function. This necessity is indeed due to the adopted assumptions: no magnetic field rotation and no electrostatic field, but the possibility of double-valued functions discovered at this occasion is actually an interesting result in itself: it is not limited

to these restricting assumptions and brings a new and potentially important ingredient when looking for general solutions. It is explained thanks to the concept of accessibility.

An infinity of solutions are shown to be found in this manner, all respecting the pressure balance with a good accuracy and corresponding to distribution functions continuous in space (including the null sheet $B = 0$ in the center of the layer), with continuous derivatives. For selecting some of these solutions, an extra-condition has to be introduced. The one used in this paper is just an example and different ones should be investigated in the future.

Some important properties, common to all solutions, have been evidenced and interpreted: due to the continuity of the distribution function, the plasma profiles have to be locally symmetric at the center of the layer, in spite of the globally asymmetrical layer. This generally results in unavoidable oscillations of the density profile. As a consequence, the density layer is always wider than the current layer. Due to the assumed isotropy of the asymptotic distributions, the pressure tensor is "gyrotropic" around the direction y normal to the layer, but not with respect to the x direction of the magnetic field.

Are the previous properties generic or can they due to the calculation technique or the simplifying hypotheses (no rotation, no electric field)? To answer this question, experimental and numerical tests can be envisaged. (1) Determining experimental profiles at the magnetopause would be actually difficult, because of the spatio-temporal ambiguity when using a single spacecraft (which is necessary to study such small scales with the existing missions) and because it may be hard to find the needed configuration in the data, i.e., crossings of a magnetic null sheet in sufficiently stationary conditions. (2) With the usual simulations, which are initialized with local Maxwellians, one cannot find stationary solutions, as explained in Introduction. Nevertheless, one can look to snapshots of the fluctuating profiles and check whether they present or not the characteristic features evidenced in this paper: extremum of the density profile at $y = 0$, corrugated profiles for both population densities, and pressure gyrotropy around the y direction. First results using a hybrid simulation provide strong indications that the results are generic. These results will be presented in a next paper. (3) The main validation of the quality of the equilibria found consists of course in implementing it as a kinetic initialization and checking directly the stationarity of the solution. Using the same hybrid code as above, this test has been done, and the results, quite satisfactory, will also be published soon.

All equilibria are not stable. Knowing which are stable or not, what are the instabilities at work, are questions which were unreachable hitherto since no realistic equilibria were available. This new possibility is now open for many future investigations.

ACKNOWLEDGMENTS

The authors acknowledge Carrie Black for her kind reading of the manuscript and her improvements of the English quality and Masha Kuznetsova for fruitful discussions.

[1]H. P. Furth, J. Killeen, and M. N. Rosenbluth, Phys. Fluids **6**, 459 (1963).
[2]K. B. Quest and F. V. Coroniti, J. Geophys. Res. **86**, 3289, doi:10.1029/JA086iA05p03289 (1981).
[3]S. A. Fuselier, K. J. Trattner, and S. M. Petrinec, J. Geophys. Res., [Space Phys.] **116**, A10227 (2011).
[4]*Magnetic Reconnection: MHD Theory and Applications*, edited by E. Priest and T. Forbes, (Cambridge University Press, New York, 2000).
[5]*Magnetic Reconnection in Plasmas*, Cambridge Monographs on Plasma Physics Vol. **3**, edited by D. Biskamp (Cambridge University Press, Cambridge, UK, 2000 xiv), 387 p.
[6]E. Harris, Il Nuovo Cimento (1955–1965) **23**, 115 (1962).
[7]L. C. Lee and J. R. Kan, J. Geophys. Res. **84**, 6417, doi:10.1029/JA084iA11p06417 (1979).
[8]M. Roth, J. de Keyser, and M. M. Kuznetsova, Space Sci. Rev. **76**, 251 (1996).
[9]M. M. Kuznetsova and M. Roth, J. Geophys. Res. **100**, 155, doi:10.1029/94JA02329 (1995).
[10]F. Mottez, Phys. Plasmas **10**, 2501 (2003).
[11]T. Neukirch, F. Wilson, and M. G. Harrison, Phys. Plasmas **16**, 122102 (2009).
[12]W. Daughton, Phys. Plasmas **6**, 1329 (1999).
[13]H. Karimabadi, W. Daughton, P. L. Pritchett, and D. Krauss-Varban, J. Geophys. Res., [Space Phys.] **108**, 1400 (2003).
[14]A. Sestero, Phys. Fluids **8**, 739 (1965).
[15]D. M. Willis, Rev. Geophys. Space Phys. **9**, 953, doi:10.1029/RG009i004p00953 (1971).
[16]S. W. H. Cowley, "Theoretical perspectives of the magnetopause: A tutorial review," in *Physics of the Magnetopause*, edited by P. Song, B. U. O. Sonnerup, and M. F. Thomsen (The American Geophysical Union, Washington, DC, 1995), p. 29.
[17]P. L. Pritchett, J. Geophys. Res., [Space Phys.] **113**, A06210 (2008).
[18]P. Angelino, A. Bottino, R. Hatzky, S. Jolliet, O. Sauter, T. M. Tran, and L. Villard, Phys. Plasmas **13**, 052304 (2006).
[19]G. Dif-Pradalier, V. Grandgirard, Y. Sarazin, X. Garbet, and P. Ghendrih, Commun. Nonlinear Sci. Numer. Simul. **13**, 65 (2008).
[20]P. J. Channell, Phys. Fluids **19**, 1541 (1976).
[21]F. Mottez, Ann. Geophys. **22**, 3033 (2004).
[22]E. C. Whipple, J. R. Hill, and J. D. Nichols, J. Geophys. Res. **89**, 1508, doi:10.1029/JA089iA03p01508 (1984).
[23]J. De Keyser and M. Roth, J. Geophys. Res. **103**, 6653, doi:10.1029/97JA03710 (1998).
[24]H. Grad, Phys. Fluids **4**, 1366 (1961).
[25]A. Sestero, Phys. Fluids **7**, 44 (1964).
[26]W. Alpers, Astrophys. Space Sci. **11**, 471 (1971).
[27]I. B. Bernstein, J. M. Greene, and M. D. Kruskal, Phys. Rev. **108**, 546 (1957).
[28]I. Zouganelis, M. Maksimovic, N. Meyer-Vernet, H. Lamy, and K. Issautier, Astrophys. J. **606**, 542 (2004).
[29]Y. T. Chiu and M. Schulz, J. Geophys. Res. **83**, 629, doi:10.1029/JA083iA02p00629 (1978).

— I —

Earth Magnetpause characteristic scales

	Magnetosheath	Magnetosphere
Magnetic field	$B \sim 60$ nT	$B \sim 60$ nT
Electric field	$E \sim 6$ mV.m^{-1}	$E \sim 0.6$ mV.m^{-1}
Electron Density	$n \sim 50 \times 10^6$ m^{-3}	$n \sim 5 \times 10^6$ m^{-3}
Temperature	$T_i \sim 200$ eV	$T_i \sim 2$ keV
	$T_e \sim 50$ eV	$T_e \sim 600$ eV
Kinetic pressure	$P_i \sim 10 \times 10^6$ keV.m^{-3}	$P_i \sim 10 \times 10^6$ keV.m^{-3}
	$P_e \sim 3 \times 10^6$ keV.m^{-3}	$P_e \sim 3 \times 10^6$ keV.m^{-3}
Magnetic pressure	$P_M \sim 10 \times 10^6$ keV.m^{-3}	$P_M \sim 10 \times 10^6$ keV.m^{-3}
Characteristic lengths	$\lambda_{Di} \sim 20$ m	$\lambda_{Di} \sim 200$ m
	$\lambda_{De} \sim 10$ m	$\lambda_{De} \sim 100$ m
	$\rho_{Li} \sim 30$ km	$\rho_{Li} \sim 100$ km
	$\rho_{Le} \sim 400$ m	$\rho_{Le} \sim 1.5$ km
	$c/\omega_{Pi} \sim 30$ km	$c/\omega_{Pi} \sim 100$ km
	$c/\omega_{Pe} \sim 700$ m	$c/\omega_{Pe} \sim 2$ km
Characteristic frequencies	$f_{Ci} \sim 1Hz$	$f_{Ci} \sim 1Hz$
	$f_{Ce} \sim 1.5$ kHz	$f_{Ce} \sim 1.5$ kHz
	$f_{Pi} \sim 1.5$ kHz	$f_{Pi} \sim 500$ Hz
	$f_{Pe} \sim 60$ kHz	$f_{Pe} \sim 20$ kHz
Characteristic velocities	$V_A \sim 200$ km.s^{-1}	$V_A \sim 600$ km.s^{-1}
	$V_{thi} \sim 200$ km.s^{-1}	$V_{thi} \sim 600$ km.s^{-1}
	$V_{the} \sim 4000$ km.s^{-1}	$V_{the} \sim 15{\times}10^3$ km.s^{-1}
	$C_s \sim 200$ km.s^{-1}	$C_s \sim 600$ km.s^{-1}

Table I.1: The Earth magnetopause thickness is ~ 800 km.

— J —

HEDP characteristic scales

	HED Plasmas	Space Plasmas
Magnetic field	100 T	60 nT
density	10^{27} m^{-3}	10^{7} m^{-3}
Temperature	400 eV	200 eV
Resistivity (Spitzer)	10^{-7} Ωm	0
Lundqvist Numb.	200	∞
Beta parameter	100	1
Ion cyclotron freq.	1.7 GHz	1 Hz
Ion skin depth	10 μm	30 km
Alfvén speed	20 km.s^{-1}	200 km.s^{-1}
Sound speed	200 km.s^{-1}	200 km.s^{-1}
Ion thermal speed	300 km.s^{-1}	200 km.s^{-1}

Table J.1: Characteristic scales in HEDP and solar wind at $\sim$ 1 AU.

— K —

The HECKLE code

Normalization

The relevant quantities are normalized as

$$m = \widetilde{m}\, m_p \tag{K.1}$$
$$q = \widetilde{q}\, e \tag{K.2}$$
$$N = \widetilde{N}\, N_o \tag{K.3}$$
$$B = \widetilde{B}\, B_0 \tag{K.4}$$

m_p is the proton mass, e the elementary charge, and n_0 et B_0 the standard particle density and magnetic field. Hence

$$v = \widetilde{v}\, V_A \tag{K.5}$$
$$t = \widetilde{t}\, \Omega_C^{-1} \tag{K.6}$$
$$l = \widetilde{l}\, c\Omega_P^{-1} \tag{K.7}$$
$$E = \widetilde{E}\, V_A B_0 \tag{K.8}$$

where Ω_C and Ω_P are the proton cyclotron pulsation and proton plasma pulsation, respectively. Hereinafter, normalized quantities are written omitting tildas.

Equations

The macroparticle motion is obtained by integration of

$$d_t \mathbf{x}_{s,h} = \mathbf{v}_{s,h} \tag{K.9}$$
$$m_s d_t \mathbf{v}_{s,h} = q_s(\mathbf{E} + \mathbf{v}_{s,h} \times \mathbf{B} - \eta \mathbf{J}) \tag{K.10}$$

Where s index is standing for the specie of particle and h index for the index of the particle. Density and fluid velocity result from the summation

$$N(\mathbf{x}) = \Sigma_{s,h} q_s S(\mathbf{x} - \mathbf{x}_{s,h})$$
$$\mathbf{V}(\mathbf{x}) = \Sigma_{s,h} \mathbf{v}_{s,h} S(\mathbf{x} - \mathbf{x}_{s,h}) / \Sigma_{s,h} S(\mathbf{x} - \mathbf{x}_{s,h})$$

$S(\mathbf{x})$ is the first order shape factor. Neglecting the transverse component of the displacement current, and assuming quasineutrality, the Maxwell equations are

$$\begin{aligned} \partial_t \mathbf{B} &= -\boldsymbol{\nabla} \times \mathbf{E} \\ \mathbf{J} &= \boldsymbol{\nabla} \times \mathbf{B} \end{aligned}$$

and the needed Ohm's law is

$$\mathbf{E} = -\mathbf{V} \times \mathbf{B} + N^{-1}(\mathbf{J} \times \mathbf{B} - \boldsymbol{\nabla}.\mathbf{P}_e) + \eta \mathbf{J} - \eta' \Delta \mathbf{J}$$

where η is resistivity and η' is hyperviscosity.
The electron pressure tensor $\mathbf{P}_e$ can be either isotherm ($P_e = NT_e$) or adiabatic. In fact, we also consider the possibility of a heat flux $\mathbf{q} = -\kappa \boldsymbol{\nabla} T_e$. Assuming the "entropy" of the plasma is $S = P_e n^{-\gamma}$ with $\gamma = 5/3$, the equations can be written

$$\partial_t s + \mathbf{u}_e.\boldsymbol{\nabla} S = (\gamma - 1)\kappa n^{-\gamma} \boldsymbol{\nabla}(S n^{\gamma - 1})$$

$\mathbf{u}_e$ being the electron flow ($\mathbf{u}_e = \mathbf{V} - \mathbf{J}/N$).

Few definitions

In direction i (standing for x, y and z), one defines the thermal velovity $V_{Ti}^2 = \langle V_i^2 \rangle / 2 = k_B T_i / m$. For isotrop and gyrotrop plasma, $V_T^2 = V_{Tx}^2 = V_{Ty}^2 = V_{Tz}^2$.
Magnetic pressure & energy :

$$E_B = \frac{B^2}{2}$$

Generalized momentum :

$$\mathbf{p}_s = m_s \mathbf{v}_s + q_s \mathbf{A}$$

Kinetic pressure :

$$P_s = n_s m_s V_{Ts}^2 = n_s T_s$$

Thermic energy :

$$E_{Ts} = \frac{3}{2} n_s T_s = \left\langle \frac{n_s m_s v_s^2}{2} \right\rangle = \frac{3}{2} n_s m_s V_{Ts}^2$$

Plasma Beta :

$$\beta = \sum_s \beta_s = \sum_s \frac{2 n_s m_s V_{Ts}^2}{B^2} = \sum_s \frac{2 n_s T_s}{B^2}$$

Thermal Larmor radius :

$$\rho_{Ls} = \frac{2m_s V_{Ts}}{B} = \frac{2}{B}\left(\frac{T_s}{m_s}\right)^{1/2} = \left(\frac{2\beta_s}{n_s m_s}\right)^{1/2}$$

Thermal velocity :

$$V_{Ts} = \left(\frac{T_s}{m_s}\right)^{1/2} = \left(\frac{\beta_s B^2}{2n_s m_s}\right)^{1/2}$$

Alfven velocity :

$$V_A = \frac{B}{n^{1/2}} = \left(\frac{2\sum_s n_s m_s V_{Ts}^2}{\beta \sum_s n_s}\right)^{1/2} = \left(\frac{2\sum_s n_s T_s}{\beta \sum_s n_s}\right)^{1/2}$$

The "Buneman" pusher (Boris 1970)

The main equation is

$$\frac{\mathbf{v}_{n+1/2} - \mathbf{v}_{n-1/2}}{\Delta t} = \frac{q}{m}\left[\mathbf{E}_n + \left(\frac{\mathbf{v}_{n+1/2} + \mathbf{v}_{n-1/2}}{2}\right) \times \mathbf{B}_n\right]$$

Defining

$$\mathbf{v}_{n-1/2} = \mathbf{v}^- - \frac{q\mathbf{E}_n}{m}\frac{\Delta t}{2} \qquad , \qquad \mathbf{v}_{n+1/2} = \mathbf{v}^+ + \frac{q\mathbf{E}_n}{m}\frac{\Delta t}{2}$$

Hence, the equation to solve is

$$\frac{\mathbf{v}^+ - \mathbf{v}^-}{\Delta t} = \frac{q}{2m}(\mathbf{v}^+ + \mathbf{v}^-) \times \mathbf{B}_n$$

Θ is the rotation angle between $\mathbf{v}^+$ and $\mathbf{v}^-$, $\left|\tan\frac{\Theta}{2}\right| = \frac{|\mathbf{v}^+ - \mathbf{v}^-|}{|\mathbf{v}^+ + \mathbf{v}^-|} = t = \frac{qB_n}{m}\frac{\Delta t}{2}$

Defining the intermediate v' quantity as

$$\mathbf{v}' = \mathbf{v}^- + \mathbf{v}^- \times \mathbf{t} \qquad , \qquad \mathbf{v}^+ = \mathbf{v}^- + \mathbf{v}' \times \mathbf{s}$$

To get $|\mathbf{v}^+| = |\mathbf{v}^-|$, one needs $s = \frac{2}{1+t^2}$.

Lets summerize :

$$F = \frac{q\Delta t}{2m} \qquad , \qquad G = \frac{2}{1 + B_n^2 F^2}$$

$$\begin{aligned} \mathbf{s} &= \mathbf{v} + F\mathbf{E}_n \\ \mathbf{u} &= \mathbf{s} + F(\mathbf{s} \times \mathbf{B}_n) \\ \mathbf{v} &= \mathbf{s} + G(\mathbf{u} \times \mathbf{B}_n) + F\mathbf{E}_n \end{aligned}$$

The algorithm

PREDICTOR :

- $\mathbf{v}_{n+1/2} = \mathbf{v}_{n-1/2} + \dfrac{q\Delta t}{m_p}\left[\mathbf{E}_n + \dfrac{\mathbf{v}_{n+1/2} + \mathbf{v}_{n-1/2}}{2} \times \mathbf{B}_n\right]$
- $\mathbf{x}_{n+1} = \mathbf{x}_n + \Delta t \mathbf{v}_{n+1/2}$
- $\mathbf{N}_{n+1/2} = \Sigma_s q_s (S_n + S_{n+1})/2, \quad \mathbf{V}_{n+1/2} = \Sigma_s (S_n + S_{n+1})\mathbf{v}_{n+1/2}/2\mathbf{N}_{n+1/2}$
- $\mathbf{B}_{n+1/2} = \mathbf{B}_n - \dfrac{\Delta t}{2}\boldsymbol{\nabla} \times \mathbf{E}_n$, and $\mathbf{J}_{n+1/2} = \boldsymbol{\nabla} \times \mathbf{B}_{n+1/2}$
- $\mathbf{P}_{n+1/2}$ with the appropriate law.
- $\mathbf{E}_{n+1/2} = -\mathbf{V}_{n+1/2} \times \mathbf{B}_{n+1/2} + \dfrac{1}{N_{n+1/2}}\left(\mathbf{J}_{n+1/2} \times \mathbf{B}_{n+1/2} - \boldsymbol{\nabla} P_{n+1/2}\right) + \eta \mathbf{J}_{n+1/2}$
- $\mathbf{E}_{n+1} = -\mathbf{E}_n + 2\mathbf{E}_{n+1/2}$
- $\mathbf{B}_{n+1} = \mathbf{B}_{n+1/2} - \dfrac{\Delta t}{2}\boldsymbol{\nabla} \times \mathbf{E}_{n+1}$, and $\mathbf{J}_n = \boldsymbol{\nabla} \times \mathbf{B}_{n+1}$

CORRECTOR :

- $\mathbf{v}_{n+3/2} = \mathbf{v}_{n+1/2} + \dfrac{q\Delta t}{m_p}\left[\mathbf{E}_{n+1} + \dfrac{\mathbf{v}_{n+3/2} + \mathbf{v}_{n+1/2}}{2} \times \mathbf{B}_{n+1}\right]$
- $\mathbf{x}_{n+2} = \mathbf{x}_{n+1} + \Delta t \mathbf{v}_{n+3/2}$
- $\mathbf{N}_{n+3/2} = \Sigma_s q_s (S_{n+1} + S_{n+2})/2, \quad \mathbf{V}_{n+3/2} = \Sigma_s (S_{n+1} + S_{n+2})\mathbf{v}_{n+3/2}/2\mathbf{N}_{n+3/2}$
- $\mathbf{B}_{n+3/2} = \mathbf{B}_{n+1} - \dfrac{\Delta t}{2}\boldsymbol{\nabla} \times \mathbf{E}_{n+1}$, and $\mathbf{J}_{n+1/2} = \boldsymbol{\nabla} \times \mathbf{B}_{n+1/2}$
- $\mathbf{P}_{n+1/2}$ with the appropriate law.
- $\mathbf{E}_{n+3/2} = -\mathbf{V}_{n+3/2} \times \mathbf{B}_{n+3/2} + \dfrac{1}{N_{n+3/2}}\left(\mathbf{J}_{n+3/2} \times \mathbf{B}_{n+3/2} - \boldsymbol{\nabla} P_{n+3/2}\right) + \eta \mathbf{J}_{n+3/2}$
- $\mathbf{E}_{n+1} = \dfrac{1}{2}(\mathbf{E}_{n+1/2} + \mathbf{E}_{n+3/2})$
- $\mathbf{B}_{n+1} = \mathbf{B}_{n+1/2} - \dfrac{\Delta t}{2}\boldsymbol{\nabla} \times \mathbf{E}_{n+1}$, and $\mathbf{J}_n = \boldsymbol{\nabla} \times \mathbf{B}_{n+1}$

Initialization

The magnetic field is initialized with the needed profile. The electric field results from the Ohm's law, and thus need not to be prescribed. The resistivity is increased near walls if not periodic. Protons (alfas...) and electrons temperature are analytically determined on the grid points.

The density profile is prescribed analytically. The weight of macro-particles is the same for all particles of specie s. The number of particles injected in each cell is linear to the local density divided by the integrated density over the whole box. To

work properly, we generally use 100 particles per cells.

A drift velocity is calculated to hold $\mathbf{J} = \boldsymbol{\nabla} \times \mathbf{B}$. We use the classical relation $J_s/T_s = \text{const}$ for each species s including electrons.
The particle velocity is determined using the Box & Muller algorithm. a and b standing for random numbers between 0 and 1 with a normal distribution, the particle velocity in direction i is

$$\sqrt{\frac{-2\ln(a)T_{si}}{m_s}}cos(2\pi b)$$

Grid definition

This code uses a simple grid representation (no Yee lattice). There is 2 grids, shifted from a half grid size. They are called `G1` and `G2`.
In one direction (both X Y and Z directions are equivalents), lets call L the size of the domain, N the number of grid cells and Δ the grid size. Of course,

$$\Delta = \frac{L}{N}$$

The `G1` grid has $N + 1$ grid points associated to N cells. Grid point labelled 0 is located at $X = 0$ and grid point labelled N is located at $X = L$.
The `G2` grid has $N + 2$ grid points associated to $N + 1$ cells. Grid point labelled 0 is located at $X = -\Delta/2$, and grid point labelled $N + 1$ is located at $X = L + \Delta/2$.
Only the magnetic field is defined on `G1`. All others quantities (electric field, electron pressure and temperature, density, fluid density, current density) are defined on `G2`. This choice is of course motivated by the centered form of the Maxwell-Faraday equation and the leap-frog scheme to push the particles. This results in an interpollation for the electron pressure tensor when integrating the Ohm's law.

Boundary conditions

Because of the definition of the 2 grids, the magnetic field results from the shape of the electric field ; only the electric field needs a boundary conditions when the code is non-periodic.

Calling N the normal direction to the boundary, and T the tangential direction, We set for the electric field

$$d_N E_N = 0, \mathbf{E}_T = 0$$

For the density, it is simply $d_N n = 0$.
For the current density and fluid velocity, we use fluid conditions to keep the plasma in the domain, and thus anihilate the flux,

$$J_N = 0, d_N \mathbf{J}_T = 0$$

To limit wave reflections at the boundaries of the domain, we set a small resistivity, increased near the walls : multiplied by 5 two grid points before the limit of the domain, multiplied by 25 one grid point before the limit of the domain, and multiplied by 125 on the boundary of the domain.

Constraints on the code

- The parameters used in classical run for $\beta = 1$ are $\Delta L = 0.4$ and $\Delta t = 0.005$.
- Grid size : it has to resolve correctly the cyclotron turn of particles. If this value is too large, any bulk velocity in perpendicular direction will be converted in velocity of gyromotion (perpendicular heating). Take at least 3 grid size for the thermal larmor radius.
- Time step : it has to satisfy the CFL condition for the faster mode : generally the whistler mode (at least in parallel direction). For this mode, $\omega \propto k^2$, meaning that time step has to evolve as the square of the grid size... The CFL associated to particle velocity is far less constraining.
- There is no clear lower limit for the grid size, except that at one point it will cost to much in time step.
- As there is no Maxwell-Gauss equation associated to neutrality, the plasma pulsation is not resolved.
- A smooth is used for the moments associated to particles : density and fluid velocity. If not, the energy conservation is generally better, but the code can turn instable, generally because the density gets too low at some given points.

Yet, the only clear acceptable way to manage this is to feed the simulation to prevent density holes.

- A small resistivity is also used. It is supposed to have some nice consequences on the stability... We use a value of 0.0001, but its role is note that clear.